TECHNISCHE UNIVERSITÄT MÜNCHEN

Lehrstuhl E23 für Technische Physik

Walther-Meißner-Institut für Tieftemperaturforschung
der Bayerischen Akademie der Wissenschaften

Magnon Hybrid Dynamics

Lukas Liensberger

Vollständiger Abdruck der von der Fakultät für Physik der Technischen Universität München zur Erlangung des akademischen Grades eines

Doktors der Naturwissenschaften

genehmigten Dissertation.

Vorsitzender:	Prof. Dr. Michael Knap
Prüfer der Dissertation:	1. Prof. Dr. Rudolf Gross
	2. Prof. Dr. Mathias Weiler

Die Dissertation wurde am 26.04.2021 bei der Technischen Universität München eingereicht und durch die Fakultät für Physik am 03.06.2021 angenommen.

Abstract

Magnons are the quantized excitations of an exchange-coupled spin system in a magnetically ordered material. Magnons can couple to other quantized excitations such as photons, phonons, plasmons etc. or other types of magnon modes, forming so-called hybridized modes. Such modes in magnon hybrid systems are potential candidates for novel systems for information storage. In such hybrid systems coherent exchange of information between the constituent modes requires strong coupling, where the effective coupling rate between the systems exceeds the loss rates of the two respective systems.

The focus of this thesis is the investigation of novel coupling mechanisms and approaches by measuring the magnetization dynamics of the magnon hybrid system. To this end, electrical detection techniques as well as spatially-resolved optical spetroscopy methods are used. We apply broadband magnetic resonance using a coplanar waveguide or cavity-based magnetic resonance spectroscopy, the established microfocused Brillouin light scattering or the novel microfocused frequency-resolved magneto-optic Kerr effect and the microfocused super-Nyquist sampling magneto-optic Kerr effect technique. In particular, we investigate the spin dynamics of the compensated ferrimagnet gadolinium iron garnet using broadband magnetic resonance. We find ultrastrong magnon-magnon coupling where the intralayer exchange interaction amplifies the coupling rate. We also study the magnon-photon coupling between a three-dimensional microwave cavity and the skyrmion host material Cu_2OSeO_3 . Here, we demonstrate the tunability of the magnon-photon cooperativity, which is a measure of the coherent exchange of interaction, at the magnetic phase boundaries using an external control parameter. Finally, the linear and non-linear magnon dynamics of a micro-patterned magnonic waveguide with an on-chip antenna is investigated using optical techniques. Here, we focus on the spatially-resolved characterization of the magnetization dynamics and use novel phase-sensitive techniques to detect the three-magnon scattering processes. We model and explain our findings, leading to a better understanding on how to utilize the spin degree of freedom of the electron for potential new spintronic applications.

Kurzfassung

Magnonen sind die quantisierten Anregungen eines austauschgekoppelten Spinsystems in einem magnetisch geordneten Material. Magnonen können mit anderen quantisierten Anregungen wie Photonen, Phononen, Plasmonen etc. oder anderen Magnonenmoden wechselwirken und dadurch so genannte hybridiseirte Moden bilden. Diese Moden in Magnon-Hybridsystemen ermöglichen viel versprechende Konzepte für neuartige Informationsspeicher. In solchen Hybridsystemen erfordert der kohärente Austausch von Infromation zwischen den konstituierenden Moden eine starke Kopplung. Hierbei bedeutet starke Kopplung, dass die effektive Kopplungsrate zwischen den Systemen größer ist als die Verlustraten der beiden einzelnen Systeme.

Der Schwerpunkt dieser Arbeit liegt auf der Untersuchung neuartiger Kopplungsmechanismen und -ansätze durch Messung der Magnetisierungsdynamik des Magnon-Hybridsystems. Zu diesem Zweck werden elektrische Detektionstechniken, wie Breitband Magnetresonanzspektroskopie unter Verwendung eines koplanaren Wellenleiters oder hohlraumbasierte Magnetresonanztechniken, sowie ortsaufgelöst optische Spektroskopieverfahren, wie die etablierte mikrofokussierte Brillouin-Lichtstreuung oder die neuartige mikrofokussierte frequenzaufgelöste magnetooptische Kerr-Effekt Methode und die mikrofokussierte Super-Nyquist-Abtastung magnetooptische Kerr-Effekt Technik, verwendet. Insbesondere untersuchen wir die Spindynamik des kompensierten Ferrimagneten Gadolinium Eisengranat unter Verwendung von Breitband Magnetresonanzspektroskopie, wo wir ultrastarke Magnon-Magnon-Kopplung, die durch die Intralayer-Austauschwechselwirkung verstärkt wird, beobachten. Die Magnon-Photon-Kopplung zwischen einem dreidimensionalen Mikrowellenresonator und dem Skyrmionen-Material Cu_2OSeO_3 wird untersucht. Es wird gezeigt, dass die Magnon-Photon-Kooperativität, die ein Maß für den kohärenten Austausch von Wechselwirkungen ist, durch einen externen Steuerparameter an den magnetischen Phasengrenzen stark verändert und beeinflusst werden kann. Abschließend wird die lineare und nichtlineare Magnonendynamik eines mikrostrukturierten magnonischen Wellenleiters mit einer On-Chip Antenne mithilfe optischer Messtechniken untersucht. Der Schwerpunkt liegt hier auf der ortsaufgelösten Charakterisierung der Magnetisierungsdynamik und der Verwendung neuer phasensensitiver Techniken zur Detektierung der Drei-Magnonen-Streuung. Wir modellieren und erklären unsere Ergebnisse, die zu einem besseren Verständnis der Fragestellung beitragen können, wie der Spinfreiheitsgrad des Elektrons für potenzielle, neue spintronische Anwendungen genutzt werden kann.

Contents

1 Introduction

For over half a century, the semiconductor silicon has proven to be a reliable and universal material in the modern technological industry. It is the key ingredient of the highly successful hardware platform for our today's information and communicatoin technology. The applications range from sensors to integrated circuits such as microprocessors or memory devices. These are routinely integrated in large numbers in todays smartphones, personal computers and servers enabling novel digital applications such as cloud-based computing. The demand for more computational power has been satisfied by increasing the clock speed, and by downscaling the transistor size, allowing to feature more transistors. With decreasing feature size, the current density increases, limiting the increase of the maximum clock frequency due to Joule heating [1]. With the advancement in lithography tools such as extreme ultraviolet (EUV) lithography [2], the semiconductor industry was able to follow the prediction of Gordon Moore [3] that the number of transistors on an integrated circuit or chip doubles about every two years (Moore's law), until today. Nowadays, semiconductor manufacturer are working on sub-10 nm process nodes to satisfy the everlasting demand for more computational power.

Downscaling the feature size on the integrated circuits does not only involve more challenging fabrication procedures and a drastic increase of research investments but also means that physical limits especially quantum effects become more relevant as the features scale down to a few tens of atoms. To overcome these problems either novel semiconductor materials are required or new physical approaches are necessary. One idea is to not only utilize the electric charge of the electron but also its spin degree of freedom. In 1988, the so-called giant magnetoresistance (GMR) was discovered [4, 5], where the relative orientation of the magnetization of two ferromagnetic layers separated by a normal metal controls the electrical conductivity. The parallel spin alignment leads to a smaller electrical resistance than the anti-parallel spin alignment [6]. The discovery of the GMR was awarded with the Nobel Price in physics in 2007. The change in resistivity depending on the relative spin orientation becomes larger when replacing the normal metal with an insulator, leadint to the so-called tunneling magnetoresistance (TMR) [7]. Since the mid 1990s, read heads in hard disk drives were based on the GMR and were later replaced by TMR-based read heads, which are still in use [8]. The associated huge increase of storage density in hard disks is a key prerequisite for our today's information search via internet.

In general, the field of spintronics studies the control and manipulation of the spin degree of freedom of electrons in a solid-state system. The most notable technological product is the magnetoresistive random access memory (MRAM). The MRAM consists of two magnetic layers separated by a tunnel barrier, where the magnetization direction of one magnetic layer is fixed and the other magnetic layer can be switched. The state of high and low resistance corresponds to “0” and “1” [9]. The desire for more computational power is accompanied by a huge increase of generated data and interim results need to be stored and accessed quickly. The MRAM has comparable or even faster read/write cycles than static or dynamic random access memory (SRAM or DRAM) and is referred as the “universal memory” [10, 11]. The advantage of the MRAM is its non-volatility (in contrast to SRAM and DRAM) at fast read/write speeds. Currently novel MRAM technologies are in development which are the spin-transfer torque RAM (STT-RAM) or the spin-orbit torque RAM (SOT-RAM) [12–14]. Another novel spintronic-based memory application are three-dimensional device approaches such as racetrack memories [15–18], where mechanical parts are absent in the storage device.

These are only some examples of spintronic-based approaches to enhance the functionality of existing devices. In addition to these potential applications in information storage, novel applications are also envisaged in information processing and information transport based on excitations of the magnetically ordered ground state, so-called spin waves or magnons. The advantage of spin wave-based processing is the possibility of vector-based calculations, the intrinsic operation frequencies in the range from GHz to THz and the minimal structure size limited by the lattice constant of the material [19, 20]. To this end, it is necessary to identify and characterize potential material systems. The materials can either be characterized by their static or dynamic properties. The latter one is especially important with regard to processing applications.

Fundamentally, the MRAM and the racetrack memory are based on the dynamics of the magnetization. Therefore, the understanding and control of the magnetization dynamics is key for the realization of these devices and to develop novel approaches. One attempt are hybrid devices where the dynamics of the magnetization is coupled to an external degree of freedom. This is realized by coupling the magnetic system to other physical systems such as a photonic, a phononic or another magnonic system [21–23]. The coupling of the quantized excitations of the subsystems (magnons, photons, phonons) leads to so-called hybridized modes – the quantized excitations of the coupled system. Within this thesis we investigate a novel coupling mechanism between magnons and magnons in a compensated ferrimagnet, where the coupling strength is enhanced by the exchange interaction and we demonstrate magnon-photon coupling between the skyrmion host material Cu_2OSeO_3 and a microwave

cavity. This might open the exciting perspective for topological systems and qubit systems [24].

In order to measure magneto-dynamical phenomena, measurement techniques with high sensitivity are necessary. Within this thesis, we study the magnetization dynamics in the GHz regime. The used measurement techniques are based on fully electric measurement techniques, such as broadband magnetic resonance spectroscopy using a coplanar waveguide or a three-dimensional microwave cavity. These techniques probe the uniform dynamics of the magnetization within a certain penetration depth. For the characterization of micro-patterned samples, generally optical measurement techniques are more suited to probe the dynamical properties locally. To this end, we developed a novel optical spectroscopy method called micro-focused frequency-resolved Kerr effect (μFR-MOKE), where the magnetization dynamics can be captured in a spatially- and phase-resolved manner.

This thesis is organized as follows: In Chapter 2, we start with a phenomenological description of the magnetization dynamics in a simple macrospin model. We herein introduce the concept of the effective magnetic field and derive the characteristic equation of motion of the magnetization namely the Landau-Lifshitz-Gilbert equation. Furthermore, we solve the equation of motion for the uniform precessional mode of the magnetic moments, which is the so-called ferromagnetic resonance. As a result, we calculate the resonance frequency of the uniform mode as a function of the external magnetic field and thus derive the Kittel equations. The concepts introduced herein will be further extended in the following Chapters.

In Chapter 3, we measure ultrastrong magnon-magnon coupling enhanced by the intralayer exchange interaction in the compensated ferrimagnet gadolinium iron garnet (GdIG). The Chapter starts with an introduction to the general properties of GdIG and we discuss the magnetization dynamics in a two-sublattice system. Close to the compensation temperature of GdIG, the system mimics the dynamics of an antiferromagnet. Experimentally the magnon-magnon coupling is investigated using broadband magnetic resonance spectroscopy with a coplanar waveguide. We demonstrate the tunability of the coupling strength due to the axial symmetry breaking induced by the small cubic anisotropy in the system depending on the direction of the external magnetic field. We model our findings with the concept of magnon hybridization and exchange-enhancement, which is confirmed by analytical and numerical calculations. Our results present a novel coupling mechanism, where the exchange interaction amplifies the originally small coupling rate of the cubic anisotropy by more than one order of magnitude.

In Chapter 4, we demonstrate the tunability of the magnon-photon cooperativity of the skyrmion host material Cu_2OSeO_3 in a three-dimensional microwave cavity using an external control parameter. Starting with an introduction to the material system Cu_2OSeO_3, we will discuss the unique properties of the rich uniform magnon

spectrum and explain the hybridized magnon-photon spectrum in the framework of the input-output formalism. The magnon-photon coupling is investigated using magnetic resonance spectroscopy using a microwave cavity (loop-gap resonator). From the measured data we extract the effective coupling rate and the loss rate of the magnons and photons, respectively. We show that the unique excitation geometry of the magnon modes in Cu_2OSeO_3 can be used to drastically change the magnon-photon cooperativity at the magnetic phase boundaries by changing the external magnetic field by a few mT.

In Chapter 5, we investigate the magnetization dynamics in a micro-patterned magnonic waveguide in the linear and non-linear regime using spatially-resolved optical spectroscopy techniques. The focus of this Chapter is on propagating magnon modes (spin waves) and on optical measurement techniques based on the magneto-optic Kerr effect (MOKE). In this Chapter, we start with an introduction to the dynamics of dipolar-exchange spin waves and derive a simplified form of the Kalinikos-Slavin equation describing the wavevector-dependence of the spin wave resonance frequency. Next, we discuss the details of the MOKE and how to excite and detect spin waves using different optical techniques, which rely on different detection principles. We show that in the linear regime of the magnetization dynamics the different measurement methods lead to the same results and that the phase-sensitive techniques are additionally able to capture the wavevector of the excited spin waves. In the non-linear regime we demonstrate the capability of the novel techniques to capture the non-linearly generated spin waves due to three-magnon scattering, which was previously only possible with Brillouin light scattering.

Finally, in Chapter 6 we summarize our results and give a brief outlook.

2 Phenomenological Description of Magnetization Dynamics

The term spin dynamics refers to the time-dependent and dynamical properties of a single spin, an ensemble of spins or the coherent spin manipulation [25]. The spin is a relativistic quantum mechanical property of particles and contributes to the total magnetic moment [26]. In an atom, the electron exhibits the largest magnetic moment due to its smaller mass compared to the proton by roughly a factor of 1840 and is responsible for magnetism in condensed matter systems [27]. In an applied magnetic field, Zeeman energy tend to align these magnetic moments parallel to magnetic field. However, there are also other effects forcing the moments to point in a particular direction such as magnetocrystalline or shape anisotropy. In magnetism, the related energies are expressed in terms of effective magnetic fields (cf. Section 2.1). Together with the applied magnetic field, they are adding up to a total effective field. In a simple picture, the magnetic moments being not parallel to the effective magnetic field experience a torque, in analogy to a compass needle. Due to the huge number of magnetic moments in a solid of macroscopic dimensions, the magnetization is introduced which is the sum over all individual magnetic moments of the spins normalized to the volume of the solid [28].

The equilibrium position of the system is reached when the magnetic moments are aligned along with the effective magnetic field. This state is reached after a finite amount of time in a dynamical process of the magnetization. These dynamic processes have invoked large attention in the research community and is known as the research field of magnetization dynamics. Depending on the type of excitation, like, e.g., an externally applied magnetic field, and on the involved interaction energies, the time scale of the spin dynamics differs. In general, spin dynamics is divided into so-called ultrafast spin dynamics happening in a time range of 10 fs to 1 ps and fast spin processes happening on the time scale between 1 ps and 100 ns [25, 29]. At ultrafast time scales, in particular the de- and re-magnetization processes are investigated by the laser-induced ultrafast demagnetization technique which was first realized by Beaurepaire *et al.* [30]. In this thesis, we will restrict ourselves to processes with timescales between sub-ns and a few hundred ns. In these timescales, the temporal dynamics of the precession of the magnetization and its damping characteristics occur [31].

In this chapter, we introduce a simple classical model to describe the spin dynamics in a single-domain ferromagnet and the equation of motion, the so-called Landau-Lifshitz-Gilbert equation (LLG). Here, we are using a continuums approach in the macrospin approximation where we are considering a single-lattice system. In the classical approximation, we assume the magnetic moments coupled by the Heisenberg exchange-interaction can follow the dynamics of their neighbors in a uniform way. This assumption will be abrogated in Chapter 5 when we discuss spin waves with a finite wavelength λ. The uniform precession is therefore the special case of a spin wave with wavelength $\lambda \to \infty$. In the second part of this chapter we derive the resonance condition of the uniform precession mode which is also known as the ferromagnetic resonance described mathematically by the Kittel equations. This chapter is foundational for the following chapters where we extend the presented model in Chapter 3 to describe the spin dynamics in a coupled two-sublattice system and in Chapter 4 to understand the dynamics of a chiral magnet coupled to a microwave cavity. An extensive discussion about magnetization dynamics can be found in Refs. [32–35].

2.1 Macrospin Model

We start our discussion by introducing the measurable macroscopic quantity of the magnetization $\boldsymbol{M}$ which is the sum of all magnetic moments $\boldsymbol{\mu}$ of the electrons in the volume V of the solid-state

$$\boldsymbol{M} = \frac{1}{V} \sum_{\boldsymbol{\mu}_i \in V} \boldsymbol{\mu}_i. \tag{2.1}$$

We assume that the single magnetic moments are ferromagnetically exchange coupled via the quantum-mechanical Heisenberg interaction [36]. This continuum approach is applicable due to the large number of electrons per volume ($\approx 10^{28}\,\mathrm{m}^{-3}$) [26], where a quantum-mechanical description of the coupled electron dynamics is not feasible. We introduce here the normalized magnetization $\boldsymbol{m} = \boldsymbol{M}/M_\mathrm{s} = [m_x\ m_y\ m_z]^\mathsf{T}$ with the saturation magnetization M_s.

Additional to the externally applied magnetic field $\boldsymbol{H}_0$, we need to take the internal fields stemming from, e.g., magnetic anisotropy into account. Therefore, we need to introduce the effective magnetic field $\boldsymbol{H}_\mathrm{eff}$ which is given by [37]

$$\mu_0 \boldsymbol{H}_\mathrm{eff} = -\left(\frac{\partial}{\partial m_x}, \frac{\partial}{\partial m_y}, \frac{\partial}{\partial m_z}\right) F_\mathrm{m} = -\nabla_{\boldsymbol{m}} F_\mathrm{m} \tag{2.2}$$

with the free energy density F_m. In the following we want to discuss the most relevant free energy density contributions to F_m for this thesis:

Zeeman energy

The Zeeman interaction describes the interplay between a magnetic moment or magnetization with an external magnetic field. The corresponding Zeeman energy density is given by [35, 38]

$$F_{\mathrm{Z}} = -\mu_0 \boldsymbol{M} \cdot \boldsymbol{H}_0. \tag{2.3}$$

It is important to note that for the Zeeman interaction only real magnetic fields are relevant and not molecular- or exchange fields [38]. The effective field stemming from the Zeeman energy is derived by plugging in Eq. (2.3) into Eq. (2.2) and is simply given by $\boldsymbol{H}_{\mathrm{Z}} = \boldsymbol{H}_0$.

Exchange energy

The quantum-mechanical exchange interaction occurs due to spin-spin interaction of electrons in combination with the Pauli-principle. Without derivation, the strength of this interaction is given by the exchange constant J_{ij} given by the exchange integral [38, 39]. In the Heisenberg-model the free energy density reads [39]

$$F_{\mathrm{ex}} = -\frac{1}{V} \sum_{i<j,\,\mathrm{n.n.}} J_{ij} \boldsymbol{S}_i \cdot \boldsymbol{S}_j \tag{2.4}$$

with the spin operators $\boldsymbol{S}_{i,j}$. The sum is iterated over all nearest neighbor (n.n.) pairs of spins. The exchange constant J_{ij} can either be positive ($J_{ij} > 0$) leading to a preferred parallel alignment of neighbouring spins, which is also known as ferromagnetic coupling, or negative ($J_{ij} < 0$) which results in an anti-parallel alignment of adjacent spins, which is known as antiferromagnetic coupling. In order to simplify this expression, we assume a spatially constant exchange parameter $J_{ij} = J$ and that the exchange energy is dependent on the relative angle θ_{ij} between the spins. The absolute size of the spin vector should also be equal ($S_i = S_j = S$). Equation (2.4) becomes

$$F_{\mathrm{ex}} = -\frac{JS^2}{V} \sum_{i<j,\,\mathrm{n.n.}} \cos\left(\theta_{ij}\right) \approx -\frac{JS^2 N_{\mathrm{n.n.}}}{V} + \frac{JS^2}{2V} \sum_{i<j,\,\mathrm{n.n.}} \theta_{ij}^2, \tag{2.5}$$

where in the second step we Taylor expanded $\cos(x) \approx 1 - x^2/2 + \ldots$ in the limit of small angles θ_{ij}. The first term is constant while the second term describes the spatially varying exchange energy and is usually smaller than the first term. The relative angle change θ_{ij} can also be expressed as a change

in distance between the spins and as a further consequence in a change in magnetization $\boldsymbol{M}$. Assuming a cubic lattice this simplifies to [39, 40]

$$F_{\mathrm{ex}} = -\frac{JS^2 N_{\mathrm{n.n.}}}{V} + A\left(\frac{\nabla \boldsymbol{M}}{M_{\mathrm{s}}}\right)^2, \tag{2.6}$$

with the exchange stiffness constant $A = S^2 a^2 J N_{\mathrm{n.n.}}/(2V)$, cubic lattice constant a, number of next neighbours $N_{\mathrm{n.n.}}$ and spin number S. For $Co_{25}Fe_{75}$ the exchange stiffness is $A = 2.6 \times 10^{-11}$ J/m [41]. Note that the second term is especially interesting in the discussion of magnetic excitations like spin waves which will be done in Chapter 5.

Uniaxial anisotropy

The magnetocrystalline anisotropy leads to a preferred crystallographic direction of the magnetization due to the finite Spin-Orbit coupling because the orbitals of the $3d$- and $4f$-electrons are not spheric but have a complicated form. This leads to a different overlap of the quantum-mechanical wave functions of neighbouring atoms and as a consequence to different energies [38]. One possible magnetocrystalline anisotropy is the uniaxial anisotropy which has one preferred axis and an isotropic plane perpendicular to it. The preferred direction of the uniaxial anisotropy is given by the unit vector $\boldsymbol{u}$. If we assume the preferred axis of the uniaxial anisotropy to be along the z-direction ($m_x^2 + m_y^2 = 1 - m_z^2$), we get for the corresponding free energy density [34, 35, 38]

$$F_{\mathrm{u}} = K_{\mathrm{u1}}(\boldsymbol{u} \cdot \boldsymbol{m})^2 = K_{\mathrm{u1}}(1 - m_z^2), \tag{2.7}$$

where we only account for terms of the uniaxial anisotropy to the first order. For the effective field $\boldsymbol{H}_{\mathrm{eff}}$, we get [35]

$$\mu_0 \boldsymbol{H}_{\mathrm{u}} = -\frac{2K_{\mathrm{u1}}}{M_{\mathrm{s}}}\,\hat{\boldsymbol{e}}_z. \tag{2.8}$$

Cubic anisotropy

Another possible magnetocrystalline anisotropy is the cubic anisotropy, where the reversal of the magnetization $\boldsymbol{M}$ and the switching of two orthogonal axes must not affect the free energy density [35]. The free energy density becomes [34, 35, 38]

$$F_{\mathrm{c}} = K_{\mathrm{c1}}(m_x^2 m_y^2 + m_x^2 m_z^2 + m_y^2 m_z^2) + K_{\mathrm{c2}}\, m_x^2 m_y^2 m_z^2, \tag{2.9}$$

where only terms of 4th and 6th order occur. To derive an expression for the effective field, we use Eq. (2.2), insert F_c and get [35]

$$\mu_0 \boldsymbol{H}_\mathrm{c} = -2K_{\mathrm{c}1} \begin{bmatrix} m_x(m_y^2+m_z^2) \\ m_y(m_x^2+m_z^2) \\ m_z(m_x^2+m_y^2) \end{bmatrix} - 2K_{\mathrm{c}2} \begin{bmatrix} m_x m_y^2 m_z^2 \\ m_y m_x^2 m_z^2 \\ m_z m_x^2 m_y^2 \end{bmatrix}. \tag{2.10}$$

Note that for the magnetocrystalline anisotropies it may be necessary to transform the coordinate system because the easy and hard axis of the anisotropy crucially depend on the specific crystal lattice. We will pick up on this topic in Chapter 3, where we will discuss the importance of magnetocrystalline anisotropies to describe mode coupling in a compensated ferrimagnet.

Shape anisotropy

In a finite sized sample, the magnetic field inside the sample differs in magnitude depending on the direction of the magnetic field due to the so-called demagnetization field. The demagnetization field arises due to induced magnetic charges at the surface of the sample, which are generating a magnetic field opposing the stray field [32, 38]. For simplicity, we assume a uniform demagnetization field inside an ellipsoid where the main axes of the ellipsoid coincide with the principle axes of the coordinate system. The free energy density then reads [40]

$$F_\mathrm{d} = \frac{\mu_0}{2} \boldsymbol{M} \overleftrightarrow{N} \boldsymbol{M} = \frac{\mu_0}{2} \sum_{i,j \in \{x,y,z\}} N_{ij} M_i^2, \tag{2.11}$$

with the demagnetization tensor

$$\overleftrightarrow{N} = \begin{bmatrix} N_{xx} & 0 & 0 \\ 0 & N_{yy} & 0 \\ 0 & 0 & N_{zz} \end{bmatrix}. \tag{2.12}$$

Note that the demagnetization tensor $\overleftrightarrow{N}$ is only diagonalized in the principal axes coordinate system of an ellipsoid [40]. For the remaining demagnetization factors N_{ii}, the relation $N_{xx} + N_{yy} + N_{zz} = 1$ holds and can be calculated by the equations provided by J. A. Osborn [42]. The demagnetization field can be calculated with Eq. (2.2) to

$$\mu_0 \boldsymbol{H}_\mathrm{d} = \mu_0 \overleftrightarrow{N} \boldsymbol{M}. \tag{2.13}$$

The assumption of a uniform demagnetization field is not sufficient in the discussion of micropatterned magnonic waveguides for propagating spin waves. In Chapter 5 we will modify the description of the dipolar fields.

The effective field is consequently the sum of all internal fields. For didactic reasons we will not consider the magnetocrystalline anisotropy and furthermore, we neglect the second term of the exchange field $\boldsymbol{H}_{\mathrm{ex}}$ where we assume a spatially homogenous magnetization and fully parallel magnetic moments [43]. The effective field is then given by

$$\boldsymbol{H}_{\mathrm{eff}} = \boldsymbol{H}_0 + \boldsymbol{H}_{\mathrm{d}} = \boldsymbol{H}_0 - \overleftrightarrow{N}\boldsymbol{M}. \tag{2.14}$$

In a classical picture, we can consider the magnetization $\boldsymbol{M}$ as a vector and the effective field $\boldsymbol{H}_{\mathrm{eff}}$ generates a torque $\boldsymbol{\tau}$ to the magnetization. This leads to a precession of the magnetization with an angular frequency ω around the effective field as depicted in Fig. 2.1. The magnetization $\boldsymbol{M}$ therefore has an angular momentum $\boldsymbol{J}$ which is given by [35]

$$\boldsymbol{M} = -\gamma \frac{\boldsymbol{J}}{V} \tag{2.15}$$

connected by the gyromagnetic ratio $\gamma = g\mu_{\mathrm{B}}/\hbar$ with the Landé-factor g, the Bohr magneton μ_{B} and the reduced Planck constant $\hbar = h/(2\pi)$. The torque τ is the rate of change of angular momentum which leads to

$$\boldsymbol{\tau} = \frac{\mathrm{d}\boldsymbol{J}}{\mathrm{d}t} = -\frac{V}{\gamma}\frac{\mathrm{d}\boldsymbol{M}}{\mathrm{d}t} = -V\mu_0 \boldsymbol{M} \times \boldsymbol{H}_{\mathrm{eff}}, \tag{2.16}$$

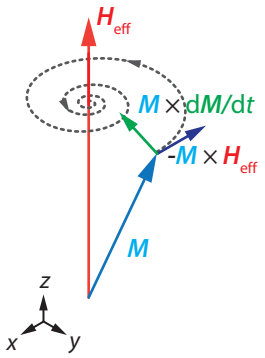

Fig. 2.1. Schematic model in the macrospin approach where the magnetization $\boldsymbol{M}$ is precessing around the effective magnetic field $\boldsymbol{H}_{\mathrm{eff}}$. We assume that the static external field $\boldsymbol{H}_0$ is parallel to the effective magnetic field $\boldsymbol{H}_{\mathrm{eff}}$.

where $\mu_0 = 1.256\,637\,061 \times 10^{-6}\,\mathrm{V\,s/(A\,m)}$ is the vacuum permeability. Reordering the variables leads to the Landau-Lifshitz equation [44]

$$\frac{\mathrm{d}\boldsymbol{M}}{\mathrm{d}t} = -\gamma\mu_0 \boldsymbol{M} \times \boldsymbol{H}_{\mathrm{eff}}. \tag{2.17}$$

This equation describes a sustained precession of the magnetization $\boldsymbol{M}$ around the effective magnetic field $\boldsymbol{H}_{\mathrm{eff}}$ as depicted in Fig. 2.1.

In the ideal case, the magnetization will precess forever around the effective field at a fixed cone angle due to the absence of damping in Eq. (2.17). In a real physical system, different dissipation mechanisms can occur like magnon-phonon relaxation, two-magnon scattering, eddy currents [25, 45] or radiative damping [46]. Disregarding the physical nature of the loss channels, we formulate the damping

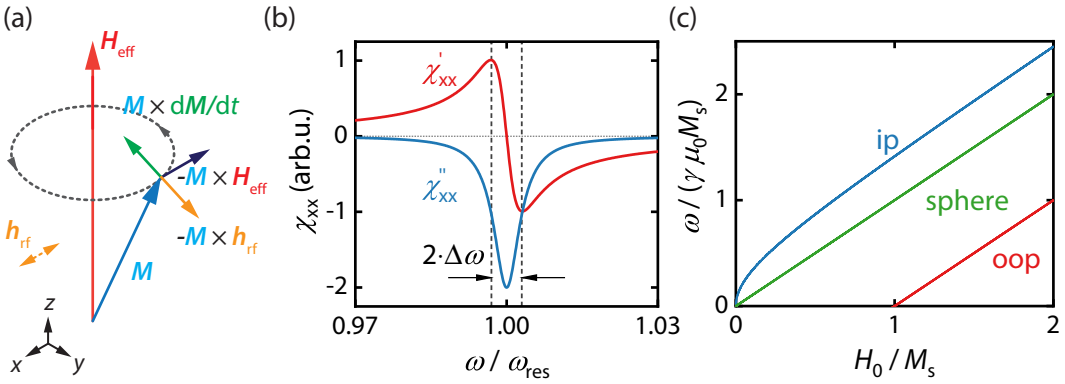

Fig. 2.2. Ferromagnetic Resonance. (a) Schematic depiction of the ferromagnetic resonance where the magnetization $\boldsymbol{M}$ precesses at a fixed cone angle due to the additional driving torque ($-\boldsymbol{M} \times \boldsymbol{h}_{\mathrm{rf}}$) opposing the damping torque ($\boldsymbol{M} \times \mathrm{d}\boldsymbol{M}/\mathrm{d}t$) due to the oscillating driving field $\boldsymbol{h}_{\mathrm{rf}}$. (b) Real and imaginary part of the $\chi_{xx} = \chi'_{xx} + i\chi''_{xx}$ component of the Polder-susceptibility. (c) Resonance frequency ω derived from the Kittel equation [Eq. (2.27)] where the solutions of the three discussed cases namely in-plane (ip), out-of-plane (oop) and sphere are shown.

term according to T. Gilbert who added a phenomenological, material-dependent damping parameter α [47]. This leads to the Landau-Lifshitz-Gilbert equation (LLG)

$$\frac{\mathrm{d}\boldsymbol{M}}{\mathrm{d}t} = -\gamma\mu_0 \boldsymbol{M} \times \boldsymbol{H}_{\mathrm{eff}} + \frac{\alpha}{M_{\mathrm{s}}} \boldsymbol{M} \times \frac{\mathrm{d}\boldsymbol{M}}{\mathrm{d}t}. \tag{2.18}$$

The second term in the above equation leads to a parallel alignment of the magnetization $\boldsymbol{M}$ with the effective field $\boldsymbol{H}_{\mathrm{eff}}$ after a finite time, which is the equilibrium position of the magnetization. This process is schematically depicted in Fig. 2.1. This system can be understood as a damped harmonic oscillator in classical mechanics. In the following section we will derive the resonance condition in the presence of an additional oscillating magnetic field.

2.2 Ferromagnetic Resonance

In the previous section, we have discussed the dynamical process of the magnetization without any external perturbation. In this case, the magnetization aligns with the effective field after a finite relaxation time. Now, an oscillating magnetic field $\boldsymbol{h}_{\mathrm{rf}}$ perpendicular to the effective field $\boldsymbol{H}_{\mathrm{eff}}$ is introduced as depicted in Fig. 2.2(a). The idea is to drive the magnetization away from its equilibrium orientation. If the frequency of the oscillating field matches the precessional frequency of the magnetization, the torque generated by the oscillating driving field $\boldsymbol{h}_{\mathrm{rf}}$ is compensating the damping torque $\boldsymbol{M} \times \mathrm{d}\boldsymbol{M}/\mathrm{d}t$, resulting in a magnetization precession with constant opening angle of the precession cone. This is analogous to a driven harmonic oscillator in classical mechanics. For the derivation of the resonance frequency the external

oscillating field $\boldsymbol{h}_{\mathrm{rf}}$ is not absolutely necessary as the resonance frequency is independent of $\boldsymbol{h}_{\mathrm{rf}}$. For didactic reasons we still keep $\boldsymbol{h}_{\mathrm{rf}}$ in the derivation. The following paragraphs are adapted in main parts from Ref. [48].

We start our derivation by assuming the effective field to point along the z-direction $\boldsymbol{H}_{\mathrm{eff}} \parallel z$ in a finite sized sample with the shape of a rotational ellipsoid with demagnetization tensor components N_{xx}, N_{yy} and N_{zz} and the oscillating driving field to lie in the xy-plane $\boldsymbol{h}_{\mathrm{rf}}(t) = [h_{\mathrm{rf},x}(t)\ h_{\mathrm{rf},y}(t)\ 0]^{\mathsf{T}}$. Adding this oscillating field to the effective field, the effective magnetic field H_{eff} modifies to

$$\boldsymbol{H}_{\mathrm{eff}} = \boldsymbol{H}_0 + \boldsymbol{H}_{\mathrm{d}} + \boldsymbol{h}_{\mathrm{rf}}(t) = \begin{bmatrix} -N_{xx}M_x^{\sim} \\ -N_{yy}M_y^{\sim} \\ H_0 - N_{zz}M_{\mathrm{s}} \end{bmatrix} + \begin{bmatrix} h_{\mathrm{rf},x}(t) \\ h_{\mathrm{rf},y}(t) \\ 0 \end{bmatrix}, \tag{2.19}$$

where the first term is the time-independent and the second term the time-dependent part of the total magnetic field. Here, we disregarded all anisotropy contributions other than shape-anisotropy. We already took into account that the driving field is also attenuated by the demagnetizing field by the dynamic components of the magnetization $\boldsymbol{M}^{\sim}(t)$. The total magnetization $\boldsymbol{M}$ can also be split into a time-independent $\boldsymbol{M}_0$ and time-dependent part $\boldsymbol{M}^{\sim}(t)$, that is

$$\boldsymbol{M} = \boldsymbol{M}_0 + \boldsymbol{M}^{\sim}(t) = \begin{bmatrix} 0 \\ 0 \\ M_{\mathrm{s}} \end{bmatrix} + \begin{bmatrix} M_x^{\sim}(t) \\ M_y^{\sim}(t) \\ 0 \end{bmatrix}. \tag{2.20}$$

We restrict ourselves to the magnetization dynamics in the linear regime where the opening cone of the magnetization relative to the effective field is supposed to be small. This assumption is equivalent to $|\boldsymbol{h}_{\mathrm{rf}}| \ll |\boldsymbol{H}_0|$ and $M_x, M_y \ll M_z$. Furthermore, we have used in Eq. (2.20) that the absolute value of the magnetization does not change ($|\boldsymbol{M}| = M_{\mathrm{s}}$) [45] and is pointing along its equilibrium position and consequently along $\boldsymbol{H}_{\mathrm{eff}}$. In the linear regime, we use an harmonic ansatz for the magnetization and oscillating magnetic field

$$\begin{aligned} \boldsymbol{h}_{\mathrm{rf}}(t) &= \begin{bmatrix} h_{\mathrm{rf},x} & h_{\mathrm{rf},y} & 0 \end{bmatrix}^{\mathsf{T}} \cdot e^{i\omega t}, \\ \boldsymbol{M}^{\sim}(t) &= \begin{bmatrix} M_x^{\sim} & M_y^{\sim} & 0 \end{bmatrix}^{\mathsf{T}} \cdot e^{i\omega t}. \end{aligned} \tag{2.21}$$

Plugging Eqs. (2.19)-(2.21) into the Landau-Lifshitz-Gilbert equation [Eq. (2.18)], results in

$$i\omega \begin{bmatrix} M_x^{\sim} \\ M_y^{\sim} \end{bmatrix} = \begin{bmatrix} \gamma\mu_0 M_{\mathrm{s}} \cdot (h_{\mathrm{rf},y} - N_{yy}M_y^{\sim}) - M_y^{\sim} \cdot [\gamma\mu_0 \cdot (H_0 - N_{zz}M_{\mathrm{s}}) + i\omega\alpha] \\ -\gamma\mu_0 M_{\mathrm{s}} \cdot (h_{\mathrm{rf},x} - N_{xx}M_x^{\sim}) + M_x^{\sim} \cdot [\gamma\mu_0 \cdot (H_0 - N_{zz}M_{\mathrm{s}}) + i\omega\alpha] \end{bmatrix}. \tag{2.22}$$

We can rewrite this equation in matrix form

$$\begin{bmatrix} h_{\mathrm{rf},x} \\ h_{\mathrm{rf},y} \end{bmatrix} = \overleftrightarrow{\chi}^{-1} \begin{bmatrix} M_x^{\sim} \\ M_y^{\sim} \end{bmatrix} \tag{2.23}$$

with

$$\overleftrightarrow{\chi}^{-1} = \frac{1}{M_\mathrm{s}} \begin{bmatrix} H_0 + (N_{xx} - N_{zz})M_\mathrm{s} + \frac{i\omega\alpha}{\gamma\mu_0} & -\frac{i\omega}{\gamma\mu_0} \\ +\frac{i\omega}{\gamma\mu_0} & H_0 + (N_{yy} - N_{zz})M_\mathrm{s} + \frac{i\omega\alpha}{\gamma\mu_0} \end{bmatrix}. \tag{2.24}$$

Inverting this expression yields the so-called Polder susceptibility [49]

$$\begin{aligned} \overleftrightarrow{\chi} &= \begin{bmatrix} \chi_{xx} & \chi_{xy} \\ \chi_{yx} & \chi_{yy} \end{bmatrix} \\ &= \frac{1}{M_\mathrm{s}} \frac{1}{\det\left(\overleftrightarrow{\chi}^{-1}\right)} \cdot \begin{bmatrix} \chi_{xx}^{\sim} & \chi_{xy}^{\sim} \\ \chi_{yx}^{\sim} & \chi_{yy}^{\sim} \end{bmatrix} \end{aligned} \tag{2.25}$$

with the determinant of the inverse susceptibility $\det\left(\overleftrightarrow{\chi}^{-1}\right)$ and the tensor entries

$$\begin{aligned} \chi_{xx}^{\sim} &= H_0 + (N_{yy} - N_{zz})M_\mathrm{s} + \frac{i\omega\alpha}{\gamma\mu_0}, \\ \chi_{xy}^{\sim} &= +\frac{i\omega}{\gamma\mu_0}, \\ \chi_{yx}^{\sim} &= -\frac{i\omega}{\gamma\mu_0}, \\ \chi_{yy}^{\sim} &= H_0 + (N_{xx} - N_{zz})M_\mathrm{s} + \frac{i\omega\alpha}{\gamma\mu_0}. \end{aligned} \tag{2.26}$$

The susceptibility represents the proportionality constant between the magnetization (linear response) and the small external perturbation ($\boldsymbol{h}_\mathrm{rf} \ll \boldsymbol{H}_0$) and is a complex quantity which can be split into its real and imaginary part $\chi = \chi' + i\chi''$. The typical lineshape of the susceptibility is exemplarily shown for the χ_{xx} component with $N_{xx} = N_{yy} = 0$, $N_{zz} = 1$ in Fig. 2.2(b). The real part of the susceptibility χ'_{xx} has the typical dispersive lineshape and describes the dissipation of the system while the imaginary part χ''_{xx} has a Lorentzian lineshape and describes the absorption of the system.

For the resonance frequency $\omega_\mathrm{res}/(2\pi)$ and the linewidth $\Delta\omega$, we need to solve the characteristic equation for ω which is given by $\det\left(\overleftrightarrow{\chi}\right) \stackrel{!}{=} 0$. This equation can either be solved for the magnetic field H_0 or for the frequency ω. The real part of the solution gives the resonance frequency ω_res (or field H_res) and is known as the famous Kittel equation [50]

$$\omega_\mathrm{res} = \gamma\mu_0 \sqrt{\left[H_0 + (N_{xx} - N_{zz})\, M_\mathrm{s}\right] \cdot \left[H_0 + (N_{yy} - N_{zz})\, M_\mathrm{s}\right]}. \tag{2.27}$$

This equation depends on the demagnetization factors N_{ii} characteristic for the specific sample shape. We briefly want to discuss three special cases:

1. **Sphere:** For a sphere the demagnetization factors are the same $N_{xx} = N_{yy} = N_{zz} = 1/3$ and therefore the demagnetization does not play any role. The Kittel equation becomes

$$\omega_{\mathrm{res}} = \gamma\mu_0 \, H_0. \tag{2.28}$$

2. **Thin-film, in-plane:** If the magnetic field is applied in the sample plane of a thin film (thickness$\ll$lateral dimensions, z-direction perpendicular to sample plane), we can assume that $N_{xx} = 1$ and $N_{yy} = N_{zz} = 0$. The Kittel equation simplifies to

$$\omega_{\mathrm{res}} = \gamma\mu_0 \sqrt{H_0 \cdot (H_0 + M_{\mathrm{s}})}. \tag{2.29}$$

3. **Thin-film, out-of-plane:** For the situation that the magnetic field is applied perpendicular to the sample plane of a thin film, the demagnetization factors can be approximated to $N_{xx} = N_{yy} = 0$ and $N_{zz} = 1$. The Kittel equation consequently results in

$$\omega_{\mathrm{res}} = \gamma\mu_0 \, (H_0 - M_{\mathrm{s}}). \tag{2.30}$$

   We emphasize here that in thin-films typically interface anisotropies play a crucial role and modify the resonance equations Eqs. (2.29) and (2.30) [51].

These three cases discussed above are shown in Fig. 2.2(c) where the effect of the sample shape is visualized.

The imaginary part of the solution characterized by the half-width-at-half-maximum (HWHM) linewidth, which is given by

$$\Delta H(\omega) = \frac{\alpha\omega}{\gamma\mu_0}. \tag{2.31}$$

This equation accounts for all kind of damping contributions, which scale linearly with frequency ω. In experiments, it is usually observed that the experimentally measured $\Delta H(\omega)$ curve does not extrapolate to zero for $\omega \to 0$. This can be attributed to e.g. long-range magnetic inhomogeneities [51] in the sample. Therefore, Eq. (2.31) is modified by an additional term ΔH_{inh} called inhomogeneous linewidth broadening accounting for inhomogeneities, which leads to

$$\Delta H(\omega) = \Delta H_{\mathrm{inh}} + \frac{\alpha\omega}{\gamma\mu_0}. \tag{2.32}$$

Note that the above derivation is only valid for the uniform precession mode with wavevector $\boldsymbol{k} = 0$ and if the equilibrium position of the magnetization and the direction of the effective field are known. The latter can lead to non-analytical solutions and therefore can be only solved numerically. Nevertheless, this chapter should give a basic understanding of magnetization dynamics which we will now extent in the following chapters. In Chapter 3 we will model a ferrimagnet as an effectively two-sublattice system with different free energy contributions. In Chapter 4 the magnetization dynamics of a chiral magnet with different uniform precessional modes coupled to a microwave resonator is considered. In Chapter 5, we discuss propagating precession modes with wavevector $\boldsymbol{k} \neq 0$, where we will particularly discuss the magnetization dynamics of so-called dipolar-exchange spin waves.

3 Magnon-Magnon Coupling in the Compensated Ferrimagnet Gadolinium Iron Garnet

Hybrid dynamic systems, where two physical systems are coupled to each other, have attracted great attention over the last years due to their potential application in coherent information exchange, sensing or communication [21]. For these applications strong coupling is especially interesting because information needs to be coherently transferred between the coupled systems, which means that the phase in these excitations needs to be preserved [23]. This is only the case if the decay rates of the systems are smaller than the coupling strength between each other.[1] Strong coupling has already been realized in e.g. coupled spin-photon [52–54] and magnon-photon systems [55–60]. Magnetic systems are interesting for frequency up-conversion [61, 62] and quantum state storage applications [24].

In all these cases, electromagnetic interactions, such as magnetic and electric dipolar interactions and magneto-optic effects, are fundamentally responsible for the coupling. The dipolar nature of the coupling between spins or magnons to photons in microwave cavities has two important consequences. First, the magnetic dipolar coupling is weak, limiting the single spin-photon coupling rates to sub-kHz-regime [63]. Second, the effective coupling rate g_{eff} of a system of spins (magnons) scales with their number N as $g_{\mathrm{eff}} \propto \sqrt{N}$ [64]. Thus, increasing g_{eff} hinges on tuning the cavity filling factor [56] or the spin density (saturation magnetization) [55, 65] in a given volume. Therefore, strong magnon-photon or cavity-mediated magnon-magnon coupling [66, 67] requires large filling factors or photon-wavelength sized, i.e., macroscopic dimensions. The dipolar interactions are typically weak compared to the energy scales of the involved excitations themselves. In magnetically ordered systems, the energy scale relevant for the magnon-magnon interaction is the quantum mechanical exchange interaction. The physical picture is introduced in Section 3.2.

While ferromagnets only feature a single uniform precessional mode, antiferromagnets, ferrimagnets or chiral magnets can host multiple magnon modes. These are

[1] Strong coupling can be easily observed with two tuning forks placed close to each other and coupled by small permanent magnets attached to one arm of the fork. If only one of the tuning forks is excited, the excitation is completely transferred to the other after a period determined by the coupling strength. In the case of strong coupling, the excitation is coherently transferred back and forth between the two tuning forks before the decay of the excitation due to damping.

the acoustic and optical mode in the canted phase and the clockwise and counter-clockwise mode in the collinear phase [34]. Recently, magnon-magnon coupling between two magnetic materials in particular the ferrimagnet yttrium iron garnet (YIG) and a ferromagnetic metal [68–70] has been demonstrated where the weak interlayer exchange interaction mediates the coupling. Here, we want to access the much stronger intralayer exchange interaction. The THz-frequency dynamics in antiferromagnets is challenging to address experimentally not only with microwave techniques but also with optical spectroscopy [71]. The charm of compensated ferrimagnets is that the sublattice magnetization can be tuned by temperature and consequently tuning the magnetization dynamics not only to an experimentally accessible range but also to investigate the dynamics in a quasi-antiferromagnetic limit.

In this chapter, we discuss the experimental observation of ultrastrong magnon-magnon coupling in the compensated ferrimagnet gadolinium iron garnet (GdIG) close to its compensation temperature with a coupling rate reaching up to 37% of the characteristic magnon frequency. Furthermore, we demonstrate the tunability of the coupling strength from the weak to ultrastrong coupling regime and propose a physical mechanism for the large coupling strength which is called exchange-enhancement. This chapter will start with an introduction to the investigated material system, namely gadolinium iron garnet, and its static sublattice magnetizations. Subsequently we will discuss the difference of the typical spatially uniform spin dynamics eigenmodes of a quasi-antiferromagnet and why it is an ideal system to investigate mode hybridization. Next, we will introduce the broadband magnetic resonance spectroscopy technique and discuss how to eliminate the microwave background. The magnon mode hybridization will be modelled by different models where we will discuss the necessary ingredients to observe coupling and the important role of the anisotropy. Finally, we will provide a full numerical model to describe the magnetization dynamics of a coupled two-sublattice system.

Main parts of this chapter (figures and text) have been published in L. Liensberger, A. Kamra, H. Maier-Flaig, S. Geprägs, A. Erb, S. T. B. Goennenwein, R. Gross, W. Belzig, H. Huebl, and M. Weiler, *Exchange-Enhanced Ultrastrong Magnon-Magnon Coupling in a Compensated Ferrimagnet*, Phys. Rev. Lett. **123**, 117204 (2019) [72].

3.1 Material System Gadolinium Iron Garnet

First, we want to emphasize the unique properties of a compensated ferrimagnet compared to a ferromagnet or an antiferromagnet. In Fig. 3.1(a) the difference between the static magnetizations between a ferrimagnet and a ferromagnet or antiferromagnet is schematically depicted. A ferromagnet has a single sublattice with

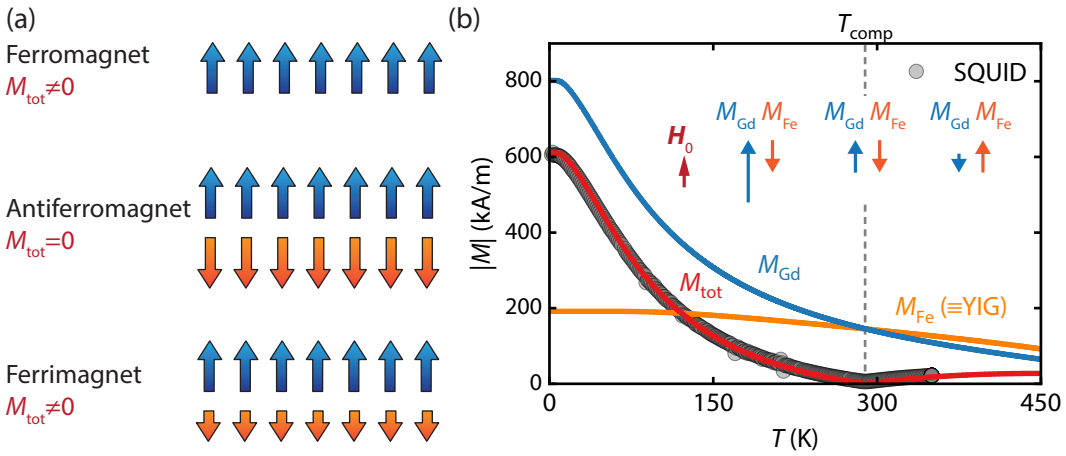

Fig. 3.1. (a) Schematic depiction of the alignment of magnetic moments in a (single-sublattice) ferromagnet, antiferromagnet and ferrimagnet. The total magnetization M_{tot} is zero for an antiferromagnet and finite for a ferromagnet and a ferrimagnet. (b) Simulated static magnetizations of the gadolinium (blue solid line) and iron (orange solid line) sublattices as well as the total magnetization M_{tot} of gadolinium iron garnet (GdIG) (red solid line) as a function of temperature T. The grey points are the measured total magnetization at a magnetic field of $\mu_0 H_0 = 1.0\,\mathrm{T}$ determined by SQUID magnetometry. The inset shows schematically the sublattice magnetization at temperatures below, above and at the compensation temperature $T_{\mathrm{comp}} = 288\,\mathrm{K}$.

the magnetic moments aligned in the same direction due to the Heisenberg exchange interaction (cf. Eq. (2.4)), where we neglect the formation of potential magnetic domains. The total magnetization M_{tot} is the sum over all magnetic moments (cf. Eq. (2.1)) and is for a ferromagnet non-zero ($M_{\mathrm{tot}} \neq 0$). In antiferromagnets and ferrimagnets the sign of the exchange constant is negative and therefore the Heisenberg exchange interaction favors the anti-parallel alignment of neighbouring magnetic moments to minimize its energy. In the particular case of an antiferromagnet the absolute value of the opposing magnetic moments are equal and therefore the total magnetization is $M_{\mathrm{tot}} = 0$. The ferrimagnet also has opposing magnetic moments but these are now imbalanced due to a different number of magnetic moments pointing up and down or due to the different magnitude of magnetic momentum due to some sort of crystallographic selection [73]. This leads to a non-zero magnetization $M_{\mathrm{tot}} \neq 0$.

Gadolinium iron garnet ($Gd_3Fe_5O_{12}$, GdIG) is a compensated ferrimagnet with a cubic crystal lattice and three magnetic sublattices. The material class of (rare-earth) iron garnet consists of an octahedrally coordinated Fe^{3+}-ions (a-)sublattice, a tetrahedral Fe^{3+}-ions (d-)sublattice and a dodecahedral rare-earth metal or yttrium (c-)sublattice [73, 74]. Due to the imbalanced magnetic moments of the sublattices and their mutual antiferromagnetic coupling, this leads to ferrimagnetism. The most famous representative of this material class is yttrium iron garnet ($Y_3Fe_5O_{12}$, YIG), where on the c-site Y^{3+}-ions are situated. These yttrium ions have a noble gas

configuration, leading to no magnetic moment. Therefore, the total magnetization is given by the strongly antiferromagnetically coupled iron-sublattices as shown in Fig. 3.1(b) (orange line). The total magnetization stemming from the coupled iron-sublattice is only weakly temperature-dependent. Nevertheless, YIG is due to its low damping characteristics and small linewidth broadly used in numerous applications like in microwave technology in filters or microwave sources [75, 76].

Gadolinium iron garnet in contrast has on the c-sublattice Gd^{3+}-ions which have an unfilled $4f$-shell leading to a finite magnetic moment. The total magnetization of the gadolinium-sublattice is strongly temperature-dependent and couples antiferromagnetically to the total magnetization of the two antiferromagnetically coupled iron-sublattice [73] in the considered temperature and magnetic field range. This results in an effective two-sublattice system. The three sublattices of gadolinium iron garnet add up to the total magnetization

$$M_{\mathrm{tot}} = M_{\mathrm{Gd}} + M_{\mathrm{Fe,a}} - M_{\mathrm{Fe,d}} = M_{\mathrm{Gd}} + M_{\mathrm{Fe}}. \tag{3.1}$$

The two iron sublattices (a- and d-site) are strongly antiferromagnetically coupled and can be treated as one effective iron sublattice $M_{\mathrm{Fe}} = M_{\mathrm{Fe,a}} - M_{\mathrm{Fe,d}}$. Therefore, the effective number of sublattices is reduced from three to two. Due to the temperature-dependence of the Gd-sublattice a compensation of the sublattice magnetizations occurs, where the net magnetization of the Gd-sublattice equals that of the net Fe-sublattice $|M_{\mathrm{Gd}}| = |M_{\mathrm{Fe}}|$ at the so-called magnetic compensation temperature T_{comp} as shown in Fig. 3.1(b). Note that for compensated iron garnets there are two compensation points: The magnetic compensation point where the net magnetization vanishes and the angular momentum compensation point where the angular momentum of the two sublattices cancel each other [77]. For gadolinium iron garnet the magnetization compensation point occurs at slightly lower temperature than the angular momentum compensation point, which can be seen from the divergence of the Landé factor as a function of temperature close to the compensation point [48, 78]. Within our experiments we cannot resolve and distinguish between these two compensation points.

In our experiments, we investigate a single crystal GdIG disk which was grown by travelling solvent floating zone method [79] by Andreas Erb (WMI) and cut to a (111)-oriented disk with diameter $d = 6.35\,\mathrm{mm}$ and thickness $t = 500\,\mu\mathrm{m}$. The magnetic alignment and the superconducting quantum interference device (SQUID) magnetometry of the single crystal were done by Stephan Geprägs (WMI). From the SQUID magnetometry measurements we can determine the magnetization compensation temperature to $T_{\mathrm{comp}} = 288\,\mathrm{K}$ (cf. Fig. 3.1(b)).

We first calculate the sublattice magnetizations at non-zero temperature as we will need them later. Following the approach proposed in Refs. [80] and [81], we

consider all three sublattice and use molecular field theory. The magnetizations M_i of the three sublattices are given by

$$M_i(T) = M_i(0) \cdot B_{S_i}(a_i), \quad i \in \{\mathrm{a,d,c}\} \tag{3.2}$$

with a=Fe_a, d=Fe_d and c=Gd. In this context, $M_i(0)$ is the magnetization at temperature $T = 0\,\mathrm{K}$ and $B_{S_i}(a_i)$ is the Brillouin function with the Boltzmann energy ratios

$$\begin{aligned} a_\mathrm{d} &= \frac{S_\mathrm{d} g \mu_\mathrm{B} \mu_0}{k_\mathrm{B} T} \cdot (N_\mathrm{dd} M_\mathrm{d} + N_\mathrm{da} M_\mathrm{a} + N_\mathrm{dc} M_\mathrm{c}), \\ a_\mathrm{a} &= \frac{S_\mathrm{a} g \mu_\mathrm{B} \mu_0}{k_\mathrm{B} T} \cdot (N_\mathrm{ad} M_\mathrm{d} + N_\mathrm{aa} M_\mathrm{a} + N_\mathrm{ac} M_\mathrm{c}), \\ a_\mathrm{c} &= \frac{J_\mathrm{c} g \mu_\mathrm{B} \mu_0}{k_\mathrm{B} T} \cdot (N_\mathrm{cd} M_\mathrm{d} + N_\mathrm{ca} M_\mathrm{a} + N_\mathrm{cc} M_\mathrm{c}), \end{aligned} \tag{3.3}$$

where the coupling between the sublattices has been taken into account. In Eq. (3.3), k_B is the Boltzmann constant, $g = 2$ the Landé factor and N_{ij} are the molecular field coefficients taken from Ref. [81]. The value N_ac is slightly adjusted from $-3.44\,\mathrm{mol/cm^3}$ to $-3.3\,\mathrm{mol/cm^3}$ to yield the compensation temperatures $T_\mathrm{comp} = 288\,\mathrm{K}$ determined from SQUID magnetometry measurements (cf. Fig. 3.1(b), grey points). The other molecular field coefficients remain unchanged and take the following values: $N_\mathrm{dd} = -30.4\,\mathrm{mol/cm^3}$, $N_\mathrm{aa} = -65.0\,\mathrm{mol/cm^3}$, $N_\mathrm{cc} = 0\,\mathrm{mol/cm^3}$, $N_\mathrm{dc} = 6.0\,\mathrm{mol/cm^3}$ and $N_\mathrm{ad} = 97.0\,\mathrm{mol/cm^3}$. The spin angular momentum S_i is for the iron sublattices $S_\mathrm{d} = S_\mathrm{a} = 5/2$ and for the gadolinium sublattice $J_\mathrm{c} = 7/2$ [73]. The sublattice magnetic moments per formula unit $M_i^\mathrm{mol}(0)$ at zero temperature are given by [81]

$$\begin{aligned} M_\mathrm{d}^\mathrm{mol}(0) &= 3 g S_\mathrm{d} \mu_\mathrm{B} N_\mathrm{A}, \\ M_\mathrm{a}^\mathrm{mol}(0) &= 2 g S_\mathrm{a} \mu_\mathrm{B} N_\mathrm{A}, \\ M_\mathrm{c}^\mathrm{mol}(0) &= 3 g J_\mathrm{c} \mu_\mathrm{B} N_\mathrm{A}, \end{aligned} \tag{3.4}$$

with the Bohr magneton μ_B and the Avogadro constant N_A. Solving the set of equations (3.2) self-consistently, the sublattice magnetization M_i^mol and consequently the total magnetization M_tot with Eq. (3.1) can be calculated. To convert from magnetic moments per formula unit M_i^mol to magnetization M_i, the density of GdIG ($\rho = 6.45\,\mathrm{g/cm^3}$ [82]) and the molar masses of the constituent elements are used [83]. The result is shown in Fig. 3.1(b) as solid lines. The inset in Fig. 3.1(b) schematically illustrates the relative orientation and magnitude of the sublattice magnetizations in a finite magnetic field. Below the compensation temperature $T < T_\mathrm{comp}$ the sublattice magnetization of the Gd-sublattice M_Gd is larger than the net magnetization of the iron sublattice M_Fe. In the temperature range above the compensation temperature

$T > T_{\mathrm{comp}}$ the magnetization of the Gd-sublattice decreases and becomes smaller than the net iron magnetization (see Fig. 3.1(b), inset). The total magnetization M_{tot} calculated with Eq. (3.1) is in good agreement with the measured SQUID data.

Note that for YIG, the Yttrium-sublattice does not posses a magnetic moment and therefore the magnetization of YIG is determined by the net iron sublattice magnetization $M_{\mathrm{Fe}} = M_{\mathrm{YIG}}$. YIG consequently does not feature a compensation point in contrast to the investigated GdIG.

3.2 Magnetization Dynamics in a Two-Sublattice System

In the previous section, we have discussed the static magnetization properties of the investigated gadolinium iron garnet and highlighted the difference between a ferromagnet, antiferromagnet and a (compensated) ferrimagnet. Now we want to turn our focus to the dynamical properties of the uniform oscillation modes [34]. We simplify our discussion by considering the magnetizations $\boldsymbol{M}_i$ in an external magnetic field $\boldsymbol{H}_0$ and an easy-axis of a magneto-crystalline anisotropy pointing along $\boldsymbol{H}_0$. In Fig. 3.2 the difference between ferromagnets, antiferromagnets and so-called quasi-antiferromagnets are summarized which we now want to discuss in detail.

Starting with a single-sublattice ferromagnet as depicted in the left column in Fig. 3.2, we expect a single uniform mode with a positive dispersion relation, that is, the resonance frequency f increases with increasing magnetic field H_0 as shown in panel (a). The theoretical description in a classical picture presented in the previous Chapter 2 is sufficient to understand the behaviour of the resonance frequency $f_\uparrow$ and can be described with the Kittel equation [Eq. (2.27)]. The result from the classical description is a magnetization precessing in the external field in the counter-clockwise direction [panels (c) & (d)]. In a quantum mechanical picture [panel (b)] spin excitations can be described as collective excitations of the spin system – so-called magnons – which in a particle picture can be viewed as quasiparticles with spin $\pm\hbar$ [84]. In a ferromagnet the excitation of the uniform precessing mode is equivalent to generation of spin-up magnons which reduces the magnetization [85].

In an antiferromagnet in the collinear-state (middle column) and with an external magnetic field $\boldsymbol{H}_0$ applied along the easy-axis of the anisotropy, we find two uniform resonance modes $f_\uparrow$ and $f_\downarrow$ which posses a positive ($\partial f/\partial H_0 > 0$) and negative dispersion ($\partial f/\partial H_0 < 0$) relation, respectively [panel (a)]. At zero magnetic field the two resonance frequencies are degenerated ($f_\uparrow = f_\downarrow$) and have a resonance frequency $f \propto H_{\mathrm{c}} = \sqrt{2H_{\mathrm{aniso}}H_{\mathrm{ex}}}$, with the anisotropy field H_{aniso} and the exchange field H_{ex}. The critical field H_{c} typically corresponds to a resonance frequency in the order of a few hundred GHz [34]. In the quantum picture [panel (b)] these resonance modes can be identified as spin-up and spin-down magnons with unit net spin $\hbar$ pointing in

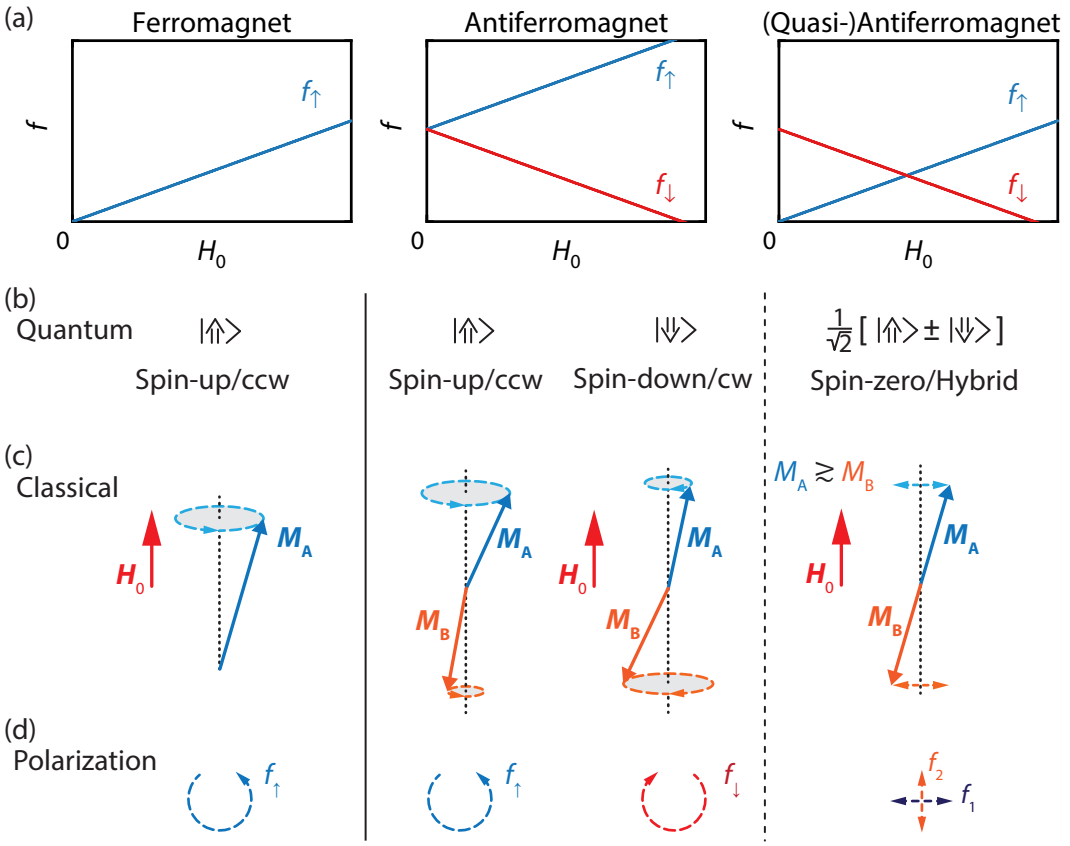

Fig. 3.2. Schematic illustration of the different magnetization dynamics in a ferromagnet (left column), an antiferromagnet (middle column) and a quasi-antiferromagnet (right column). The (a) frequency dispersion f vs. magnetic field H_0 for a spheric sample, (b) the quantum representation, (c) the dynamic modes in a classical picture and (d) the polarization of the precessional eigenmodes are compared. Note that the quasi-antiferromagnet can, additionally to the ccw and cw-precessional mode of an antiferromagnet, feature two linearly polarized hybrid mode with frequencies f_1 and f_2, which are orthogonal to each other. The angles between the two sublattice magnetizations have been exaggerated for clarity. Refer to main text for details.

opposite directions collinear with the equilibrium sublattice magnetizations [72, 84]. In the classical picture the two opposing sublattice magnetizations M_A and M_B with equal magnitude are either precessing in the clockwise (cw) or counter-clockwise direction (ccw) as depicted in panels (c) and (d).

A compensated ferrimagnet close to its compensation point, where the two sublattice magnetizations are nearly identical $M_\mathrm{A} \gtrsim M_\mathrm{B}$, can be viewed as a "quasi-antiferromagnet" with similar magnetization dynamics. In a quasi-antiferromagnet (right column) we expect the same uniform resonance modes as in a classical antiferromagnet with counter-clockwise and clockwise uniform rotational modes which have a positive and negative resonance frequency vs. magnetic field dispersion. The main difference in the resonance frequencies of the two precessional modes is the fact that at zero magnetic field the resonance frequencies of the spin-up $f_\uparrow$ and

spin-down mode $f_\downarrow$ are not degenerate anymore and have a finite frequency difference. At a certain magnetic field H_0 the two resonance frequencies cross and under certain circumstances can couple to each other. The new hybridized modes can be viewed as spin-zero magnons in a quantum-mechanical picture and are symmetric and anti-symmetric superposition of spin-up and spin-down magnons [72, 84]. The polarizations of the two resonance modes are linear and they are orthogonal to each other.[2] This is also true for an antiferromagnet at $H_0 = 0$ in the collinear state if the degeneracy at this point can be lifted.

After discussing the main differences in the magnetization dynamics, we want to emphasize a few points: The frequency dispersion of the quasi-antiferromagnet (cf. Fig. 3.2(a), right column) is similar to an antiferromagnet where the magnetic field is applied perpendicular to the easy axis of the crystalline anisotropy as any source of anisotropy lifts the degeneracy of the resonance frequencies of the two uniform precessional modes at zero magnetic field. In this configuration the two sublattice magnetizations are no longer collinear but in a canted state. The precessional modes are then called acoustic and optical mode. It is well known that these two modes can couple to each other [34, 86]. The physical pictures discussed above cannot be applied to a canted antiferromagnet.

In a ferrimagnet in the collinear state an anticrossing is at first sight not expected. In our experiments we will later observe a tunable exchange-enhanced coupling, and the concomitant hybridization, between the up- and down-spin magnons. In order to achieve this, we need two essential ingredients, namely mode coupling and exchange-enhancement. These are intuitively understood within the quantum picture as follows. Note that the description of the observed physical phenomena is equivalently done in a classical or quantum-mechanical picture. We will switch between them as per convenience.

The two eigenexcitations or magnons of the ferrimagnetic collinear ground states possess unit ($\hbar$) net spins in opposite directions collinear with the equilibrium sublattice magnetizations. When two modes couple, it means that energy can be transferred from one mode to the other. In the quantum picture, this implies that one mode can be converted into the other. This mode interconversion, and thus the coupling, has to satisfy the conservation laws in the system. As a result, a spin-up magnon is not allowed to couple with (transmute into) its spin-down counterpart, if the spin along the magnon spin axis is a conserved quantity. In order to achieve this, a mechanism that violates the conservation of spin along the sublattice magnetization, and consequently the magnon spin, direction is required [84] and cannot stem from the isotropic exchange interaction. Since the conservation of spin along a direction is mathematically a consequence of axial symmetry about this direction, the spin-

[2] This is completely analog to the superposition of left- and right-circularly polarized light resulting in linearly polarized light.

nonconserving mechanism required for the magnon-magnon coupling is provided by an anisotropy about the magnon spin axis. A locally varying axial anisotropy correspondingly allows to vary the resultant magnon-magnon coupling.

However, the typically weak magnetocrystalline anisotropy may not be expected to yield observable effects and, therefore, has typically been disregarded. This is where exchange-enhancement in a quasi-antiferromagnet makes the crucial difference. The antiferromagnetic magnons, despite their unit net spin, are formed by large, nearly equal and opposite spins on the two sublattices [87]. The anisotropy-mediated mode coupling results from, and is proportional to, this large sublattice spin instead of the unit net spin, and is therefore strongly amplified. This amplification effect is termed exchange-enhancement within the classical description [87–89].

This briefly summarizes the most important physics for our experiment. We will pick them up again during this chapter and explain them in more detail when we establish the theoretical framework of the observed tunable exchange-enhanced magnon-magnon coupling. In the following section we will discuss the experimental realization and results.

3.3 Broadband Magnetic Resonance Spectroscopy

In our corresponding experiments, we study the magnetization dynamics of a (111)-oriented single crystal GdIG-disk by broadband magnetic resonance (BMR) using a Keysight N5242A PNA-X vector network analyzer (VNA) with a microwave frequency range $f \leq 26.5\,\mathrm{GHz}$ [48, 90]. A schematic depiction of the setup is shown in Fig. 3.3. The VNA is used to record the complex transmission S_{21} as a function of the microwave frequency f and the external magnetic field $\boldsymbol{H}_0$ applied in the (111)-plane. The applied microwave power is $P = 0\,\mathrm{dBm}$ and we confirmed that the magnetization dynamics of the system are in the linear regime. In the following subsection we want to discuss the VNA-based BMR measurement technique in more detail.

3.3.1 Experimental Setup

A typical broadband magnetic resonance setup based on a vector network analyzer in a simple scheme consists of three different parts: (i) An electromagnet to generate a controllable static magnetic field to saturate and align the magnetization of the sample and to determine the magnetic resonance frequency. (ii) A coplanar waveguide (CPW) that converts the microwave current into oscillating magnetic fields to excite the ferromagnetic resonance. Due to reciprocity, the CPW also picks up uniform magnetization dynamics according to Faraday's law of induction. (iii) A device

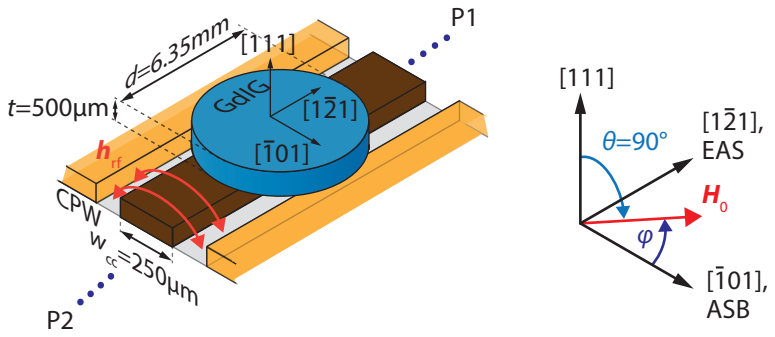

Fig. 3.3. Schematic broadband magnetic resonance (BMR) setup, with the (111)-oriented gadolinium iron garnet (GdIG) disk placed on the coplanar waveguide (CPW) with centerconductor width w_{cc}. The microwave current in the center conductor (brown) generates an oscillating magnetic field $\boldsymbol{h}_{\mathrm{rf}}$ to excite the magnetic resonance and separated by a gap are the ground planes (yellow) which are connected with each other via the backside of the CPW. The ports P1 and P2 are connected to a vector network analyzer (not shown). The angle φ in the coordinate system on the right defines the in-plane direction in the (111)-disk plane of the magnetic field $\boldsymbol{H}_0$. For the origin of the nomenclature of the effectively axially symmetric (EAS) and the axial symmetry broken (ASB) directions, refer to main text.

to generate and detect microwaves typically in the frequency range from 0.01 GHz to 50 GHz which in our case is both achieved by a vector network analyzer.

The static magnetic field required for ferromagnetic resonance is typically in the range of at most a few T which can be accomplished by a room-temperature electromagnet consisting of two opposing coils with an inserted iron yoke where the maximum achievable magnetic field can be up to $\mu_0 H_0 \leq 3\,\mathrm{T}$ or at low temperatures using a pair of superconducting coils or solenoids where magnetic fields up to $\mu_0 H_0 \leq 20\,\mathrm{T}$ can be achieved. The working principle is for both systems the same: A dc current is applied to the (superconducting) wires of the coils of the magnet which produce by Ampère's law a homogenous magnetic field between them. In our experiments we use a superconducting 3D-vector magnet consisting of a solenoid and two pairs of coils in Helmholtz configuration in a liquid helium bath at a temperature of $T = 4.2\,\mathrm{K}$ (boiling point of liquid helium). The static magnetic field can be applied in an arbitrary direction with a field strength of up to $\mu_0|\boldsymbol{H}_0| \leq 2.5\,\mathrm{T}$ and up to $\mu_0|\boldsymbol{H}_0| \leq 6.0\,\mathrm{T}$ along the direction of the solenoid.

The coplanar waveguide (CPW) consists of a low-loss dielectric substrate with a high dielectric constant with a metallic thin film deposited on both sides. The top metallization is patterned into a center conductor with a certain conductor width w_{cc} and separated by a gap on each side are the ground planes. These are connected to the metallized back side of the antenna by vias which are metallized bore holes to connect the front- and backside of the CPW [91, 92]. For the design of the CPW it is crucial that the impedance matches $Z_0 = 50\,\Omega$ of the whole microwave setup (cables,

connectors etc.) in order to reduce back-reflections. Especially the dimensions of the center conductor are crucial for the experiment because the microwave in the center conductor is converted into an oscillating magnetic field $\boldsymbol{h}_{\mathrm{rf}}$ by Ampère's law which depends on the width of the center conductor w_{cc}. Assuming the microwave current flow I along the x-direction, the resulting oscillating magnetic field is consequently given by the Karlqvist equations [48, 93, 94]

$$h_{\mathrm{rf},y}(y,z) = \frac{1}{\pi}\frac{I}{2w_{\mathrm{cc}}}\left[\arctan\left(\frac{y+\frac{w_{\mathrm{cc}}}{2}}{z}\right) - \arctan\left(\frac{y-\frac{w_{\mathrm{cc}}}{2}}{z}\right)\right] \tag{3.5}$$

$$h_{\mathrm{rf},z}(y,z) = \frac{1}{2\pi}\frac{I}{2w_{\mathrm{cc}}}\ln\left(\frac{\left(y+\frac{w_{\mathrm{cc}}}{2}\right)^2+z^2}{\left(y-\frac{w_{\mathrm{cc}}}{2}\right)^2+z^2}\right), \tag{3.6}$$

where the z-direction is pointing perpendicular to the CPW-plane and y along the CPW-plane perpendicular to the current flow. The current I can be related to the applied microwave power P via $I = \sqrt{P/Z_0}$.

For broadband magnetic resonance spectroscopy experiments, it is necessary to have a device to generate microwaves, which are coupled into the center conductor of the CPW using an endlaunch connector, and a device to detect the signal change at the magnetic resonance frequency. In our experiments we use a vector network analyzer (VNA) which combines the two required capabilities: excitation and detection. The VNA generates a microwave with frequency f and microwave power P at port 1. The microwave travels through the microwave circuit and is consequently detected at port 2 at the same frequency. In a simple picture the VNA measures the difference between the outgoing and incoming microwave. Due to the heterodyne detection scheme, the VNA is not limited to evaluate the amplitude change but can also measure the phase change. The vector network analyzer calculates the complex scattering parameters S_{ij} which are defined as

$$S_{ij} \equiv \frac{V_i^{\mathrm{in}}}{V_j^{\mathrm{out}}} \quad \text{with } V_i^{\mathrm{in}}, V_j^{\mathrm{out}} \in \mathbb{C}, \tag{3.7}$$

where i and j are the VNA port numbers and V_i the detected voltages at the ports. In a magnetic resonance measurement we expect at resonance a change in the transmission of the rf circuit. Therefore, we measure in our experiments the complex-transmission parameter S_{21} given by

$$S_{21} = \frac{V_2}{V_1} = \frac{|V_2|}{|V_1|}e^{i\phi}, \tag{3.8}$$

where $\phi = \phi_2 - \phi_1$ is the relative phase between the outgoing and incoming microwave. In the heterodyne detection scheme the outgoing and detected signal at the excitation frequency are downconverted to an intermediate frequency (IF), subsequently filtered

by an adjustable bandpass filter and digitized by an analog-to-digital converter [95]. The smaller the bandwidth of the IF bandpass filter is chosen, the smaller the noise figure. Therefore better signal-to-noise ratio is achieved at the cost of an increased measurement time, where the IF bandwidth is ideally given by $f_{\mathrm{IFBW}} = 1/\Delta t$ with the measurement time Δt. The terminology of heterodyne detection scheme stems from the fact that the phase and amplitude analysis of the signals are at a different frequency compared to the excitation frequency. A full discussion of the working principle of the vector network analyzer can be found in Ref. [95]. Later in Section 5.3.2, we will discuss more advanced measurement schemes of the VNA and go into more detail of the detection scheme inside the VNA.

After having discussed the three main parts to perform broadband magnetic resonance spectroscopy, we now want to derive an expression for the measured S_{21}-parameter and relate it to the detected magnetic resonance. In the experiment, the sample is placed onto the CPW where we assume a solely inductive coupling to the CPW. The static magnetic field $\boldsymbol{H}_0$ aligns the magnetization along a certain direction and the magnetization starts to precess at its resonance frequency given by the Kittel equation [Eq. (2.27)]. The VNA generates a microwave current with a certain frequency f and power P which is coupled via endlaunch connectors to the center conductor of the CPW where the resulting microwave field $\boldsymbol{h}_{\mathrm{rf}}$ applies a torque to the magnetization. In the classical driven harmonic oscillator analogon the frequency of the driven excitation needs to match the frequency of the physical system. As we discussed in Section 2.2, we expect a change of absorbed energy of the magnetic system when the resonance condition is fulfilled. Additionally, the precessing magnetization generates an oscillating magnetic field which is converted to an alternating current in the center conductor of the CPW via Faraday's law [48, 96]. The VNA detects the change in amplitude and phase by measuring the complex transmission parameter S_{21}, which consists of the contribution stemming from the microwave background S_{21}^0, originating from the frequency-dependent transmission of the whole microwave setup (cables, endlaunches, CPW etc.), and of the contribution from the sample ΔS_{21}. To extract the contribution from the sample we calculate the transmission change

$$\Delta S_{21} = \frac{S_{21} - S_{21}^0}{S_{21}^0}, \tag{3.9}$$

where we neglect the reflection of the microwave by assuming $S_{11} = 0$. This simplification is made under the assumption that loading the CPW with the sample does not result in a substantial deviation of the sample-CPW impedance from the unloaded CPW impedance $Z_0 = 50\,\Omega$. The coupling between the CPW and the sample can

be modelled in a voltage-divider model where the inductance of the sample L_0 is in series with the impedance Z_0 of the microwave setup

$$\Delta S_{21} = \frac{1}{2}\frac{-i\omega L_0}{Z_0 - i\omega L_0}, \tag{3.10}$$

where the factor $1/2$ is stemming from the fact that the voltage is measured between signal line and ground of the CPW and not between port 1 and 2 of the VNA [96]. The calculation of the signal strength ΔS_{21} measured in BMR measurements depends on the sample size, magnetic field and CPW geometry. Especially the precise evaluation of the amplitude is an involved task which is not topic of this thesis. Here, we do not want to present a full derivation and refer here to Refs. [48, 94, 96–99].

The precessing magnetization in the sample has an inductance L_0, which is proportional to the Polder susceptibility $L_0 \propto \chi(\omega,H_0)$. To derive an expression for the S_{21}-parameter we will use Eq. (3.9) and insert Eq. (3.10) with the assumption that $\omega L_0 \ll Z_0$ which leads to $\Delta S_{21} = -i\omega L_0/(2Z_0)$. We obtain for the complex transmission parameter

$$\begin{aligned} S_{21} &= S_{21}^0(\omega) + S_{21}^0(\omega)\,\Delta S_{21}, \\ &= S_{21}^0(\omega) - iAe^{i\phi}\chi(\omega,H_0) \end{aligned} \tag{3.11}$$

with a real valued amplitude A, accounting for all constants and geometry parameters, and a phase ϕ due to the microwave background transmission $S_{21}^0(\omega)$. Depending on the measurement geometry, we use for the susceptibility $\chi(\omega,H_0) = \chi_{\mathrm{yy}}(\omega,H_0)$ if the magnetic field is applied perpendicular to the CPW plane, $\chi(\omega,H_0) = \chi_{xx}(\omega,H_0)$ if the magnetic field is applied in the CPW plane but perpendicular to the center conductor, and $\chi(\omega,H_0) = 1/2\ (\chi_{xx}(\omega,H_0) + \chi_{yy}(\omega,H_0))$ for the magnetic field applied in the CPW plane and parallel to the center conductor [97].

In the experiment there are as already mentioned two possibilities to drive the system to resonance as described by the Kittel equation. It can either be fulfilled by setting the static magnetic field $|\boldsymbol{H}_0|$ fixed and sweeping the microwave frequency f which is the so-called “frequency-swept BMR” or vice versa, where the excitation frequency is fixed and the magnetic field is changed which is the “field-swept BMR”. In this thesis, we will not use the “field-swept BMR” and therefore spare the discussion. In the following section we will discuss the data processing required for the frequency-swept BMR due to the present background microwave transmission during the measurement.

3.3.2 Data Processing

In this section we will discuss the frequency-swept BMR as performed in our experiment in more detail which is adapted from Ref. [48]. In this measurement procedure, we set the magnetic field $|\boldsymbol{H}_0|$ at a fixed value and sweep the microwave frequency of the VNA $f = \omega/(2\pi)$ and measure the complex transmission parameter $S_{21}(f)$. The magnetic field H_0 is then incremented/decremented by $\pm\Delta H_0$ and the measurement procedure is repeated for a series of magnetic field values. The microwave background transmission S_{21}^0 is frequency-dependent even in the absence of magnetic resonances, due to the frequency-dependent transmission through the microwave cables and CPW. This frequency-dependence is always superimposed on any magnetic resonance signal and typically dominates over the magnetic signature. This makes a background-correction necessary.

To demonstrate the necessity of a sophisticated background-correction we measure at a temperature $T = 250\,\mathrm{K}$ far below the compensation point T_{comp} with the magnetic field $\boldsymbol{H}_0$ applied along the EAS direction. The transmission S_{21} as a function of the applied magnetic field H_0 and microwave frequency f is shown in Fig. 3.4(a). The visible field-dependent, weak signal is the ferromagnetic resonance of the system. In the frequency trace taken at $\mu_0 H_0 = 0.5\,\mathrm{T}$, the resonance is hardly visible at $f \approx 15\,\mathrm{GHz}$ which is superimposed on the background transmission. Background removal in VNA measurements is typically done by calibration. A full rf network calibration, however, is a tedious task and additionally would need to be done for all temperatures. Thus, we here discuss possible ways to remove the background in data post-processing.

One way to isolate the signal from the background transmission is to assume that the microwave background is magnetic field independent. Therefore, a frequency-trace at fixed magnetic field far away from the magnetic resonance $S_{21}^{\mathrm{ref}}(\omega)|_{H_0}$ can be used as a reference and all other frequency traces at different magnetic fields normalized to the transmission at this "reference" field, resulting in

$$S_{21}^{\mathrm{ds}}(\omega,H_0) = \frac{S_{21}(\omega,H_0)}{S_{21}^{\mathrm{ref}}(\omega)|_{H_0}}. \tag{3.12}$$

For our measured data, we choose the maximum available magnetic field as a reference ($\mu_0 H_0 = 3.0\,\mathrm{T}$) and calculate $S_{21}^{\mathrm{ds}}(\omega,H_0) = S_{21}(\omega,H_0)/S_{21}^{\mathrm{ref}}(\omega)|_{\mu_0 H_0 = 3.0\,\mathrm{T}}$ as shown in Fig. 3.4(b). The signature of the magnetic resonance is now clearly visible and the microwave background eliminated. As shown in the frequency trace at $\mu_0 H_0 = 0.5\,\mathrm{T}$, the characteristic line shape of the ferromagnetic resonance given by the Polder susceptibility is observed (cf. Fig. 2.2(b)). Due to the applied data process-

ing we need to modify our fitting formula Eq. (3.11) by dividing by the background transmission which results in

$$S_{21}^{\mathrm{ds}}(\omega)|_{H_0} = 1 - iA'e^{i\phi'}\chi(\omega,H_0) \tag{3.13}$$

with a new amplitude factor $A' = A/|S_{21}^0|$ and a new phase $\phi' = \phi - \arg\left(S_{21}^0\right)$ introduced. The signal-to-background ratio in Fig. 3.4(b) is evidently vastly improved compared to Fig. 3.4(a). However, note that some background signature remains, which is attributed mostly to a temporal drift of S_{21}.

The spurious influence of such temporal drift in the microwave background can be minimized by calculating the symmetric difference quotient of S_{21}. This is the so-called "derivative divide" method where the numerical derivative of the measured complex transmission parameter S_{21} with respect to the magnetic field H_0 is calculated [100]

$$\begin{aligned}\partial_{\mathrm{D}} S_{21}/\partial H_0 &= \frac{S_{21}(\omega, H_0+\Delta H) - S_{21}(\omega, H_0-\Delta H)}{S_{21}(\omega,H_0)\Delta H} && (3.14)\\ &= -iA\,\frac{\chi(\omega, H_0+\Delta H) - \chi(\omega, H_0-\Delta H)}{\Delta H} + \mathcal{O}(A^2),\\ &\approx -iA\,\frac{\partial\chi(\omega, H_0)}{\partial H_0}, && (3.15)\end{aligned}$$

with the fixed magnetic field step size ΔH. For the approximation Eq. (3.15) in the last step we used that the chosen magnetic field step size is small $\Delta H \to 0$. Due to the division with the measured signal S_{21}, the microwave background S_{21}^0 is eliminated as shown in Fig. 3.4(c). The advantage of derivative divide is, that signatures with a stronger magnetic field dependence are stronger pronounced than small variations of the background which vary faster or slower with the magnetic field than with the step size ΔH [100]. This results in a superior signal-to-background ratio as visible by comparing Fig. 3.4(b) and (c). The modified fitting formula to describe our measured S_{21} data becomes

$$\partial_{\mathrm{D}} S_{21}/\partial H_0|_{H_0} = A'\,\frac{\chi(\omega, H_0+\Delta H) - \chi(\omega, H_0-\Delta H)}{(A'\chi(\omega,H_0)+1)\cdot\Delta H}. \tag{3.16}$$

In the following experiments we will use the derivative divide algorithm for our data processing as the observed magnetic resonance signatures are small in amplitude. Unless stated otherwise, we will use Eq. (3.14) to process our data.

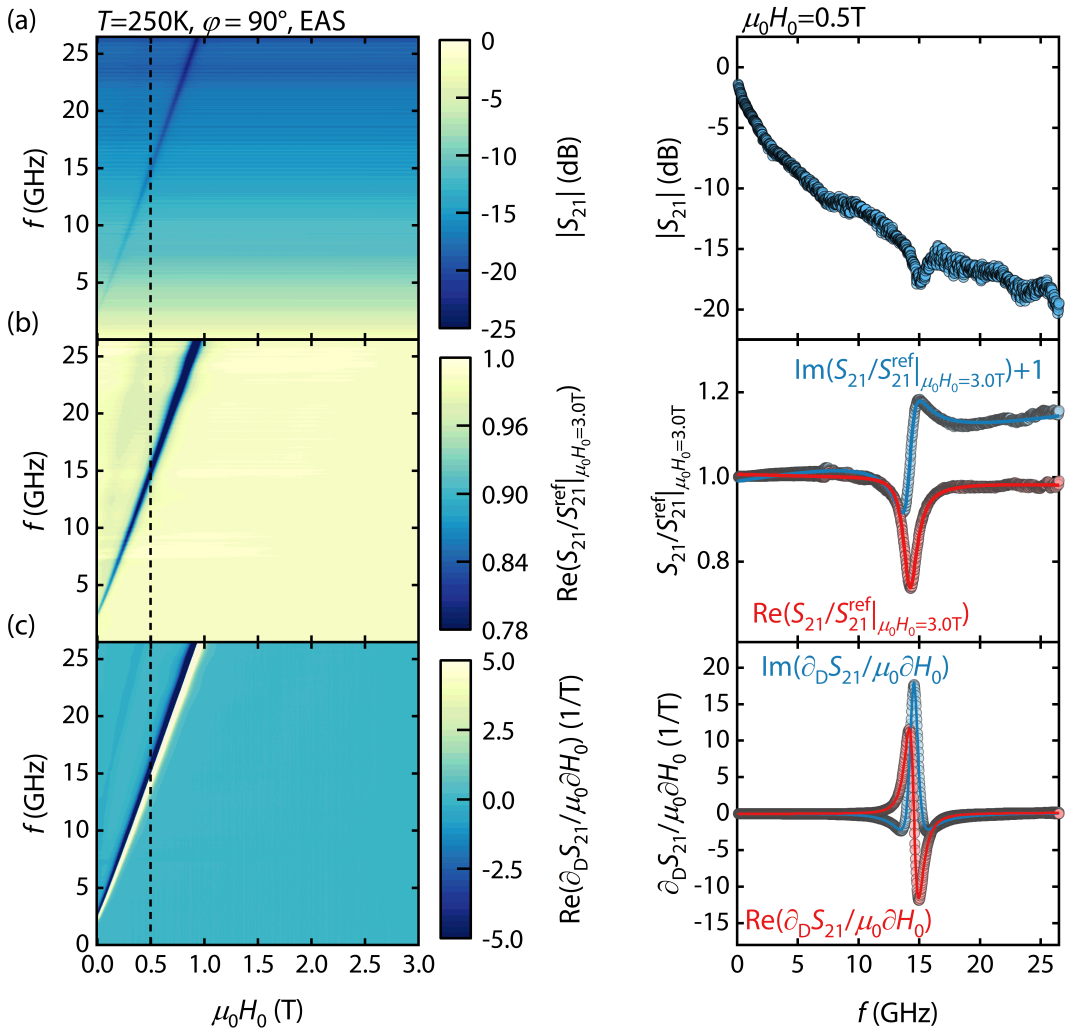

Fig. 3.4. Exemplary data of a frequency-swept broadband magnetic resonance experiment at a temperature of $T = 250\,\mathrm{K}$, far below the compensation temperature of the gadolinium iron garnet single crystal. (a) Magnitude of raw data (complex transmission parameter S_{21}) on a logarithmic scale. (b) Microwave background subtraction by dividing every S_{21}-trace at fixed field with a frequency trace at large fields e.g. $\mu_0 H_0 = 3.0\,\mathrm{T}$. (c) Using derivative divide, the microwave background is eliminated by taking the symmetric difference quotient [Eq. (3.14)]. The line traces on the right side are frequency-traces at fixed magnetic field $\mu_0 H_0 = 0.5\,\mathrm{T}$ (indicated by dashed vertical line in color plots on left side) with the ferromagnetic resonance at $f \approx 15\,\mathrm{GHz}$. For details refer to main text. Figure adapted from [48].

3.3.3 Spin Dynamics Close to the Compensation Point

As previously discussed in Section 3.2 the advantage of a compensated ferrimagnet is the tunability of the sublattice magnetizations and therefore it is possible to investigate the magnetization dynamics of a “quasi-antiferromagnet” close to the compensation point T_{comp} using the previously discussed broadband magnetic resonance (BMR) technique by measuring the complex transmission parameter S_{21}. We now choose temperatures below ($T = 280\,\mathrm{K}$ & $T = 282\,\mathrm{K}$) and above ($T = 294\,\mathrm{K}$) the compensation temperature T_{comp}. Furthermore, we apply the static magnetic field $\boldsymbol{H}_0$ along the effectively axially symmetric (EAS) direction with an angle $\phi = 90°$ and also along the axial symmetry broken (ASB) direction with $\phi = 0°$ (cf. Fig. 3.3). We will explain in Section 3.4 where the name of the two distinct directions comes from. The magnetic field is swept from $\mu_0|\boldsymbol{H_0}| = 2.0\,\mathrm{T}$ to zero with a field step size of $\mu_0\Delta H = 10\,\mathrm{mT}$. The microwave frequency is linearly swept in the range $0.1\,\mathrm{GHz} \leq f \leq 26.5\,\mathrm{GHz}$ with a frequency resolution of approximately $25\,\mathrm{MHz}$. The results of the BMR measurements for the different temperatures T and magnetic field $\boldsymbol{H}_0$ directions are shown in Fig. 3.5.

Along the EAS direction [Figs. 3.5 (a), (c) and (e)] we observe two resonance modes which we identify as the spin-up $f_\uparrow$ and the spin-down $f_\downarrow$ mode. These two modes are identified by their frequency dispersion f as a function of the external magnetic field H_0 as we will see below. The spin-down mode is weak in spectral weight and therefore barely visible. For $T < T_{\mathrm{comp}}$, we observe a shift of the spin-down mode to higher resonance frequencies with decreasing temperature. The resonance visible at low magnetic fields is stemming from the setup and is observed in all temperature regions and magnetic field directions.

In the ASB case [Figs. 3.5 (b), (d) and (f)] we see a splitting between the spin-up and spin-down modes which can be identified as an anti-crossing between the two resonance modes. The frequency splitting between the two modes is largest at $T = 282\,\mathrm{K} < T_{\mathrm{comp}}$ and becomes smaller with decreasing temperature. The physics remains unchanged with the temperature above the compensation point $T > T_{\mathrm{comp}}$. Evidently, only the temperature difference to the compensation temperature T_{comp} is crucial. This corresponds to the difference of the two sublattice magnetizations which becomes larger and therefore the net magnetic moment increases (cf. Section 3.1). The dashed lines in Fig. 3.5 are the results of the numerical simulations which we will discuss in Section 3.5.3.

We now will quantify the observed phenomena and will focus on the temperature $T = 282\,\mathrm{K} < T_{\mathrm{comp}}$ if not stated differently. In Fig. 3.6(a), we show the normalized background-corrected field-derivative of S_{21} recorded at fixed magnetic field magnitude $\mu_0 H_0 = 0.58\,\mathrm{T}$ applied at $\varphi = 90°$ along the EAS direction. In this situation we

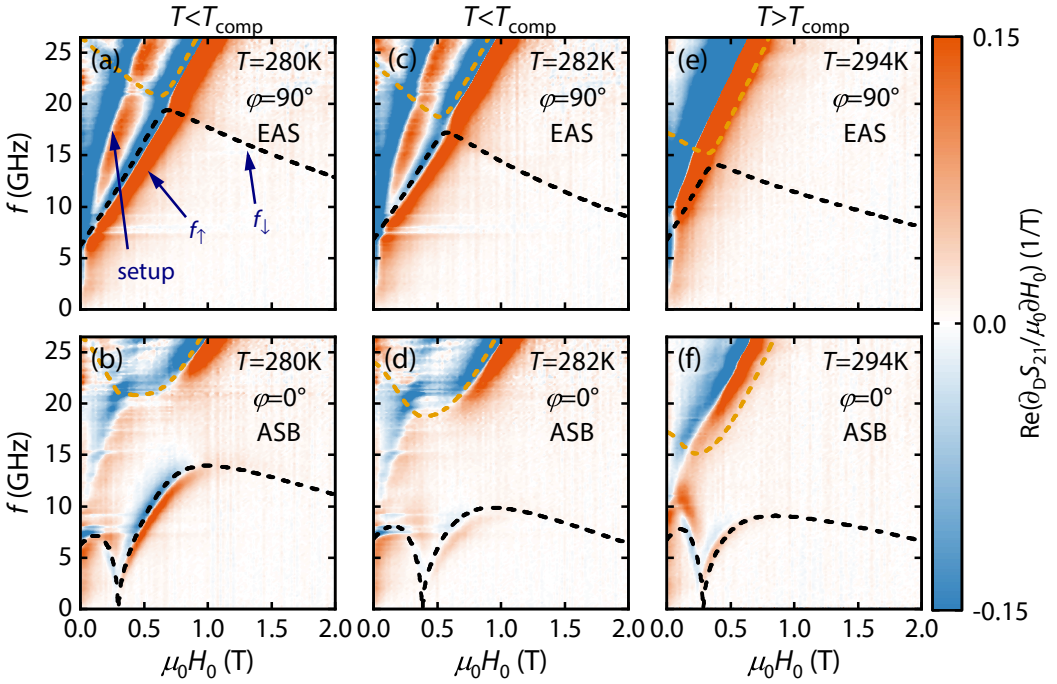

Fig. 3.5. Broadband ferromagnetic resonance spectroscopy data of the real part of the normalized magnetic field derivative of the complex transmission parameter $\partial_{\mathrm{D}} S_{21}/\partial H_0$ as a function of the external magnetic field H_0 and microwave frequency f at temperatures (a),(b) $T = 280$ K and (c),(d) $T = 282$ K below the compensation temperature $T_{\mathrm{comp}} = 288$ K and (e),(f) $T = 294$ K above the compensation point. The external magnetic field is either applied along (a),(c),(e) the effectively axially symmetric (EAS) direction ($\varphi = 90°$) or along (b),(d),(f) the axial symmetry broken (ASB) direction ($\varphi = 0°$). The resonance visible at low magnetic fields is stemming from the setup and is present in all temperature regions. The dashed lines are the results from the numerical simulations where the orange line corresponds to the high frequency and the black line to the low frequency branch (see Section 3.5.3).

observe two resonances close to each other. The spectra can be fitted by modifying Eq. (3.16) to account for two resonances as follows

$$\partial_{\mathrm{D}} S_{21}/\partial H_0|_{H_0} = \sum_{i=1}^{2} \left[A_i' \frac{\chi_i(\omega, H_0 + \Delta H) - \chi_i(\omega, H_0 - \Delta H)}{(A_i' \chi_i(\omega, H_0) + 1) \cdot \Delta H} \right] + C, \tag{3.17}$$

where we allow for a complex linear offset $C = C_0 + C_1 \cdot \omega$ and use the following form of the susceptibility [100]

$$\chi_i(\omega, H_0) = \frac{\gamma \mu_0 |\boldsymbol{M}| \ (|\gamma'| \mu_0 H_0 - i 2\kappa_i)}{\omega_i^2 - \omega^2 - i\omega \, 2\kappa_i} \tag{3.18}$$

with $|\gamma'|$ the gyromagnetic ratio and $|\boldsymbol{M}|$ the magnetization. By fitting the data to Eq. (3.17), we extract the resonance frequencies f_1 and f_2 of the two observed resonances, their difference Δf_{res} and their linewidths κ_1 and κ_2. In Fig. 3.6(b) we show corresponding data and fits for the ASB direction $\varphi = 0°$ and $\mu_0 H_0 = 0.65$ T.

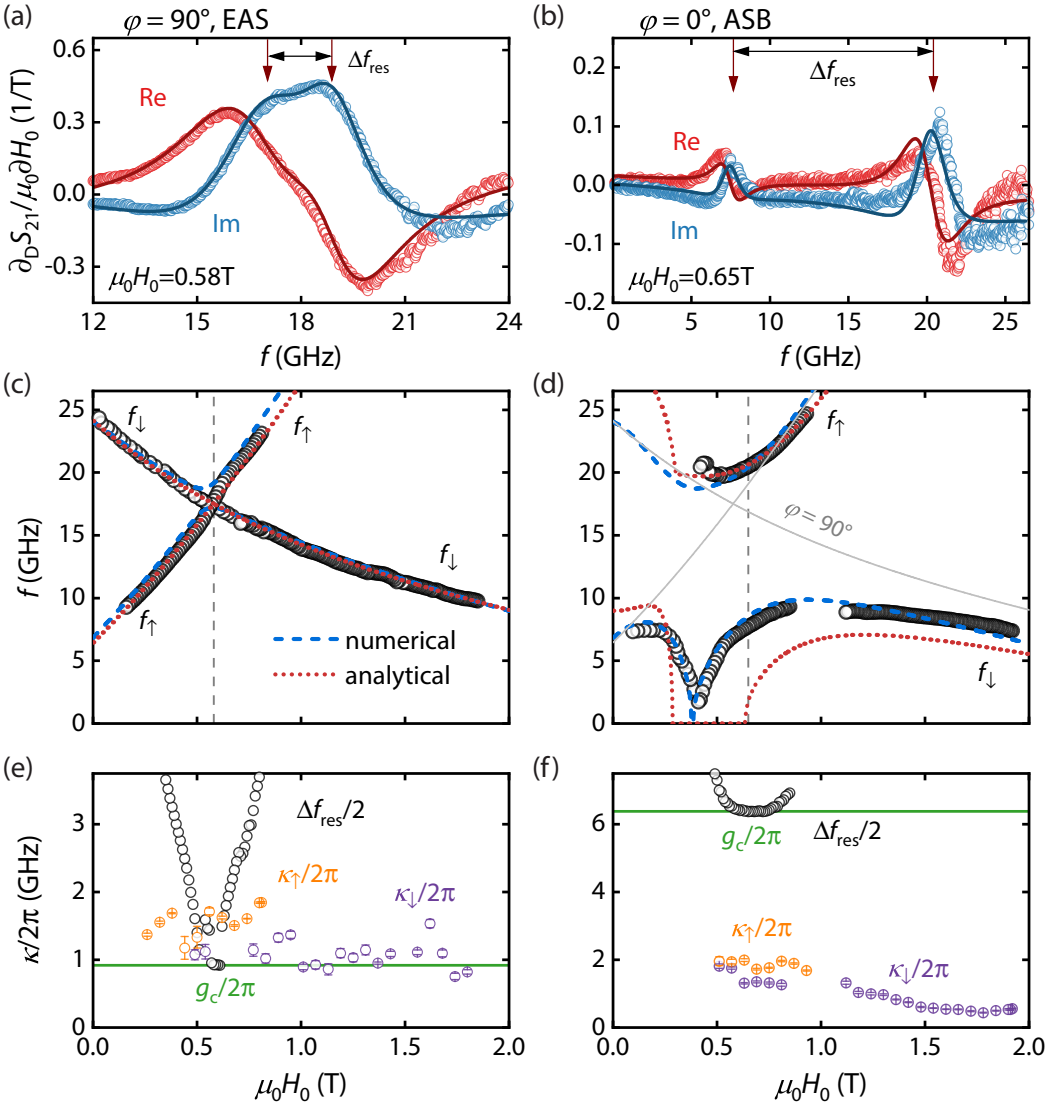

Fig. 3.6. (a),(b) Broadband ferromagnetic resonance spectra obtained at $T = 282\,\mathrm{K}$ and fixed magnetic field strengths applied along the (a) effectively axial symmetric (EAS) direction in the (111)-plane ($\varphi = 90°$) at $\mu_0 H_0 = 0.58\,\mathrm{T}$ and along the (b) axial symmetry broken (ASB) direction ($\varphi = 0°$) at $\mu_0 H_0 = 0.65\,\mathrm{T}$. The solid lines are fits to Eq. (3.17). The arrows indicate the resonance frequencies and Δf_{res} their difference. (c),(d) Mode frequencies as a function of the magnetic field strength where the open circles denote the extracted resonance frequencies. The dashed blue line are results from the numerical simulations and the dotted red curve is the result from the analytical model. The solid gray lines in (d) represent the uncoupled case taken from the analytical solution in (c) where $\varphi = 90°$. The vertical dashed line indicates the magnetic field, where the frequency traces of $\partial_{\mathrm{D}} S_{21}/\partial H_0$ from (a) and (b) are taken from, respectively. (e),(f) Linewidths $\kappa/2\pi$ of the spin-up $\kappa_\uparrow$ and spin-down $\kappa_\downarrow$ modes, and resonance frequency splitting $\Delta f_{\mathrm{res}}/2$ as a function of H_0. The coupling strength $g_{\mathrm{c}}/2\pi$ is given by the minimum of $\Delta f_{\mathrm{res}}/2$.

Again, two resonances are observed but in contrast to the data in Fig. 3.6(a), the resonances are now clearly separated.

We repeat this procedure for a range of magnetic field magnitudes H_0 applied along the two directions (EAS and ASB) of interest. The obtained resonance frequencies are shown as symbols in Figs. 3.6(c) and (d). In the EAS case shown in Fig. 3.6(c), we clearly observe two resonance modes. The first one follows $\partial f_{\mathrm{res}}/\partial H_0 > 0$ and is the spin-up mode $f_\uparrow$ and the second resonance with $\partial f_{\mathrm{res}}/\partial H_0 < 0$ is the spin-down mode $f_\downarrow$. The vertical dashed line corresponds to $\mu_0 H_0 = 0.58\,\mathrm{T}$ where Δf_{res} is minimized and the data shown in Fig. 3.6(a) is obtained. The blue dashed and red dotted lines are the solutions from numerical and analytical calculations to the Landau-Lifshitz equation and are in excellent agreement with the measured data. We will discuss the analytical calculations and the numerical simulations in Sections 3.5.2 and 3.5.3 in detail.

When applying $\boldsymbol{H}_0$ along the ASB axis, we obtain the resonance frequencies shown in Fig. 3.6(d). Here, we observe a more complex evolution of the resonance frequencies for two reasons. First, for $\mu_0 H_0 \lessapprox 0.4\,\mathrm{T}$, the equilibrium net magnetization is titled away from $\boldsymbol{H}_0$ and varies with H_0 (cf. Section 3.4). Second, and crucially, $f_\uparrow$ and $f_\downarrow$ exhibit a pronounced avoided crossing. The dashed vertical line indicates the value of H_0 of minimal Δf_{res} where also the data shown in Fig. 3.6(b) is taken from.

We plot Δf_{res} and the half-width-at-half-maximum (HWHM) linewidths $\kappa_\uparrow$ and $\kappa_\downarrow$ as a function of the magnetic field H_0 in Figs. 3.6(e) and (f) for the EAS and ASB cases, respectively. We find the mutual coupling strength $g_{\mathrm{c}}/2\pi = \min|\Delta f_{\mathrm{res}}/2| = 0.92\,\mathrm{GHz}$ for the EAS case and $g_{\mathrm{c}}/2\pi = 6.38\,\mathrm{GHz}$ for the ASB configuration. In the former case, $g_{\mathrm{c}} \lesssim \kappa_\uparrow,\kappa_\downarrow$ [Fig. 3.6(e)] and thus the system is in the weak to intermediate coupling regime. For the ASB case, the linewidths κ are at least three times smaller than g_{c}. Hence the condition for strong coupling $g_{\mathrm{c}} > \kappa_\uparrow,\kappa_\downarrow$ is clearly satisfied. Furthermore, the extracted coupling rate of $g_{\mathrm{c}}/2\pi = 6.38\,\mathrm{GHz}$ is comparable to the intrinsic excitation frequency $f_{\mathrm{r}} = (f_1 + f_2)/2 = 17.2\,\mathrm{GHz}$. The normalized coupling rate $\eta = g_{\mathrm{c}}/(2\pi f_{\mathrm{r}})$ [56, 101] evaluates to $\eta = 0.37$. Consequently, we observe magnon-magnon hybridization in the ultrastrong coupling regime [102]. Importantly, the measured g_{c} is the intrinsic coupling strength between spin-up and spin-down magnons and is independent of geometrical factors, in particular, sample volume or filling factor. This is in stark contrast to the magnon-photon or cavity-mediated magnon-magnon coupling typically observed in spin cavitronics [56, 63–67]. For the sake of completeness we can also calculate the normalized coupling rate for the temperatures $T = 280\,\mathrm{K} < T_{\mathrm{comp}}$ and $T = 294\,\mathrm{K} > T_{\mathrm{comp}}$ as shown in Figs. 3.5(b) and (f). We extract $\eta(280\,\mathrm{K}) = 0.24$ and $\eta(294\,\mathrm{K}) = 0.35$ so the system remains in the ultrastrong coupling regime.

In a last experiment, we want to demonstrate the tunability of the coupling strength as we have discussed the extreme cases so far. We rotate $\boldsymbol{H}_0$ with fixed magnetic

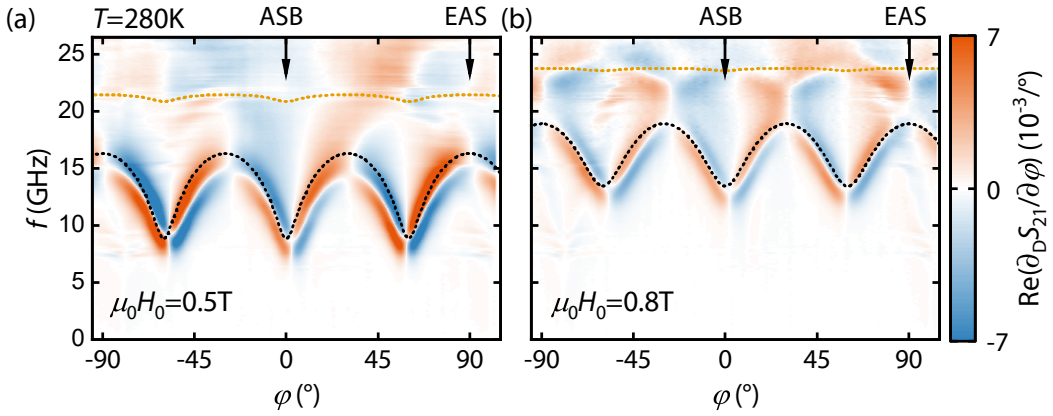

Fig. 3.7. Measured broadband ferromagnetic resonance spectrum at fixed magnetic field magnitude at (a) $\mu_0 H_0 = 0.5\,\mathrm{T}$ (below the hybridization point) and (b) $\mu_0 H_0 = 0.8\,\mathrm{T}$ (above the hybridization point) as a function of the magnetic field orientation $\boldsymbol{H}_0$ in the (111)-disk plane parameterized by the in-plane angle φ at $T = 280\,\mathrm{K}$. The dashed lines are the results from the numerical simulations where the orange line corresponds to the high frequency and the black line to the low frequency branch (see Section 3.5.3).

field magnitude in the (111)-plane at $T = 280\,\mathrm{K}$ as a function of the in-plane angle φ with a step size of $\Delta\varphi = 1°$ as defined in Fig. 3.3. For the microwave background correction of the measure S_{21} parameter we adapted the "derivative divide" algorithm for angle rotations at fixed magnetic field and calculate

$$\partial_{\mathrm{D}} S_{21}/\partial\varphi = \frac{S_{21}(\omega,H_0,\varphi+\Delta\varphi) - S_{21}(\omega,H_0,\varphi-\Delta\varphi)}{S_{21}(\omega,H_0,\varphi)\cdot\Delta\varphi}. \tag{3.19}$$

The background corrected transmission parameter as a function of the angle φ is shown in Fig. 3.7(a) and (b) for $\mu_0 H_0 = 0.5\,\mathrm{T}$ and $\mu_0 H_0 = 0.8\,\mathrm{T}$, respectively. These magnetic field magnitudes correspond to H_0 slightly below and above the hybridization point at $T = 280\,\mathrm{K}$ as the magnetic field magnitude H_0 where the frequency splitting is smallest is slightly shifting between the EAS and ASB direction [Fig. 3.5(a) and (b)]. For both H_0 values, we observe two resonances for each value of φ, where the lower resonance frequency depends strongly on φ while the upper one is nearly independent of φ. Overall, these results strongly indicate a φ-dependent level repulsion that allows to continuously adjust the coupling strength. The dashed lines in Fig. 3.7 are the results from numerical simulations which we will discuss in Section 3.5.3.

As already discussed in Section 3.2, it requires two key ingredients to observe mode hybridization in the (ultra-)strong coupling regime which are (i) nonzero mode coupling arising from the violation of spin conservation by an axial anisotropy [84] and (ii) a strong amplification of the otherwise weak coupling via an exchange-enhancement effect characteristic of (quasi-)antiferromagnetic magnons [87]. In the

next Section we will address the first point (i) and discuss the anisotropy landscape of GdIG while in Section 3.5 we will model the data and discuss the physics of exchange-enhancement.

3.4 Nonzero Mode Coupling, Anisotropy Landscape

For the calculation of the free energy density F and consequently the anisotropy landscape, we follow the approach already presented in Section 2.1 and sum over all relevant energy contributions in the system. Additionally, we need to account for the energies of both sublattice magnetizations which we denote with the subscripts A and B which refer to the Gd- and Fe-sublattice, respectively. The free energy density of GdIG then reads

$$\begin{aligned} F = &- J_{\mathrm{AB}}\, \boldsymbol{M}_{\mathrm{A}} \cdot \boldsymbol{M}_{\mathrm{B}} \\ &- \mu_0 \boldsymbol{H}_0 \cdot (\boldsymbol{M}_{\mathrm{A}} + \boldsymbol{M}_{\mathrm{B}}) \\ &+ \frac{\mu_0}{2} (\boldsymbol{M}_{\mathrm{A}} + \boldsymbol{M}_{\mathrm{B}})\, \overleftrightarrow{N}\, (\boldsymbol{M}_{\mathrm{A}} + \boldsymbol{M}_{\mathrm{B}}) \\ &+ K_{c1} (\alpha_{\mathrm{A}}^2\beta_{\mathrm{A}}^2 + \alpha_{\mathrm{A}}^2\delta_{\mathrm{A}}^2 + \beta_{\mathrm{A}}^2\delta_{\mathrm{A}}^2 + \alpha_{\mathrm{B}}^2\beta_{\mathrm{B}}^2 + \alpha_{\mathrm{B}}^2\delta_{\mathrm{B}}^2 + \beta_{\mathrm{B}}^2\delta_{\mathrm{B}}^2) \\ &+ K_{c2} (\alpha_{\mathrm{A}}^2\beta_{\mathrm{A}}^2\delta_{\mathrm{A}}^2 + \alpha_{\mathrm{B}}^2\beta_{\mathrm{B}}^2\delta_{\mathrm{B}}^2). \end{aligned} \tag{3.20}$$

The first term is the exchange interaction energy between the two sublattice magnetizations and is characterized by the intersublattice antiferromagnetic exchange constant J_{AB}. To keep the notation and the following equations simple, we write $J = J_{\mathrm{AB}}$.[3] The second term is the Zeeman energy of the two sublattice magnetizations and the third term is the demagnetization tensor $\overleftrightarrow{N}$ for the disk-shaped sample [42]. Finally, the fourth and fifth term are the first and second order terms of the magnetocrystalline cubic anisotropy with the 1st and 2nd order cubic anisotropy constants K_{c1} and K_{c2}. In this context, $\alpha_{\mathrm{A,B}}$, $\beta_{\mathrm{A,B}}$ and $\delta_{\mathrm{A,B}}$ are the direction cosines of the magnetizations $\boldsymbol{M}_{\mathrm{A,B}}$ with respect to the cubic (100)-axes.

It is known for GdIG that the cubic anisotropy has its easy axis along (111) and the hard axis along (100) [103]. The free energy density F is plotted in Fig. 3.8(a) using the parameters compiled in Tab. 3.2, which were adjusted for the numerical simulation to fit the measured data (see Section 3.5.3) and setting the sublattice magnetizations exemplarily to $M_{\mathrm{B}0} = 0$ and $M_{\mathrm{A}0} = 10\,\mathrm{mT}/\mu_0$. The z-axis corresponds to the [111]-direction. In the top-down view shown in Fig. 3.8(b) it becomes evident that the [111]-direction is a crystalline easy axis and that the crystalline hard axes in the upper and lower plane are shifted by 60° with respect to each other. For the geometry relevant to our experiments, where the [111]-direction is pointing perpendicular to

[3] Note that in Eq. (2.4), J_{ij} is the exchange constant between the i^{th} and j^{th} spins. Here, J_{AB} describes the intersublattice exchange constant between the two magnetizations M_{A} and M_{B}. Therefore, J_{AB} is equivalent to an averaged mean field constant [28, 38].

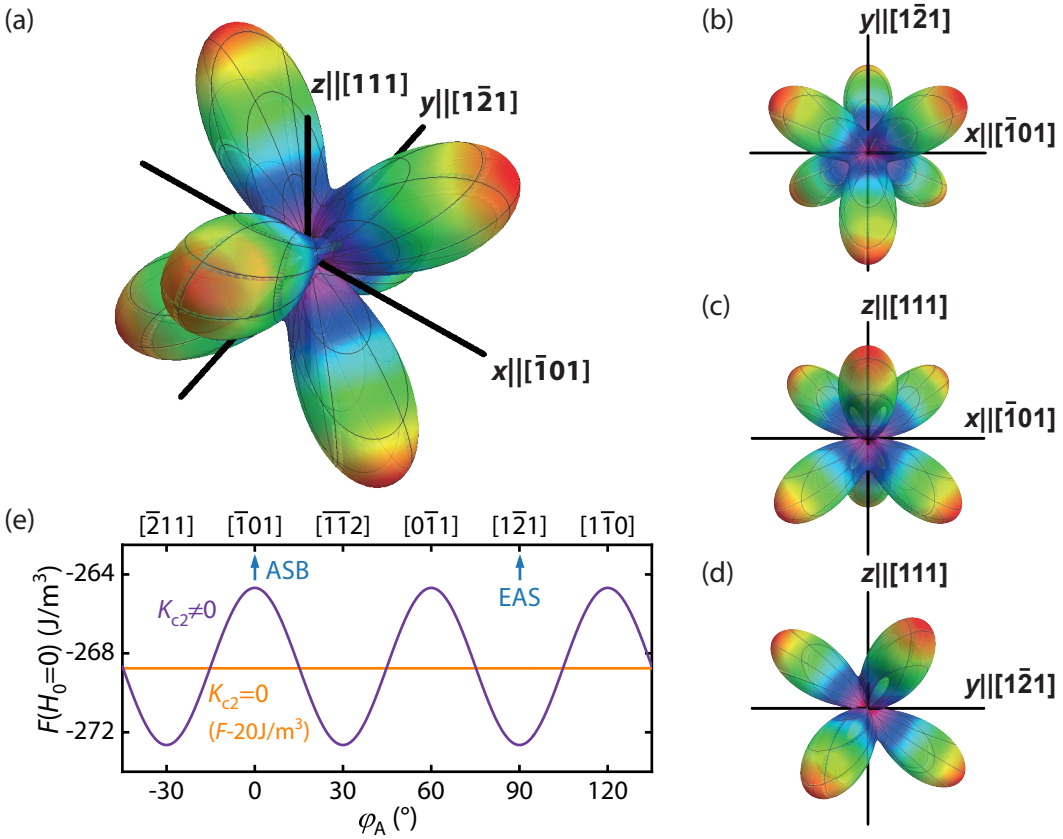

Fig. 3.8. Free energy density of gadolinium iron garnet (GdIG) at $T = 282\,\mathrm{K}$ and $H_0 = 0$ calculated with Eq. (3.20). The sublattice magnetizations are set to $M_{\mathrm{B}0} = 0$ and $M_{\mathrm{A}0} = 10\,\mathrm{mT}/\mu_0$, respectively. (a) 3D-illustration, (b),(c),(d) two-dimensional projection along the (b) z-axis (disk normal), (c) y-axis and (d) x-axis. (e) Free energy density F as a function of the in-plane angle φ_A in the xy-plane (disk-plane, $\theta_\mathrm{A} = 90°$). The angles ϕ_A and θ_A denote the orientation of $\boldsymbol{M}_\mathrm{A}$ and are analogously defined to φ and θ in Fig. 3.3. The crystallographic axes of the GdIG-disk are indicated at the top. For $K_{\mathrm{c}2} = 0$ (orange line) the (111)-disk plane is isotropic. The blue arrows denote the axial symmetry broken axis (ASB) and effectively axially symmetric axis (EAS).

the disk plane, we consider the change of the free energy F in the disk plane as a function of the in-plane angle φ as shown in Fig. 3.8(e). For $K_{\mathrm{c}2} = 0$, the free energy landscape is isotropic and for $K_{\mathrm{c}2} \neq 0$ local easy and hard axes emerge. Nevertheless, the second order cubic anisotropy has a negligible contribution to the magnon-magnon coupling as it does not further break the rotational symmetry of the free energy density.

After this discussion of the free energy density, we want to go back to the question why we observe a nonzero mode coupling between the spin-up and spin-down magnons and what the physical origin of the tunability of the coupling strength shown in Fig. 3.7 is. Therefore, we project the three-dimensional free energy density plotted in Fig. 3.8(a) to a two-dimensional colormap as a function of the angles θ_A and φ_A

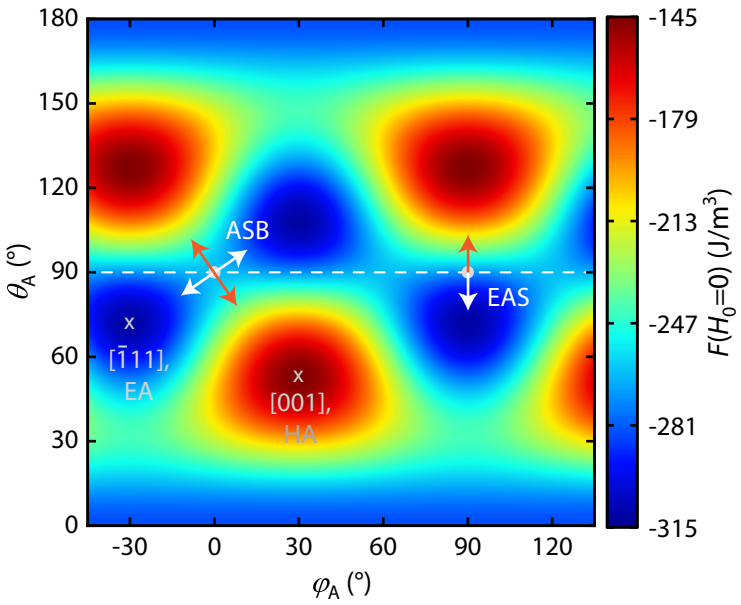

Fig. 3.9. Colormap of the free-energy density F for $H_0 = 0$, $M_{\mathrm{B}0} = 0$ and $M_{\mathrm{A}0} = 10\,\mathrm{mT}/\mu_0$ which is the two-dimensional projection of the 3D-landscape shown in Fig. 3.8. The angles ϕ_{A} and θ_{A} denote the orientation of $\boldsymbol{M}_{\mathrm{A}}$ and are analogously defined to φ and θ in Fig. 3.3. The dashed horizontal line at $\theta_{\mathrm{A}} = 90°$ corresponds to the (111)-disk plane. The orange and white arrows at the effectively axially symmetric (EAS) ($\varphi_{\mathrm{A}} = 90°$) and axial symmetry broken (ASB) ($\varphi_{\mathrm{A}} = 0°$) orientations point towards increasing and decreasing free energy density, respectively. The [001]-direction denotes a crystalline hard axis (HA) and $[\bar{1}11]$ a crystalline easy axis (EA).

of the Gd-sublattice magnetization as shown in Fig. 3.9. The applied field directions for the EAS and ASB cases are indicated by the two grey dots. The sublattice magnetizations as well as the magnon spin axis are assumed to be collinear with the applied field.

As we will derive rigorously in the following Section 3.5, coupling between the opposite-spin magnons is proportional to the degree of anisotropy in the free energy about the magnon spin axis [84]. Moreover, since they represent small and symmetric deviations of magnetization about the equilibrium configuration, the magnons can only sense anisotropy variations that are local and averaged over antiparallel directions. Considering the ASB configuration first, if the magnetization deviates from equilibrium along the orange (white) arrows, it experiences an increase (a decrease) in energy. Therefore, the free energy change depends on the direction of deviation and the symmetry about the magnon spin axis in this configuration is clearly broken by anisotropy. This causes a non-zero mode-coupling in the ASB configuration. In contrast, for the EAS configuration, an averaging over the two antiparallel directions results in a nearly vanishing and direction-independent change in the free energy, thereby effectively maintaining axial symmetry. This is prominently seen when considering the direction collinear with the orange and white arrows, which nearly

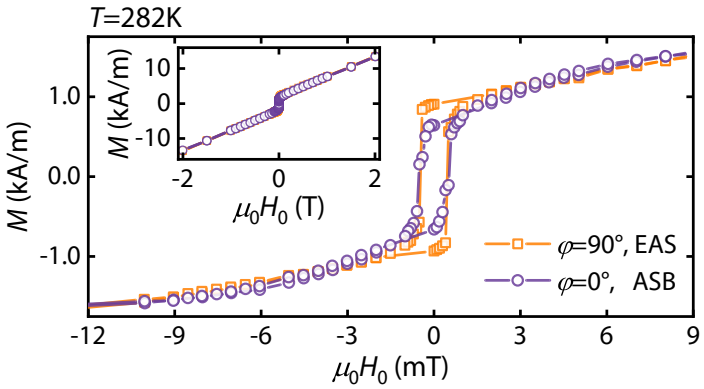

Fig. 3.10. Measured magnetic field-dependence of the total magnetization M_{tot} along the EAS (orange) and ASB direction (purple) at $T = 282\,\mathrm{K}$. The inset show the SQUID magnetometry measurement with the full magnetic field range $\mu_0|H_0| \leq 2.0\,\mathrm{T}$. From the shape of the hysterisis we can determine the EAS-direction to be a local easy axis and the ASB-direction to be a local hard axis (for details see main text).

cancel each other's effect on averaging. This configuration is thus named effectively axially symmetric (EAS). The corresponding degree of axial anisotropy, and thus mode-coupling, varies smoothly with φ between these two extreme cases.

We additionally want to highlight that the second order cubic anisotropy constant $K_{\mathrm{c}2}$ is not the (dominant) cause for the re-orientation of the magnetization for small external magnetic fields applied along the ASB direction. In the ASB configuration and for sufficiently small external magnetic fields, the antiparallel sublattice magnetizations can rigidly rotate towards the adjacent easy [111]-equivalent directions. This re-orientation is the cause of the minimum in f vs. H_0 in Fig. 3.6(d). In the EAS configuration a rigid (uncanted) rotation of both antiparallel sublattice magnetizations towards the adjacent [111] directions is not possible and consequently we do not observe such re-orientation phenomena in Fig. 3.6(c). Thus, the EAS and ASB directions are local magnetically easy and hard directions even for $K_{\mathrm{c}2} = 0$ where they are energetically degenerate (see Fig. 3.8(e)).

In order to see wether our assumption of local easy and hard axes is true, we measured the magnetic field dependence of the total magnetization M_{tot} at $T = 282\,\mathrm{K}$ as shown in Fig. 3.10. We observe the expected hysteresis loop due to the switching of the total magnetization. Comparing the two directions in the (111)-plane of the GdIG-disk (EAS and ASB), it can be seen from the shape of the hysteresis that along the EAS, the curve "jumps" at the coercive field as expected for an easy axis in a Stoner-Wolfarth model [104]. Along the ASB direction, the hysteresis is more rounded at the coercive field which in comparison to the EAS direction is a magnetic harder axis. This small difference stems from the small cubic anisotropy as discussed above.

Now we understand why we observe mode hybridization and where the symmetry breaking required for mode coupling is coming from. The second question left is the origin of the large coupling strength. We will answer this in the next Section.

3.5 Exchange-Enhancement, Modelling of Data

In this Section, we will develop a theoretical model to describe the observed mode hybridization phenomena. To this end, we will neglect dissipative effects and solve the Landau-Lifshitz equation [Eq. (2.17)] for the two-sublattice system by calculating the effective field H_{eff} which depends on the free energy F of the system [Eq. (2.2)]. Using the free energy density F given by Eq. (3.20) we encounter the problem that especially the mathematical form of the cubic anisotropy leads to not analytically solvable equations. In this sense, we need to make simplifications and assumptions to get an analytical solution.

We will structure this Section as follows: First, we will establish the simplest analytical model to explain the mode coupling. Then we will present a sophisticated analytical model developed by Akashdeep Kamra (NTNU Trondheim, QuSpin) and Wolfgang Belzig (University of Konstanz) to fully explain the so-called exchange enhancement. In a last step, we consider the full free energy density F and solve the Landau-Lifshitz equations numerically.

3.5.1 Minimal Analytical Model

In this Section, we develop a minimal model to describe the origin of the mode hybridization. As discussed in the previous Section, mode coupling requires to break the axial symmetry. We will therefore reduce the number of terms in the free energy density F in Eq. (3.20) and only consider the terms stemming from the exchange and Zeeman interaction (first and second term in Eq. (3.20)). Furthermore, we introduce an uniaxial symmetry with the uniaxial anisotropy constant K_{u} which is orthogonal to the equilibrium orientation. This means that $K_{\mathrm{u}} = 0$ corresponds to the absence of symmetry breaking equivalent to the effectively axial symmetric (EAS) case and $K_{\mathrm{u}} \neq 0$ to the case of broken axial symmetry which is analog to the axial symmetry broken (ASB) situation. With these assumptions the free energy density F_{s} takes the simple form

$$F_{\mathrm{s}} = -J\boldsymbol{M}_{\mathrm{A}} \cdot \boldsymbol{M}_{\mathrm{B}} - \mu_0 \boldsymbol{H}_0 \cdot (\boldsymbol{M}_{\mathrm{A}} + \boldsymbol{M}_{\mathrm{B}}) + K_u \left(m_{x\mathrm{A}}^2 + m_{x\mathrm{B}}^2\right). \tag{3.21}$$

Note that $J < 0$ for antiferromagnetically coupled sublattices and, hence, the first terms results in a reduction of the free energy density for M_{A} antiparallel to M_{B}. We assume that the equilibrium orientation of the sublattice magnetizations is along the

z-direction parallel to the external magnetic field $\boldsymbol{H}_0 = H_0\,\hat{\boldsymbol{e}}_z$ and the precession of the magnetization is in the xy-plane. We write for the normalized sublattice magnetizations

$$\boldsymbol{m}_{\mathrm{A,B}} = \frac{\boldsymbol{M}_{\mathrm{A,B}}}{M_{\mathrm{sA,sB}}} = \begin{bmatrix} m_{x\mathrm{A},x\mathrm{B}}(t) \\ m_{y\mathrm{A},y\mathrm{B}}(t) \\ m_{z\mathrm{A},z\mathrm{B}} \end{bmatrix}. \tag{3.22}$$

We calculate the effective field using Eq. (2.2) for each sublattice magnetization, respectively, and include the external oscillating driving field $\boldsymbol{h}_{\mathrm{rf}}(t)$ oscillating in the xy-plane. We obtain

$$\begin{aligned} \mu_0 \boldsymbol{H}_{\mathrm{eff},\{\mathrm{A,B}\}} &= -\nabla_{\boldsymbol{m}_{\mathrm{A,B}}} F_{\mathrm{s}} + \mu_0 \boldsymbol{h}_{\mathrm{rf},\{\mathrm{A,B}\}}(t) \\ &= \begin{bmatrix} \mu_0 h_{x\mathrm{A},x\mathrm{B}}(t) - \frac{2K_{\mathrm{u}} m_{x\mathrm{A},x\mathrm{B}}(t)}{M_{\mathrm{sA,sB}}} + J M_{\mathrm{sB,sA}} m_{x\mathrm{B},x\mathrm{A}}(t) \\ \mu_0 h_{y\mathrm{A},y\mathrm{B}}(t) + J M_{\mathrm{sB,sA}} m_{y\mathrm{B},y\mathrm{A}}(t) \\ \mu_0 H_0 + J M_{\mathrm{sB,sA}} m_{z\mathrm{B},z\mathrm{A}} \end{bmatrix} \end{aligned} \tag{3.23}$$

and solve the coupled Landau-Lifshitz equation [Eq. (2.17)]

$$\begin{aligned} \frac{\mathrm{d}\boldsymbol{m}_{\mathrm{A}}}{\mathrm{d}t} &= -\gamma\mu_0\, \boldsymbol{m}_{\mathrm{A}} \times \boldsymbol{H}_{\mathrm{eff,A}} \\ \frac{\mathrm{d}\boldsymbol{m}_{\mathrm{B}}}{\mathrm{d}t} &= -\gamma\mu_0\, \boldsymbol{m}_{\mathrm{B}} \times \boldsymbol{H}_{\mathrm{eff,B}} \end{aligned} \tag{3.24}$$

using a harmonic Ansatz [Eq. (2.21)] and assuming that the gyromagnetic ratio γ is the same for both sublattices. We furthermore take into account that the z-component of the Gd-sublattice is pointing along the external field $m_{z\mathrm{A}} = 1$ and that of the Fe-sublattice is antiparallel to the static magnetic field $m_{z,\mathrm{B}} = -1$ as the magnitude of the sublattice magnetization of the Gd-sublattice is larger at the temperature of interest. Solving Eq. (3.24) results in the characteristic equation [Eq. (2.23)]

$$\begin{aligned} \boldsymbol{h}_{\mathrm{rf}} &= \overleftrightarrow{\chi}^{-1} (\boldsymbol{m} \odot \boldsymbol{M}_{\mathrm{s}}) \\ \begin{bmatrix} h_{x\mathrm{A}} \\ h_{y\mathrm{A}} \\ h_{x\mathrm{B}} \\ h_{y\mathrm{B}} \end{bmatrix} &= \overleftrightarrow{\chi}^{-1} \begin{bmatrix} m_{x\mathrm{A}} M_{\mathrm{sA}} \\ m_{y\mathrm{A}} M_{\mathrm{sA}} \\ m_{x\mathrm{B}} M_{\mathrm{sB}} \\ m_{y\mathrm{B}} M_{\mathrm{sB}} \end{bmatrix} \end{aligned} \tag{3.25}$$

with the Polder-susceptibility tensor

$$\overleftrightarrow{\chi}^{-1} = \frac{1}{\mu_0}\begin{bmatrix} \frac{2K_\mathrm{u}+\mu_0 H_0 M_\mathrm{sA}-JM_\mathrm{sA}M_\mathrm{sB}}{M_\mathrm{sA}} & -\frac{i\omega}{\gamma} & -JM_\mathrm{sB} & 0 \\ \frac{i\omega}{\gamma} & -JM_\mathrm{sB}+\mu_0 H_0 & 0 & -JM_\mathrm{sB} \\ -JM_\mathrm{sA} & 0 & \frac{2K_\mathrm{u}-\mu_0 H_0 M_\mathrm{sB}-JM_\mathrm{sA}M_\mathrm{sB}}{M_\mathrm{sB}} & \frac{i\omega}{\gamma} \\ 0 & -JM_\mathrm{sA} & -\frac{i\omega}{\gamma} & -JM_\mathrm{sA}-\mu_0 H_0 \end{bmatrix}. \tag{3.26}$$

The resonance frequency $\omega = 2\pi f$ is now given by $\det\left(\overleftrightarrow{\chi}^{-1}\right) \stackrel{!}{=} 0$ which leads to two physical solutions with $\omega > 0$. The two results for the resonance frequency f are shown in Fig. 3.11 for $M_\mathrm{sA} = 0.2\,\mathrm{T}/\mu_0$, $M_\mathrm{sB} = 0.195\,\mathrm{T}/\mu_0$ and $J = -2.5\,\mathrm{V\,s}/(\mathrm{A\,m})$. We distinguish the cases where we assume to have no axial symmetry breaking with $K_\mathrm{u} = 0$ (dashed lines) corresponding to the EAS case, and the situation where we have axial symmetry breaking and set $K_\mathrm{u} = 500\,\mathrm{J/m^3}$ (solid lines). As shown in Fig. 3.11 our simple model is already sufficient to observe the mode hybridization.

From this simple analytical model we can derive two other results. The first result is the field of hybridization H_hybr which we can derive from the crossing point of the resonance frequencies $f_{\mathrm{res},i}$ with the uniaxial anisotropy constant turned off $K_\mathrm{u} = 0$. It is determined by $f_{\mathrm{res},1}(H_\mathrm{hybr}) \stackrel{!}{=} f_{\mathrm{res},2}(H_\mathrm{hybr})$. The hybridization field is given by

$$\mu_0 H_\mathrm{hybr} = \frac{1}{2} J\left(M_\mathrm{sB} - M_\mathrm{sA}\right). \tag{3.27}$$

For our used parameters given above, we calculate $\mu_0 H_\mathrm{hybr} = 0.5\,\mathrm{T}$.

The second result is an analytical expression for the coupling rate g_eff which is given by half the difference of the resonance frequencies at the magnetic field of hybridization $g_\mathrm{eff}/(2\pi) = 1/2(f_{\mathrm{res},2} - f_{\mathrm{res},1})|_{H_\mathrm{hybr}}$. From this we derive for the coupling strength

$$\begin{aligned} \frac{g_\mathrm{eff}}{2\pi} = \frac{1}{4}\frac{\gamma\sqrt{|J|}}{\sqrt{M_\mathrm{sA}M_\mathrm{sB}}}\Bigg[\Bigg(&2\sqrt{K_\mathrm{u}^2\left(M_\mathrm{sA}^4 + 14M_\mathrm{sA}^2M_\mathrm{sB}^2 + M_\mathrm{sB}^4\right)} \\ &+2K_\mathrm{u}(M_\mathrm{sA}+M_\mathrm{sB})^2 - JM_\mathrm{sA}M_\mathrm{sB}(M_\mathrm{sA}-M_\mathrm{sB})^2\Bigg) \\ &-\Bigg(-2\sqrt{K_\mathrm{u}^2\left(M_\mathrm{sA}^4 + 14M_\mathrm{sA}^2M_\mathrm{sB}^2 + M_\mathrm{sB}^4\right)} \\ &+2K_\mathrm{u}(M_\mathrm{sA}+M_\mathrm{sB})^2 - JM_\mathrm{sA}M_\mathrm{sB}(M_\mathrm{sA}-M_\mathrm{sB})^2\Bigg)\Bigg]^{\frac{1}{2}}. \end{aligned} \tag{3.28}$$

In the limit of an antiferromagnet $M_\mathrm{sA} = M_\mathrm{sB}$ and $J < 0$, the coupling strength simplifies to the expression

$$\frac{g_\mathrm{eff}}{2\pi} = \gamma\sqrt{K_\mathrm{u}|J|}. \tag{3.29}$$

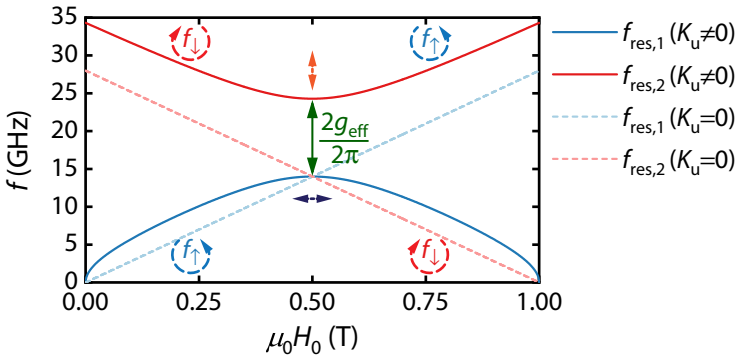

Fig. 3.11. Minimal hybridization model to demonstrate mode coupling. The dashed lines indicate the unperturbed precessional modes in the absence of a uniaxial anisotropy $K_\mathrm{u} = 0$. In the presence of a finite uniaxial anisotropy $K_\mathrm{u} \neq 0$ which breaks the symmetry, the typical anticrossing behaviour is observed with a frequency splitting of $2g_\mathrm{eff}/(2\pi)$.

We see from the result above that the uniaxial anisotropy is multiplied or amplified by the exchange interaction which is for the given physical system in the collinear state generally a large quantity compared to the anisotropy constant. Furthermore, we note that in the limit of a quasi-antiferromagnet like our GdIG close to its compensation temperature, Eq. (3.29) is a good approximation and already shows the exchange-enhancement.

3.5.2 Full Analytical Model

We have seen in the previous section that a uniaxial symmetry is sufficient to observe mode hybridization. In the following, we introduce a theoretical model developed by Akashdeep Kamra (NTNU Trondheim, QuSpin) and Wolfgang Belzig (University of Konstanz). This model is based on squeezed antiferromagnetic magnons leading to exchange-enhancement. In this section, we will only give a short overview and do not perform the full calculations involved. Here, we refer the reader to the supplemental information of Ref. [72] for the full classical calculation and Ref. [87] for the full quantum-mechanical description. We emphasize that the classical and quantum-mechanical description are equivalent and lead to the same results.

Gadolinium iron garnet has a cubic magneto-crystalline anisotropy which leads to non-analytically solvable equations. Therefore, the cubic anisotropy is approximated by two uniaxial anisotropies. One uniaxial anisotropy to capture the easy and hard axis anisotropy which leads to the re-orientation of the equilibrium magnetization direction with the external magnetic field applied along the ASB direction. A second weak uniaxial anisotropy that breaks the axial symmetry about the applied field

direction which is required to observe the mode hybridization. The free energy density F_{m} within the analytical model takes the form

$$\begin{aligned} F_{\mathrm{m}} = &- \mu_0 H_0 (M_{z\mathrm{A}} + M_{z\mathrm{B}}) \mp K_{\mathrm{A}} M_{z\mathrm{A}}^2 \mp K_{\mathrm{B}} M_{z\mathrm{B}}^2 - J \boldsymbol{M}_{\mathrm{A}} \cdot \boldsymbol{M}_{\mathrm{B}} \\ &+ K_{x\mathrm{a}} \left(M_{x\mathrm{A}}^2 + M_{x\mathrm{B}}^2 \right) + K_{y\mathrm{a}} \left(M_{y\mathrm{A}}^2 + M_{y\mathrm{B}}^2 \right) + \frac{\mu_0}{2} (M_{x\mathrm{A}} + M_{x\mathrm{B}})^2, \end{aligned} \tag{3.30}$$

where $J\,(<0)$ parameterizes the inter-sublattice antiferromagnetic exchange, $K_{\mathrm{A,B}}\,(>0)$ account for easy-axis (upper sign) and hard-axis anisotropies (lower sign) along the applied field $H_0 \hat{\boldsymbol{e}}_z$, $K_{x\mathrm{a},y\mathrm{a}}$ anisotropy contributions allow for the axial symmetry-breaking about the z-axis when $K_{x\mathrm{a}} \neq K_{y\mathrm{a}}$, and the last term stems from shape anisotropy of our disk shaped sample corresponding to the demagnetization tensor elements $N_{xx} = 1$, $N_{yy,zz} = 0$. We further assume the following hierarchy of interactions $J \gg K_{\mathrm{A,B}} \gg |K_{x\mathrm{a},y\mathrm{a}}|$.

The equilibrium configuration is determined by minimizing the free energy density F_{m} with respect to the spatially uniform sublattice magnetization directions. With the assumed energy hierarchy, the axial symmetry-breaking $K_{x\mathrm{a},y\mathrm{a}}$ minorly affects the equilibrium state. We again solve the Landau-Lifshitz equation [Eq. (2.17)] by minimizing the free energy density F_{m}

$$\frac{\partial \boldsymbol{M}_{\mathrm{A,B}}}{\partial t} = -|\gamma_{\mathrm{A,B}}| \left[\boldsymbol{M}_{\mathrm{A,B}} \times \left(-\frac{\partial F_{\mathrm{m}}}{\partial \boldsymbol{M}_{\mathrm{A,B}}} \right) \right]. \tag{3.31}$$

We define a new coordinate system with the static magnetizations (nearly) collinear with $\hat{\boldsymbol{e}}_{z'}$ which is set by the equilibrium configuration. Using a harmonic ansatz $M_{x'\mathrm{A}} = M_{x'\mathrm{A}}^{\sim} e^{i\omega t}$ and a circular basis via $M_{\mathrm{A}\pm}^{\sim} = M_{x'\mathrm{A}}^{\sim} \pm i M_{y'\mathrm{A}}^{\sim}$, the eigenvalue problem can be formulated in terms of 4×4 matrices

$$\left(\tilde{P}_0 + \tilde{P}_{\mathrm{a}} + \tilde{P}_{\mathrm{d}} \right) \tilde{\boldsymbol{M}} = 0, \tag{3.32}$$

with the magnetization vector $\tilde{\boldsymbol{M}}^{\intercal} \equiv \left[M_{\mathrm{A}+}^{\sim} \; M_{\mathrm{B}+}^{\sim} \; M_{\mathrm{A}-}^{\sim} \; M_{\mathrm{B}-}^{\sim} \right]$. Theses 4×4 matrixes describe the dynamics and eigenmodes and are given by

$$\tilde{P}_0 = \begin{bmatrix} (-\omega + \Omega_{\mathrm{A}}) & -\Omega_{\mathrm{E1}} & 0 & 0 \\ -\Omega_{\mathrm{E2}} & (\omega + \Omega_{\mathrm{B}}) & 0 & 0 \\ 0 & 0 & (\omega + \Omega_{\mathrm{A}}) & -\Omega_{\mathrm{E1}} \\ 0 & 0 & -\Omega_{\mathrm{E2}} & (-\omega + \Omega_{\mathrm{B}}) \end{bmatrix}, \tag{3.33}$$

$$\tilde{P}_{\mathrm{a}} = \begin{bmatrix} \omega_{\mathrm{uA}} & 0 & \omega_{\mathrm{cA}} & 0 \\ 0 & \omega_{\mathrm{uB}} & 0 & \omega_{\mathrm{cB}} \\ \omega_{\mathrm{cA}} & 0 & \omega_{\mathrm{uA}} & 0 \\ 0 & \omega_{\mathrm{cB}} & 0 & \omega_{\mathrm{uB}} \end{bmatrix}, \tag{3.34}$$

$$\tilde{P}_{\mathrm{d}} = \frac{1}{2}\begin{bmatrix} \omega_{\mathrm{sA}} & \omega_{\mathrm{sA}} & \omega_{\mathrm{sA}} & \omega_{\mathrm{sA}} \\ \omega_{\mathrm{sB}} & \omega_{\mathrm{sB}} & \omega_{\mathrm{sB}} & \omega_{\mathrm{sB}} \\ \omega_{\mathrm{sA}} & \omega_{\mathrm{sA}} & \omega_{\mathrm{sA}} & \omega_{\mathrm{sA}} \\ \omega_{\mathrm{sB}} & \omega_{\mathrm{sB}} & \omega_{\mathrm{sB}} & \omega_{\mathrm{sB}} \end{bmatrix} \tag{3.35}$$

with the definitions

$$\begin{aligned} \bar{K}_{\mathrm{a}} &\equiv (K_{x\mathrm{a}} + K_{y\mathrm{a}})/2, \\ \Delta\bar{K}_{\mathrm{a}} &\equiv (K_{x\mathrm{a}} - K_{y\mathrm{a}})/2, \\ \Omega_{\mathrm{A}} &\equiv |\gamma_{\mathrm{A}}|(-JM_{\mathrm{sB}} \pm 2K_{\mathrm{A}}M_{\mathrm{sA}} + \mu_0 H_0), \\ \Omega_{\mathrm{B}} &\equiv |\gamma_{\mathrm{B}}|(-JM_{\mathrm{sA}} \pm 2K_{\mathrm{B}}M_{\mathrm{sB}} - \mu_0 H_0), \\ \Omega_{\mathrm{E1}} &\equiv |\gamma_{\mathrm{A}}|JM_{\mathrm{sA}}, \\ \Omega_{\mathrm{E2}} &\equiv |\gamma_{\mathrm{B}}|JM_{\mathrm{sB}}, \\ \omega_{\mathrm{uA,uB}} &\equiv 2|\gamma_{\mathrm{A,B}}|\bar{K}_{\mathrm{a}}M_{\mathrm{sA,sB}}, \\ \omega_{\mathrm{cA,cB}} &\equiv 2|\gamma_{\mathrm{A,B}}|\Delta\bar{K}_{\mathrm{a}}M_{\mathrm{sA,sB}}, \\ \omega_{\mathrm{sA,sB}} &\equiv |\gamma_{\mathrm{A,B}}|\mu_0 M_{\mathrm{sA,sB}}, \end{aligned} \tag{3.36}$$

and additionally account for a field-dependent Gd-magnetization using $M_{\mathrm{sA}} = M_{0\mathrm{A}} + \chi_{\mathrm{a}}H_0$ determined from SQUID-magnetometry (cf. Fig. 3.10) and for the Fe-magnetization $M_{\mathrm{sB}} = M_{0\mathrm{B}}$. The plus sign corresponds to the EAS case and the minus sign to the ASB situation. Note that for the ASB case these dynamical matrices are only valid in the high field regime where the sublattice magnetization is collinear with the magnetic field. In the low field regime where we observe the re-orientation [Fig. 3.6(d)] it is necessary to account for a finite angle between the sublattice magnetizations and the applied magnetic field where the sublattice magnetizations rotate to align with the magnetic field with increasing field magnitude. We will omit this discussion for simplicity and refer to Ref. [72] for the full discussion.

The dynamic matrix $\tilde{P}_0$ is block-diagonal in 2×2 sub-matrices and represents the two uncoupled eigenmodes delocalized over the two sublattices. $\tilde{P}_{\mathrm{a}}$ captures the off-diagonal, anisotropy-mediated contributions that cause an exchange-enhanced coupling between the two modes. $\tilde{P}_{\mathrm{d}}$ represents the shape anisotropy or dipolar interaction terms which are not exchange-enhanced, and thus do not significantly contribute to the observed coupling. This is because the 2×2 sub-matrices that constitute $\tilde{P}_{\mathrm{d}}$ have a vanishing determinant. The corresponding physical interpretation is that close to compensation, i.e. when $M_{0\mathrm{A}} \approx M_{0\mathrm{B}}$, the static net magnetization nearly vanishes and only the small magnetic moment resulting from the dynamics causes dipolar interaction or shape anisotropy.

The resonance frequency $f = \omega/(2\pi)$ is given by solving the eigenvalue problem Eq. (3.32). The result of the analytical calculations with the parameters summarized

Tab. 3.1. Parameters used in the analytical calculations for $T = 282\,\mathrm{K}$. For parameters with adjusted reference value (adj.), adjustments were less than 10% for better agreement with experimental data.

Variable	Value	Unit	Source
$M_{0\mathrm{A}}$	1.602×10^5	$\mathrm{A/m}$	from Fig. 3.1(b), adj.
$M_{0\mathrm{B}}$	1.576×10^5	$\mathrm{A/m}$	from Fig. 3.1(b), adj.
$\lvert\gamma_{\mathrm{A}}\rvert$	1.754×10^{11}	$1/(\mathrm{T\,s})$	[78, 105]
$\lvert\gamma_{\mathrm{B}}\rvert$	1.773×10^{11}	$1/(\mathrm{T\,s})$	[78, 105]
K_{A}	7.2×10^{-9}	$\mathrm{V\,s/(A\,m)}$	[105], adj.
K_{B}	2×10^{-8}	$\mathrm{V\,s/(A\,m)}$	[105], adj.
K_{a}	3.58×10^{-8}	$\mathrm{V\,s/(A\,m)}$	adj.
J	-1.44×10^{-4}	$\mathrm{V\,s/(A\,m)}$	[105], adj.
χ_{a}	0.0078		from Fig 3.10, adj.

in Tab. 3.1 is shown in Fig. 3.6(c) and (d) for the EAS and ASB case, respectively. The analytical results are in good agreement with the experimental data. All parameters listed in Tab. 3.1 are either measured or taken from literature. Furthermore, the parameters in the table show that the anisotropy parameters employed to reproduce the experimental curves do not respect the hierarchy of interactions assumed, in order to enable an analytical solution, herein. This underlies the relatively minor deviations of the eigenmode frequencies evaluated within our analytic model from their experimentally measured counterparts.

In this analytical model, it is possible to give an analytical expression for the exchange-enhanced frequency splitting. Therefore, the eigenvalue problem Eq. (3.32) is simplified by neglecting the contribution of the shape anisotropy $\tilde{P}_{\mathrm{d}}$ as it is not exchange-enhanced and therefore has only a negligible influence. Without any derivation (see Ref. [72]) the frequency splitting can be analytically calculated close to the compensation temperature and is given by

$$2\pi\Delta f_{\mathrm{res}} = \omega_{\mathrm{c}}\sqrt{\frac{16|J|M_0^2}{|J|\left(M_{0\mathrm{A}} - M_{0\mathrm{B}}\right)^2 + 16KM_0^2}} \tag{3.37}$$

with the bare coupling rate $\omega_{\mathrm{c}} = |\gamma||K_{\mathrm{a}}|M_0$ considering $\gamma_{\mathrm{A}} \approx \gamma_{\mathrm{B}} \equiv \gamma$ and $M_{0\mathrm{A}} \approx M_{0\mathrm{B}} \equiv M_0$. The maximum enhancement, given by $\sqrt{|J|/K}$, is achieved at compensation of the two-sublattices ($M_{0\mathrm{A}} = M_{0\mathrm{B}}$). We find that the small bare coupling rate $2\pi\omega_{\mathrm{c}} = 160\,\mathrm{MHz}$ originating from the weak cubic anisotropy is greatly enhanced to several GHz due to the exchange-enhancement effect [78, 87–89].

This (exchange-)enhancement has its origin in strong antiferromagnetic quantum fluctuations [87] which we want to briefly discuss in the following. A schematic depiction of the antiferromagnetic eigenmodes is shown in Fig. 3.12. The antiferromagnetic ground state is a superposition of states with equal number of spin-up and spin-down sublattice magnons with spin $\pm\hbar$. The net spin of the ground state is zero. The excited

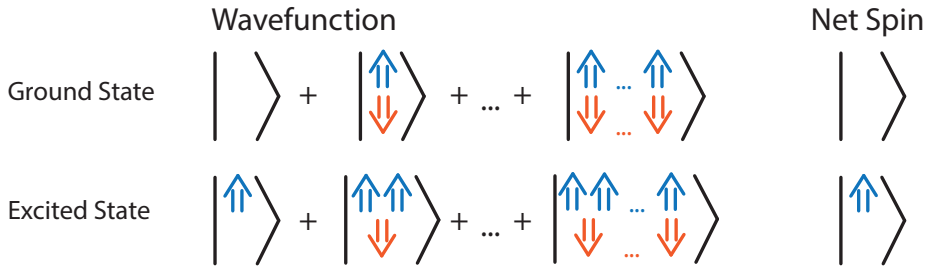

Fig. 3.12. Schematic depiction of the quantum-mechanical wavefunction of the ground and excited spin-up state of an (quasi-)antiferromagnet. An empty ket denotes the perfect antiferromagnetic state while the blue and orange arrows are spin-up and spin-down sublattice magnons. Figure adapted from [87, 106].

state spin-up magnon state is a superposition of N spin-up and $N-1$ spin-down magnons where N is a large number [87]. Despite the unit net spin, the number of spins on each of the sublattices is rather larger ($\sim \sqrt{|J|/K}$). Any interaction which is mediated by the sublattice spin, instead of the net spin, is therefore amplified by the large sublattice spin ($\sim \sqrt{|J|/K}$) [87]. This effect is termed exchange-enhancement since it is mediated by and increases with the antiferromagnetic exchange interaction. It is evident from Eq. (3.30) that the anisotropy-mediated mode-coupling is governed by the sublattice magnetizations or spins (free energy $\sim M_{x\mathrm{A}}^2 + M_{x\mathrm{B}}^2$) and not the net magnetization or spin ($\sim (M_{x\mathrm{A}} + M_{x\mathrm{B}})$). Thus, the mode-coupling is accordingly amplified via the exchange-enhancement effect described by Eq. (3.37) when the ferrimagnet is close to its compensation temperature and behaves like an antiferromagnet.

3.5.3 Numerical Model

In this last section, we will solve the full free energy density F described by Eq. (3.20) numerically. We herein follow the approach by Dreher *et al.* [37]. In the first step, we introduce a new coordinate system which we will refer to as the 1,2,3-coordinate system where the equilibrium direction of the magnetization defines the 3-direction and the 1- and 2-axes are along the dynamic components. In Fig. 3.13 the coordinate system with the real world coordinate axes x,y,z and the transformed coordinate system 1,2,3 are schematically depicted. In order to transform the two sublattice magnetizations we need to define a transformation matrix $\hat{U}_{\mathrm{A}}$. Our transformation rule for the two-sublattice magnetizations, respectively, is then [37]

$$\boldsymbol{M}_{\mathrm{A,B}}^{1,2,3} = \hat{U}_{\mathrm{A,B}} \cdot \boldsymbol{M}_{\mathrm{A,B}}^{x,y,z},$$

$$\begin{bmatrix} M_{1\mathrm{A},1\mathrm{B}} \\ M_{2\mathrm{A},2\mathrm{B}} \\ M_{3\mathrm{A},3\mathrm{B}} \end{bmatrix} = \begin{bmatrix} \cos\theta_{\mathrm{A,B}} \cos\varphi_{\mathrm{A,B}} & -\sin\varphi_{\mathrm{A,B}} & \sin\theta_{\mathrm{A,B}} \cos\varphi_{\mathrm{A,B}} \\ \cos\theta_{\mathrm{A,B}} \sin\varphi_{\mathrm{A,B}} & \cos\varphi_{\mathrm{A,B}} & \sin\theta_{\mathrm{A,B}} \sin\varphi_{\mathrm{A,B}} \\ -\sin\theta_{\mathrm{A,B}} & 0 & \cos\theta_{\mathrm{A,B}} \end{bmatrix} \cdot \begin{bmatrix} M_{x\mathrm{A},x\mathrm{B}} \\ M_{y\mathrm{A},y\mathrm{B}} \\ M_{z\mathrm{A},z\mathrm{B}} \end{bmatrix}. \tag{3.38}$$

On a more technical side, we transform the direction cosines $\alpha_{\mathrm{A,B}}$, $\beta_{\mathrm{A,B}}$ and $\delta_{\mathrm{A,B}}$ in the free energy density F, so the easy axis of the magnetocrystalline anisotropy (111) coincides with the z-axis of the coordinate system and reflects the sample geometry (cf. Fig. 3.13). To this end, we use the pre-defined Wolfram Mathematica function `RotationTransform[{{0, 0, 1}, {1, 1, 1}}]` which calculates the rotation matrix $\hat{U}_{\mathrm{R}}$ to transform the vector $\boldsymbol{z} = [0\ 0\ 1]^{\mathsf{T}}$ to the direction of the vector $[1\ 1\ 1]^{\mathsf{T}}$. For the transformed direction cosines $\alpha'_{\mathrm{A,B}}$, $\beta'_{\mathrm{A,B}}$ and $\delta'_{\mathrm{A,B}}$ we calculate

$$\begin{bmatrix} \alpha'_{\mathrm{A,B}} \\ \beta'_{\mathrm{A,B}} \\ \delta'_{\mathrm{A,B}} \end{bmatrix} = \hat{U}_{\mathrm{R}} \cdot \begin{bmatrix} \alpha_{\mathrm{A,B}} \\ \beta_{\mathrm{A,B}} \\ \delta_{\mathrm{A,B}} \end{bmatrix} = \begin{bmatrix} \frac{1}{6}\left(3+\sqrt{3}\right) & \frac{1}{6}\left(-3+\sqrt{3}\right) & \frac{1}{\sqrt{3}} \\ \frac{1}{6}\left(-3+\sqrt{3}\right) & \frac{1}{6}\left(3+\sqrt{3}\right) & \frac{1}{\sqrt{3}} \\ -\frac{1}{\sqrt{3}} & -\frac{1}{\sqrt{3}} & \frac{1}{\sqrt{3}} \end{bmatrix} \cdot \begin{bmatrix} \sin\theta_{\mathrm{A,B}}\ \cos\varphi_{\mathrm{A,B}} \\ \sin\theta_{\mathrm{A,B}}\ \sin\varphi_{\mathrm{A,B}} \\ \cos\theta_{\mathrm{A,B}} \end{bmatrix} \tag{3.39}$$

and replace the direction cosines in Eq. (3.20) with $\alpha'_{\mathrm{A,B}}$, $\beta'_{\mathrm{A,B}}$ and $\delta'_{\mathrm{A,B}}$, respectively.

By minimizing the free energy density F for each magnetic field magnitude H_0 numerically, the angles $\theta_{\mathrm{A,B}}$ and $\varphi_{\mathrm{A,B}}$ are determined. In order to distinguish between the EAS and ASB case, we parameterize the external magnetic field in the lab frame $\boldsymbol{H}_0^{x,y,z} = |H_0|\,[\sin\theta_{\mathrm{H}}\cos\varphi_{\mathrm{H}}\ \ \sin\theta_{\mathrm{H}}\sin\varphi_{\mathrm{H}}\ \ \cos\theta_{\mathrm{H}}]^{\mathsf{T}}$, where we set $\theta_{\mathrm{H}} = 90°$ and for the EAS case $\varphi_{\mathrm{H}} = 0°$ and for the ASB direction $\varphi_{\mathrm{H}} = 90°$ (cf. Fig. 3.9).

We solve the coupled Landau-Lifshitz equations given by Eq. (3.31) using a harmonic Ansatz for the magnetizations $M_{1\mathrm{A},2\mathrm{B}} = m_{1,2}e^{i\omega t}$ and $M_{3\mathrm{A},3\mathrm{B}} = M_{\mathrm{sA,sB}}$. The lengths of the $\boldsymbol{M}_{3\mathrm{A},3\mathrm{B}}$ vectors are the saturation magnetizations $M_{\mathrm{sB}} = M_{0\mathrm{B}}$ and $M_{\mathrm{sA}} = M_{0\mathrm{A}} + \chi_{\mathrm{a}}H_0$, where we account for a field-dependent Gd-magnetization.

The eigenvalue problem is formulated as $\boldsymbol{h}^{1,2,3} = \overset{\leftrightarrow}{\chi}^{-1}\boldsymbol{m'}^{1,2,3}$ with the inverse susceptibility $\overset{\leftrightarrow}{\chi}^{-1}$ which is a 4×4 matrix, the oscillating driving field $\boldsymbol{h}^{1,2,3} = \left[h_{1\mathrm{A}}e^{i\omega t}\ h_{2\mathrm{A}}e^{i\omega t}\ h_{1\mathrm{B}}e^{i\omega t}\ h_{2\mathrm{B}}e^{i\omega t}\right]^{\mathsf{T}}$ and the magnetization $\boldsymbol{m'} = [\boldsymbol{m'}_{\mathrm{A}}\ \boldsymbol{m'}_{\mathrm{B}}]^{\mathsf{T}} = [m_{1\mathrm{A}}\ m_{2\mathrm{A}}\ m_{1\mathrm{B}}\ m_{2\mathrm{B}}]^{\mathsf{T}}$. The resonance frequencies are obtained by setting $\det\left(\overset{\leftrightarrow}{\chi}^{-1}\right) = 0$ and solving for $\omega = 2\pi f$.

The resulting resonance frequencies from the numerical calculations in the magnetic field sweep experiment with the magnetic field applied along the EAS and ASB direction are shown as dashed blue lines in Figs. 3.6(c) and (d) respectively. Additionally, we performed the calculations also for the other temperatures ($T = 280\,\mathrm{K}$ and $T = 294\,\mathrm{K}$) shown in Fig. 3.5 in dashed black and orange lines. Furthermore, we can also use the numerical simulation to calculate the resonance frequencies as a function of the magnetic field direction in the disk plane at fixed magnitude. The resulting resonance frequencies are shown as dashed black and orange lines in Fig. 3.7 demonstrating the tunability of the coupling strength. The parameters used for the numerical calculations are listed in Tab. 3.2. The results from the numerical simulation are in excellent agreement with the measurement data. Importantly, the numerical calculations demonstrate that the observed magnon-magnon coupling is captured by the linearized Landau-Lifshitz equation.

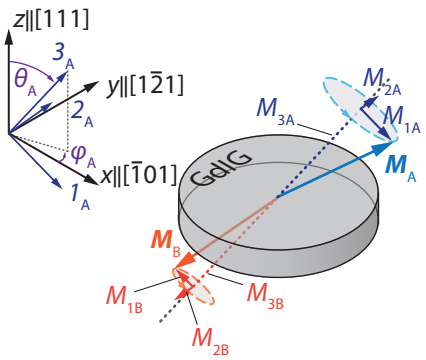

Fig. 3.13. Employed coordinate systems for the numerical simulation. The x,y,z-coordinate system is the real coordinate system with the corresponding crystallographic axes of the GdIG-crystal. The 1,2,3-coordinate system is rotated by the angles θ and φ so the 3-axis points along the equilibrium direction of the normalized magnetization $\boldsymbol{m}$ which is employed for the Gd- and Fe-sublattice indicated by the subscripts A and B. Note that the transformation of the Fe-sublattice is equivalent to the Gd-sublattice but not shown in the coordinate system on the left for clarity.

As a last step we calculate the ellipticity of the dynamical magnetization precession in the 1,2,3-frame where we will limit the calculations to the Gd-sublattice although the calculations are equivalent for the Fe-sublattice. The calculated susceptibility $\overleftrightarrow{\chi}$ will be simplified to the response of the magnetization $\boldsymbol{m}'$ to a driving field $\boldsymbol{h}^{1,2,3} = [h_{1\mathrm{A}} \cos(\omega t)\ 0\ 0\ 0]^{\mathsf{T}}$ so we only need to consider the first column of the susceptibility tensor. The ellipticity of the magnetization precession is defined as

$$\epsilon = 1 - \frac{\min\left(|\boldsymbol{m}'_{\mathrm{A}}(t)|\right)}{\max\left(|\boldsymbol{m}'_{\mathrm{A}}(t)|\right)} \tag{3.40}$$

which is the ratio of the shortest divided by the longest half axis of the precessional ellipse. The determination of the minimum and maximum length of the dynamical magnetization component is repeated for all magnetic field magnitudes H_0. The resulting ellipticity for the Gd-sublattice is shown in Fig. 3.14(a) for the field sweep experiment at fixed magnetic field directions (cf. Fig. 3.6). An ellipticity of $\epsilon = 0$ corresponds to a circular precession while a ellipticity of $\epsilon = 1$ describes a linear

Tab. 3.2. Used parameter sets for the numerical solving of the Landau-Lifshitz equation at $T = 280\,\mathrm{K}$, $T = 282\,\mathrm{K}$ and $T = 294\,\mathrm{K}$. For parameters with adjusted reference value (adj.), adjustments were less than 10% for better agreement with experimental data.

Variable	Value	Unit	Source
$M_{0\mathrm{A}}$ (280 K)	1.614×10^5	$\mathrm{A/m}$	from Fig. 3.1(b), adj.
$M_{0\mathrm{A}}$ (282 K)	1.606×10^5	$\mathrm{A/m}$	from Fig. 3.1(b), adj.
$M_{0\mathrm{A}}$ (294 K)	1.500×10^5	$\mathrm{A/m}$	from Fig. 3.1(b), adj.
$M_{0\mathrm{B}}$ (280 K)	1.568×10^5	$\mathrm{A/m}$	from Fig. 3.1(b), adj.
$M_{0\mathrm{B}}$ (282 K)	1.568×10^5	$\mathrm{A/m}$	from Fig. 3.1(b), adj.
$M_{0\mathrm{B}}$ (294 K)	1.534×10^5	$\mathrm{A/m}$	from Fig. 3.1(b), adj.
$\lvert\gamma_{\mathrm{A}}\rvert$	1.754×10^{11}	$1/(\mathrm{T\,s})$	[78, 105]
$\lvert\gamma_{\mathrm{B}}\rvert$	1.773×10^{11}	$1/(\mathrm{T\,s})$	[78, 105]
K_{c1} (280 K, 282 K)	-430	$\mathrm{J/m^3}$	adj.
K_{c1} (294 K)	-300	$\mathrm{J/m^3}$	adj.
K_{c2} (280 K, 282 K)	-400	$\mathrm{J/m^3}$	adj.
K_{c2} (294 K)	-300	$\mathrm{J/m^3}$	adj.
J	-1.40×10^{-4}	$\mathrm{V\,s/(A\,m)}$	[105], adj.
χ_{a} (280 K)	0.0079		from magnetometry, adj.
χ_{a} (282 K)	0.0077		from Fig 3.10, adj.
χ_{a} (294 K)	-0.0080		from magnetometry, adj.

polarization. The solid black line corresponds to the branch of the resonance frequency at lower frequencies and the orange line to the resonance frequencies at higher frequencies which is also used in the figures with experimental data.

The point in time t where the minimum and maximum length of the dynamic magnetization precession is observed can be used to calculate the rotation of the precessional ellipse in the $1,2,3$-coordinate system. The mode frequency as a function of the external magnetic field is shown in Fig. 3.14(b), where the symbol size and form encodes the ellipticity and rotation of the magnetization precession. The color gradient indicates the hybridization from the spin-up to spin-down magnon and vice versa. We observe for the ellipticity that magnons are linearly polarized at the anti-crossing point, consistent with the small, but non-zero splitting observed along the EAS direction. In the ASB case a more complicated evolution of the ellipticity close to the hybridization point is observed. This complexity is rooted in several factors including evolution of the equilibrium configuration, ultrastrong nature of the hybridization, and a finite static susceptibility of the Gd-sublattice. The linear polarization at the hybridization point is consistent with our expectations from Section 3.2.

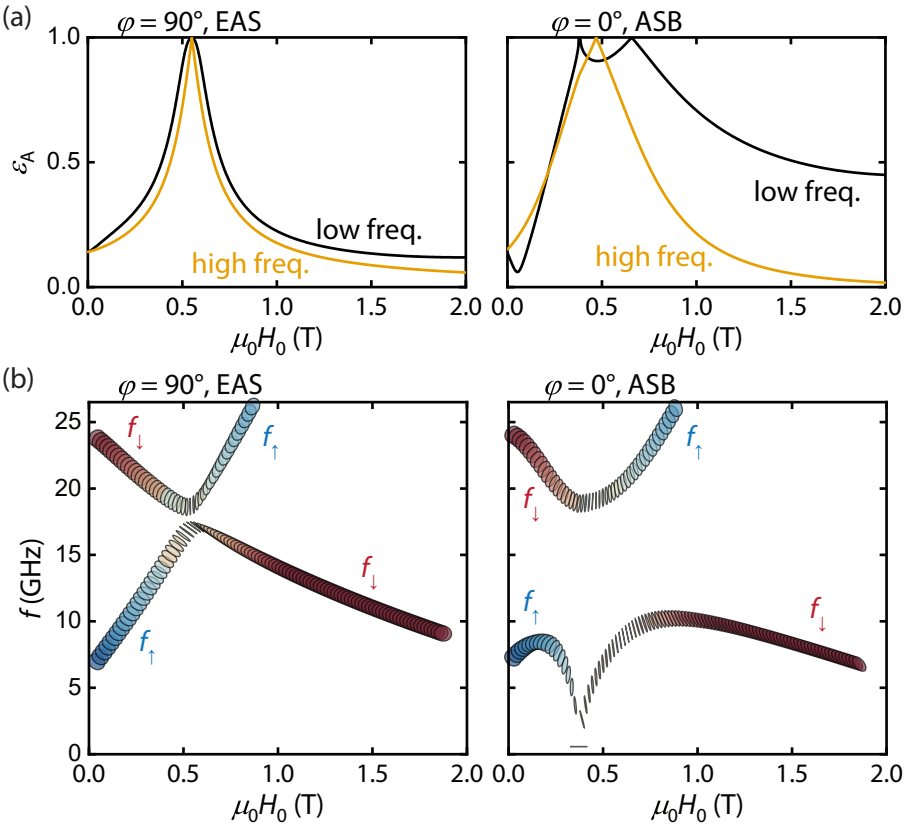

Fig. 3.14. Calculated ellipticities of the Gd-sublattice magnetization precession from numerical simulations. (a) Ellipticity ϵ_{A} shown as a function of the magnetic field H_0 applied along the effectively axial symmetric (EAS) (left column) and the axial symmetry broken (ASB) direction (right column). An ellipticity of $\epsilon = 0$ corresponds to a circular precession and $\epsilon = 1$ corresponds to linear polarization. (b) Mode frequencies as a function of the magnetic field strength with the ellipticity and rotation of the Gd-sublattice magnetization precession encoded as elliptical points.

3.6 Summary

In conclusion, we investigated the magnetization dynamics of a compensated ferrimagnet gadolinium iron garnet (GdIG) single crystal. The disk-shaped sample is placed onto a coplanar waveguide and broadband magnetic resonance is measured using a vector network analyzer. Gadolinium iron garnet features a compensation temperature, where the magnetizations of the two-sublattices compensate for each other and the system mimics a “quasi-antiferromagnet”. We choose a temperature slightly below the compensation temperature and measure the dynamic magnetic response of the GdIG magnetization. The observed (ultra-)strong magnon-magnon coupling between spin-up and spin-down magnons can be modelled using analytical and numerical calculations. The calculated results are in excellent agreement with the measurement data and explain the observed tunable coupling with axial symmetry

breaking due to a small cubic anisotropy violating the spin conservation and, in turn, amplifying the coupling strength by the intralayer exchange interaction.

These findings demonstrate that previously typically neglected details of the magnetocrystalline anisotropy can lead to giant effects on spin dynamics if they have the appropriate symmetry. The exchange-enhanced ultrastrong magnon-magnon coupling reported here opens exciting perspectives for studying ultrastrong coupling effects in nanoscale devices and exploring quantum-mechanical coupling phenomena beyond classical electrodynamics. The reported effect also enables the engineering of novel material systems to investigate the dynamics of quasi-antiferromagnetic magnon modes such as in tunable synthetic antiferromagnets. This physical concept is not restricted to uniform modes presented herein but can also be applied to propagating magnon modes [107].

Magnon-Photon Coupling in the Chiral Magnet Cu_2OSeO_3

4

As discussed in the previous chapter, the coupling of two physical systems has attracted great attention over the last years. Strongly coupled magnon-photon systems, where the magnitude of the effective coupling rate between the magnons and photons in a microwave resonator exceeds their respective loss rates, become particularly interesting. In this limit, coherent exchange of the quantized excitations is established [22, 102]. The magnon-photon coupling in ferromagnets and ferrimagnets has been extensively studied [55–58, 60]. The cooperativity of coupled spin-cavity systems is a measure of the coherent exchange of excitations. The possibility to tune the cooperativity in-situ by an external control parameter is interesting by itself and a promising tool for applications. A large tunability can be expected at the boundaries of different phases of the spin system. To experimentally demonstrate this concept, we have used the skyrmion host material Cu_2OSeO_3, featuring several magnetic phases in a small magnetic field and temperature window.

Skyrmions are topologically stabilized spin solitons [108–118]. They can form ordered phases featuring a rich spectrum of collective excitations of the spin texture known as magnons. The magnetization dynamics of skyrmion phases has been extensively studied in the limit of weak coupling to microwave circuits [119–122]. For potential applications such as realizing novel magnetic state storage [23], it is necessary to strongly couple the magnons to other quantized excitations such as photons [24]. While the coupling of the higher order helimagnon modes [121] to an X-band (9.8 GHz) photonic resonator has been demonstrated already in Cu_2OSeO_3 [123] the coupling in the skyrmion lattice phase and the potential for tunable cooperativity associated with it remained an open issue so far.

In this chapter, we report the coupling of uniform-mode excitations of the insulating chiral magnet Cu_2OSeO_3 to microwave photons in a three-dimensional microwave cavity with a resonance frequency of 683.8 MHz. In contrast to earlier experiments [123], the magnon-photon coupling was addressed in all magnetic phases including the skyrmion lattice phase. We find a large coupling rate of the breathing-mode skyrmion excitation to the cavity photons resulting in a high cooperativity $C = g_{\mathrm{eff}}^2/(\kappa_{\mathrm{mag}}\,\kappa_{\mathrm{res}}) > 50$. Most importantly, the cooperativity can be tuned values as low as 1 by changing the externally applied magnetic field magnitude by only $\sim 10\,\mathrm{mT}$.

This chapter is structured as follows: We start with an introduction to the magnetization dynamics of bulk skyrmion host materials and show broadband magnetic resonance spectroscopy to pre-characterize the used Cu_2OSeO_3 single crystal over a large microwave frequency range. We will then describe the characterization of the coupled magnon-photon systems by microwave spectroscopy experiments. To this end, we discuss the modelling of these experiments by the input-output formalism, allowing us to derive the expected spectrum of a microwave resonator dispersively coupled to the magnon system. Finally, the experimental details and results of the cavity-based magnetic resonance spectroscopy with the self-designed loop-gap resonator is discussed and modelled using the input-output formalism to demonstrate the tunability of the cooperativity.

4.1 Chiral Magnets as Skyrmion Host Materials

Chiral magnets possess a broken inversion symmetry of their crystal structure, which leads with additional strong spin-orbit coupling to the so-called Dzyaloshinskii-Moriya interaction (DMI) [124, 125]. One class of chiral magnets are non-centrosymmetric cubic crystals with space group $P2_13$. Prominent examples are for example MnSi, FeGe, $Fe_{0.8}Co_{0.2}Si$ or Cu_2OSeO_3 [116]. The Hamiltonian of the DMI reads [38]

$$\mathcal{H}_{\mathrm{DMI}} = \boldsymbol{D}_{ij} \cdot (\boldsymbol{S}_i \times \boldsymbol{S}_j) \tag{4.1}$$

with the DMI vector $\boldsymbol{D}_{ij}$, which determines the strength and direction of the DMI. The DMI leads to a canting of neighbouring spins $\boldsymbol{S}_{i,j}$ either in clockwise or counterclockwise direction depending on the orientation of the DMI vector $\boldsymbol{D}_{ij}$. This is in contrast to the Heisenberg exchange interaction, which, depending on the sign of the exchange integral J_{ij}, favors either parallel ($J_{ij} > 0$) or anti-parallel alignment ($J_{ij} < 0$) of the magnetic moments. We emphasize that the DMI is not only present in crystals or intrinsically broken crystal classes but also at interfaces and surfaces leading to interfacial-DMI [126].

Chiral magnets feature a rich magnetic mode spectrum, which is in contrast to the ferro- or ferrimagnets as discussed in the previous chapter. This is due to the different relevant energy scales of the interactions, which are in descending strength the Heisenberg exchange interaction, the DMI and higher-order spin-orbit coupling terms such as magneto-crystalline (cubic) anisotropy [118]. The total free energy density F of a chiral magnet is given by [116]

$$F = F_{\mathrm{ex}} + F_{\mathrm{DMI}} + F_{\mathrm{aniso}} + F_{\mathrm{Z}} + F_{\mathrm{dip}}, \tag{4.2}$$

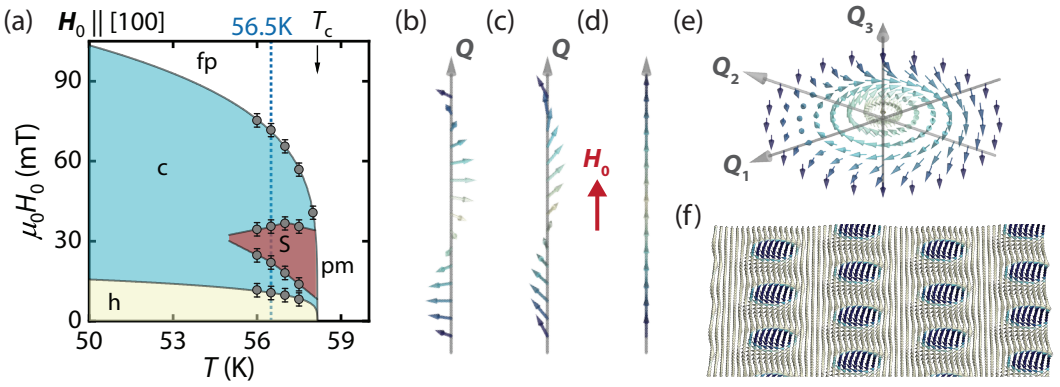

Fig. 4.1. (a) Magnetic phase diagram of Cu_2OSeO_3 extracted from broadband magnetic resonance spectroscopy, representative for Bloch-skyrmion host materials. The magnetic phases can be identified coming from a large magnetic field H_0 as the field-polarized (fp), conical (c) and helical (h) phase. Close to the critical temperature T_c a skyrmion lattice phase (S) forms. Above T_c the system is paramagnetic (pm). Illustration of the local magnetic moments (b) in a helical and (c) in a conical spin texture along the helical propagation vector $\boldsymbol{Q} \parallel \boldsymbol{H}_0$ and (d) of the field-polarized state. (e) Spin texture of an individual Bloch-type skyrmion, forming (f) a hexagonal lattice in the plane perpendicular to the external magnetic field $\boldsymbol{H}_0$. Note that an individual skyrmion as shown in (e) is composed of three helical spirals with pitch vectors $\boldsymbol{Q}_i$ arranged in one plane with an angle of 60° to each other. Figure adapted from Refs. [116] and [127].

with the free energy density contributions from the exchange interaction F_{ex}, the DMI F_{DMI}, magneto-crystalline anisotropy F_{aniso}, Zeeman interaction F_{Z} and dipolar interaction F_{dip}. A representative magnetic phase diagram of a chiral magnet is shown in Fig. 4.1(a), which in this particular case is extracted by broadband magnetic resonance (BMR) spectroscopy of a Cu_2OSeO_3 single crystal with the magnetic field applied $\boldsymbol{H}_0 \parallel [100]$, which is used in the experiments described below (cf. Section 4.3). The magnetic moments in the chiral magnet order below a critical temperature T_c. For $T > T_c$, the magnetic moments in the system are disordered and the system is in a paramagnetic state (pm). Below T_c and at low magnetic fields H_0, the magnetic moments in the system order in the helical phase with the spins aligned in a periodic helix along the pitch vector $\boldsymbol{Q}$ as depicted in Fig. 4.1(b). At low magnetic fields the orientation of the pitch vector $\boldsymbol{Q}$ is determined by the magnetic anisotropy [128–130]. With the pitch vector along the z-direction $\boldsymbol{Q} = Q\hat{\boldsymbol{e}}_z$ and using the continuum approximation [131], the local magnetization as a function of the position vector $\boldsymbol{r} = [x\ y\ z]^{\mathsf{T}}$ is given by [108, 121]

$$\boldsymbol{m}_{\mathrm{H}}(\boldsymbol{r},\boldsymbol{Q}) = \hat{\boldsymbol{e}}_x \cos(\boldsymbol{Q}\cdot\boldsymbol{r}) + \hat{\boldsymbol{e}}_y \sin(\boldsymbol{Q}\cdot\boldsymbol{r})\,. \tag{4.3}$$

This equation is used to calculate the spin alignment shown in Fig. 4.1(b).

With increasing magnetic field, the magnetic moments in the helix tilt towards the pitch vector $\boldsymbol{Q}$, which at the critical field points along the external magnetic field $\boldsymbol{Q} \parallel$

$\boldsymbol{H}_0$ as depicted in Fig. 4.1(c). In this so-called conical phase, the magnetic moments have a finite projection along the external magnetic field leading to a finite macroscopic magnetization. Assuming the magnetic field to point along the z-direction $\boldsymbol{H}_0 = H_0\hat{\boldsymbol{e}}_z$ and consequently the pitch vector $\boldsymbol{Q}$ parallel to it, the magnetization as a function of the position vector reads [121, 127]

$$\boldsymbol{m}_{\mathrm{C}}(\boldsymbol{r},\boldsymbol{Q}) = \cos\theta\,\hat{\boldsymbol{e}}_z + \sin\theta\,\boldsymbol{m}_{\mathrm{H}}, \tag{4.4}$$

with $\cos\theta = H_0/H_{c2}$ and the critical magnetic field H_{c2}. Above H_{c2} the magnetic field aligns all magnetic moments parallel to $\boldsymbol{H}_0$, so the system is in the field-polarized state (fp) similar to the ferro- or ferrimagnetic state. The schematic alignment of the magnetic moments in the system is depicted in Fig. 4.1(d). Close to the critical temperature T_{c} a topologically-protected skyrmion lattice phase forms due to fluctuations close to T_{c}. A skyrmion can be described as a superposition of three helices with equal chirality and pitch length with a relative angle of 120° in the plane perpendicular to the applied magnetic field [108, 132]. The magnetization of a skyrmion in the continuums approach can be described by [108]

$$\boldsymbol{m}_{\mathrm{S}}(\boldsymbol{r}) = \boldsymbol{m}_{\mathrm{f}} + \sum_{i=1}^{3} \boldsymbol{m}_{\mathrm{H}}\left(\boldsymbol{r} + \Delta\boldsymbol{r}_i, \boldsymbol{Q}_i\right), \tag{4.5}$$

where $\boldsymbol{m}_{\mathrm{f}}$ is a finite uniform magnetization component and $\boldsymbol{Q}_i \cdot \Delta\boldsymbol{r}_i$ is the phase of a single helix [132]. The arrangement of the spins in a single, isolated skyrmion is depicted in Fig. 4.1(e) while the complete skyrmion lattice with the hexagonal symmetry is schematically shown in Fig. 4.1(f), calculated using Eq. (4.5). We want to emphasize that the shown single skyrmion in Fig. 4.1(e) is a Bloch-type skyrmion meaning that by taking a cut through the center of the skyrmion the spins are aligned in a helix. The counterpart is the Néel-type skyrmion where the spins are aligned on a cycloid due to the different direction of the DMI vector $\boldsymbol{D}$. This type of skyrmions is prominently observed in thin-films [114, 133] or in bulk GaV_4S_8 [134].

Due to the periodic, long-range order of the skyrmions, they can be detected using small angle neutron scattering (SANS) [108, 110], resonant elastic x-ray scattering (REXS) [135, 136] or using real-space imaging techniques such as Lorentz transmission electron microscopy (LTEM) [112, 137] or magnetic force microscopy (MFM) [130, 138, 139]. The magnetization dynamics of chiral magnets and in particular the skyrmion dynamics are well understood [116, 140] and have been extensively investigated [119–122]. In the following section, we will discuss the magnetization dynamics of a chiral magnet in the context of a coupled magnon-cavity system and introduce the concept of the input-output formalism.

4.2 Magnon-Photon Coupling and Magnetization Dynamics in a Chiral Magnet

In this section, we will provide a basic understanding on the magnon-photon coupling in a chiral magnet using the input-output formalism. The magnon-photon system can in a very simple, classical model be understood as two harmonic oscillators coupled to each other. Each of the oscillators possesses an eigenfrequency f_i and a certain decay rate κ_i, describing the damping in each system. Energy can now be transferred between the two coupled oscillators, where the coupling strength is parameterized by the effective coupling rate g_{eff}. The details of the origin of the coupling are not relevant for the discussion. If the eigenfrequencies of the two harmonic oscillators are modified by an external control parameter and they cross each other, the eigenmodes can hybridize. Depending on the relative magnitude of the decay rates κ_i to the effective coupling rate g_{eff}, strong coupling with the characteristic anti-crossing is observed if $g_{\mathrm{eff}} > \kappa_1$,$\kappa_2$ holds. If one or both decay rates exceed the effective coupling rate, the anti-crossing disappears.

Using this simple analogy from classical mechanics, we can understand the magnon-photon coupling between a magnetically ordered system and a microwave cavity as schematically depicted in Fig. 4.2(a). The microwave photons inside the cavity possess a resonance frequency f_{res} and a loss rate $\kappa_{\mathrm{res}} = \kappa_{\mathrm{int}} + \kappa_{\mathrm{ext}}$, consisting of the internal κ_{int} and the external cavity loss rate κ_{ext}. These parameters are determined by the specific geometry, feedline design, used materials and dielectric substrates of the microwave cavity design and are usually magnetic field independent. The external loss rate κ_{ext} thereby quantifies the coupling strength of the cavity to the feedline and κ_{int} quantifies the inverse lifetime of cavity photons.

The magnon system has an excitation frequency characterized by f_{mag} and a decay rate of κ_{mag}. Generally, the magnon resonance frequency f_{mag} is magnetic field dependent and can be tuned with this control parameter. Tuning f_{mag} into resonance with f_{res} allows one to observe the magnon-photon hybridization. The coupling of the magnons with the photons is herby mediated by the dipolar interaction [55]. This approach of mode hybridization, where f_{mag} and f_{res} cross and hybridize, is called resonant coupling and has been extensively studied in previous works in the limit of different relative magnitudes of g_{eff}, κ_{mag} and κ_{res} [23, 55, 56, 65, 83].

A different approach is to measure dispersively, where the magnon frequency cannot be tuned to the cavity frequency so they never cross. This is for example the case if the cavity frequency is lower than the magnon resonance frequency. In this case, it is still possible to couple to the magnon system with the cavity photons but in contrast to the resonant coupling, no coherent exchange of excitations takes place. Nevertheless, there is a second order coupling due to virtual exchange of

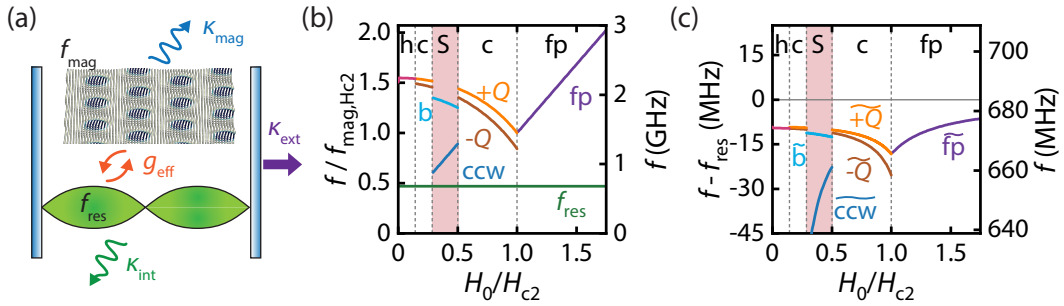

Fig. 4.2. Schematic depiction of the input-output formalism. (a) Illustration of the system parameters used in the input-output formalism described by Eq. (4.7). The magnons of the chiral magnet with resonance frequency f_{mag} and loss rate κ_{mag} couple with the effective coupling rate g_{eff} to the photons of the cavity resonance mode with frequency f_{res}. The total resonator loss rate is given by the internal κ_{int} and external loss rate κ_{ext}. The resonance frequencies in the input-output formalism manifest themselves in the scattering parameters. (b) Schematic magnetic field dependence of the uncoupled, uniform resonance frequencies of the magnon modes f_{mag} present in a chiral magnet. The resonance frequency of the resonator f_{res} is lower than all magnon frequencies. Normalized and absolute frequencies are shown on the left and right ordinate respectively. (c) Frequency shift of the resonator mode in a coupled magnon-photon system as calculated using the input-output-formalism with constant coupling rate $g_{\mathrm{eff}}/(2\pi) = 120\,\mathrm{MHz}$ in all magnetic phases. The hybridized magnon-cavity modes are denoted by tildes.

excitations. Typically, this coupling exhibits itself by a dispersive shift of the cavity frequency which can be detected in the experiment [123].

For a simple ferromagnet, the ferromagnetic resonance is given by the Kittel equation [Eq. (2.27)]. In a chiral magnet due to the multiple magnetic phases, the situation is more complicated. A calculated, exemplary mode spectrum for an uncoupled chiral magnet is shown in Fig. 4.2(b). The right vertical axis shows absolute frequencies calculated for Cu_2OSeO_3. For the field-polarized mode (fp), we expect a single mode, which is equivalent to the uniform mode in a ferromagnet and can be described by the Kittel equation given by Eq. (2.27) [116, 120]. In the conical mode (c), two resonant magnon modes are present, which are the $+Q$ and $-Q$ mode. Here, the net magnetic moments are either precessing in the positive or negative sense [119]. Depending on the details of the demagnetization, the degeneracy of the two modes is lifted by the dipolar interaction [120, 121]. The analytical formula to describe the resonance frequency of the conical modes as a function of magnetic field, takes a complicated form and is given in Refs. [120, 121].

In the skyrmion lattice phase three different uniform magnon modes exist, which are with increasing resonance frequency the counter-clockwise (ccw), the breathing (b) and the clockwise mode (cw). The clockwise and counter-clockwise modes are gyrating modes, where the core of the skyrmion rotates clockwise or counter-clockwise, respectively. The breathing mode is the topological non-trivial mode, where the core of the skyrmion expands and shrinks periodically. These modes differ

in their excitation geometry, where the gyrating modes are excited with an oscillating magnetic field perpendicular to the static field $\boldsymbol{h}_{\mathrm{ac}} \perp \boldsymbol{H}_0$ while the breathing mode couples to $\boldsymbol{h}_{\mathrm{ac}} \parallel \boldsymbol{H}_0$. All other uniform magnetic modes present in the chiral magnet are expected to couple to $\boldsymbol{H}_0 \perp \boldsymbol{h}_{\mathrm{ac}}$ [116, 119, 120, 140]. The clockwise mode has the lowest spectral weight compared to the breathing and counter-clockwise skyrmion modes and is thus usually not observed in experiments. Therefore, the clockwise mode is neglected in the spectrum in Fig. 4.2(b).

At low magnetic fields in the helical phase, we expect the same uniform magnon excitations as in the conical phase. Below the critical field of the phase transition h↔c, the helix reorients from the magnetic field direction to the magnetic easy axis of the magneto-crystalline anisotropy [116]. With the possible formation of domains depending on the temperature and magnetic field history, there is no analytical formula to describe the magnetic field-dependent resonance frequency.

After the discussion of the uncoupled, uniform magnon dynamics in a chiral magnet, we now discuss the coupled dynamics of the magnon-photon system and introduce the input-output formalism. Using the quantum mechanical picture, the Hamiltonian of the magnon-photon system can be formulated in the rotating wave approximation as [55, 141–144]

$$\mathcal{H}_{\mathrm{cp}} = \hbar\omega_{\mathrm{res}} a^\dagger a + \hbar\omega_{\mathrm{mag}} b^\dagger b + \hbar g_0 \left(a b^\dagger + a^\dagger b \right) \tag{4.6}$$

with the reduced Planck constant $\hbar = h/(2\pi)$ and the generation and annihilation operator for the photon excitations in the microwave cavity ($a^\dagger$,a) and for the magnon excitations ($b^\dagger$,b). The eigenfrequency of the magnon and photon system are denoted by $\omega_{\mathrm{mag}} = 2\pi f_{\mathrm{mag}}$ and $\omega_{\mathrm{res}} = 2\pi f_{\mathrm{res}}$, respectively. The first and the second term in Eq. (4.6) describe the total energy of the uncoupled photon and magnon system, respectively. The third term describes the coupling between the two systems with the single spin coupling rate g_0. The generation (annihilation) of a magnon in the magnetic system is associated with the annihilation (generation) of a photon of the cavity. Due to the large number of spins N in the system, the effective coupling strength in the system is enhanced by $g_{\mathrm{eff}} = g_0\sqrt{N}$ [55, 145], where a constant single spin coupling rate g_0 for all spins is assumed.

By solving the above Hamiltonian and calculating the temporal dynamics, it is possible to relate the results to the measured quantities of the vector network analyzer. Using the input-output formalism the final result for the reflection parameter S_{11} is derived as [123, 142, 145, 146]

$$S_{11}(f) = -1 + \frac{\kappa_{\mathrm{ext}}}{i \cdot 2\pi(f_{\mathrm{res}} - f) + \kappa_{\mathrm{res}} + \frac{g_{\mathrm{eff}}^2}{i \cdot 2\pi(f_{\mathrm{mag}} - f) + \kappa_{\mathrm{mag}}}}, \tag{4.7}$$

with $\kappa_{\mathrm{res}} = \kappa_{ext} + \kappa_{\mathrm{int}}$. Fitting the experimental data by the prediction of the input-output formalism allows one to characterize the magnon-photon coupling in the different coupling regimes. Due to the complex uniform magnon spectrum present in the chiral magnet and the used microwave cavity with resonance frequency $f_{\mathrm{res}} = 683.8\,\mathrm{MHz}$, which is lower than all resonance frequencies of the magnon modes (green line in Fig. 4.2(b)), we want to calculate the modified resonance frequencies of the coupled magnon-cavity system close to $680\,\mathrm{MHz}$. The resonance frequencies are obtained by minimizing $|S_{11}|$ from Eq. (4.7) by varying f and keeping further parameters constant. The significant detuning of the cavity resonance frequency relative to the uniform magnon resonance frequency limits our analysis to the dispersive regime. Using the resonance frequencies f_{mag} and f_{res} depicted in Fig. 4.2(b) and a effective coupling rate $g_{\mathrm{eff}}/(2\pi) = 120\,\mathrm{MHz}$ (compatible to the values we find later), we calculate the coupled mode spectrum shown in Fig. 4.2(c), where the left vertical axis describes the relative shift of the cavity frequency and the right vertical axis the absolute frequencies for a coupled Cu_2OSeO_3-cavity system. In all magnetic phases, the frequency of the hybridized magnon-photon modes (denoted by overset tilde in the figure) is reduced to values well below the resonance frequency f_{res} of the unperturbed cavity due to the formation of normal modes.

After this introduction to magnetization dynamics of chiral magnets and the description of the response of the coupled magnon-photon dynamics using the input-output formalism, we now switch to the experimental results. First, we perform broadband magnetic resonance spectroscopy equivalent to pre-characterize our Cu_2OSeO_3 single-crystal and then switch to cavity-based magnetic resonance measurements.

4.3 Pre-Characterization of Cu_2OSeO_3 Single Crystal Using Broadband Magnetic Resonance Spectroscopy

For the pre-characterization of the Cu_2OSeO_3 single crystal, we perform broadband magnetic resonance (BMR) spectroscopy using a coplanar waveguide (CPW) and a vector network analyzer (VNA). The principle and the data processing of the BMR technique are discussed in detail in Section 3.3. The irregularly shaped Cu_2OSeO_3 single crystal with maximum dimensions of the main axis $l_x = 3.4\,\mathrm{mm}$, $l_y = 7.7\,\mathrm{mm}$ and $l_z = 12.9\,\mathrm{mm}$, is placed onto a CPW with center conductor width $w_{\mathrm{cc}} = 340\,\mu\mathrm{m}$ as schematically depicted in Fig. 4.3. The VNA (Keysight N5225B PNA) is connected via microwave cables and endlaunch connectors to the CPW, which is mounted on a dipstick and inserted into a 3D-vector magnet cryostat. We perform frequency-swept BMR measurements, where we set the magnetic field H_0 to a fixed value and

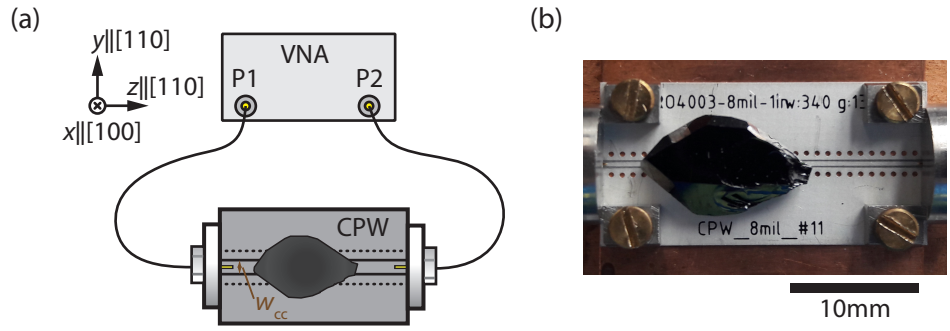

Fig. 4.3. (a) Schematic setup of the broadband magnetic resonance spectroscopy measurement of the Cu_2OSeO_3 single crystal. For details refer to main text. (b) Photograph of the Cu_2OSeO_3 single crystal on the used coplanar waveguide (CPW).

sweep the microwave frequency linearly in the range $0.1\,\mathrm{GHz} \leq f \leq 3.25\,\mathrm{GHz}$ with a resolution of $15.75\,\mathrm{MHz}$ and a microwave power of $P = 0\,\mathrm{dBm}$. In this way, we measure the complex transmission parameter S_{21} for a series of magnetic fields in the range $-90\,\mathrm{mT} \leq \mu_0 H_0 \leq 90\,\mathrm{mT}$, where we sweep from positive to negative fields with a step size of approx. $0.5\,\mathrm{mT}$. The magnetic field $\boldsymbol{H}_0$ is applied along the $\boldsymbol{H_0} \parallel x \parallel [100]$ and along $\boldsymbol{H_0} \parallel z \parallel [110]$. We will discuss in Section 4.4, why we have chosen these two directions. The measurements are performed at $T = 56.5\,\mathrm{K}$ as indicated by the dashed blue line in the magnetic phase diagram in Fig. 4.1(a).

The microwave background of the measured complex transmission parameter S_{21} is eliminated by using the "derivative divide" method as explained in Section 3.3.2 and in Ref. [100]. The real part of the background-corrected field-derivative $\partial_\mathrm{D} S_{21}/\partial H_0$ is shown in Fig. 4.4(a). The magnetic phase transitions cause "vertical features" due to the changing magnetic field-dependence of the resonance frequency of the different magnetic modes in the chiral magnet. The phase boundaries are indicated by gray vertical arrows. Due to the irregularly shaped single crystal, the demagnetization fields and thus magnetic phases are non-uniform over the crystal. Consequently, the phase boundaries especially of the skyrmion lattice phase are not sharp but rather broad. We indicate this region by an orange shading to show that this region neither belongs to the skyrmion lattice phase (S) nor to the conical phase (c). In the data, we only show the positive magnetic field magnitudes as we expect the measured data to be symmetric for positive and negative fields. From the phase transition from the field-polarized to the conical phase at positive and negative field magnitudes, we correct the data by the trapped magnetic flux in the superconducting coils of the 3D-vector magnet, which is in the order of a few mT. The difference in the magnetic fields between the two different directions stems from the anisotropic demagnetization fields in the single crystal.

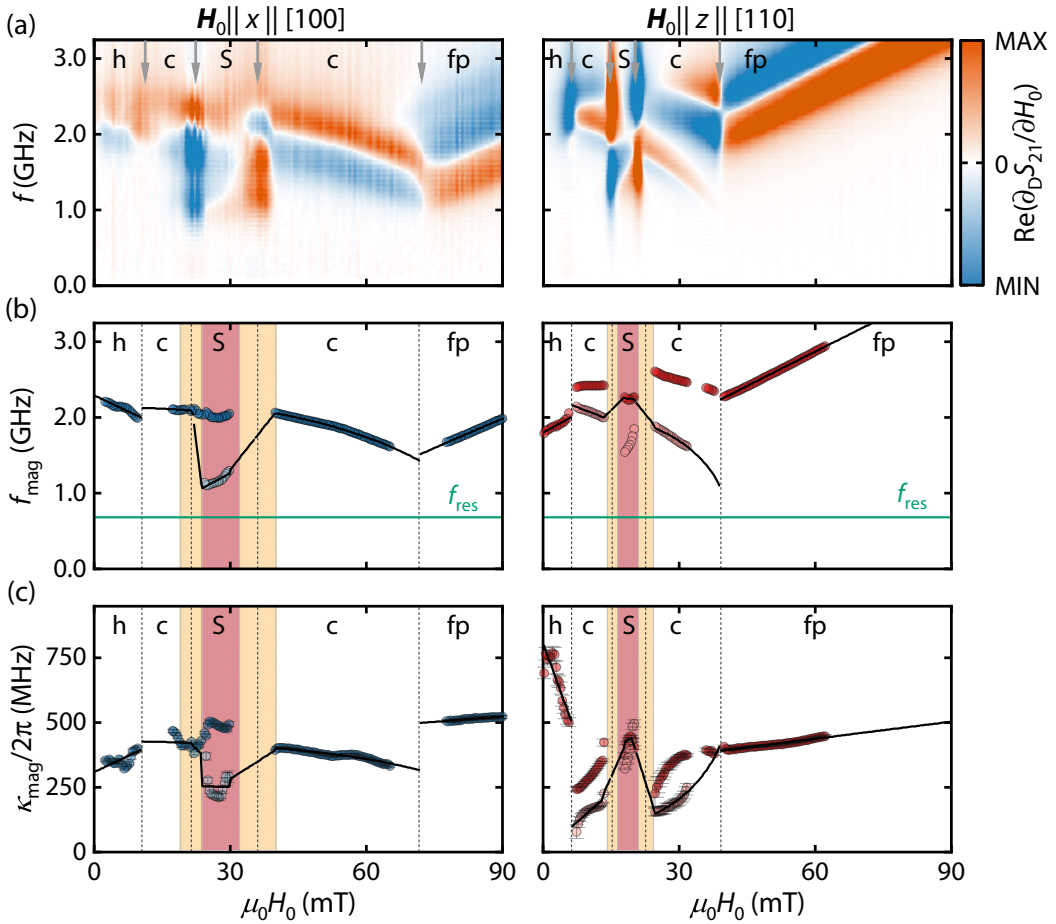

Fig. 4.4. Broadband magnetic resonance spectroscopy of the Cu_2OSeO_3 single-crystal. (a) Color-coded background corrected transmission parameter $\partial_D S_{21}/\partial H_0$ as a function of microwave frequency f and magnetic field H_0 with the magnetic field applied along $\boldsymbol{H}_0 \parallel [100]$ and along $\boldsymbol{H}_0 \parallel [110]$. The phase boundaries are indicated by gray arrows. (b) Fitted resonance frequency of the uniform magnon modes f_{mag} The error bars are smaller than symbol size. The horizontal green line indicates the resonance frequency of the microwave cavity f_{res} and is added as a guide to the eye. (c) Extracted half-width-at-half-maximum linewidth κ_{mag} as a function of the magnetic field H_0. The resonance frequency f_{mag} and the linewidth κ_{mag} are extracted by fitting frequency traces of the data shown in (a) at fixed magnetic field H_0 to Eq. (3.17). The solid black lines in (b) and (c) are fits and interpolations to the data. For details refer to main text.

The details of the demagnetization play a crucial role for the observation of the $+Q$ and $-Q$ modes in the conical phase [127]. Therefore, we observe with the magnetic field along $\boldsymbol{H}_0 \parallel z$ both the $+Q$ and $-Q$ mode but not along $\boldsymbol{H}_0 \parallel x$ which could also be due to the lower spectral weight of the $-Q$ mode [120].

From the data, we fit frequency traces at fixed magnetic field to Eq. (3.17) and extract the resonance frequency f_{mag} and the half-width-at-half-maximum linewidth κ_{mag} of the uniform magnon modes. We plot the extracted fit parameters as a function of the magnetic field in Fig. 4.4(b) and (c) for f_{mag} and κ_{mag} respectively. The skyrmion

lattice phase is indicated by the red shaded area. The extracted values for f_{mag} and κ_{mag} are in good agreement with the expected behaviour shown in Section 4.2 and with earlier observations [119, 120]. In Fig. 4.4(b), the resonance frequency of the microwave cavity f_{res} is indicated by a horizontal green line. As already discussed before, the cavity frequency f_{res} is below all uniform magnon mode frequencies f_{mag}, so we expect dispersive coupling when performing cavity-based magnetic resonance measurements as discussed in the next section.

For the modelling of our cavity-based magnetic resonance data in Section 4.4.3, we need the information of the magnetic field-dependence of f_{mag} and κ_{mag} over the whole field range. Therefore, we fit the resonance frequencies f_{mag} in the field-polarized (fp) and in the conical mode (c) to the Kittel equation [Eq. (2.27)] and to Eq. (1) proposed in Ref. [121], respectively. As no analytical formulas are available in the skyrmion lattice phase and in the helical phase, the magnetic field-dependence of f_{mag} is fitted to a linear function. In the phase transition region S↔c, we linearly interpolate between the last extracted value of f_{mag} in the skyrmion lattice phase (S) and the conical phase (c). For the magnon decay rates κ_{mag}, the data is fitted linearly using $\kappa_{\mathrm{mag}}/(2\pi) = \alpha \cdot f_{\mathrm{mag}} + \Delta f$ with a damping parameter α and an inhomogeneous linewidth Δf. The results for f_{mag} and κ_{mag} are shown as solid black lines in Fig. 4.4(b) and (c) respectively.

4.4 Cavity-based Magnetic Resonance Spectroscopy

The Cu_2OSeO_3 single crystal is placed into a 3D cavity resonator in order to observe magnon-photon coupling. The resonator experiments differ from those performed with the CPW in various aspects. Most important is the different frequency range of the devices. The CPW features a broad frequency response which can reach up to 100 GHz while the resonator is only sensitive to a certain frequency determined by the geometry, used material of the resonator and dielectric substrate. Commercially available 3D cavity resonators typically have resonance frequencies particularly designed for electron paramagnetic resonance spectroscopy, which is typically in the X-band (9.8 GHz). For this purpose, we designed a loop-gap resonator, which we will explain in more detail below. Subsequently, we discuss the experimental results from the cavity-based magnetic resonance spectroscopy and the modelling of the data.

4.4.1 Experimental Setup and Loop-Gap Resonator Design

The magnon-photon coupling in the chiral magnet Cu_2OSeO_3 using a commercial X-band resonator has already been demonstrated [123]. Due to the high resonance frequency, coupling has been observed between the microwave photons and higher

order helimagnon modes [121]. As we have seen in the section before, in order to observe coupling of photons with the fundamental uniform magnon modes in Cu_2OSeO_3, it is necessary to use a resonator with a resonance frequency $\lesssim 1\,\mathrm{GHz}$. There is no commercial resonator available with these low resonance frequencies combined with a sample space in the order of the crystal size. Therefore, we designed a so-called loop-gap resonator, which is schematically depicted in Fig. 4.5(a). In the simplest design, the loop-gap resonator is a cylinder with a gap on one side. This resonator design has the advantage of a large filling factor, low resonance frequencies within a reasonable physical size and a homogenous driving field inside the cavity [147].

For a first concept, the resonance frequency of the loop-gap resonator was calculated analytically and then confirmed by finite element simulations using CST microwave studios. The resonance frequency of a resonator is given by its inductance L_{res} and its capacitance C_{res} related by [147]

$$2\pi f_{\mathrm{res}} = \frac{1}{\sqrt{L_{\mathrm{res}} C_{\mathrm{res}}}}. \tag{4.8}$$

The inductance L_{res} is given by the hole of the cylinder, representing a single loop, which is mathematically given by

$$L_{\mathrm{res}} = \frac{\mu_0 \pi d^2}{4h} \tag{4.9}$$

with the height h and the inner diameter d of the loop-gap resonator. The capacitance C_{res} is given by the gap, which is modelled as a plate capacitor, described by

$$C_{\mathrm{res}} = \epsilon_0 \epsilon_{\mathrm{r}} \frac{h \cdot (D-d)}{2g}, \tag{4.10}$$

where ϵ_0 is the vacuum permittivity, ϵ_{r} is the dielectric constant of the substrate in the gap with size g, and D is the outer diameter of the loop-gap resonator. The dimensions of the aluminum cylinder are height $h = 22\,\mathrm{mm}$, inner diameter $d = 10\,\mathrm{mm}$, outer diameter $D = 22\,\mathrm{mm}$ and gap width $g = 0.6\,\mathrm{mm}$. The high dielectric constant substrate is a Rogers Corporation RO3010 with a nominal dielectric constant of $\epsilon_{\mathrm{r}} = 10.2$. A photograph of the loop-gap resonator is shown in Fig. 4.5(b) mounted by Teflon screws to a copper base.

One advantage of the loop-gap resonator is the homogenous driving field inside at the sample location. The driving field $\boldsymbol{h}_{\mathrm{ac}}$ is coupled into the resonator using a self-designed feedline consisting of a copper loop soldered to a SMA connector. A vector network analyzer (Rohde&Schwarz ZVA 8) is connected to the feedline and applies a microwave current I_{ac} with frequency f and power P. The feedline then

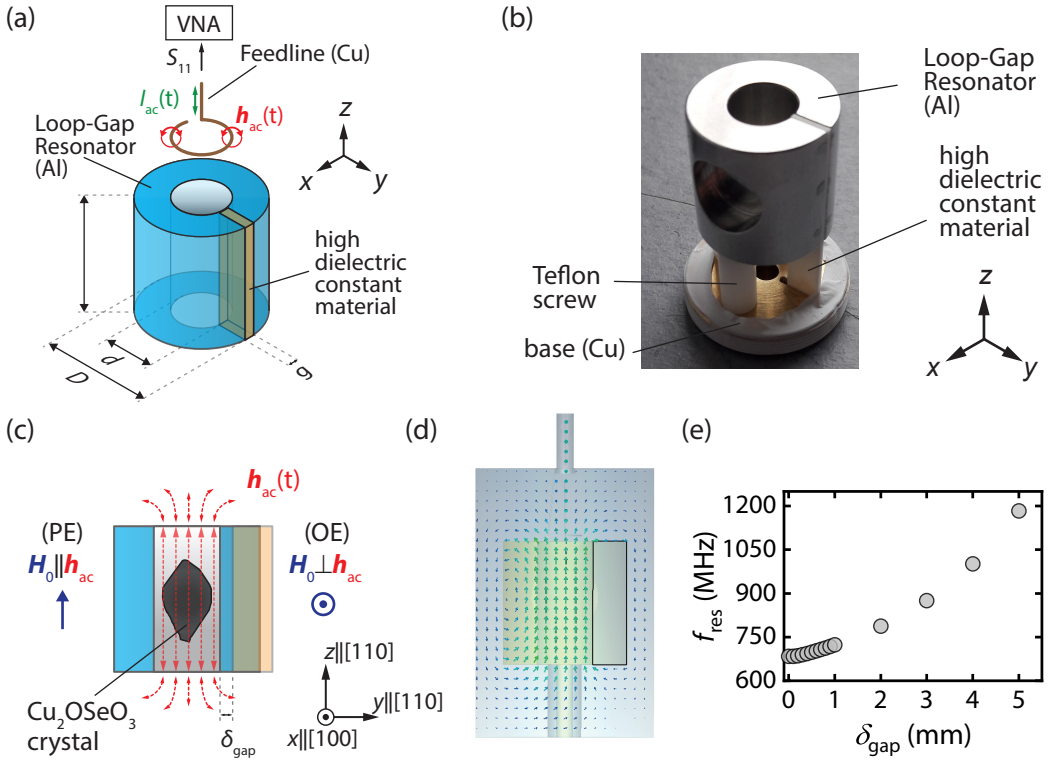

Fig. 4.5. (a) Schematic of the experimental setup with the loop-gap resonator and feedline design. (b) Image of the loop-gap resonator with the high dielectric material in the gap. (c) Side-view of the resonator and the Cu_2OSeO_3 crystal inside the cavity. Note the different configurations of static external magnetic field $\boldsymbol{H}_0$ relative to the oscillating magnetic field $\boldsymbol{h}_{\mathrm{ac}}$. (d) CST simulation of the magnetic field strength inside and outside of the cavity. The magnitude of the oscillating magnetic field is indicated by the size of the arrows. The gray square represents the high dielectric constant material. (e) Resonance frequency f_{res} of the loop-gap resonator depending on the horizontal offset δ_{gap} of the high dielectric constant material in the gap. A value of $\delta_{\mathrm{gap}} = 0\,\mathrm{mm}$ means the gap is fully filled by the material and a value of $5\,\mathrm{mm}$ denotes an almost fully air-filled gap as shown in panel (c).

inductively couples $\boldsymbol{h}_{\mathrm{ac}}$ to the resonator. The distance of the feedline to the cavity can be adjusted by the rotatable radiation shield and optimized to maximize the absorbed microwave power by the cavity measuring the complex reflection parameter S_{11}. In the schematic side view in Fig. 4.5(c) the oscillating driving field $\boldsymbol{h}_{\mathrm{ac}}$ is shown. The Cu_2OSeO_3 single crystal is mounted on a brass rod and placed in the center of the cavity.

The modelling and simulation of the loop-gap resonator is done in CST microwave studio. The loop-gap resonator is fully simulated including the Teflon screws and the radiation shield. The result of the oscillating driving field is shown in Fig. 4.5(d), where the arrows denote the direction and the size of the oscillating magnetic field $\boldsymbol{h}_{\mathrm{ac}}$. From the simulations, it is possible to extract the resonance frequency f_{res}. Due to the chosen design of the loop-gap resonator it is possible to adjust the filling factor of the high dielectric constant material in the gap. This is parameterized by the length δ_{gap},

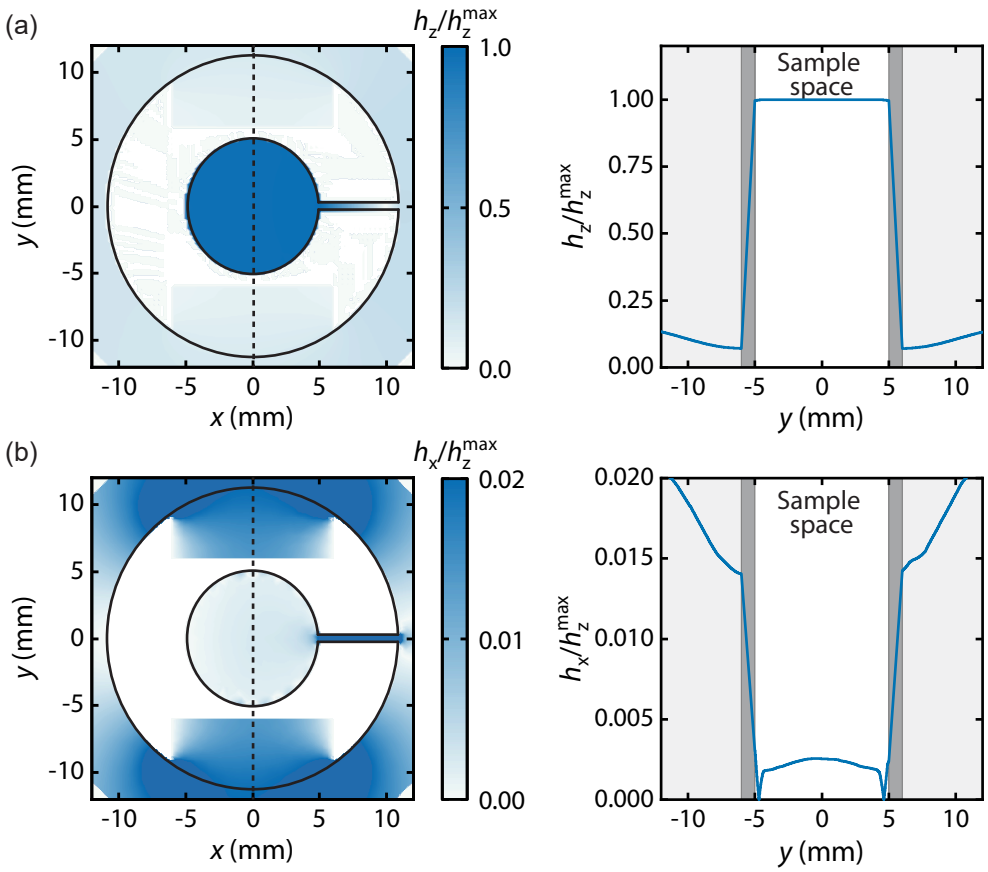

Fig. 4.6. Finite-element simulation of the magnetic field inside the loop-gap resonator performed with CST microwave studio. Magnetic field strength of (a) the out-of-plane component h_z and (b) the in-plane component h_x normalized to the maximum field $h_z^{\max} = \max(h_z)$ in the center of the microwave cavity where the sample is placed. The solid black lines indicate the contour of the loop-gap resonator. In the right panels a cut through the center of the cavity (indicated by the dashed black line in the left figures) is shown, demonstrating the homogeneity the magnetic field inside the microwave cavity. The dark gray shaded area indicates the aluminum and in light gray area the space outside the resonator (air).

which defines the width of the air pitch in the gap as shown in Fig. 4.5(c). A value of $\delta_{\mathrm{gap}} = 0\,\mathrm{mm}$ defines a fully filled gap with the high dielectric constant material. The dependence of the resonance frequency of the cavity f_{res} as function of δ_{gap} is shown in Fig. 4.5(e). Due to this geometry it is possible to tune the resonance frequency in the range $683\,\mathrm{MHz} \lesssim f_{\mathrm{res}} \lesssim 1.2\,\mathrm{GHz}$ by inserting the high dielectric constant material more or less into the gap. For our experiments, the gap was fully filled by the substrate, where we measure a resonance frequency of $f_{\mathrm{res}} = 683.8\,\mathrm{MHz}$ and a loaded quality factor of $Q = 2\pi f_{\mathrm{res}}/(2\kappa_{\mathrm{res}}) = 350 \pm 26$.

Before discussing the experimental results, we want to briefly discuss the field homogeneity inside the cavity. To estimate the homogeneity, the magnetic field distribution at the center of the cavity is calculated for the oscillating magnetic

field $\boldsymbol{h}_{\mathrm{ac}} = [h_x\ h_y\ h_z]^{\mathsf{T}}$, where we consider the field component along h_z and perpendicular to the cylinder axis h_x as shown in Fig. 4.6. The simulation is performed with a normalized microwave pulse, so the resulting field magnitudes are normalized to the maximum value of the z-component $h_z^{\max} = \max(h_z)$. The magnetic field h_z at the sample location is homogenous and varies by less than 1% over the whole sample space. This is also indicated by the linecut through the center of the cavity. The transverse component h_x is roughly three order of magnitude smaller than h_z, indicating that this driving field component is negligible for exciting the magnetization dynamics. We confirmed that the same argument holds for h_y.

We emphasize here that the homogenous and clearly defined oscillating driving field $\boldsymbol{h}_{\mathrm{ac}}$ of the loop-gap resonator is in stark contrast to a CPW, where driving field components in the in-plane and out-of-plane direction are present as described by the Karlqvist equations [Eqs. (3.5) and (3.6)]. As discussed in the previous section, the breathing and gyrating modes have different excitation geometries. In a BMR measurement with a CPW both modes are excited and observed (cf. Fig. 4.4). With the loop-gap resonator it is possible to selectively excite either the breathing mode or the gyrating modes. Therefore, in the experiment, two distinct configurations will be considered: The situation where the oscillating driving field is perpendicular to the static magnetic field $\boldsymbol{H}_0 \parallel \boldsymbol{h}_{\mathrm{ac}}$ denoted as orthogonal excitation (OE), and the situation of parallel excitation (PE) where $\boldsymbol{H}_0 \perp \boldsymbol{h}_{\mathrm{ac}}$ holds.

4.4.2 Experimental Results

In the experiment, the Cu_2OSeO_3 single crystal is mounted inside the assembled loop-gap resonator and the temperature is adjusted to different temperature regimes to get a first intuition of the temperature-dependence of the coupled magnon-photon system. In order to demonstrate the tunable cooperativity, the system is cooled down to $T = 56.5\,\mathrm{K}$, which is below the critical temperature $T_{\mathrm{c}} \approx 58\,\mathrm{K}$ as shown in the phase diagram in Fig. 4.1(a). The external magnetic field is swept in the range $-126\,\mathrm{mT} \leq \mu_0|\boldsymbol{H}_0| \leq 126\,\mathrm{mT}$ from positive to negative fields with a step size of approx. $0.3\,\mathrm{mT}$. The flux trapping in the coils of the superconducting vector magnet is corrected in the post-processing, similar to the situation in the BMR measurements (cf. Section 4.3). The VNA measures the complex reflection parameter S_{11} in the frequency range $500\,\mathrm{MHz} \leq f \leq 850\,\mathrm{MHz}$ with a resolution of approx. $4\,\mathrm{kHz}$ and an intermediate frequency filter bandwidth of $2\,\mathrm{kHz}$. The applied microwave power is $0\,\mathrm{dBm}$ and we confirmed that the magnetization dynamics of the system are in the linear regime. In the following, we will first explain the performed microwave background correction procedure and then discuss the results of the cavity-based magnetic resonance spectroscopy and the modelling of the data.

4.4.2.1. Background correction

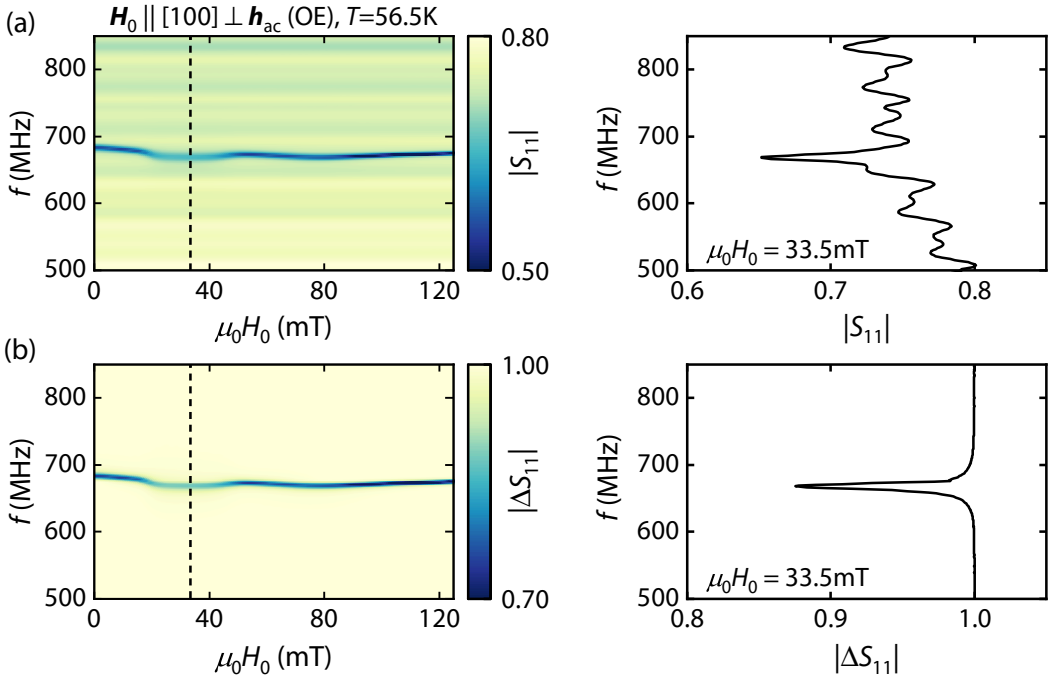

Fig. 4.7. (a) Measured complex reflection parameter S_{11} of the loaded resonator with a VNA without any background correction. The dashed black line shows the magnetic field ($\mu_0 H_0 = 33.5\,\mathrm{mT}$), where the frequency trace is extracted from. To eliminate the field-independent microwave background a piece-wise defined function S_{bg} is defined, where we take frequency-traces at magnetic fields where no resonance of the cavity is observable. The measured S_{11} is then divided by the newly defined function $\Delta S_{11} = S_{11}/S_{\mathrm{bg}}$. The result is shown in panel (b) with the corresponding frequency-trace at $\mu_0 H_0 = 33.5\,\mathrm{mT}$.

Similar to frequency-swept BMR experiments, the frequency-dependent transmission of the used microwave equipment is superimposed on the magnetic resonance signal. Exemplary data from the cavity magnetic resonance experiments is shown in Fig. 4.7(a). Due to the small impedance mismatch in the used microwave setup especially of the feedline and due to the frequency-dependent attenuation of the microwave, an oscillating standing wave pattern is measured as shown in the lineplot at fixed magnetic field. Therefore, an appropriate post-processing procedure needs to be applied to remove the background signal. In an equivalent way as discussed for BMR measurements (cf. Section 3.3.2), we define a piece-wise defined function S_{bg}, where we take frequency-traces at magnetic fields, where no resonance of the magnon-cavity system is observable [123]. This is similar to the “divide slice” method for BMR measurements with the modification, that the background function S_{bg} is piece-wise defined as the resonance of the microwave cavity is visible for all magnetic fields. Due to the dispersive coupling, the resonance frequency of the

cavity shifts with magnetic field. The assumption that the microwave background does not change with changing magnetic field, needs to be satisfied.

The measured reflection parameter S_{11} is consequently divided by the background function S_{bg}, resulting in the newly defined function $\Delta S_{11} = S_{11}/S_{\mathrm{bg}}$ shown in Fig. 4.7(b). As seen in the frequency-trace at fixed magnetic field, only the absorbed energy of the cavity-magnon system is observed.

4.4.2.2. Temperature-dependence of the coupled Magnon-Photon System

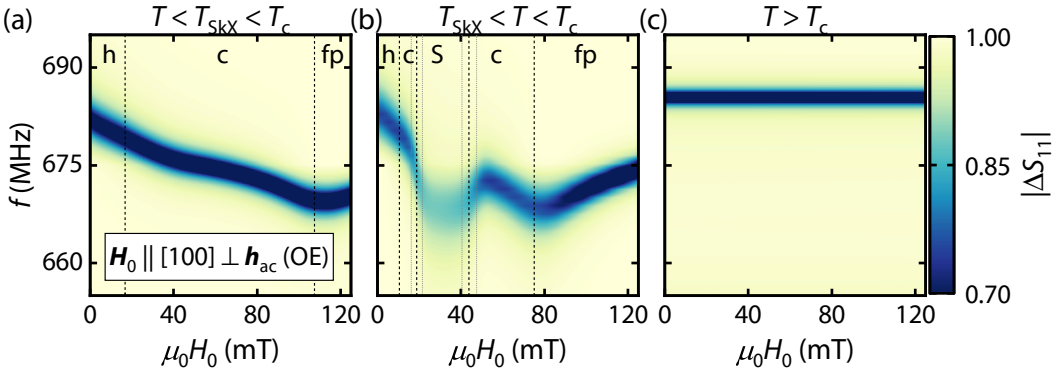

Fig. 4.8. Cavity-based magnetic resonance measurements at different temperatures for the external magnetic field applied along the OE case ($\boldsymbol{H}_0 \parallel [100] \perp \boldsymbol{h}_{\mathrm{ac}}$). (a) The temperature is chosen too low for the skyrmion lattice phase to be able to form ($T < T_{\mathrm{SkX}} < T_{\mathrm{c}}$). (b) The temperature is close to the transition temperature ($T_{\mathrm{c}} \approx 58\,\mathrm{K}$), where magnon-photon coupling in the skyrmion lattice phase (S) is observed. Due to the irregular shape of the crystal and therefore inhomogeneous demagnetization fields, the phase transition from conical (c) to the skyrmion lattice phase (S) is not sharp, indicated by the dashed gray lines. (c) The temperature is chosen larger than the transition temperature T_{c}, where the spin system is no longer ordered. In this regime the magnetic field-independent cavity resonance is observed.

For a first intuition, the temperature T is set to three different temperature regimes and the microwave frequency- and magnetic field-dependent reflection parameter S_{11} is measured as shown in Fig. 4.8 for the magnetic field applied in the OE-direction. At temperatures below a "skyrmion lattice temperature" T_{SkX} we do not expect to observe a skyrmion lattice phase. We define the "skyrmion lattice temperature" T_{SkX} as the lower temperature boundary, where a skyrmion lattice phase emerges. This means that the skyrmion lattice phase exists in the temperature range $T_{\mathrm{SkX}} \leq T \leq T_{\mathrm{c}}$. As seen from the results in Fig. 4.8(a), a shift in the resonance frequency of the cavity is observed. The transition from the field-polarized (fp) to the conical phase (c) is identified by the changing frequency-dependence of the cavity with decreasing magnetic field. As the magnetic field where the transition fp↔c occurs is strongly temperature-dependent as shown in the magnetic phase diagram 4.1(a), this field is used to determine the temperature of the crystal. The temperature of the single

crystal and the microwave cavity is strongly influenced by the helium flow in the variable temperature inset of the cryostat and we found this procedure of temperature calibration to be very reliable. The vertical dashed lines in the figure represent the magnetic phase boundaries determined from broadband magnetic resonance spectroscopy.

Increasing the temperature into the regime of the skyrmion lattice phase, $T_{\mathrm{SkX}} < T < T_{\mathrm{c}}$, the measured response of the coupled magnon-photon system changes. As shown in Fig. 4.8(b), the frequency-shift in the field-polarized and conical phase is still observed, while in the skyrmion lattice phase (S) a different signal characteristic is observed. This is a clear indication that coupling between photons and magnons in the skyrmion lattice phase is realized. We will discuss this in more detail below.

If the temperature is set above the critical temperature $T > T_{\mathrm{c}}$, the chiral magnet becomes paramagnetic and only the magnetic field-independent response of the microwave cavity is measured. The spectrum in Fig. 4.8(c) is not background-corrected, compared to panel (a) and (b), because with the presented procedure above, it is impossible to take frequency-traces without the cavity resonance observable. Therefore, the spectrum in panel (c) is scaled to the same magnitude as in the other panels.

4.4.2.3. Experimental Data of Magnon-Photon Coupling in the Skyrmion Lattice Phase

The temperature is set to $T = 56.5\,\mathrm{K}$ corresponding to the case where $T_{\mathrm{SkX}} < T < T_{\mathrm{c}}$ holds. The magnetic field $\boldsymbol{H}_0$ is applied along the OE ($\boldsymbol{H}_0 \parallel [100] \perp \boldsymbol{h}_{\mathrm{ac}}$) and PE direction ($\boldsymbol{H}_0 \parallel [110] \parallel \boldsymbol{h}_{\mathrm{ac}}$). As discussed before, in the skyrmion lattice phase, the gyrating and breathing mode possess different excitation configurations as schematically depicted in Fig. 4.9(a). In the ccw-mode, the core of the skyrmion rotates in the counter-clockwise direction, while in the breathing mode the core shrinks and expands alternately with the characteristic uniform magnon frequency f_{mag} [119].

The results of the reflection measurements are shown in Fig. 4.9(b). In order to account for different demagnetization fields, the magnetic field is normalized to the critical field H_{c2}, namely $71.7\,\mathrm{mT}$ for OE and $39.1\,\mathrm{mT}$ for PE extracted from BMR measurements shown above. For OE a shift of the cavity resonance frequency is observed in the field-polarized and conical phase in agreement with Fig. 4.2(c). In the skyrmion lattice phase, we observe coupling between the ccw mode and the cavity photons. There is no distinct transition from the conical to the helical phase because the external magnetic field $\boldsymbol{H}_0$ is applied along the magnetic easy axis of the cubic anisotropy in Cu_2OSeO_3 [128], where the system does not rearrange in energetically unfavorable domains upon decreasing field but keeps a small net moment along $\boldsymbol{H}_0$ [129, 130, 148].

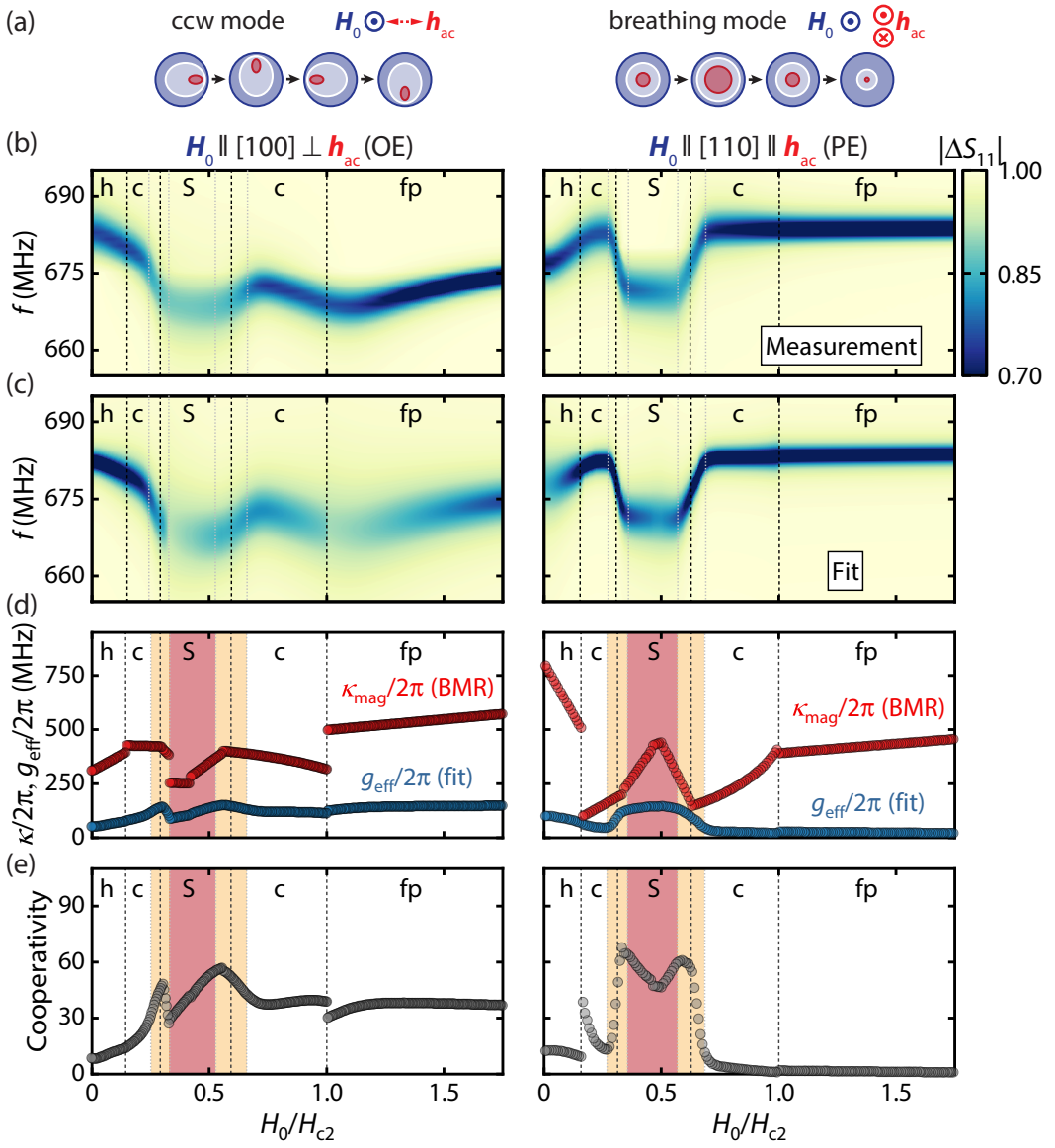

Fig. 4.9. Magnon-photon coupling in a skyrmion host material. (a) Illustration of the two relevant skyrmion resonance modes, where the oscillating driving field $\boldsymbol{h}_{\mathrm{ac}}$ is either orthogonal (ccw mode) or parallel (breathing mode) to the external magnetic field $\boldsymbol{H}_0$ and consequently to the skyrmion lattice. (b) Background-corrected reflection parameter $|\Delta S_{11}|$ as a function of the magnetic field H_0 and the applied microwave frequency f. The vertical dashed lines indicate the magnetic phase boundaries slightly adjusted from BMR measurements (cf. Fig. 4.4) to account for the different probing volumina in cavity and BMR measurements (see main text for details). The magnetic fields are normalized to the critical field H_{c2}. The gray dashed lines indicate the broadened phase transition between S↔c. (c) Simulated spectrum calculated with Eq. (4.7). The fitted rates g_{eff} and κ_{mag} used to calculate the spectrum are shown in (d), extracted by fitting Eq. (4.7) to frequency traces taken at fixed magnetic field. The orange shaded area indicates the broadened S↔c phase transition. The fit error bars are smaller than the symbol size. (e) Cooperativity calculated by using Eq. (4.11) for orthogonal excitation (OE) and for parallel excitation (PE). The cooperativity is calculated by using the parameters shown in (d). In the PE case, the cooperativity can be tuned from $1 \lesssim C \lesssim 60$. The fit error bars are smaller than the symbol size.

If the static magnetic field is parallel to the oscillating driving field (PE), no coupling is observed in the field-polarized and conical phase. As the magnetic moments are aligned with $\boldsymbol{H}_0$, the driving field $\boldsymbol{h}_{\mathrm{ac}}$ cannot exert a torque on the precessing magnetic moments. In the skyrmion lattice phase, we clearly observe coupled dynamics of the cavity and the breathing mode of the Cu_2OSeO_3 spin system. This coupling is most efficient for driving field $\boldsymbol{h}_{\mathrm{ac}}$ parallel to the static field $\boldsymbol{H}_0$ [Fig. 4.9(a)]. In the helical phase, a finite coupling is observed in contrast to the OE case. The domain population in the helical phase crucially depends on the field direction as well as on the temperature and field history. For decreasing magnetic field along the $\langle 110 \rangle$-direction, two domains are equally populated leading to a finite angle between them [129, 130, 148]. Consequently, a finite coupling in the helical phase is observed.

4.4.3 Modelling of Cavity-Based Magnetic Resonance Data using the Input-Output Formalism

We now turn to a quantitative evaluation of the magnon-photon coupling employing the input-output formalism in the following manner consisting of three steps: First, we extract the external loss rate κ_{ext}, the total loss rate κ_{res}, and resonance frequency f_{res} of the cavity by fitting Eq. (4.7) to a frequency trace of the background-corrected reflection parameter $|\Delta S_{11}|$ at the largest static magnetic field available ($\mu_0 H_0 = 126\,\mathrm{mT}$ for PE). The system is assumed to be unperturbed and therefore $g_{\mathrm{eff}} = 0$. The following values are inferred: $f_{\mathrm{res}} = 683.8\,\mathrm{MHz}$, $\kappa_{\mathrm{res}}/(2\pi) = (1.041 \pm 0.004)\,\mathrm{MHz}$, and $\kappa_{\mathrm{ext}}/(2\pi) = (0.848 \pm 0.004)\,\mathrm{MHz}$. The internal loss rate of the cavity κ_{int} is smaller than the external loss rate κ_{ext}, indicating that the cavity is overcoupled [149].

In a second step, we keep these parameters fixed and fit Eq. (4.7) to all frequency traces of $|S_{11}|$ for a series of external magnetic fields H_0 along both magnetic field directions. From these fits, the coupling strength g_{eff} is extracted. The magnon decay rate κ_{mag} and the field-dependent resonance frequency of the different magnon modes f_{mag} are taken from BMR spectroscopy data on the same crystal (see Fig. 4.4). We emphasize that the cavity-based magnetic resonance technique probes the whole sample volume while the BMR technique is sensitive to a spin dynamics within the first few µm of the sample volume measured from the CPW. The penetration depth of the microwave magnetic field is expected to be similar to the width of the CPW center conductor (here 340 µm) according to Eqs. (3.5) and (3.6). Because of the irregular shape of the crystal, its demagnetization fields are inhomogeneous, such that phase transitions and magnetic resonance phenomena are inhomogeneously broadened in different ways for cavity and BMR measurements. Thus, minor deviations in the magnetic fields of the phase transitions, in the resonance frequencies and linewidths of the magnetic excitations are expected when comparing the cavity and BMR measurements.

Using the extracted parameters allows to recalculate $|S_{11}|$ using Eq. (4.7), which is displayed in Fig. 4.9(c). This fit and the measurement shown in Fig. 4.9(b) are in good agreement. The used parameters κ_{mag} and g_{eff} are shown in Fig. 4.9(d). The magnon decay rate κ_{mag} is larger than the coupling strength g_{eff} in all magnetic phases which classifies the system to be in the Purcell coupling regime with $\kappa_{\mathrm{res}} < g_{\mathrm{eff}} < \kappa_{\mathrm{mag}}$ [56]. For PE the coupling strength outside the skyrmion and helical phase becomes small. In the skyrmion lattice phase, the breathing mode couples to the cavity and we extract almost the same effective coupling rate g_{eff} as for the counter-clockwise rotation mode. Note that the resonator properties may subtly evolve with magnetic field, also leading to minor changes in g_{eff}.

In the third and final step, the magnon-photon cooperativity C of the system is calculated as a measure for the coherent exchange of excitations. The cooperativity defined as [55, 56, 65, 150]

$$C = \frac{g_{\mathrm{eff}}^2}{\kappa_{\mathrm{res}} \cdot \kappa_{\mathrm{mag}}} \tag{4.11}$$

is shown in Fig. 4.9(e). For OE, the cooperativity increases from $C \approx 8$ in the helical phase to a high cooperativity of $C \approx 50$ in the skyrmion lattice phase. In the conical and field-polarized phase a rather constant cooperativity of $C \approx 40$ is observed. At the magnetic phase boundaries, the magnon-photon cooperativity shows a strong change with magnetic field due to the induced phase transition.

For PE, the cooperativity C is small or close to unity in the field-polarized and conical phase. A drastic change of the cooperativity is observed when a magnetic phase transition into the skyrmion lattice phase is induced by a small variation of the magnetic field. The cooperativity reaches a maximum value of $C \approx 60$ and can be tuned between its maximum and minimum value by changing the external magnetic field by $\sim 10\,\mathrm{mT}$. The change of the magnetic field induces a magnetic phase transition which in turn allows us to control the effective coupling rate g_{eff} between the microwave photons and the magnons in Cu_2OSeO_3. Here, we utilize that the breathing mode exhibits a different excitation geometry compared to the magnon excitations in the other magnetic phases. This property is unique to the topologically protected skyrmion lattice phase. At the phase boundaries , the magnon-photon cooperativity distinctly changes with magnetic field due to the induced phase transition. Similarly, at the boundary of the helical phase, when the helices reorientate under decreasing magnetic field and gain components orthogonal to $\boldsymbol{h}_{\mathrm{ac}}$, the microwave photons can more efficiently couple to the spin system. However, such transitions lack the pronounced excitation efficiency.

4.5 Summary

In conclusion, we experimentally demonstrated the magnon-photon coupling between the fundamental, uniform magnetic excitations in the chiral magnet Cu_2OSeO_3 and photons inside a three-dimensional microwave cavity using magnetic resonance spectroscopy. The resonance frequency of the self-designed loop-gap resonator is below all magnon mode frequencies limiting the analysis to the dispersive regime. The coupling between the photons in the cavity and all magnetic modes including those in the topologically protected skyrmion lattice phase of the chiral magnet, which is mediated by the dipolar interaction, is observed and a high magnon-photon cooperativity of up to $C \leq 60$ is measured. By changing the magnetic field in a small field range, the system undergoes a topological phase transition resulting in a strong tunability of the magnon-photon rate and therefore the magnon-photon cooperativity. The phase change is induced by means of a control parameter, which can either be magnetic field, temperature, or electric field [151–153].

In our presented study, the magnon-photon cooperativity is mainly tuned via the effective coupling strength due to the induced phase transition. The used chiral magnet Cu_2OSeO_3 is a prototypical system to demonstrate the concept of tunable magnon-photon cooperativity. The presented scheme using an external control parameter is not limited to chiral magnets but can also be applied to other material systems, which feature different magnetic phases with magnon excitations with unique excitation geometries. In chiral magnets the breathing mode in the skyrmion lattice phase possesses this unique excitation geometry with $\boldsymbol{h}_{\mathrm{ac}} \parallel \boldsymbol{H}_0$. Tuning the magnon-photon cooperativity in a dispersive read-out scheme can have great potential for novel hybrid systems such as magnon-qubit systems [22, 154].

5 Spatially-Resolved Magnetization Dynamics in a Magnonic Device

In the recent years, huge progress in the research and development of novel approaches for the microelectronics industry utilizing the spin degree of freedom of the electrons has been made. Two highlight applications are novel non-volatile magnetic memories such as magnetic random-access memories (MRAMs) or spin-transfer torque (STT) and spin-orbit torque (SOT) RAMs, and new logic devices for new computational devices [155]. For the latter, the angular momentum of quantized collective excitations in exchange-coupled magnetic systems are utilized to transport and store information [19]. These quantized excitations are called magnons. In magnon spintronics especially insulating magnetic materials with low intrinsic damping are used such as yttrium iron garnet (YIG) [156]. The choice of the used magnetic material is essential as long spin-wave propagation lengths and high group velocities are desired [20, 157]. The large advantage of insulating magnetic materials is the absence of free electrons and less Joule heating [19, 158]. Especially liquid-phase epitaxially (LPE) grown YIG with micrometer thickness has extraordinary large propagation lengths and large magnon group velocities. Nevertheless, for the use in e.g. CMOS-based devices, the integration of single-crystals is unfavorable due to the necessary use of gadolinium gallium garnet (GGG) as a growth substrate for YIG. Unfortunately, in thinner YIG grown by other deposition techniques such as pulsed laser deposition, these favorable properties are lost to some extend.

In contrast, metallic magnetic materials generally have higher damping due to the scattering of magnons with the conduction electrons [159]. Although the damping is larger, metallic magnetic materials feature a larger group velocity and a large saturation magnetization. Recently, a metallic low damping alloy was found which is sputtered $Co_{25}Fe_{75}$ [159], where the numbers in the subscripts give the composition in atomic percent. This material has comparable damping characteristics to thin LPE-YIG. In recent experiments, the spin wave characteristics of thin film $Co_{25}Fe_{75}$ were investigated, which demonstrate large propagation lengths in the range of $\sim 6\,\mu m$ for a $10\,nm$ thick $Co_{25}Fe_{75}$ [41, 51, 160]. Due to the low damping properties, this system can also be operated in the non-linear regime without the necessity of very large driving power. Non-linear effects such as 3- or 4-magnon scattering can be investigated, and lead to an increased damping due to the additional loss channels [161].

The development of suitable spectroscopy techniques to determine the material parameters is key to designing magnonic devices. For unstructured thin films the broadband ferromagnetic resonance technique with a vector network analyzer (cf. Section 3.3.1) is state-of-the-art and routinely used to measure the magnetization dynamics phase-sensitively [90, 96]. For nano- and micro-structured samples this technique is not applicable and also lacks the ability to measure the magnetization dynamics in a spatially-resolved way. For the latter, optical measurement techniques are employed using microfocusing methods to bring the spot size of the laser beam to the Abbe diffraction limit. The majority of these techniques rely on the magneto-optic Kerr effect (MOKE) such as microfocused time-resolved magneto-optic Kerr effect (μTR-MOKE) [162–164] or microfocused Brillouin light scattering (μBLS) [165–167]. Especially, the latter technique is well established and allows not only to measure coherently excited magnetization dynamics but also incoherent processes such as thermal magnons [168]. The μBLS technique measures the intensity (not the amplitude) and can also be extended for phase- and temporal resolution but at the cost of largely increased measurement time [167, 169–171].

In this chapter, we present our results on the experimental study of the magnetization dynamics of the low damping metallic ferromagnet $Co_{25}Fe_{75}$ in the linear and non-linear regime. We used a micro-structured $Co_{25}Fe_{75}$ waveguide with a coplanar waveguide-like antenna design to coherently excite the magnetization dynamics. The sample is investigated with three different optical spectroscopy techniques which are the well-established microfocused Brillouin light scattering (μBLS), the microfocused Super-Nyquist sampling magneto-optic Kerr effect (μSNS-MOKE) originally developed by the group of Georg Woltersdorf (Martin Luther University Halle-Wittenberg) [172] and the microfocused frequency-resolved magneto-optic Kerr effect (μFR-MOKE) technique developed by us [160]. These spectroscopy techniques are all integrated into a single optical setup to allow for the comparison of them without removing the sample.

This chapter is structured as follows: We will start with an introduction on the magnetization dynamics of dipolar-exchange spin waves. Subsequently, we discuss the underlying detection principle of the used measurement techniques which is the magneto-optic Kerr effect (MOKE) and continue with a detailed explanation of the different measurement techniques. We will then discuss the experimental results of the magnetization dynamics in the linear regime and then in the non-linear regime. Finally, we will present an electrical 2-tone spectroscopy approach of the μFR-MOKE technique.

5.1 Magnetization Dynamics of Spin Waves

In the previous chapters, we have considered and investigated the magnetization dynamics of more complicated configurations of the magnetic moments such as a compensated ferrimagnet (Chapter 3) or a chiral magnet (Chapter 4) in an extended, unpatterned single-crystal. Here, in this chapter we will go back to the simple case of a ferromagnet where the magnetic moments $\boldsymbol{\mu}_i$ are all parallelly aligned with each other due to the Heisenberg exchange interaction (cf. Section 2.1) and pointing along the effective magnetic field $\boldsymbol{H}_{\mathrm{eff}}$. In the presence of an additional oscillating magnetic field to drive the magnetization to resonance or due to thermal excitations, the magnetic moments $\boldsymbol{\mu}_i$ are all precessing in-phase as schematically depicted in Fig. 5.1(a). This is the so-called ferromagnetic resonance (FMR) as we derived it in Section 2.2.

We can also explain the ferromagnetic resonance as an excitation of the ferromagnetic ground state where all magnetic moments are pointing along the same direction. Flipping one of the magnetic moments into the anti-parallel direction relative to the other magnetic moments, leads to an energetically unfavorable state with an additional energy depending on the exchange constant J and the number of next neighbours. Another possibility for an excitation of the ordered spin lattice is to (slightly) tilt the magnetic moments away from their parallel alignment. In this case, we get a collective excitation of the whole spin lattice. These are so-called spin waves and their quantized excitation are called magnons [38].

As a consequence of the tilting of the magnetic moments, they are not aligned with the effective field anymore leading to a precession of the magnetic moments due to the torque from the effective magnetic field on the magnetic moments. The precessing magnetic moments do not necessarily need to precess all in-phase like in the previously discussed ferromagnetic resonance excitation but can also have a fixed phase shift between each other as shown in Fig. 5.1(b). We call these excitations with a finite phase shift between the magnetic moments spin waves. Due to the finite phase shift, we can define a wavelength λ and correspondingly a wavevector $|\boldsymbol{k}| = k = 2\pi/\lambda$. The FMR can be understood as a non-propagating spin wave with infinite wavelength $\lambda = \infty$ or equivalently with wavevector $|\boldsymbol{k}| = 0$. Therefore, a spin wave with $|\boldsymbol{k}| = 0$ does not transport any information. This is due to the vanishing group velocity v_{g} which generally vanishes at $|\boldsymbol{k}| = 0$ but can also become zero at finite wavevectors $|\boldsymbol{k}| \neq 0$ due to the competition between the dynamic dipolar and exchange fields [20].

In this chapter, we want to switch our focus to propagating spin waves $\boldsymbol{k} \neq 0$ in the limit where the film thickness d is much smaller than the lateral dimensions of the magnonic waveguide. In this regime not only the Heisenberg exchange interaction needs to be considered but also the dipolar interaction between the magnetic

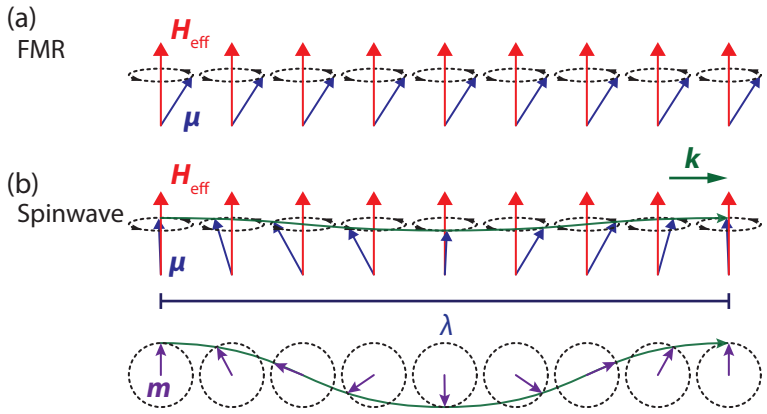

Fig. 5.1. Locally precessing magnetic moments $\boldsymbol{\mu}$ around the effective field $\boldsymbol{H}_{\mathrm{eff}}$. (a) Uniform precessing mode where all magnetic moments are precessing in-phase which is also known as ferromagnetic resonance (FMR). (b) Magnetic excitation of a spin wave where the spin-flip of a single magnetic moment is distributed over all other magnetic moments leading to a propagating spin wave mode with wavelength λ and wavevector $\boldsymbol{k}$. The lowest panel shows the top-down view of the dynamic magnetization $\boldsymbol{m}$ of the locally precessing magnetic moments μ.

moments. The relevant length scale to characterize the competition between the dipolar and exchange interaction is the exchange length l_{ex} (typically a few nm) given by $l_{\mathrm{ex}}^2 = 2A/\left(\mu_0 M_{\mathrm{s}}^2\right)$ with the exchange stiffness constant A. If length scales smaller than the exchange length are considered, corresponding to small wavelengths λ or large wavevectors $|\boldsymbol{k}|$, the exchange interaction is dominant and the magnetization becomes uniform. For length scales larger than l_{ex}, the dipolar interaction is dominant and domains with different magnetization orientations can be formed [20]. These spin waves are the so-called dipolar-exchange spin waves. We will see later that the wavelength of pure exchange spin waves is smaller than the optical diffraction limit and cannot be optically resolved. Note, as demonstrated by Nembach *et al.* [126], the wavelength of pure exchange spin waves can be in the range of µm if the thickness of the film goes to zero $d \to 0$ due to the vanishing dipolar interaction. This special case is not topic of this chapter.

We want to start with a derivation of the resonance frequency for dipolar-exchange spin waves for in-plane magnetized thin films. Unfortunately, the derivation for arbitrary geometries is not analytically possible. However, in the thin film limit $N_{yy} = 1$ for an in-plane magnetized ferromagnet, the dipolar magnetic fields arising due to the sample shape can be calculated analytically assuming that the precession of the magnetization is uniform along the film thickness d. This has been derived by B. A. Kalinkos and A. N. Slavin in 1986 [173]. Our approach is to start with the effective magnetic field from Eq. (2.2) and modify the procedure in Section 2.2 to allow for solutions for $\boldsymbol{k} \neq 0$ using the coordinate system shown in Fig. 5.2 and in the limit $kd \ll 1$.

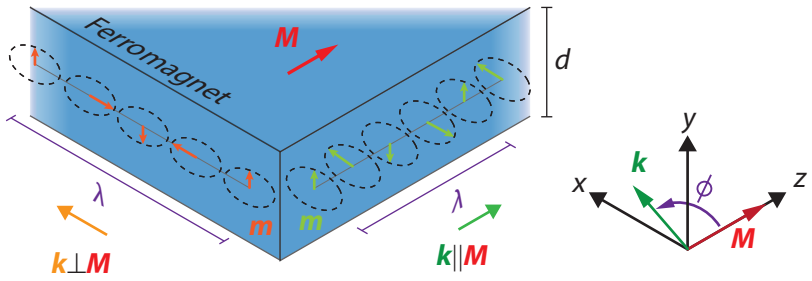

Fig. 5.2. Schematic illustration of dipolar-exchange spin waves in a magnetic material with magnetization $\boldsymbol{M}$ which lies in the plane of the waveguide with thickness d. In the backward volume configuration the spin wave is propagating in the same direction as the magnetization is pointing ($\boldsymbol{k} \parallel \boldsymbol{M}$). For the surface spin waves the propagation direction is perpendicular to the magnetization ($\boldsymbol{k} \perp \boldsymbol{M}$). In this configuration the spin waves are also called Damon-Eshbach modes.

For our derivation we start with the magnetization $\boldsymbol{M}$ where we use a plane wave ansatz $\exp\left(i(\omega t - \boldsymbol{kr})\right)$ for the time-varying components of the magnetization $\boldsymbol{M}^{\sim}(t)$ resulting in [174, 175]

$$\boldsymbol{M} = \boldsymbol{M}_0 + \boldsymbol{M}^{\sim}(t) = \begin{bmatrix} 0 \\ 0 \\ M_\mathrm{s} \end{bmatrix} + \begin{bmatrix} M_x^{\sim}(t) \\ M_y^{\sim}(t) \\ M_z^{\sim}(t) \end{bmatrix} = \begin{bmatrix} 0 \\ 0 \\ M_\mathrm{s} \end{bmatrix} + \begin{bmatrix} M_x^{\sim} e^{i(\omega t - \boldsymbol{kr})} \\ M_y^{\sim} e^{i(\omega t - \boldsymbol{kr})} \\ 0 \end{bmatrix} \tag{5.1}$$

with an arbitrary space vector $\boldsymbol{r} = x\hat{\boldsymbol{e}}_x + z\hat{\boldsymbol{e}}_z$ in the disk plane and the wavevector $\boldsymbol{k} = k_x\hat{\boldsymbol{e}}_x + k_z\hat{\boldsymbol{e}}_z$ also restricted to the disk plane. We consider the Zeeman energy Eq. (2.3), the exchange energy Eq. (2.6), the dipolar interaction energy and the shape anisotropy $N_{yy} = 1$. The total magnetic field $\boldsymbol{H}$, with the external magnetic field applied along the z-direction $\boldsymbol{H}_0 = H_0\hat{\boldsymbol{e}}_z$ and the effective magnetic field $\boldsymbol{H}_\mathrm{eff}$, takes the form

$$\boldsymbol{H} = \boldsymbol{H}_\mathrm{eff} + \boldsymbol{h}_\mathrm{rf}(t) = \begin{bmatrix} -H_{\mathrm{d}x} \\ -H_{\mathrm{d}y} \\ H_0 + H_\mathrm{ex} \end{bmatrix} + \begin{bmatrix} h_{\mathrm{rf},x}(t) \\ h_{\mathrm{rf},y}(t) \\ 0 \end{bmatrix}. \tag{5.2}$$

The exchange field can be derived by inserting Eq. (5.1) into (2.6) and calculating the effective field with Eq. (2.2), which results in

$$\mu_0 H_\mathrm{ex} = \frac{2A}{M_\mathrm{s}} k^2, \tag{5.3}$$

with the exchange stiffness constant A.

The dipolar fields $H_{\mathrm{d}x}$ and $H_{\mathrm{d}y}$ are derived in Ref. [173] in the limit $kd \ll 1$ and take the form

$$\begin{aligned} H_{\mathrm{d}x} &= M_{\mathrm{s}} \left(1 - \frac{1 - e^{-kd}}{kd}\right) \sin^2 \phi, \\ H_{\mathrm{d}y} &= M_{\mathrm{s}} \frac{1 - e^{-kd}}{kd}, \end{aligned} \tag{5.4}$$

with the in-plane angle ϕ between the magnetization $\boldsymbol{M}$ and the wavevector $\boldsymbol{k}$ as defined in Fig. 5.2. Plugging the above Eqs. (5.1) and (5.2) into the Landau-Lifshitz-Gilbert equation [Eq. (2.18)] results in

$$i\omega \begin{bmatrix} M_x^{\sim} \\ M_y^{\sim} \end{bmatrix} = \begin{bmatrix} \gamma\mu_0 M_{\mathrm{s}} \cdot h_{\mathrm{rf},y} - M_y^{\sim} \cdot [\gamma\mu_0 \cdot (H_0 + H_{\mathrm{ex}} + H_{\mathrm{d}y}) + i\omega\alpha] \\ -\gamma\mu_0 M_{\mathrm{s}} \cdot h_{\mathrm{rf},x} + M_x^{\sim} \cdot [\gamma\mu_0 \cdot (H_0 + H_{\mathrm{ex}} + H_{\mathrm{d}x}) + i\omega\alpha] \end{bmatrix}. \tag{5.5}$$

Consequently, by solving the above equation for $\boldsymbol{h}_{\mathrm{rf}} = \overleftrightarrow{\chi}^{-1} \boldsymbol{M}^{\sim}$, the inverse susceptibility takes the form

$$\overleftrightarrow{\chi}^{-1} = \frac{1}{M_{\mathrm{s}}} \begin{bmatrix} H_0 + H_{\mathrm{ex}} + H_{\mathrm{d}x} + \frac{i\omega\alpha}{\gamma\mu_0} & -\frac{i\omega}{\gamma\mu_0} \\ +\frac{i\omega}{\gamma\mu_0} & H_0 + H_{\mathrm{ex}} + H_{\mathrm{d}y} + \frac{i\omega\alpha}{\gamma\mu_0} \end{bmatrix}. \tag{5.6}$$

Comparing the susceptibility with the one derived for the ferromagnetic resonance [Eq. (2.24)], we find a very similar form with slight modifications in the diagonal terms, where we now account for an exchange field H_{ex} and for the dipolar fields $\boldsymbol{H}_{\mathrm{d}}$. The resonance frequency for dipolar-exchange spin waves is given by solving $\det\left(\overleftrightarrow{\chi}^{-1}\right) \stackrel{!}{=} 0$ for $\omega = 2\pi f$. The real part of the solution describes the resonance frequency and we recover the famous Kalinikos-Slavin equation [173]

$$\omega = \gamma\mu_0 \sqrt{(H_0 + H_{\mathrm{ex}} + H_{\mathrm{d}x}) \cdot (H_0 + H_{\mathrm{ex}} + H_{\mathrm{d}y})}. \tag{5.7}$$

Before we discuss the dispersion relation of the dipolar-exchange spin waves, we want to discuss two particular limits of Eq. (5.7). First, the limit of infinite wavelength spin waves $k \to 0$ where the dipolar fields become $H_{\mathrm{d}x} = M_{\mathrm{s}}$ and $H_{\mathrm{d}y} = 0$ and the exchange field $H_{\mathrm{ex}} = 0$. In this case, we recover the Kittel equation $\omega = \gamma\mu_0 \sqrt{H_0 \cdot (H_0 + M_{\mathrm{s}})}$ for an in-plane magnetized film [Eq. (2.29)]. The second limit we want to discuss is for short-wavelength spin waves where the wavevector k becomes large. In this case the dipolar fields can be neglected as $(1 - \exp(-kd))/(kd)|_{k \gg d} = 0$ so the dispersion relation becomes $\omega(k) = \gamma\mu_0 \, (H_0 + H_{\mathrm{ex}}) \propto k^2$. These exchange spin waves feature a parabolic dispersion in k and have wavelengths $\lambda = 2\pi/k$ in the range of 100 nm and smaller.

The dispersion relation for $Co_{25}Fe_{75}$ at fixed magnetic field $\mu_0 H_0 = 50$ mT calculated with Eq. (5.7) is shown in Fig. 5.3(a). The used parameters to produce the figure are: $A = 2.6 \times 10^{-11}$ J/m [41], $\mu_0 M_{\mathrm{s}} = 2.36$ T [51], $d = 30$ nm and $\alpha = 0.003$.

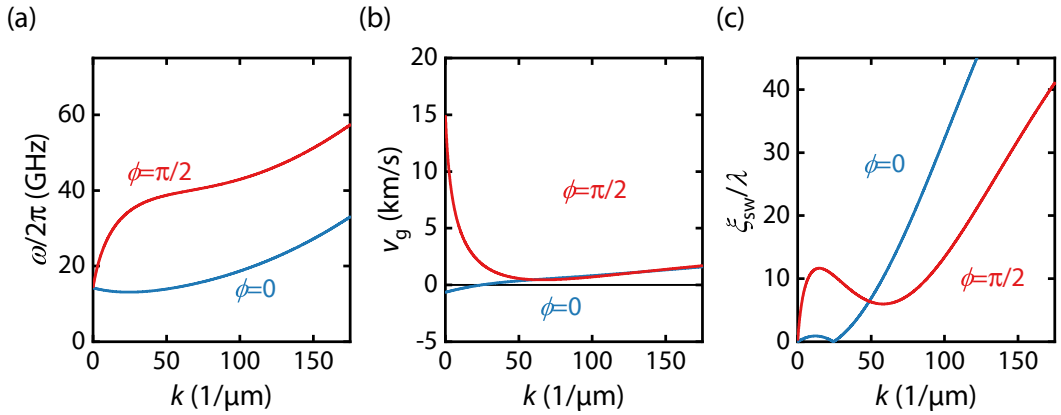

Fig. 5.3. (a) Calculated dispersion relation from Kalinikos-Slavin equation [Eq. (5.7)] as a function of the wavevector k for backward volume ($\phi = 0$) and Damon-Eshbach spin wave modes ($\phi = \pi/2$) in $d = 30\,\mathrm{nm}$ thick $Co_{25}Fe_{75}$ and an external magnetic field of $\mu_0 H_0 = 100\,\mathrm{mT}$. The other material parameters are given in the main text. (b) The group velocity v_g resulting from the wavevector-derivative of the spin wave resonance frequency $v_g = \partial\omega(k)/\partial k$. (c) Spin wave propagation length normalized to the wavelength of the spin wave, calculated using Eq. (5.10).

Furthermore, we distinguish two particular cases of the Kalinikos-Slavin equation which is for spin wave propagation along the direction of the magnetization $\phi = 0$ and propagation perpendicular to the magnetization $\phi = \pi/2$ as depicted in Fig. 5.2. The latter one are the so-called magneto-static surface modes or Damon-Eshbach modes [176] and are localized on one of the surfaces of the volume in which they propagate [177]. Spin waves propagating along the direction of magnetization are so-called backward volume magnetostatic waves and are, in contrast to Damon-Eshbach modes, volume modes. Furthermore, these modes feature a negative frequency vs. wavevector dispersion $\partial\omega(k)/\partial k < 0$. For large wavevectors k the dispersion increases quadratically as the system enters the exchange dominated regime.

An important characterization parameter for spin waves is their group velocity v_g which is given by the slope of their dispersion

$$v_g = \frac{\partial\omega(k)}{\partial k}. \tag{5.8}$$

The group velocity of the backward volume and the Damon-Eshbach spin wave modes are shown in Fig. 5.3(b). For the backward volume mode ($\phi = 0$) we find a negative group velocity which is antiparallel to the positive phase velocity, which is the origin of their name. The Damon-Eshbach modes possesses a larger group velocity which is comparable to LPE-YIG [20, 157].

With the Kalinikos-Slavin equation it is possible to calculate the lifetime and propagation length of spin waves. Therefore, we consider the imaginary part of the solution of $\det\left(\overleftrightarrow{\chi}^{-1}\right) \stackrel{!}{=} 0$ solved for ω and get for the spin wave linewidth

$$\Delta\omega = \gamma\mu_0 \left(H_0 + H_{\mathrm{ex}} + \frac{H_{\mathrm{d}x}}{2} + \frac{H_{\mathrm{d}y}}{2} \right). \tag{5.9}$$

The lifetime of spin wave is given by the inverse of the spin wave linewidth $\tau = 1/\Delta\omega$ which is the typical timescale on which the amplitude of the spin wave exponentially decays after the external excitation field is removed. The spin wave propagation length is the characteristic distance a spin wave travels before its amplitude decreased to $1/e$ due to the damping and is given by

$$\xi_{\mathrm{sw}} = v_{\mathrm{g}} \cdot \tau. \tag{5.10}$$

The spin wave propagation length normalized to the wavelength of the spin wave is shown in Fig. 5.3(c). We expect for the Damon-Eshbach modes ($\phi = \pi/2$) a larger propagation length due their larger group velocity. For applications a large propagation length is desirable because less information is lost over travelling distance. A large group velocity is also favorable because information can be transported faster [20]. Obviously, in the exchange interaction dominated regime at large wavevectors k the number of wavefronts observed before attenuation is much larger and desired to utilize in novel spin wave computing devices.

We want to emphasize that there also exists so-called forward volume spin wave mode where the magnetic thin film is magnetized perpendicular to the film plane and the propagation direction of the spin waves is perpendicular to the magnetization. In order to access these spin wave modes it is necessary to align the magnetization in the out-of-plane direction which in the case of $Co_{25}Fe_{75}$ requires a static magnetic field of more than $2\,\mathrm{T}$. We do not discuss these modes as in our experiments they are not accessible by our setup due to the limited magnetic field range available in the out-of-plane direction.

5.2 Experimental Details on Spatially-Resolved Magnetization Dynamics

After this general discussion of dipolar-exchange spin waves, we want to switch our focus to the experimental techniques to excite and detect spin waves. In order to excite spin waves we use a microwave antenna patterned on top of the magnonic waveguide. Our detection of spin waves relies on the magneto-optic Kerr effect (MOKE) which induces a rotation of the polarization plane when linear polarized light

interacts with magnetization. This physical mechanism we utilize in three different measurement techniques namely the microfocused frequency-resolve magneto-optic Kerr effect (μFR-MOKE), microfocused super Nyquist-sampling magneto-optic Kerr effect (μSNS-MOKE) and microfocused Brillouin light scattering (μBLS). In this section, we will discuss the excitation as well as the detection of spin waves with the aforementioned spectroscopy techniques in detail.

5.2.1 Magneto-Optic Kerr Effect

The magneto-optic Kerr effect (MOKE) was first discovered in 1877 by John Kerr [178] while examining the polarization of backreflected light from an electromagnet pole. The magneto-optic effect itself and thus the interaction between magnetism and light was found earlier by Michael Faraday in 1845 when investigating the polarization rotation of a “heavy” glass containing traces of lead under the influence of an electromagnet [179]. Nowadays the rotation of the polarization plane of polarized light when transmitting through a magnetized material is known as Faraday effect and the reflection from a material is known as Kerr effect. For our experiments, we are only interested in the Kerr effect and therefore will discuss it in more detail below. Nevertheless, the discussion is equivalent for the description of the Faraday effect.

We now want to quantify the MOKE by the so-called Kerr angle θ_{K} which is a complex quantity. To this end, we will provide a short derivation without the claim of completeness. For an extensive discussion and a complete derivation of the magneto-optic effects refer to Refs. [31, 179–185]. We will herin follow the derivation presented in Ref. [184]. We start with the Maxwell equations [186]

$$\nabla \times \boldsymbol{E}_{\mathrm{l}} = -\mu_0 \frac{\partial \boldsymbol{H}_{\mathrm{l}}}{\partial t} \tag{5.11}$$

$$\nabla \times \boldsymbol{H}_{\mathrm{l}} = \epsilon_0 \left(1 + \overleftrightarrow{\chi}_{\mathrm{e}}(\omega)\right) \frac{\partial \boldsymbol{E}_{\mathrm{l}}}{\partial t} \tag{5.12}$$

with the electric field $\boldsymbol{E}_{\mathrm{l}}$ and the magnetic field $\boldsymbol{H}_{\mathrm{l}}$ of the electromagnetic wave, the vacuum permittivity ϵ_0 and the polarizability $\overleftrightarrow{\chi}_{\mathrm{e}}$ of the magnetic system. Generally, the magnetic permeability $\overleftrightarrow{\mu}(\omega)$ also needs to be taken into account but for optical phenomena such as the magneto-optic effect, its contribution is negligible so we assume $\overleftrightarrow{\mu} = \mu_0 \mathbb{1}$ with the identity matrix $\mathbb{1}$ [184]. The frequency-dependent dielectric constant is related to the polarizability by the relation $\overleftrightarrow{\epsilon}(\omega) = \mathbb{1} + \overleftrightarrow{\chi}_{\mathrm{e}}(\omega)$ and is dependent on the applied field direction. The dielectric displacement vector is given by

$$\boldsymbol{D}_{\mathrm{l}} = \epsilon_0 \overleftrightarrow{\epsilon}(\omega) \boldsymbol{E}_{\mathrm{l}} \tag{5.13}$$

and the dielectric tensor takes the form

$$\overleftrightarrow{\epsilon}(\boldsymbol{M},\omega) = \begin{bmatrix} \epsilon_{xx} & \epsilon_{xy} & \epsilon_{xz} \\ \epsilon_{yx} & \epsilon_{yy} & \epsilon_{yz} \\ \epsilon_{zx} & \epsilon_{zy} & \epsilon_{zz} \end{bmatrix} = \begin{bmatrix} \epsilon_{xx} & \epsilon_{xy} & 0 \\ -\epsilon_{xy} & \epsilon_{xx} & 0 \\ 0 & 0 & \epsilon_{zz} \end{bmatrix}, \tag{5.14}$$

where in the second step we used the symmetry of a cubic crystal with a magnetization pointing along the z-direction which in our case is the out-of-plane direction. The entries of the dielectric tensor are complex quantities $\epsilon_{ij} = \epsilon'_{ij} + i\epsilon''_{ij}$ and follow the Onsager relation $\epsilon_{ij}(-\boldsymbol{M},\omega) = \epsilon_{ji}(\boldsymbol{M},\omega)$ [187]. We solve the Maxwell equations by using a plane wave ansatz for the electric and magnetic field (i.e. $\boldsymbol{H}_\mathrm{l} = \boldsymbol{H}_{0\mathrm{l}} \exp\left[i(\omega t - \boldsymbol{kr})\right]$) and get

$$\begin{aligned} \boldsymbol{k} \times \boldsymbol{E}_\mathrm{l} &= \omega\mu_0 \boldsymbol{H}_\mathrm{l}, \\ \boldsymbol{k} \times \boldsymbol{H}_\mathrm{l} &= -\omega\epsilon_0 \overleftrightarrow{\epsilon} \boldsymbol{E}_\mathrm{l}. \end{aligned} \tag{5.15}$$

Eliminating the magnetic field in the above equation leads to [184]

$$\begin{bmatrix} \bar{\boldsymbol{k}}^2 - \epsilon_{xx} & -\epsilon_{xy} & 0 \\ \epsilon_{xy} & \bar{\boldsymbol{k}}^2 - \epsilon_{xx} & 0 \\ 0 & 0 & \bar{\boldsymbol{k}}^2 - \epsilon_{zz} \end{bmatrix} \cdot \begin{bmatrix} E_{x\mathrm{l}} \\ E_{y\mathrm{l}} \\ E_{z\mathrm{l}} \end{bmatrix} = 0 \tag{5.16}$$

with the normalized wavevector $\bar{\boldsymbol{k}} = \boldsymbol{k}/k_0$ and the wavevector for light propagation in vacuum $k_0 = \omega^2\mu_0\epsilon_0$. In order to further simplify and solve Eq. (5.16) we assume the light propagation to be parallel to the magnetization along z so $\bar{\boldsymbol{k}} = \begin{bmatrix} 0 & 0 & \bar{k} \end{bmatrix}^\mathsf{T}$. We can neglect the last row in Eq. (5.16) as $E_{z\mathrm{l}} = 0$ and get the equation system

$$\begin{aligned} \left(\bar{k}^2 - \epsilon_{xx}\right) E_{x\mathrm{l}} - \epsilon_{xy} E_{y\mathrm{l}} &= 0, \\ \epsilon_{xy} E_{x\mathrm{l}} + \left(\bar{k}^2 - \epsilon_{xx}\right) E_{y\mathrm{l}} &= 0, \end{aligned} \tag{5.17}$$

with the non-trivial solutions

$$\bar{k}_\pm^2 = \epsilon_{xx} \pm i\epsilon_{xy} \quad \text{and} \quad \pm i E_{x\mathrm{l}} = E_{y\mathrm{l}}. \tag{5.18}$$

The normal modes of the light in the sample are then $D_{\pm\mathrm{l}} = \epsilon_0 \bar{k}_\pm^2 \left(E_{x\mathrm{l}} \pm i E_{y\mathrm{l}}\right)$ corresponding to right and left circularly polarized light. In a Kerr experiment the reflected light is measured so the reflection coefficients for the reflected light are given by the Fresnel equations [184, 188, 189]

$$r_\pm = \frac{\bar{k}_\pm - 1}{\bar{k}_\pm + 1}. \tag{5.19}$$

In our experiment we assume a linearly polarized incident light $\boldsymbol{E}_{\mathrm{in,l}} = \begin{bmatrix} E_{x\mathrm{l}} & 0 & 0 \end{bmatrix}^\mathsf{T}$ on the surface of the ferromagnet. The linearly polarized light can be understood as a

superposition of right- and left-circularly polarized light. Therefore, the reflection coefficients are given by $r_x = (r_+ + r_-)/2$ and $r_y = -i\,(r_+ - r_-)/2$ and consequently the backreflected light is given by $\boldsymbol{E}_{\mathrm{out,l}} = [r_x E_{x\mathrm{l}}\; r_y E_{x\mathrm{l}}\; 0]^{\mathsf{T}}$. The complex Kerr angle is given by [184]

$$\begin{aligned}\Phi_{\mathrm{K}} = \theta_{\mathrm{K}} + i\eta_{\mathrm{K}} &= -\frac{r_y E_{x\mathrm{l}}}{r_x E_{x\mathrm{l}}} = i\frac{r_+ - r_-}{r_+ + r_-},\\ &= i\,\frac{\bar{k}_+ - \bar{k}_-}{\bar{k}_+\bar{k}_- - 1},\end{aligned} \tag{5.20}$$

with the real-valued Kerr rotation θ_{K} and the Kerr ellipticity η_{K}. We see from the above equation that the linearly polarized light is converted to elliptically polarized light due to the different magnitudes of the right- and left-circular polarized light. The phase difference between the opposite circular polarizations leads to the rotation from the initial polarization. This is described by the Kerr angle θ_{K} due to circular dichroism. The Kerr ellipticity η_{K} describes the imbalance of the opposite circular polarization states and is due to the circular birefringence [31].

Before switching to the discussion of the dynamic MOKE, we want to emphasize that the MOKE can be measured in different configurations. The discussion above where the magnetization $\boldsymbol{M}$ is pointing perpendicular to the sample surface and parallel to the plane of incidents is the so-called polar MOKE. If the magnetization is parallel to the sample surface and to the plane of incidents defined by the incident and reflected light beam, it is the so-called longitudinal MOKE. The last configuration, the transverse MOKE, is given if the magnetization is parallel to the sample surface but perpendicular to the plane of incidents [190]. In our experiments the relevant effect is the polar MOKE as this effect is roughly one order of magnitudes larger than the longitudinal MOKE and approximately two orders of magnitudes larger than the transverse MOKE [191]. Due to symmetry reasons the longitudinal and transverse MOKE are not observed in our experiment, which will be discussed below. We further want to note that the polar and longitudinal MOKE induce a rotation and ellipticity to the polarization while the transverse MOKE only changes the intensity which makes it due to its small effect size challenging to measure.

After the discussion of the static MOKE and the basic description of the physical effect, we want to switch our focus back to the detection of magnetization dynamics utilizing the MOKE. In Fig. 5.4 the MOKE process when the laser light interacts with the magnetization dynamics of the spin wave is schematically depicted. The incident laser light has linear polarization and is directed to the ferromagnetic material. The laser light does not reflect at the interface but travels through a certain thickness of the ferromagnet where the intensity of the laser is attenuated and the phase of the light is delayed. Due to the oscillating magnetization $\boldsymbol{M}$ parallel to the sample plane, the dynamic component of the magnetization $\boldsymbol{m}(t)$ oscillates as a function of

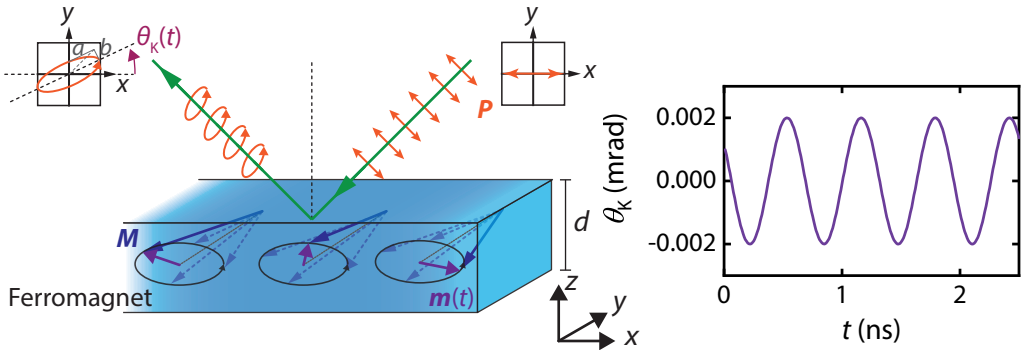

Fig. 5.4. Schematic illustration of the dynamic magneto-optic Kerr effect (MOKE). The linear polarized light with polarization $\boldsymbol{P}$ interacts with the out-of-plane component of the precessing magnetization $\boldsymbol{M}$ via the polar MOKE. This leads to a rotation of the polarization plane by the Kerr angle θ_K and to elliptical polarization, parameterized by the semi-major and semi-minor axis a and b respectively. Due to the oscillating magnetization and therefore its dynamic out-of-plane component, the Kerr angle is oscillating at the same frequency as the magnetization dynamics. In the graph on the right the Kerr angle $\theta_\mathrm{K}(t)$ as a function of time t is shown.

time with frequency $\omega_\mathrm{sw} = 2\pi f_\mathrm{sw}$. Therefore, the dynamic component $\boldsymbol{m}(t)$ oscillates between the out-of-plane and the in-plane direction which for the polar MOKE means that it is either zero, minimal or maximal. Due to the oscillating magnetization also the Kerr angle $\theta_\mathrm{K}(t)$ becomes time-dependent and is oscillating at the frequency of the magnetization dynamics as schematically shown in the right graph in Fig. 5.4. We want to note that in this configuration the longitudinal MOKE has the same response as the polar MOKE but has a phase shift of 90°. The dynamic magnetization $\boldsymbol{m}(t)$ for the polar and longitudinal MOKE, corresponding to the spin wave amplitudes, can be described by [191]

$$\begin{aligned} m_\mathrm{P}(z,t) &= m_{0\mathrm{P}}(z)\sin(\omega_\mathrm{sw}t)\,, \\ m_\mathrm{L}(z,t) &= m_{0\mathrm{L}}(z)\cos(\omega_\mathrm{sw}t)\,, \end{aligned} \tag{5.21}$$

where the subscript denotes the polar (out-of-plane) component and longitudinal (in-plane) component of the dynamic magnetization. The complex Kerr angle is then a superposition of the polar and longitudinal MOKE originating from different depths of the magnetic material and can be written as [191–195]

$$\begin{aligned} \theta_\mathrm{K}(t) &= \int_0^d \left[L(z)m_\mathrm{L}(z,t) + P(z)m_\mathrm{P}(z,t)\right]\mathrm{d}z, \\ &= \theta_\mathrm{K}\sin(\omega_\mathrm{sw}t + \phi) \end{aligned} \tag{5.22}$$

with the thickness of the ferromagnet d, the phase shift ϕ and the complex MOKE depth sensitivity functions $L(z)$ and $P(z)$ related to longitudinal and polar MOKE. We neglect the details of the dependence of the Kerr angle θ_K on the polarization of the

incident light. The sensitivity functions basically describe the exponential decay of the laser amplitude in the magnetic material and consequently the decreased sensitivity of the MOKE with increasing penetration depth. Typically the MOKE probing depth is in the range of tens of nm and depends on the wavelength of the used laser [191].

From Eq. (5.22) we see that the Kerr angle $\theta_{\mathrm{K}}(t)$ is oscillating with the frequency of the magnetization dynamics ω_{sw} as schematically depicted in Fig. 5.4. This is essential as the oscillation of the Kerr angle θ_{K} is in the microwave regime which is easily accessible with conventional microwave techniques compared to the frequency of the laser light in the range of a few hundred THz. We will discuss in Sections 5.2.3-5.2.5 how the oscillating Kerr angle can be utilized in different optical spectroscopy techniques to measure the magnetization dynamics. Before, we want to briefly discuss the complete excitation and detection scheme in order to investigate spatially-resolved magnetization dynamics.

5.2.2 Excitation and Detection of Spin Waves

In this section we will discuss how to excite and detect magnetization dynamics of propagating spin waves. We will start with the excitation of spin waves where we use a microstrip antenna which is patterned on top of the magnonic waveguide as schematically depicted in Fig. 5.5. A static magnetic field $\boldsymbol{H}_0$ is applied in the plane to fix the direction of the magnetization $\boldsymbol{M}$. A microwave source generates a microwave with a certain frequency f_{MW} and power P_{MW} which is coupled to the patterned antenna and generates an oscillating magnetic field $\boldsymbol{h}_{\mathrm{rf}}$ by Ampère's law. The magnetic fields generated by the microstrips can be calculated by the Karlqvist equations given by Eqs. (3.5) and (3.6). From the side view shown in Fig. 5.5(b) we see that the oscillating fields generated by each microstrip add up in the gap due to the opposing microwave currents I_{rf} in neighboring microstrips. In this particular example, the rf current in the outer microstrips flows in the same direction and the center line's current is opposing them. This periodicity in the rf currents given by the distance of the two outer microstrips, determines the most efficiently excited wavelength $\lambda = 2\pi/k$ of the spin wave. The efficiency of the antenna is given by the Fourier transform of the current distribution of the antenna, where we neglect the details of the Skin effect and a constant current density through the microstrips is assumed [196, 197]. We will calculate the efficiency of the used antenna in our experiment in Section 5.3.

The spin wave is coherently excited at the antenna where the dynamic magnetization $\boldsymbol{m}(t)$ couples to the oscillating driving field $\boldsymbol{h}_{\mathrm{rf}}$ if the microwave frequency f_{MW} matches the spin wave dispersion for the given static magnetic field $\boldsymbol{H}_0$ as described by Eq. (5.7). The coherently excited spin wave starts to propagate away from the antenna but the phase between the local, dynamic magnetization $\boldsymbol{m}(t)$ and the

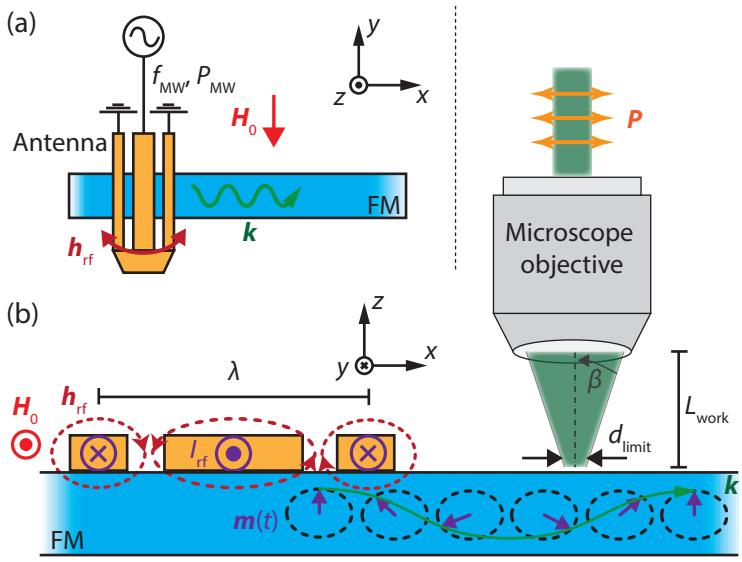

Fig. 5.5. Excitation principle of coherent spin waves in (a) top view and (b) side view. A static magnetic field $\boldsymbol{H}_0$ is applied to the ferromagnet (FM) to fix the direction of the magnetization. A microwave current I_{rf} is applied to an on-chip patterned antenna generating an oscillating magnetic field $\boldsymbol{h}_{\mathrm{rf}}$ which couples to the dynamic magnetization $\boldsymbol{m}(t)$. The periodicity of the antenna determines the efficiency to excite spin waves with a certain wavevector $\boldsymbol{k}$ and wavelength λ. The microscope objective focuses the polarized laser light to a diffraction limited spot size with diameter d_{limit} at its working distance L_{work} to spatially resolve the magnetization dynamics.

phase of the excitation field $\boldsymbol{h}_{\mathrm{rf}}$ and consequently the microwave source is retained due to the dipolar and exchange interaction. The dynamics of the magnetization is measured using a linearly polarized laser which is focused onto the ferromagnet using a microscope objective. With the microscope objective the laser light is collimated and collected in a cone with a certain angle β. Due to symmetry reasons the Kerr rotation and ellipticity induced by the longitudinal Kerr effect are averaged to zero. The polarization of laser light from opposite directions of the microscope objective experience a Kerr rotation of $+\theta_{\mathrm{K}}$ and $-\theta_{\mathrm{K}}$ respectively and consequently cancel each other out. The same argument holds for the transverse MOKE. Only the polar MOKE remains and is not vanishing.

The polarization of the laser light gets rotated and elliptical due to the MOKE where the Kerr angle θ_{K} oscillates now as a function of time as explained before [Section 5.2.1]. The backreflected light with the phase-information comprised is collected by the microscope objective and is returned to the optical setup. In the experiment, the microscope objective is fixed at a certain position in order to guarantee the alignment of the optical setup but the sample is mounted on piezo-based nanopositioners to allow the movement of the sample in all three dimensions and therefore the scanning of the magnonic waveguide.

Before we switch to the discussion of the different measurement techniques and how to analyze the oscillating Kerr angle θ_{K}, we want to briefly discuss the properties of the microscope objective especially with regard to our used one[1]. The (infinity-corrected) microscope objective is used to focus parallel light with a typical diameter of a few mm to a diffraction limited spot depending on the magnification and numerical aperture. The distance from the exit of the light at the microscope objective to the focus point is the so-called working distance L_{work}. For these kind of experiments a large working distance is desired as the sample is typically contacted by bond wires or picoprobes and a large working distance prevents to scratch the sample or rip off the bond wires. Our long distance microscope objectives has a working distance of $L_{\mathrm{work}} = 4.1\,\mathrm{mm}$.

The optical resolution of the microscope objective is given by the Abbe limit [188, 198]

$$d_{\mathrm{limit}} = \frac{\lambda_{\mathrm{l}}}{2n \cdot \sin\beta} = \frac{\lambda_{\mathrm{l}}}{2\,\mathrm{N.A.}}, \tag{5.23}$$

with the wavelength of the laser[2] $\lambda_{\mathrm{l}} = 532.2\,\mathrm{nm}$ and the refractive index n of the medium of light propagation which in our case is air ($n_{\mathrm{air}} \simeq 1.0$). For the second equal sign in Eq. (5.23), we introduced the numerical aperture $\mathrm{N.A.} = n \cdot \sin\beta$ which is determined by the opening angle β of the microscope objective and consequently defines the magnification. For our microscope objective the numerical aperture is $\mathrm{N.A.} = 0.75$ corresponding to an angle $\beta \simeq 48.6°$. The diffraction limit spot size is calculated to $d_{\mathrm{limit}} \approx 355\,\mathrm{nm}$. This value determines the minimal detectable wavelength of an in-plane excited spin wave [167].

In the following sections, we want to discuss three different measurement techniques, namely the microfocused frequency-resolved MOKE (µFR-MOKE), the microfocused Super-Nyquist sampling MOKE (µSNS-MOKE) and the microfocused Brillouin light scattering (µBLS) technique, integrated into a single optical setup to analyze the Kerr rotation in more detail.

[1] Zeiss LD EC Epiplan-Neofluar 100x/0,75 HD DIC M27
[2] Laser Quantum Torus 532

5.2.3 Frequency-Resolved Magneto-Optic Kerr Effect

The microfocused frequency-resolved magneto-optic Kerr effect (µFR-MOKE) technique is a relatively new technique based on the FR-MOKE technique [199–201] adapted for detecting the magnetization dynamics in a spatially-resolved manner [160]. The principle idea is to adapt the vector network analyzer based broadband magnetic resonance (VNA-BMR) technique (cf. Section 3.3.1), with its powerful phase-resolving capability and its frequency accuracy to capture the magnetization dynamics locally. The optical experimental setup is schematically depicted in Fig. 5.6(a). The full optical setup including all optical elements is shown in the Appendix A.1.

We use a continuous wave (cw) laser (Laser Quantum Torus 532, $\lambda_\mathrm{l} = 532.2\,\mathrm{nm}$, $P_{\mathrm{l,max}} = 180\,\mathrm{mW}$) passing through a neutral density filter (NDF) to adjust the laser power to the desired value as the laser needs to run at full power to ensure the correct laser mode-locking. After that the laser light passes through a Glan-Thompson polarizer to have a clearly defined linear polarization before focusing the laser beam onto the sample through the microscope objective (MO). In order to "see" the sample and allow for a measurement in a spatially-resolved manner, we build a Köhler-illumination, routinely implemented in commercial microscopes, to homogenously illuminate the sample. Combined with piezo-based nanopositioners allowing the movement of the sample in all three dimensions (spatial scan and focus) this enables us to precisely determine the position of the laser spot on the sample. For this, the backreflected blue LED light of the Köhler illumination is measured using a CCD camera. For details on the Köhler illumination refer to Appendix A.1.1.

The backreflected laser light, with its oscillating polarization angle at the frequency of the magnetization dynamics ω_sw, is reflected by a non-polarizing beamsplitter, where 90% of the light is reflected and consequently transmitted through another beamsplitter cube, used for the image acquisition of the sample. Now the laser beam is at the crucial part of the setup, where the oscillation of the polarization is converted to a change in intensity by using another polarizer (analyzer). In our experimental setup, this polarizer is substituted by a zero-order half-wave plate and a polarizing beam splitter cube in order to allow the fast change of the desired polarization angle to switch between µFR-MOKE (transmitted beam) and µBLS (reflected beam) measurements (see Appendix A.1 for details). We confirmed that the lower extinction ratio of the polarizing beam splitter cube compared to the Glan-Thompson polarizer has no significant impact on the measured signal-to-noise ratio. In this context, we will refer to the half wave-plate and the polarizing beam splitter as the analyzer. We set the angle of the analyzer to $\varphi_\mathrm{analy} = 45°$ with respect to the first polarizer, which is the optimal angle for FR-MOKE detection as we will derive below.

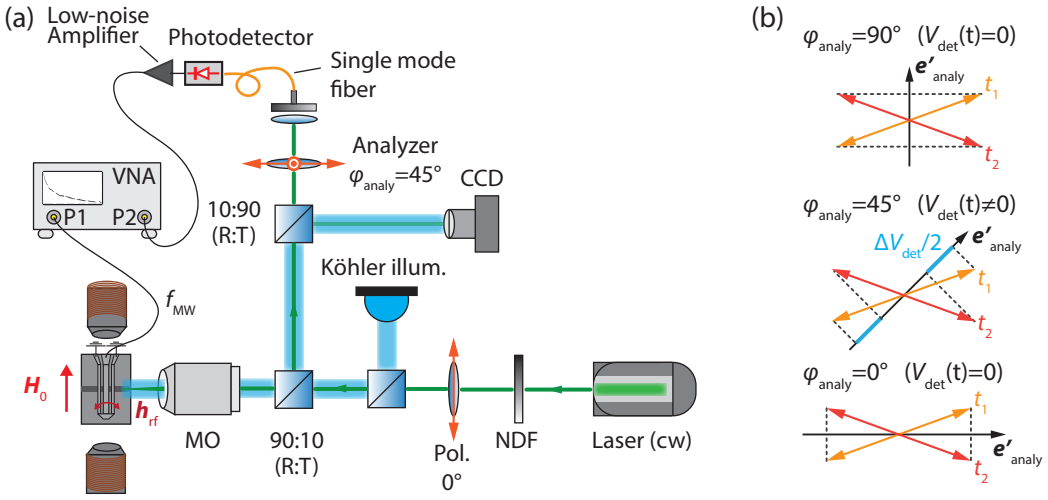

Fig. 5.6. (a) Schematic depiction of the microfocused frequency-resolved magneto-optic Kerr effect (µFR-MOKE) setup. For details refer to main text. (b) Different angle positions φ_{analy} for the analyzer to visualize the detected voltage at the photodetector $V_{\mathrm{det}}(t)$ depending on the direction of the polarization axis $\boldsymbol{e}'_{\mathrm{analy}}$. The red and orange arrow illustrate the two extreme values of polarization at times t_1 and t_2 and are exaggerated for clarity.

After the oscillating polarization of the laser beam is converted to an oscillating laser intensity, we couple the laser light into a single-mode FC/APC optical fiber with a fiber coupling efficiency of ∼55% of the laser intensity into the fiber. The optical fiber impinges through the anti-reflection coated FC/PC end on a fast broadband photodetector with a bandwidth of 25 GHz. The dc-signal of the photodetector is proportional to the total laser power coupled into the optical fiber. This voltage is measured by a multimeter and used to actively stabilize the focusing of the laser on the sample. For the fiber coupling of the backreflected laser light from the sample, it is critical to have parallel laser light which is only obtained if the laser spot is in focus on the sample.

The ac-signal of the photodetector is amplified by a low-noise amplifier and sent to the port 2 of the VNA. The VNA phase-sensitively analyzes the signal and calculates the complex transmission parameter $S_{21} = V_2/V_1$ with an intermediate frequency filter bandwidth of 1 Hz to minimize the noise [160]. The VNA is also used to apply a microwave frequency f_{MW} at port 1 and coupled into the microstrip antenna to excite the magnetization dynamics. In this context, V_2 is the measured voltage of the photodetector and V_1 the applied voltage to the microstrip antenna.

We now want to answer why we set the angle of the analyzer to $\varphi_{\mathrm{analy}} = 45°$. In our derivation, the change of the electric field of the laser beam $\boldsymbol{E}_{\mathrm{l}}$ is considered in

its initial state, after the interaction with the sample and after it passes through the analyzer. We can write the electric field vector of the laser beam $\boldsymbol{E}_\mathrm{l}$ as follows

$$\boldsymbol{E}_\mathrm{l} = \begin{bmatrix} E_{x\mathrm{l}} \\ 0 \\ 0 \end{bmatrix}_{\boldsymbol{x}}, \tag{5.24}$$

$$\xrightarrow{\text{polar MOKE}} \begin{bmatrix} E_{x\mathrm{l}} \cdot \cos\theta_\mathrm{K}(t) \\ E_{x\mathrm{l}} \cdot \sin\theta_\mathrm{K}(t) \\ 0 \end{bmatrix}_{\boldsymbol{x}}, \tag{5.25}$$

$$\xrightarrow{\text{Analyzer}} \begin{bmatrix} E_{x\mathrm{l}} \cdot \cos\theta_\mathrm{K}(t) \cdot \cos\left(\varphi_\mathrm{analy}\right) + E_{x\mathrm{l}} \cdot \sin\theta_\mathrm{K}(t) \cdot \sin\left(\varphi_\mathrm{analy}\right) \\ 0 \\ 0 \end{bmatrix}_{\boldsymbol{x}'}. \tag{5.26}$$

Going through the steps in the equations above: First, we write the linearly polarized laser light with a single component in the $\boldsymbol{x}$ coordinate system [Eq. (5.24)]. After the interaction of the linearly polarized light with the magnetization dynamics, the polarization of the laser light becomes elliptically polarized and the polarization plane rotates due to the polar MOKE [Eq. (5.25)]. The ellipticity of the laser light will be neglected for simplicity. The analyzer projects the electric field or polarization of the laser light onto the polarization axis of the analyzer as schematically depicted in Fig. 5.6(b). Additionally, we transformed the coordinate system into the $\boldsymbol{x}'$ system so the second and third component of the electric field vector are zero [Eq. (5.26)].

For the µFR-MOKE we are using an ac-detector so the measured voltage on the diode detector can be calculated to

$$\begin{aligned} V_\mathrm{det}(t) &= \left[E_{x\mathrm{l}} \cdot \cos\theta_\mathrm{K}(t) \cdot \cos\left(\varphi_\mathrm{analy}\right) + E_{x\mathrm{l}} \cdot \sin\theta_\mathrm{K}(t) \cdot \sin\left(\varphi_\mathrm{analy}\right)\right]^2, \\ &= E_{x\mathrm{l}}^2 \cdot \cos^2\theta_\mathrm{K}(t) \cdot \cos^2\left(\varphi_\mathrm{analy}\right) + E_{x\mathrm{l}}^2 \cdot \sin^2\theta_\mathrm{K}(t) \cdot \sin^2\left(\varphi_\mathrm{analy}\right) \\ &\quad + 2E_{x\mathrm{l}}^2 \cdot \cos\theta_\mathrm{K}(t) \cdot \sin\theta_\mathrm{K}(t) \cdot \cos\left(\varphi_\mathrm{analy}\right) \cdot \sin\left(\varphi_\mathrm{analy}\right), \\ &\approx E_{x\mathrm{l}}^2 \cdot \cos^2\left(\varphi_\mathrm{analy}\right) + 2E_{x\mathrm{l}}^2\,\theta_\mathrm{K}(t) \cdot \cos\left(\varphi_\mathrm{analy}\right) \cdot \sin\left(\varphi_\mathrm{analy}\right). \end{aligned} \tag{5.27}$$

In the last step, we used $\cos\theta_\mathrm{k}(t) \approx 1+\mathcal{O}(\theta_\mathrm{K}^2)$, $\sin\theta_\mathrm{k}(t) \approx \theta_\mathrm{K}(t)+\mathcal{O}(\theta_\mathrm{K}^3)$ and $\cos\theta_\mathrm{k}(t)\cdot\sin\theta_\mathrm{k}(t) \approx \theta_\mathrm{K}(t)+\mathcal{O}(\theta_\mathrm{K}^3)$ in the approximation for small Kerr angles $\theta_\mathrm{K}(t)$. The first term is an offset term independent of the Kerr angle, while the second term is linearly dependent on the Kerr angle $\theta_\mathrm{K}(t)$ possessing all the information on the magnetization dynamics. The second term is maximized by $\max\left[\cos\left(\varphi_\mathrm{analy}\right)\sin\left(\varphi_\mathrm{analy}\right)\right] = 1/2$ if the angle of the analyzer is set to $\varphi_\mathrm{analy} = 45°$. The total voltage measured on the ac detector is then

$$V_\mathrm{det}(t) \approx \frac{E_{x\mathrm{l}}^2}{2} + E_{x\mathrm{l}}^2\,\theta_\mathrm{K}(t). \tag{5.28}$$

The chosen $\varphi_{\mathrm{analy}} = 45°$ can also be understood with the schematics shown in Fig. 5.6(b). Here, the oscillating polarization after the interaction with the magnetization dynamics via the MOKE is shown for two different points in time t_1 and t_2 at the extreme values of the polarization. For simplicity, the ellipticity of the polarization is omitted. The polarization is oscillating between t_1 and t_2 with the frequency of the magnetization dynamics (typically $f_{\mathrm{MW}} \sim 10\,\mathrm{GHz}$) and within the arrow (front to back) with the frequency corresponding to the laser wavelength ($\sim 560\,\mathrm{THz}$). By changing the angle of the analyzer φ_{analy} and consequently the polarization vectors of the analyzer $\boldsymbol{e}'_{\mathrm{analy}}$, the projection of the oscillating polarization on the analyzer vector is considered. For $\varphi_{\mathrm{analy}} = 0°$ and $\varphi_{\mathrm{analy}} = 90°$ the projection of the polarization leads to no voltage on the detector $V_{\mathrm{det}}(t) = 0$ as it leads to the same point on the analyzer axes $\boldsymbol{e}'_{\mathrm{analy}}$. For the situation where $\varphi_{\mathrm{analy}} = 45°$ the polarizations do not project to the same point on the analyzer axis $\boldsymbol{e}'_{\mathrm{analy}}$ leading to a finite difference in the laser intensity and consequently to a measurable voltage at the detector $V_{\mathrm{det}}(t) \neq 0$. We want to emphasize that any angle between $0°$ and $90°$ leads to a difference in laser intensity after the analyzer but, as mathematically derived above, the effect is largest at $\varphi_{\mathrm{analy}} = 45°$.

5.2.4 Brillouin Light Scattering

The Brillouin light scattering (BLS) technique is a widely-used and well established optical spectroscopy technique. The large advantage of BLS is its sensitivity not only to coherent processes, such as the excitation of magnetization dynamics with a microstrip antenna, but also to incoherent processes like thermal spin waves [168]. The BLS technique can be adapted to study the magnetization dynamics also in a spatially- [165, 167], wavevector- [126, 202], temporal- [203–205] and phase-resolved [169–171] manner [20, 167]. Before we go into details of the spatially-resolved, microfocused BLS technique, we first want to discuss the BLS principle and the tandem Fabry-Pérot interferometer.

The physical principle utilized in BLS measurements is best explained in a quantum picture as schematically depicted in Fig. 5.7(a). The photons of the laser possess an energy depending on the frequency ω and a momentum described by the wavevector $\boldsymbol{k}$. These photons can either generate or annihilate an excitation in the ferromagnet. These excitations are known as magnons and posses an energy $\hbar\omega_{\mathrm{sw}}$ and a momentum $\hbar\boldsymbol{k}_{\mathrm{sw}}$. The scattered photon experiences a frequency shift $\omega \pm \omega_{\mathrm{sw}}$ and a change in momentum $\boldsymbol{k} \pm \boldsymbol{k}_{\mathrm{sw}}$ due to the energy and momentum conservation. The process of generating a magnon is the so-called Stokes process and the annihilation of a magnon is the anti-Stokes process.

In order to analyze the energy transfer, a (3+3)-pass tandem Fabry-Pérot interferometer (TFPI) designed by J. R. Sandercock is used as shown in Fig. 5.7(b). The

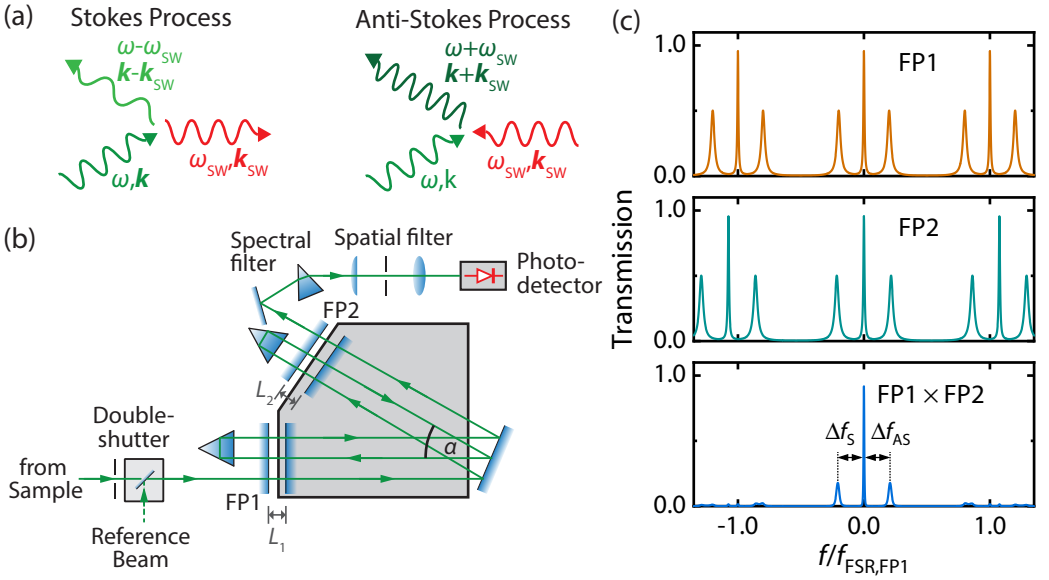

Fig. 5.7. (a) Principle of Brillouin light scattering (BLS). The incident light with frequency ω and wavevector $\boldsymbol{k}$ generates or annihilates a magnon with frequency ω_{sw} and wavevector $\boldsymbol{k}_{\mathrm{sw}}$ which is the so-called Anti-Stokes or Stokes process, respectively. The scattered light experiences a shift in frequency $\omega \pm \omega_{\mathrm{sw}}$ and momentum $\boldsymbol{k} \pm \boldsymbol{k}_{\mathrm{sw}}$ due to the momentum and energy conversion. (b) Schematic of the tandem Fabry-Pérot interferometer (TFPI) with the two etalons FP1 and FP2. For details refer to main text. (c) Transmission of the two etalons as a function of the frequency shift f. The scattering of magnons leads to the frequency shift Δf_{S} and Δf_{AS} for the Stokes- and Anti-Stokes process, respectively.

TFPI consists of two Fabry-Pérot interferometers (FPI) aligned in series which again consists of two parallel, highly reflective mirrors. The demand on the TFPI is to resolve small signals (single photons), due to the small inelastic scattering cross section compared to the large elastic scattering, and to measure small frequency shifts in the laser frequency [25]. To achieve a high contrast and to allow for frequency resolution, the laser beam passes three times through each FPI. The second Fabry-Pérot interferometer (FP2) lies with an angle α with the scan direction (FP1) so the stage translation for the second interferometer becomes $L_2 = L_1 \cos\alpha$.

A FPI functions as a frequency or wavelength analyzer where laser light is reflected multiple times within the two mirrors and constructively interferes if the mirror distance L is an integer multiple of half the wavelength of the laser light $L = n\lambda/2$ with $n \in \mathbb{N}$ [25]. This means that the elastically scattered light is transmitted after one scan by $\lambda/2$ which is known as the free spectral range (FSR) [206]

$$f_{\mathrm{FSR}} = \frac{c}{2L} \tag{5.29}$$

with the speed of light c. In order to suppress the unwanted higher order elastic peaks after every FSR scan, the distance travelled by FP2 is slightly different to FP1 leading

to a suppression of higher order transmissions when the laser light travels through both FPIs as shown in Fig. 5.7(c) (lower panel). The remaining peaks in the TFPI spectrum are stemming from the elastically scattered light, known as the Rayleigh peak, and the peaks from the inelastically scattered photons due to the Stokes and anti-Stokes process leading to a frequency shift Δf_{S} and Δf_{AS}, respectively. The mirror spacing of FP1 can be adjusted with motors to access a FSR between 5 GHz and ~ 1.5 THz ($L = 0.1\,\mathrm{mm} - 30\,\mathrm{mm}$) while the stage scan with piezo motors is in the range of a few µm [206].

The frequency resolution δf of the TFPI is given by the finesse $\mathcal{F}$ which is a measure for the number of interfering beams in the FPI and reflects the quality of the interferometer. The finesse of a FPI is given by [198]

$$\mathcal{F} = \frac{f_{\mathrm{FSR}}}{\delta f}. \tag{5.30}$$

The typical finesse of the TFPI is between 100 and 120 [206]. In our experiments the mirror spacing was set to $L_1 = 6\,\mathrm{mm}$ leading to a FSR of $f_{\mathrm{FSR}} = 25\,\mathrm{GHz}$ and a frequency resolution of $\delta f \approx 250\,\mathrm{MHz}$. Therefore, it is crucial to use a laser with a smaller linewidth than the TFPI resolution (Laser Quantum Torus 532, $\Delta f_{\mathrm{l}} = 1\,\mathrm{MHz}$) to eliminate the potential limitation of the measured signal by the laser linewidth. Note that the finesse and transmission function as shown in Fig. 5.7(c) crucially depends on the parallelism of the mirrors of the two FPIs and the correct mirror spacing of FP2 with respect to FP1. To this end, one of each FPI mirrors is equipped with a pair of piezo motors to adjust the polar and azimuthal angle of the mirror.

After passing the two FPIs, the laser light is passed through a spectral and a spatial filter before the photons are analyzed by a single photon detector[3]. The counted photons are correlated with the scanning mirror spacing so the photon counts are assigned to a frequency shift. As most of the photons will be elastically scattered, the intensity is large enough to damage the photodetector. To prevent this, a double-shutter system is present at the entrance of the interferometer. If the scanned mirror spacing comes close to the Rayleigh peak, the double-shutter closes the entrance from the sample and opens the beam path to the so-called reference-beam which is a low intensity laser light directly from the laser. The reference beam is also used to "stabilize" the TFPI. During this PhD-thesis an automated software was developed to actively stabilize (adjust FPI mirrors for parallelism and correct spacing of FP2), control (e.g. double-shutter) and perform measurements with the TFPI (see Appendix A.2).

In our experiment, we perform spatially-resolved, microfocused Brillouin light scattering experiments with the setup schematically depicted in Fig. 5.8. The optical path remains compared to the µFR-MOKE up to the analyzer unchanged (cf.

[3] Hamamatsu H10682

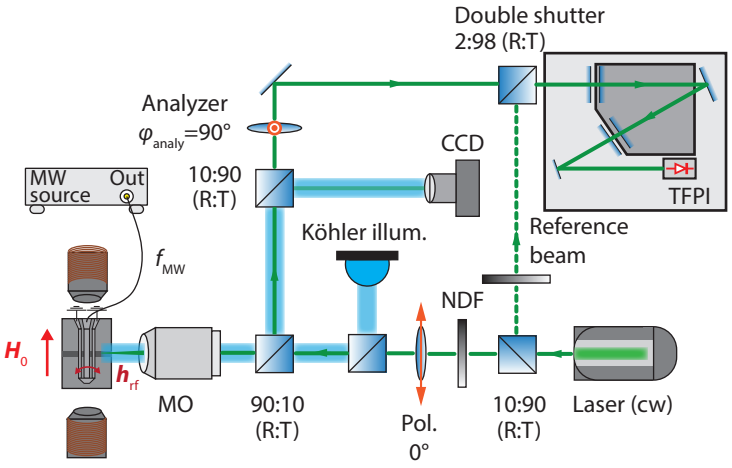

Fig. 5.8. Schematic depiction of the microfocused Brillouin light scattering (μBLS) setup. For details refer to main text.

Section 5.2.3). After the analyzer, the laser beam is routed into the TFPI. For the reference path of the TFPI, a 10:90 beam splitter is placed after the laser with a neutral density filter (NDF) to adjust the laser power. Due to the usage of a microscope objective in the μBLS the change in momentum cannot be measured because the laser light cone averages over the contributions $\pm\boldsymbol{k}_{\mathrm{sw}}$. In wavevector-resolved BLS a low N.A. lens is used to focus the laser beam and the sample is rotated to change the angle of incidents and consequently the wavevector. Additionally, the wavevector conservation is only valid for the in-plane component of the wavevector but not for the out-of-plane component in thin films [167].

The analyzer in the μBLS measurements is set to $\varphi_{\mathrm{analy}} = 90°$ with respect to the first polarizer. We will now show mathematically why we chose $\varphi_{\mathrm{analy}} = 90°$ and how the optical sidebands (Stokes- and anti-Stokes peak) occur. Starting again with the electric field vector of the laser beam described by Eqs. (5.24)-(5.26), we can write

$$E(t) = E_{xl}\left[\cos\theta_{\mathrm{K}}(t)\cdot\cos\left(\varphi_{\mathrm{analy}}\right) + \sin\theta_{\mathrm{K}}(t)\cdot\sin\left(\varphi_{\mathrm{analy}}\right)\right], \tag{5.31}$$

$$= E_{xl}\cos\left(\theta_{\mathrm{K}}(t) - \varphi_{\mathrm{analy}}\right). \tag{5.32}$$

From Eq. (5.32), it is clear that φ_{analy} changes the background of the measured signal as the Kerr angle $\theta_{\mathrm{K}}(t)$ is very small ($<$ mdeg). To minimize the background primarily coming from the elastically scattered light, the angle of the analyzer is set

to $\varphi_{\mathrm{ang}} = 90° = \pi/2$. Utilizing $\cos(\theta_{\mathrm{k}}(t) - \pi/2) = \sin\theta_{\mathrm{K}}(t)$ and Taylor expanding $\sin\theta_{\mathrm{k}}(t) \approx \theta_{\mathrm{K}}(t) + \mathcal{O}(\theta_{\mathrm{K}}^3)$ for small $\theta_{\mathrm{K}}(t)$, we find

$$E(t) = E_{x\mathrm{l}}\theta_{\mathrm{K}}(t), \tag{5.33}$$

$$= E_{x\mathrm{l}}^0 \cos(\omega_{\mathrm{l}} t)\, \theta_{\mathrm{K}} \cos(\omega_{\mathrm{sw}} t)\,,$$

$$= \frac{E_{x\mathrm{l}}^0 \theta_{\mathrm{K}}}{2} \left[\cos((\omega_{\mathrm{l}} - \omega_{\mathrm{sw}})t) + \cos((\omega_{\mathrm{l}} + \omega_{\mathrm{sw}})t)\right], \tag{5.34}$$

where we used $E_{x\mathrm{l}} = E_{x\mathrm{l}}^0 \cos(\omega_{\mathrm{l}} t)$ with the laser frequency $\omega_{\mathrm{l}} = 2\pi\, c/\lambda_{\mathrm{l}}$. From Eq. (5.34) we get optical sidebands with frequencies $\omega_{\mathrm{l}} \pm \omega_{\mathrm{sw}}$ corresponding to the Stokes- and anti-Stokes peak. The installed single photon detector in the TFPI is in contrast to the µFR-MOKE a dc detector. The measured signal after frequency filtering with the TFPI and low-pass filtering is

$$V_{\mathrm{DC}} \propto \left[E_{x\mathrm{l}}^0\, \theta_{\mathrm{K}}\right]^2. \tag{5.35}$$

As seen from the above equation, the detected signal is tiny but there is no background in the measured signal, which is distinct from the µFR-MOKE (cf. Eq. (5.27)), due to the analyzer rotated orthogonally with respect to the first polarizer. Therefore, a single photon detector with a low dark count rate is required to detect these small signals. In the µBLS the intensity is measured and not the amplitude and therefore the phase-information is lost. This problem can be overcome by performing phase-resolved µBLS measurements where an electro-optic modulator (EOM) is inserted after the polarizer [169–171]. The limiting factor of the phase-resolved µBLS is the limited frequency range of the EOM. Consequently, the accessible frequency range of the magnetization dynamics is restricted.

5.2.5 Super-Nyquist Sampling Magneto-Optic Kerr Effect

The microfocused super-Nyquist sampling MOKE (µSNS-MOKE) is an improved measurement scheme based on the classical time-resolved MOKE (TR-MOKE) [41, 164, 207, 208] and was developed by the group of Georg Woltersdorf (Martin Luther University Halle-Wittenberg) [172]. The optical setup is schematically depicted in Fig. 5.9(a). In our experiment, we are using a pulsed laser (NKT Photonics Origami) with a wavelength of $\lambda_{\mathrm{l}} = 515.6\,\mathrm{nm}$, a repetition rate of $f_{\mathrm{rep}} = 80\,\mathrm{MHz}$, a gaussian pulse length of $\tau_{\mathrm{pulse}} = 146\,\mathrm{fs}$ and a cw laser power of $P_{\mathrm{l}} = 78\,\mathrm{mW}$ corresponding to a pulse energy of $975.0\,\mathrm{pJ}$. The laser light passes through the same optical path as in the µFR-MOKE and µBLS measurements. The optical setup differs in the measurement of the oscillating polarization due to the polar MOKE. For the µSNS-MOKE, a Wollaston prism is used to separate the ordinary and extraordinary ray, corresponding to the two orthogonal polarization states, by an angle of $20°$. These two

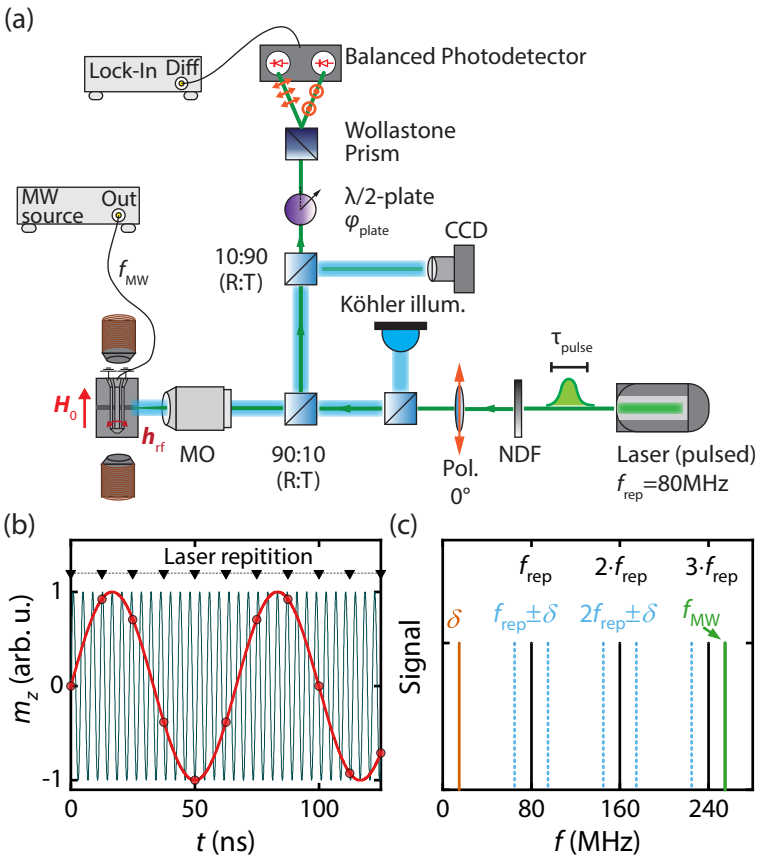

Fig. 5.9. (a) Schematic depiction of the microfocused Super-Nyquist sampling magneto-optic Kerr effect (μSNS-MOKE) setup. For details refer to main text. (b) Nyquist-sampling principle where a slow oscillating signal with frequency δ (red line) is generated due to the non-stroboscopic detection of the oscillating out-of-plane component of the dynamic magnetization m_z (black line) with frequency f_{MW} and the laser repetition rate f_{rep} (black triangles). (c) Fourier spectrum of the frequency combs generated by pulsed laser. For illustration purposes the used parameter values for panels (b) and (c) are $f_{\mathrm{MW}} = 255\,\mathrm{MHz}$, $f_{\mathrm{rep}} = 80\,\mathrm{MHz}$ and $\delta = 15\,\mathrm{MHz}$.

beams are then focused by 15 mm lenses (not shown in figure) onto the detectors of a balanced photodetector with a fast monitor output and a frequency response between dc and 350 MHz. In front of the Wollaston prism a zero-order half-wave plate is placed to rotate the polarization plane such that the subtracted signal of the two balanced detector inputs is zero. The output signal of the balanced photodetector is measured by a lock-in amplifier (Zurich Instruments UHFLI, frequency range $f \leq 600\,\mathrm{MHz}$).

The crucial part is the synchronization of the laser with the lock-in amplifier and the microwave source, used to excite the magnetization dynamics with frequency f_{MW}, on the same timebase. The laser features a synchronization module to stabilize the laser to an external signal with ultra-low jitter and frequency equal to the laser repetition rate f_{rep}. This is necessary to maintain a fixed phase relation between the microwave used to excite spin waves and the laser pulses used to detect the spin wave dynamics.

In our experiment we used the lock-in amplifier to generate the synchronization signal for the laser and the 10 MHz reference output to synchronize the microwave source. Note that the measurements can also be performed with a lock-in amplifier with a frequency range lower than the laser repetition rate (e.g. Zurich Instruments MFLI, $f \leq 500\,\mathrm{kHz}$). However, in this case the usable microwave frequencies are constrained. For the synchronization, a waveform generator (Keysight 33600A) is then additionally used to generate the synchronization signal for the laser (80 MHz) and for the other microwave equipment (10 MHz). The excitation of the magnetization dynamics is done by the microwave source (Rohde&Schwarz SMF100A) generating a cw microwave with frequency f_{MW} and power P_{MW} coupled into the microstrip antenna.

In the traditional TR-MOKE, measurements are performed in a stroboscopic manner, such that the microwave excitation frequency $f_{\mathrm{MW}} = n \cdot f_{\mathrm{rep}}$ with $n \in \mathbb{N}$. For SNS-MOKE, we allow an arbitrary offset between the microwave frequency f_{MW} and multiples of the laser repetition rate f_{rep} [172]. This can be expressed by $f_{\mathrm{MW}} = n \cdot f_{\mathrm{rep}} + \delta$, where δ is an arbitrary frequency offset in the range $0 < \delta < 80\,\mathrm{MHz}$. In Figs. 5.9(b) and (c) the Nyquist sampling process is shown in the time- and frequency-domain, respectively. The oscillations of the out-of-plane component of the dynamic magnetization m_z is faster than the repetition rate of the laser. Due to the frequency offset δ, the laser pulse probes m_z at different times and not always at the same periodic time as in the stroboscopic measurement scheme ($f_{\mathrm{MW}} = n \cdot f_{\mathrm{rep}}$) as depicted by the red points in Fig. 5.9(b). This periodic wave (red line) oscillates with a frequency δ. The down-conversion to frequency δ by the frequency combs of the pulsed laser occurs coherently as shown in Fig. 5.9(c), which conserves the phase-information of the magnetization precession relative to the microwave excitation of the microwave source [172]. Due to this undersampling of the magnetization dynamics, this technique is called super-Nyquist sampling. The lock-in amplifier can consequently be set to δ and the real and imaginary part of the susceptibility can be measured. Therefore, also this technique is phase-sensitive and measures the amplitude of the magnetization dynamics. The measured voltage on the photodetector can be equivalently estimated with the approach in Section 5.2.3. The first term in Eq. (5.28) vanishes in the µSNS-MOKE measurement due to the usage of the balanced photodetector where as mentioned before the two input signals are subtracted. The resulting ac voltage is consequently

$$V_{\mathrm{det}}(t) \approx 2E_{x1}^2 \theta'_{\mathrm{K}}(t). \tag{5.36}$$

Note that the Kerr angle is not oscillating with f_{MW} but with δ. The time-dependent Kerr angle takes the form $\theta'_{\mathrm{K}}(t) = \theta_{\mathrm{K}} \sin(\delta t + \phi)$ similar to Eq. (5.22). This measurement technique will in the following be used to cross-check some of the results of the

µFR-MOKE as from the measurement principle they are very similar and are both phase-sensitive. The main focus of this chapter will be on the µFR-MOKE technique and its capabilities.

5.3 Low-Damping Spin Wave Dynamics in $Co_{25}Fe_{75}$

For the following experiments, a microstructured $Co_{25}Fe_{75}$ sample is used as shown in the camera image in Fig. 5.10(a), which was taken by the CCD of the optical setup. The sample is structured on a silicon substrate with a thermal oxide layer with a thickness of $1\,\mu m$ on top using electron beam lithography. The magnonic waveguide with width $w = 1.5\,\mu m$ is written using positive resist (Allresist AR-P 617.08). After development, the $Co_{25}Fe_{75}$ is deposited using dc sputtering technique in the SUPERBOWL facility at the WMI. The complete stack sequence is substrate/Pt(3)/Cu(3)/$Co_{25}Fe_{75}$(50)/Cu(3)/Ta(3), where the numbers in the brackets denote the nominal thickness in nm. This composition features excellent low damping properties as demonstrated in Ref. [51].

After lift-off in acetone, the procedure is repeated for the microwave antenna and markers, used for optical drift stabilization of the sample stage. For the markers and the antenna a $30\,nm$ thick SiOx layer was rf sputtered first to ensure electrical and thermal isolation. Afterwards $100\,nm$ of gold (Au) was in-situ dc sputtered in the SUPERBOWL. The antenna is contacted using bond wires from a coplanar waveguide which is connected to port 1 of the VNA or the output port of a microwave source.

The antenna is designed as a coplanar waveguide-like microstrip antenna consisting of a single center strip and two ground lines shorted at the end of the antenna. The width of the center conductor is $1.5\,\mu m$, the width of the ground lines $0.75\,\mu m$ and the gap between them is $0.5\,\mu m$. The idealized current distribution in the antenna is shown in Fig. 5.10(b). The widths were chosen so that the current densities in the center and ground lines are equal. As already discussed in Section 5.2.2, it is possible from the given current distribution in the sample to calculate the excitation efficiency of spin waves by Fourier transformation [196]. The excitation efficiency of the antenna is shown in Fig. 5.10(c), where we get a peak efficiency at $|k|_{max} = 1.77\,\mu m^{-1}$. The non-propagating spin waves with $k = 0$ are excited with roughly half the efficiency compared to the most efficiently excited magnons.

In this section, we will use the aforementioned optical spectroscopy techniques to investigate the magnetization dynamics of the low damping ferromagnet in the linear regime, such as spin wave propagation, and non-linear regime, such as magnon-scattering. We especially will focus on the µFR-MOKE technique and use the other two (µBLS and µSNS-MOKE) to compare the results or to get additional insights.

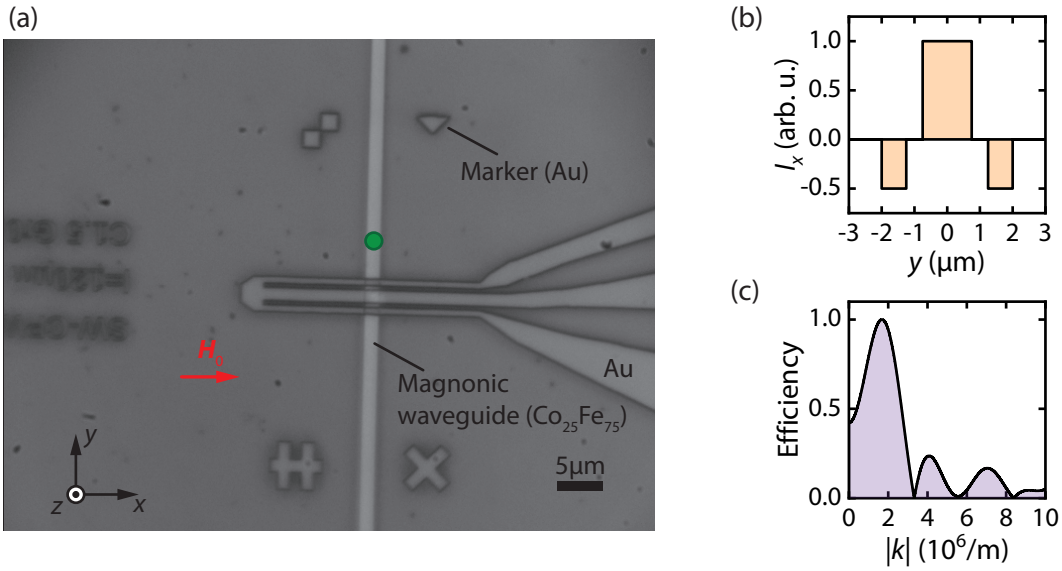

Fig. 5.10. (a) Camera image of the investigated magnonic device taken by the CCD camera. The static magnetic field $\boldsymbol{H}_0$ is orientated perpendicular to the $Co_{25}Fe_{75}$ strip. (b) Current distribution I_x through the antenna. (c) Fourier transform of the current distribution I_x which gives the excitation efficiency of the antenna as a function of the wavevector k.

First, the linear magnon dynamics is discussed and in Section 5.3.2 the non-linear dynamics with a focus on measurement technique is addressed.

5.3.1 Spin Wave Dynamics in the Linear Regime

In this section, we present our results on the study of the magnetization dynamics of spin waves in the linear regime with the focus on spin wave propagation characteristics. In the presented experiments, the cw laser power before the microscope objective is set to $P_\mathrm{l} = 1.85\,\mathrm{mW}$ for the cw laser in the µFR-MOKE and µBLS measurements and $P_\mathrm{l} = 0.90\,\mathrm{mW}$ for the pulsed laser in the µSNS-MOKE measurements. The microwave power of the VNA or the microwave source is set to $P_\mathrm{MW} = 10\,\mathrm{dBm}$ and the number of averages in the µBLS is set to 1500, if not stated differently. Due to the need to slightly change the optical path when either measuring with the cw laser (µFR-MOKE & µBLS) or the pulsed laser (µSNS-MOKE), the spot positions on the sample cannot be perfectly reproduced leading to small deviations between the spectra. Additionally, the beam diameter of the two lasers are different and the beam shape of the pulsed laser is elliptical and slightly divergent, what results in different focused spot sizes on the sample. While for the cw laser the spot size is in the diffraction limit, for the pulsed laser this is not the case and therefore the resolution will be slightly worse.

First, we will briefly compare the typical spectra of the three aforementioned optical spectroscopy techniques in magnetic field sweep experiments at fixed spot position before discussing the propagation characteristics.

5.3.1.1. Comparison of Fieldsweep Spectra with Different Optical Spectroscopy Techniques

In these experiments, the laser spot is focused on the center of the magnonic waveguide roughly $4.5\,\mu\mathrm{m}$ away from the microwave antenna to minimize the near-field excitation of the antenna. The spot location on the sample is indicated by the green circle in Fig. 5.10(a). The applied microwave frequency is $f_{\mathrm{MW}} = 12\,\mathrm{GHz}$. The magnetic field H_0 is swept in the range from $145\,\mathrm{mT}$ to $0\,\mathrm{mT}$ with a resolution of $1.0\,\mathrm{mT}$. For the µSNS-MOKE the frequency offset is chosen to $\delta = 10\,\mathrm{kHz}$ resulting in a excitation frequency of $f_{\mathrm{MW}} = 12\,\mathrm{GHz}+\delta$. The lock-in frequency is set to $\delta+80\,\mathrm{MHz} = 80.01\,\mathrm{MHz}$ for a better voltage noise density of the used lock-in amplifier [209].

In Fig. 5.11(a) the measured complex S_{21}-parameter of the µFR-MOKE measurement and in Fig. 5.11(b) the measured lock-in voltage U_i of the µSNS-MOKE measurement with the laser spot at a fixed position are shown. These two spectroscopy techniques are as already mentioned phase-sensitive and proportional the susceptibility of the magnetization dynamics. At $\mu_0 H_0 \simeq 110\,\mathrm{mT}$, a large spin wave resonance is observed and at fields between $\mu_0 H_0 = 40\,\mathrm{mT} - 50\,\mathrm{mT}$ some small fast changing resonance are measured. We confirmed that the spin waves with fast changing resonancess are not a non-linear effect by decreasing the microwave power and are not an excitation of higher order harmonics of the microwave source by inserting a low-pass filter after port 1 of the VNA.

We attribute the small background in the µFR-MOKE measurements to spurious signals stemming from free space electromagnetic radiation of the sample, to the mobile network and other microwave signals in free space. The detector and the low-noise amplifier in the µFR-MOKE are placed into a self-made aluminum box with a copper mesh cladded on the walls and the lid of the box to reduce the pick up of such spurious signals by the amplifier.

The measured spectrum of the µBLS shown in Fig. 5.11(c) is completely different as the TFPI periodically changes the mirror spacing and therefore the full frequency response f_{BLS} to a given excitation frequency f_{MW} is obtained as seen in the colormap. The strong signal at $f_{\mathrm{BLS}} = 12\,\mathrm{GHz}$ is the intensity of the spin waves excited at f_{MW}. The weak, almost magnetic field-independent signal around $f_{\mathrm{BLS}} = 14.5\,\mathrm{GHz}$

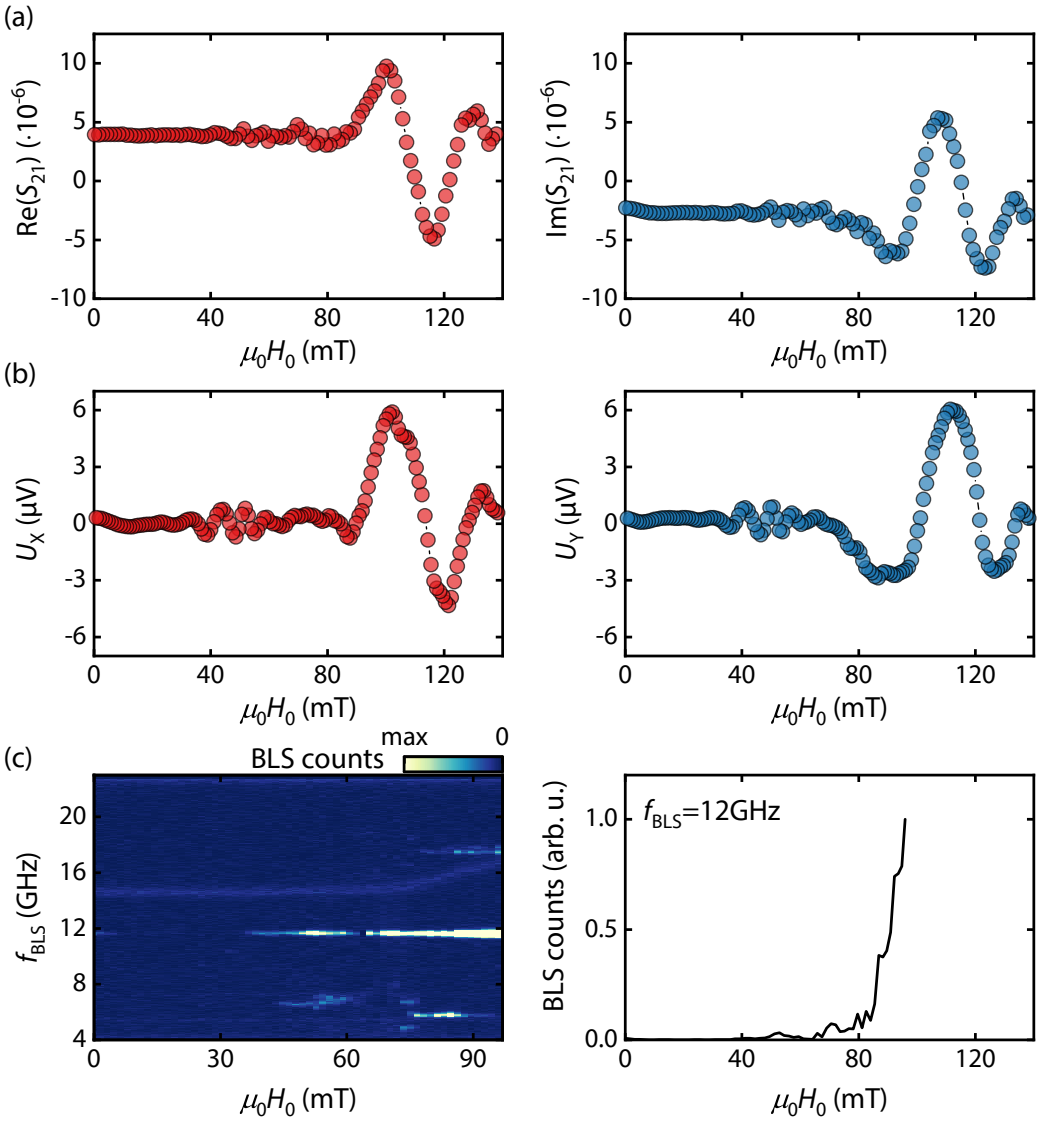

Fig. 5.11. Magnetic field dependence of the (a) real and imaginary part of the complex transmission parameter S_{21} from μFR-MOKE, (b) the real and imaginary part of the lock-in voltage U_{X} and U_{Y}, respectively, from μSNS-MOKE and (c) the photon counts from BLS measurements at microwave frequency $f_{\mathrm{MW}} = 12\,\mathrm{GHz}$ and fixed spot position (cf. Fig. 5.10(a), green circle). For the μBLS measurements the complete frequency f information is retained and not only at the excitation frequency f_{MW}. The non-linear dynamics are discussed in Sec. 5.3.2. Note that for $\mu_0 H_0 > 100\,\mathrm{mT}$ in the μBLS measurements the temperature interlock of the electromagnet triggers as the measurements require to keep the magnetic field constant for a longer period of time.

is due to thermal magnons. As these magnons are thermally excited, the measured signal is proportional to the magnon spectral density $\rho(f)$ described by [168]

$$\rho(f) = D(f)n(f) = \frac{D(f)}{\exp\left(\frac{hf}{k_\mathrm{B}T}\right) - 1}, \tag{5.37}$$

with the Bose-Einstein distribution $n(f)$, the Planck constant h, the Boltzmann constant k_B and the temperature T. The magnon density of states is given by

$$D(f) = \int \frac{\mathrm{d}\boldsymbol{k}}{(2\pi)^3}\delta(f - f(\boldsymbol{k})) \tag{5.38}$$

with the dispersion relation $f(\boldsymbol{k})$ described by the Kalinikos-Slavin equation [Eq. (5.7)]. Due to the large saturation magnetization of $Co_{25}Fe_{75}$ ($M_\mathrm{sat} = 2.36\,\mathrm{T}/\mu_0$ [51]), the demagnetization field produced by the magnonic waveguide is also large $H_\mathrm{d} = -N_{xx}M_\mathrm{sat}$. The magnetization of the thermal magnons is confined along the waveguide and at a magnetic field of $\mu_0 H_0 \simeq 75\,\mathrm{mT}$ the magnetization is tilted along the direction of the magnetic field. To give an estimation of the demagnetization field, we assume that the demagnetization factor N_{xx} is given by the ratio of the $Co_{25}Fe_{75}$ thickness $t_\mathrm{FM} = 50\,\mathrm{nm}$ and the width of the magnonic waveguide w. The demagnetization factor is consequently $N_{xx} = t_\mathrm{FM}/w = 1/30$ as along the magnonic waveguide we do not expect any demagnetization fields. For the demagnetization field, we calculate $\mu_0 H_\mathrm{d} \approx 79\,\mathrm{mT}$ which is in good agreement with the observed behaviour.

The BLS signals at $f_\mathrm{BLS} = 6\,\mathrm{GHz}$ and $f_\mathrm{BLS} = 18\,\mathrm{GHz}$ are due to three-magnon scattering [210] as the applied microwave power P_MW is sufficiently large to drive the system in the non-linear regime. We will discuss this in more detail in Section 5.3.2.

If we take the spectrum at fixed interferometer frequency f_BLS, we get a spectrum as shown in the right panel which can be compared to the other spectroscopy techniques. Note that in BLS the intensity is measured and in FR-MOKE and SNS-MOKE the amplitude of the spin wave susceptibility. The obtained data is in full agreement with each other although the magnetic field in the µBLS is not sufficiently large to compare the full spectrum. This is due to the temperature interlock on the electromagnet that prevents overheating. For the µBLS the magnetic field is fixed for a longer period of time, which causes especially at large magnetic fields $\mu_0|H_0| > 100\,\mathrm{mT}$ a lot of Joule heating. In the µFR-MOKE and µSNS-MOKE measurements this is not an issue as each magnetic field point needs to be measured for only 1 s. The comparison of the magnitude of the spectra will be done later in Section 5.3.2.3. We briefly comment on the signal-to-noise ratio and the measurement time. The µFR-MOKE and µSNS-MOKE measurements have a comparable signal-to-noise ratio at the same measurement time of roughly 35 min. The µBLS instead took more measurement time ($\approx$ 19 h) but features more information because the full

frequency response of the magnonic system at a certain excitation frequency f_{MW} is captured. The signal-to-noise ratio in µBLS crucially depends on the number of averages performed and on the quantum efficiency and dark count rate of the single photodetector.

From these measurements, we observe two pronounced sets of spin wave resonances: The first at magnetic fields of around $\mu_0 H_0 \simeq 100\,\mathrm{mT}$ where we observe a large spin wave resonance and at fields around $\mu_0 H_0 \simeq 45\,\mathrm{mT}$ with small magnitude but fast variation with field. These different behaviours can be attributed to the large demagnetization fields. In the following, we will have a closer look at this behaviour.

5.3.1.2. Spin Wave Propagation Characteristics while Changing the Magnetic Field

In this experiment, the spin wave propagation characteristics are measured while changing the external magnetic field. The measurement scheme is as follows: The magnetic field H_0 is set in the range from $115\,\mathrm{mT}$ to $0\,\mathrm{mT}$ with a step size of $0.7\,\mathrm{mT}$. After the magnetic field is stabilized, the laser spot is scanned along the center of the magnonic waveguide with a step size of roughly $150\,\mathrm{nm}$ and the complex S_{21}-parameter or the lock-in voltage U_i in the µFR-MOKE or µSNS-MOKE measurement are measured, respectively. The microwave frequency is set to the fixed value of $f_{\mathrm{MW}} = 10\,\mathrm{GHz}$. We do not measure in this scheme with the µBLS technique as it is not feasible due to the large required measurement time. For the µSNS-MOKE the frequency offset is $\delta = 10\,\mathrm{kHz}$ resulting in an excitation frequency of $f_{\mathrm{MW}} = 10\,\mathrm{GHz} + \delta$ and a lock-in frequency of $80.01\,\mathrm{MHz}$.

The results are compiled in Fig. 5.12. In the left column the dc voltage of the fast photodetector (µFR-MOKE) and the dc voltage of the “Monitor+” output of the balanced photodetector (µSNS-MOKE) are shown and are a measure of the reflectivity of the sample at the laser spot location. In this regard, we want to briefly discuss the different automated focusing routines established in µFR-MOKE/µBLS and in µSNS-MOKE respectively. In the µFR-MOKE and µBLS we couple (parts of) the laser light into the optical fiber and consequently to the fast photodetector (cf. full optical setup shown in Appendix A.1). Inside the fast photodetector the signal is split into its dc and ac component, where the dc signal is proportional to the laser power coupled into the optical fiber as seen from Eq. (5.28) in the first term. The laser light is most efficiently coupled into the optical fiber if the laser light is perfectly parallel before focused into the fiber. The reflected light from the sample, which is collected by the infinity-corrected microscope objective, is only parallel after the entrance pupil if the laser spot is in focus on the sample. Otherwise the laser light is divergent. By moving the nanopositioners in small steps closer or further away from the microscope objective, we measure the change of the dc voltage detected at

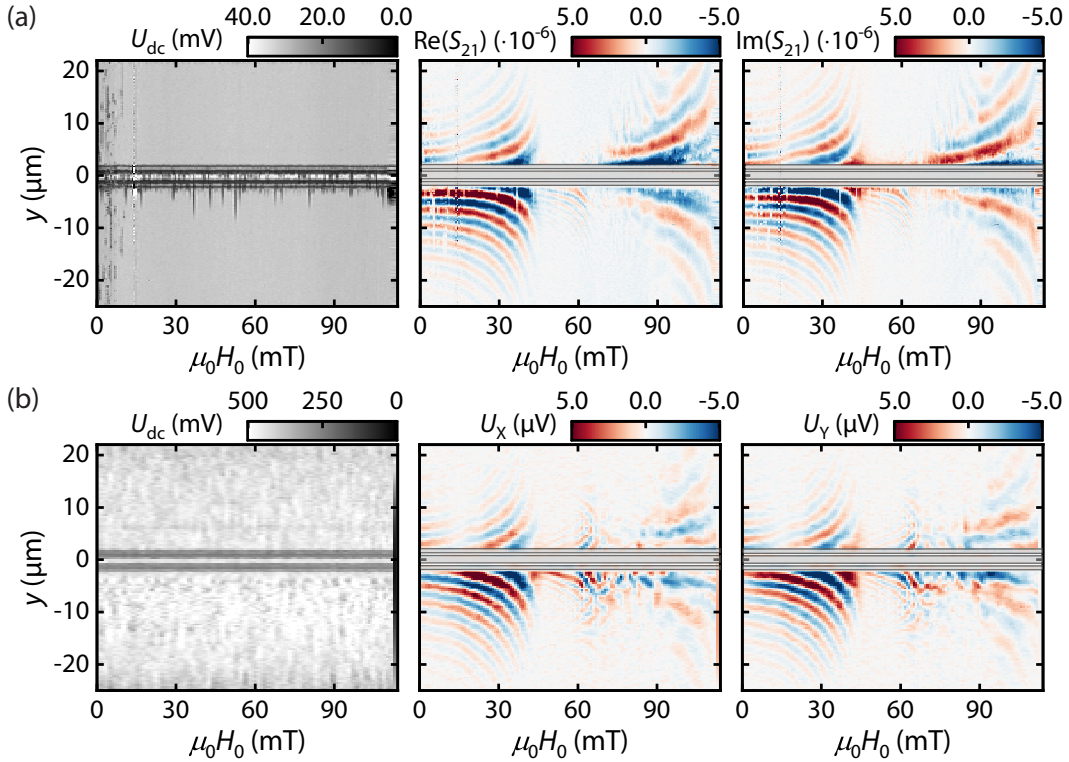

Fig. 5.12. Line scan along the middle of the magnonic waveguide with a combined magnetic field sweep at $f_{\mathrm{MW}} = 10\,\mathrm{GHz}$ using (a) µFR-MOKE and (b) µSNS-MOKE. The left column shows the dc voltage U_{dc} of the respective photodetector which is a measure for the reflectivity. The structure around $y = 0\,\mu\mathrm{m}$ is the antenna structure used for the excitation of the spin waves. The middle and right column show the real and imaginary part (a) of the complex-transmission parameter S_{21} of the µFR-MOKE and (b) of the lock-in voltages U_{X} and U_{Y} of the µSNS-MOKE measurement.

the fast photodetector with a multimeter and maximize the dc signal by moving the sample stage.

In the µSNS-MOKE technique, we cannot use the optical fiber due to the different optical paths (cf. Fig. A.1). Here, we fully rely on image detection. In the imaging acquisition software we select a certain region of the optical image and use pre-defined routines from National Instruments Vision Development Module and determine the "sharpness" of the selected region. We optimize the sharpness of the optical image by moving the sample stage. Additionally, we monitor the voltage of one of the balanced photodetector inputs "Monitor+" to observe differences in the reflected laser light intensity. Note that this routine does not have the same sensitivity to changes in the focus than the auto-focusing routine used in the µFR-MOKE/µBLS, where already small deviations are detectable.

From the changing reflectivity, the antenna can be clearly identified as well as the stability of the software automated focusing routine can be checked. The different scales in the dc voltage between the two measurement techniques is due to the

different electronics in the photodetectors. From the reflectivity, we observe a difference in the resolution between these methods where the µFR-MOKE features a better resolution which is due to the aforementioned smaller spot size on the sample.

In the center and right column in Fig. 5.12, the real and imaginary part of the complex S_{21}-parameter and the lock-in voltage U_i are shown. In the measured spectra two main features are observed: The spin wave dynamics can be divided into three distinct regions. The first region at large magnetic fields between $\mu_0 H_0 \simeq 75\,\mathrm{mT} - 115\,\mathrm{mT}$, where we observe spin waves in the Damon-Eshbach regime ($\boldsymbol{M} \perp \boldsymbol{k}$). As discussed in the previous section, the magnetic field H_0 is large enough to overcome the demagnetization field H_d. The second regime is between $\mu_0 H_0 \simeq 45\,\mathrm{mT} - 75\,\mathrm{mT}$ and the third regime between $\mu_0 H_0 \simeq 0\,\mathrm{mT} - 45\,\mathrm{mT}$, where spin waves in an intermediate configuration between backward-volume and Damon-Eshbach, and in the backward-volume regime are excited. Especially interesting is the second regime, where spin waves with small wavelengths are excited. This is a consequence of the large demagnetization fields as the magnetization is pointing at low magnetic fields along the magnonic waveguide and with increasing magnetic field starts to rotate towards the external magnetic field $\boldsymbol{H}_0$ perpendicular to the waveguide because this is a magnetic hard axis. Between these two extreme cases the spin waves are neither backward-volume nor Damon-Eshbach modes but in an intermediate state, which can be calculated using the Kalinikos-Slavin equation [Eq. (5.7)] by first determining the equilibrium position parameterized by the in-plane angle ϕ of the magnetization at a given magnetic field strength.

The second feature is the different amplitude above and below the antenna. This spin wave non-reciprocity of the spin wave amplitude is most prominently seen for the Damon-Eshbach spin waves which are surface modes and is attributed to the antenna non-reciprocity. The physical origin for this non-reciprocity is the relative orientation of the spin wave wavevector and the external magnetic field leading to different coupling efficiencies of the microwave field of the antenna to the dynamic magnetization of the spin wave [211, 212].

In a more quantitative approach, the propagation properties of the coherently excited spin waves are extracted by considering the spatial-dependence of the complex S_{21}-parameter and the lock-in voltage U_i at fixed magnetic field H_0. Exemplary spectra at $\mu_0 H_0 \approx 26.5\,\mathrm{mT}$ for both measurement techniques are shown in Fig. 5.13. The grey points represent the measured data from Fig. 5.12 and show an oscillating behaviour corresponding to the wavefronts of the spin wave superimposed with an exponential decay due to the finite damping in the system. Due to the phase-sensitivity of both spectroscopy technique, it is possible to extract the wavevector k and spin wave propagation length ξ_sw by fitting the µFR-MOKE data to [160]

$$S_{21}(y) = A \cdot \exp\left(-\frac{y}{\xi_\mathrm{sw}}\right) \cdot e^{iky+\phi} + C_0, \tag{5.39}$$

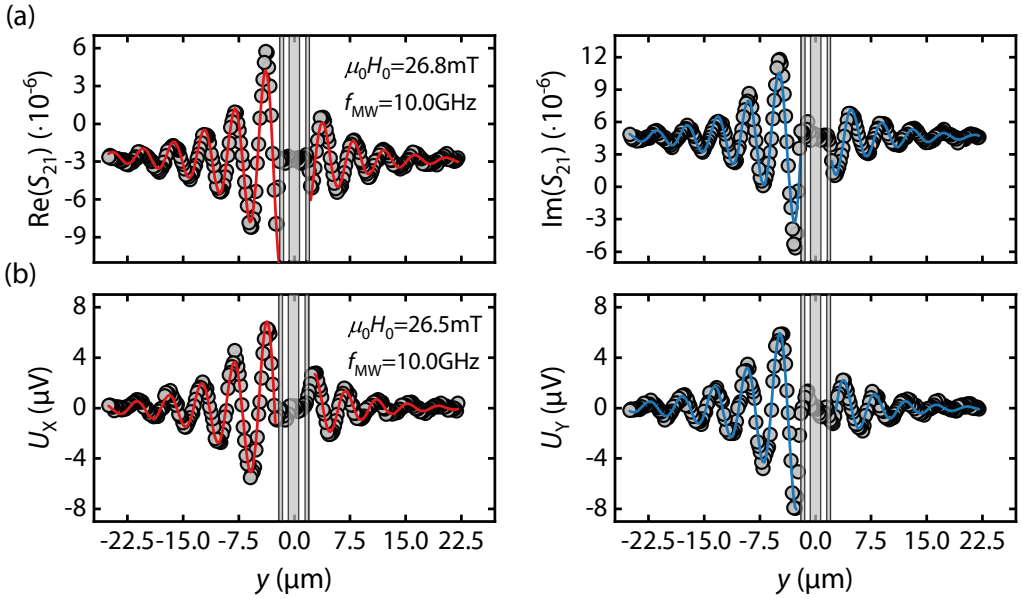

Fig. 5.13. Line scans of the (a) µFR-MOKE and (b) µSNS-MOKE signal shown in Fig. 5.12 along the y-axis at fixed magnetic field $\mu_0 H_0 \approx 26.5\,\mathrm{mT}$. The grey points are the measured data. The solid red and blue lines are the fits to the real and imaginary part, respectively, by using Eq. (5.39) in (a) for the µFR-MOKE and Eq. (5.40) in (b) for the µSNS-MOKE data.

with an amplitude parameter A, a phase factor ϕ and a complex offset C_0. The µSNS-MOKE data is equivalently fitted with [41]

$$\begin{aligned} U_X(y) &= B \cdot \exp\left(-\frac{y}{\xi_{\mathrm{sw}}}\right) \cdot \cos\left(ky + \phi'\right) + C_{0X}, \\ U_Y(y) &= B \cdot \exp\left(-\frac{y}{\xi_{\mathrm{sw}}}\right) \cdot \sin\left(ky + \phi'\right) + C_{0Y}, \end{aligned} \tag{5.40}$$

where B is the amplitude, ϕ' a phase factor, and C_{0X} and C_{0Y} are offset parameters. The real and imaginary part of S_{21} and of the lock-in voltages U_X and U_Y are fitted simultaneously with the equations above but data to either side of the antenna is fitted separately. The solid lines in Fig. 5.14 show the fits to the data.

This procedure is repeated for all available magnetic fields H_0. The extracted fit parameters, namely the wavevector k and propagation length ξ_{sw} of the spin wave, are shown in Fig. 5.14. In the magnetic field-dependence of the wavevector we observe again the aforementioned three different spin wave regimes. Especially in the second regime $\mu_0 H_0 \simeq 45\,\mathrm{mT} - 75\,\mathrm{mT}$ we find large wavevectors up to $|k| \leq 4.1\,\mu\mathrm{m}^{-1}$ while in the other two regimes (lower backward volume and Damon-Eshbach spin waves) the wavevectors are $|k| \leq 2.0\,\mu\mathrm{m}^{-1}$. The reason for this behaviour is as already mentioned the changing magnetization direction in the magnonic waveguide from parallel to the waveguide to perpendicular with increasing magnetic field due to the large demagnetization fields. The spin wave propagation length for the backward

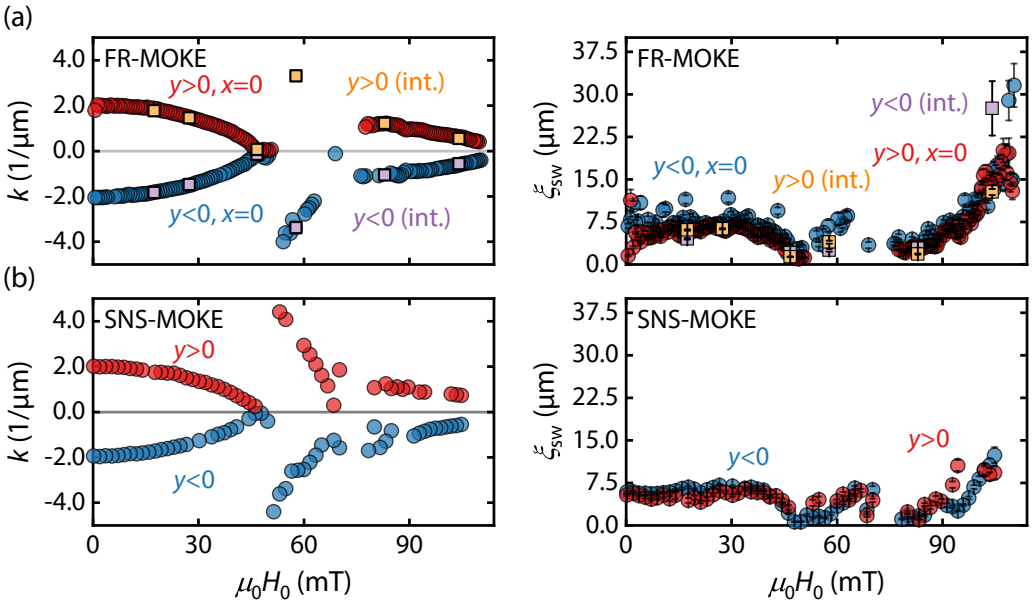

Fig. 5.14. Extracted wave vector of the spin wave k and spin wave propagation length ξ_{sw} as a function of the magnetic field H_0 from the line scans at fixed microwave frequency $f_{\mathrm{MW}} = 10\,\mathrm{GHz}$ with combined magnetic field sweep shown in Fig. 5.12 for (a) the µFR-MOKE and (b) the µSNS-MOKE measurements. The orange and purple square symbols are the results from the spatial xy-scans (cf. Section 5.3.1.3), where the signal is integrated over the width w of the magnonic waveguide and then fitted. The error bars for the wavevector k are smaller than symbol size.

volume mode in the magnetic field range $\mu_0 H_0 \simeq 0\,\mathrm{mT} - 75\,\mathrm{mT}$ is on average $\bar{\xi}_{\mathrm{sw}} = (7 \pm 1)\,\mu\mathrm{m}$. In the Damon-Eshbach regime $\mu_0 H_0 \gtrsim 75\,\mathrm{mT}$ the propagation length increases up to a large value of $\xi_{\mathrm{sw}} \approx 30\,\mu\mathrm{m}$ for spin waves with a large wavelength, which is compatible with the findings in Ref. [51]. Due their larger group velocity the Damon-Eshbach surface modes are expected to have a larger propagation length.

At this point we want to emphasize that this measurement scheme, where we measure the magnetic field dependence of the spin wave propagation length and the wavevector by scanning the laser spot through the center of the magnonic waveguide, can give misleading results. From earlier observations [160, 166, 213] it is known for spin waves in patterned waveguides to have a multimode character. This is explained by the restricted possible wavevectors in the sample plane $\boldsymbol{k} = [k_x\ k_y]^{\intercal}$. Along the (in our case) x-direction, the wavevector k_x can take values $k_x^n = n\pi/w$ with $n \in \mathbb{N}$ in the limit $t_{\mathrm{FM}} \ll w$ due to the formation of resonant standing waves in the direction perpendicular to the waveguide [166]. In an extended film, the wavevectors k_x and k_y can both change continuously.

In order to observe this multimode character, we will perform spatial xy-scans of the magnonic waveguide at fixed microwave frequency and magnetic field in the following section.

5.3.1.3. Spatial Propagation Characteristics of Spin Waves

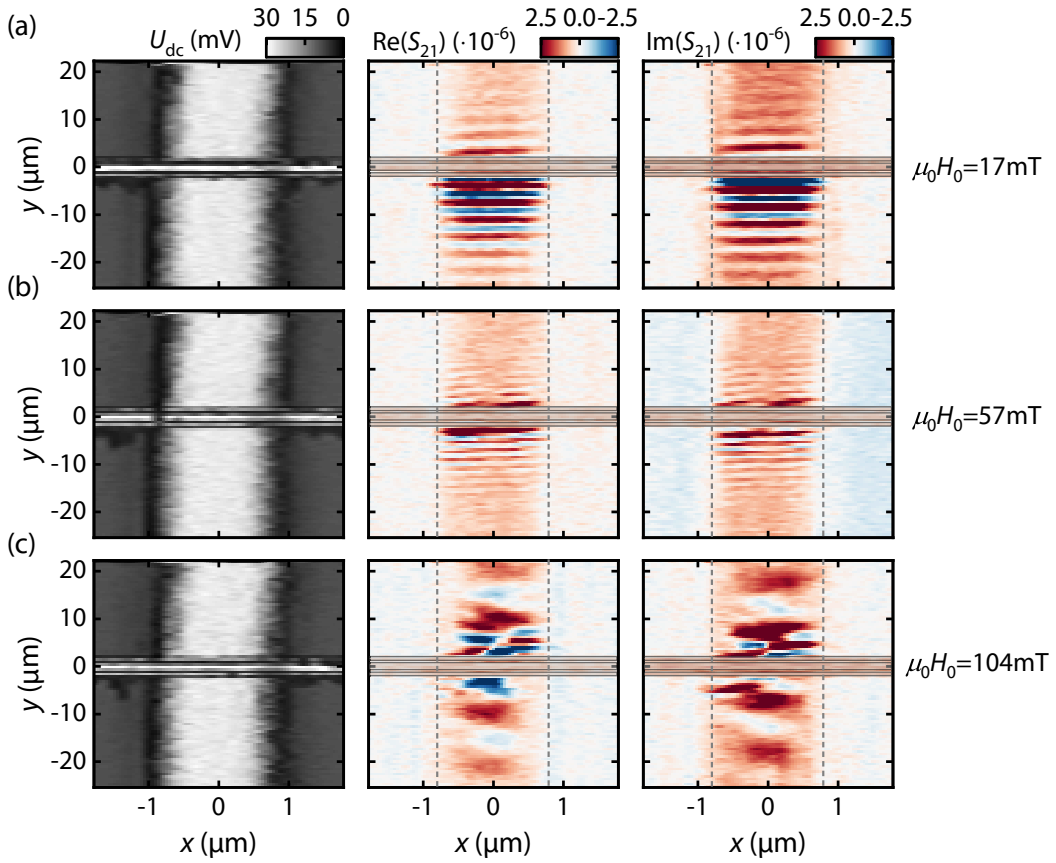

Fig. 5.15. Two-dimensional spatial maps obtained by scanning the laser spot across the magnonic waveguide at fixed microwave frequency $f_{\mathrm{MW}} = 10\,\mathrm{GHz}$ and fixed magnetic fields (a) $\mu_0 H_0 = 17\,\mathrm{mT}$, (b) $\mu_0 H_0 = 57\,\mathrm{mT}$ and (c) $\mu_0 H_0 = 104\,\mathrm{mT}$ using µFR-MOKE spectroscopy. In the left column the dc-voltage of the photodiode U_{dc}, which is a measure of the reflectivity at the laser spot position, is shown. In the middle and right column the real and imaginary parts of the complex S_{21}-parameter are shown. The dashed grey lines indicate the width of the magnonic waveguide extracted from the reflectivity measurements shown in the left column.

In this experiment, we resolve the wavefronts of the spin waves in the magnonic waveguide by performing a spatial 2D scan using the µFR-MOKE technique. The laser spot is scanned in the xy-plane with a step size of roughly $140\,\mathrm{nm}$ along both directions. The "fast" scan axis during the experiment is the y-direction. The microwave frequency is fixed to $f_{\mathrm{MW}} = 10\,\mathrm{GHz}$ and the magnetic field is fixed to certain field magnitudes. Exemplary colormaps of the spatial-dependence of the complex S_{21}-parameter measured with µFR-MOKE spectroscopy are shown in Fig. 5.15. In the left column U_{dc} of the fast photodetector is shown, which is proportional to the reflectivity of the sample. From the reflectivity data we can clearly distinguish between the magnonic waveguide and the substrate due to the much smaller reflectivity of the Si/SiOx-substrate. From these measurements we determine

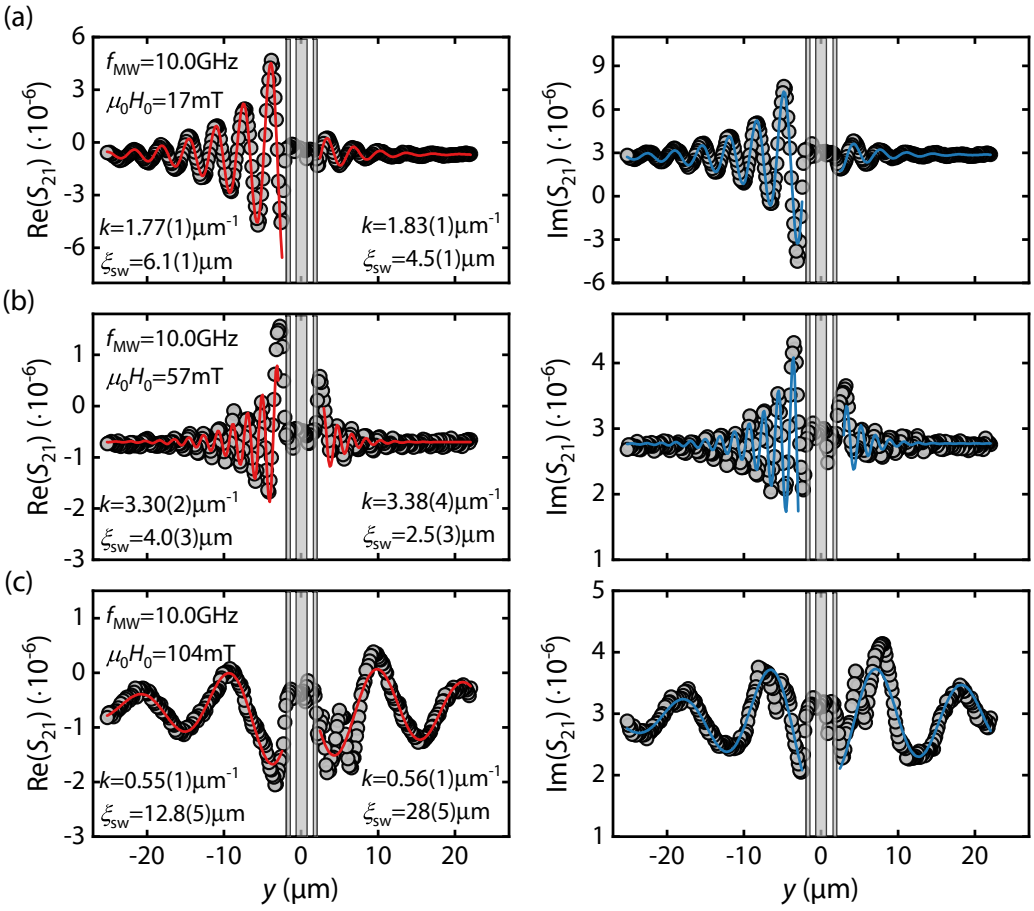

Fig. 5.16. Linescan obtained by averaging the data over the data shown in Fig. 5.15 averaged over the width of the magnonic waveguide at fixed microwave frequency $f_{\mathrm{MW}} = 10\,\mathrm{GHz}$ and fixed magnetic fields (a) $\mu_0 H_0 = 17\,\mathrm{mT}$, (b) $\mu_0 H_0 = 57\,\mathrm{mT}$ and (c) $\mu_0 H_0 = 104\,\mathrm{mT}$. The points are the averaged data points and the solid red and blue lines are the fits to the real and imaginary part respectively by using Eq. (5.39).

the optical width of the magnonic waveguide and indicate them with dashed grey lines into the data shown in the middle and right column, where the real and imaginary part of the S_{21}-parameter are shown.

The magnetic fields H_0 in Fig. 5.15 are chosen so that the different regimes discussed in the previous Section 5.3.1.2 can be investigated. In panel (a) and (b) the wavefronts of the spin waves are resolved due to the phase-sensitive measurement enabled by the heterodyne detection scheme of the VNA. For a magnetic field of $\mu_0 H_0 = 57\,\mathrm{mT}$ as shown in panel (b), the distance of the wavefronts is reduced drastically corresponding to a smaller wavelength λ of the spin wave. In Fig. 5.15(c) the spin waves are in the Damon-Eshbach regime and the wavefronts of the spin waves become distorted. This is due to the aforementioned multimode character of the spin waves [160, 166, 213], which can be clearly resolved with the µFR-MOKE technique. We speculate that the signal next to the magnonic waveguide

and therefore coming from the substrate is from some spurious effects where small deviations in the laser light intensity are observed.

For the analysis of the wavevector k and propagation length ξ_{sw} the signal is averaged over the width of the waveguide marked by the dashed grey lines in Fig. 5.15 along the x-direction. The resulting real and imaginary part of the S_{21}-parameter are shown in Fig. 5.16. We perform the same fitting procedure as in the section before, and fit $\mathrm{Re}(S_{21})$ and $\mathrm{Im}(S_{21})$ simultaneously to Eq. (5.39). The extracted fit parameters for the wavevector k and propagation length ξ_{sw} for the two respective sides of the antenna are denoted in the panels. For comparison, these values are added to the results in Fig. 5.14 as orange and purple symbols. We find good agreement between these two different detection schemes, although there are some deviations especially in the propagation length. This is attributed to the multimode character of the spin waves mainly due to the presence of the second and third transverse modes [160, 166, 213]. We want to emphasize that when extracting the propagation length ξ_{sw}, a single linescan along the magnonic waveguide can lead to different results compared to a full 2D map. To overcome this problem, the width of the magnonic waveguide can be reduced to roughly the spot size of the laser. In this case, a single measurement the laser spot then averages over the multiple modes.

5.3.1.4. Mapping the Dispersion Relation of Spin Waves

In the previous two sections, we discussed the dynamics of spin waves at fixed microwave frequency f_{MW}, changed the magnetic field and consequently the magnetization state. In this experiment, we perform the same measurement procedure as in Section 5.3.1.2 but keep the magnetic field H_0 fixed and change the microwave frequency in the range $f_{\mathrm{MW}} = 6\,\mathrm{GHz} - 16\,\mathrm{GHz}$ with a step size of $100\,\mathrm{MHz}$. For each frequency, the laser spot is scanned along the center of the magnonic waveguide and the complex S_{21}-parameter is measured using µFR-MOKE technique. For the magnetic fields H_0 we choose three different field magnitudes in order to investigate each of the three different regime.

The measured spectra are shown in Fig. 5.17. In the left column again the reflectivity, given by the dc voltage U_{dc} of the fast photodetector, is shown. In the center column the real part of the S_{21}-parameter as measured by the VNA is depicted. Due to the changing microwave frequency f_{MW} the transmission through the microwave cables changes. Additionally, the phase alters due to electrical length of the cables and the optical path. The signal originating from the magnetization dynamics is superimposed by the large microwave background. In order to eliminate the background,

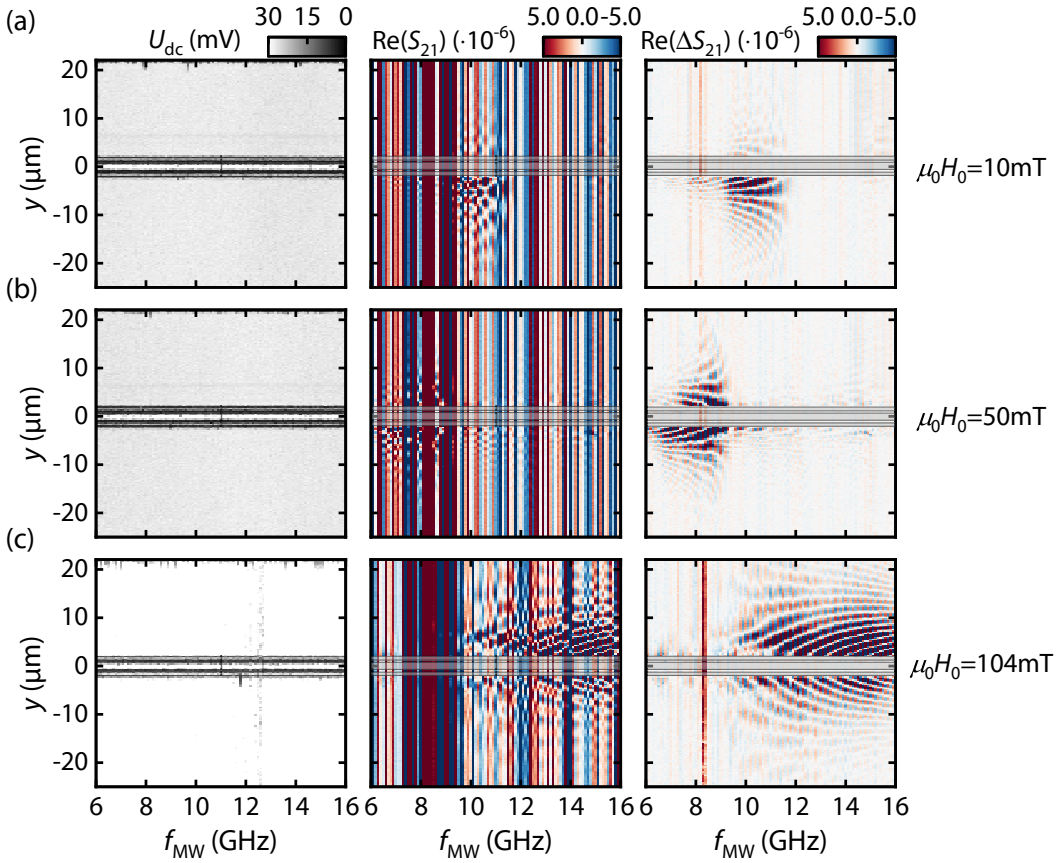

Fig. 5.17. Line scans along the middle of the magnonic waveguide recorded for different microwave frequencies f_{MW} at fixed magnetic fields (a) $\mu_0 H_0 = 10\,\mathrm{mT}$, (b) $\mu_0 H_0 = 50\,\mathrm{mT}$ and (c) $\mu_0 H_0 = 104\,\mathrm{mT}$ using µFR-MOKE spectroscopy. The left column shows the dc-voltage U_{dc} of the respective photodetector, which is a measure for the reflectivity. The middle column shows the measured real part of the complex-transmission parameter S_{21}. The right column is the real part of the microwave-background corrected ΔS_{21}.

we use the fact that the microwave background has no spatial-dependence while scanning the laser spot. We therefore calculate

$$\Delta S_{21}(f,y) = S_{21}(f,y) - S_{21}(f,y_0)|_{y_0=\mathrm{fixed}}, \tag{5.41}$$

where each frequency trace of S_{21} at every laser spot position y is subtracted by a frequency trace of S_{21} typically at spot location y_0 where no signal from the sample is expected. In our case, y_0 is set to $y_0 = -25\,\mu\mathrm{m}$. The resulting frequency and spatial-dependence of the real part of ΔS_{21} is shown in Fig. 5.17 in the right column. This background-subtraction method can lead to artifacts as seen in Fig. 5.17(c) at $f_{\mathrm{MW}} \approx 8.2\,\mathrm{GHz}$.

From these spectra it is now possible to extract the magnon dispersion. In this sense, we repeat the fitting procedure as discussed in Section 5.3.1.2 and fit at fixed

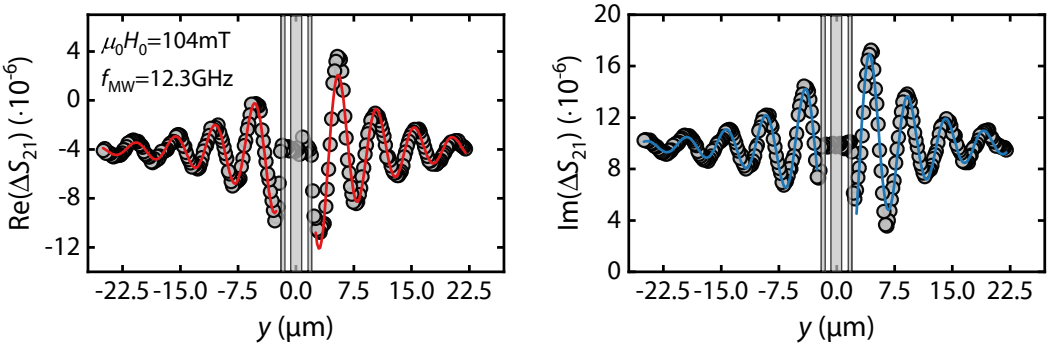

Fig. 5.18. Exemplary spatial y-dependence of the measurement data shown in Fig. 5.17(c) at fixed magnetic field $\mu_0 H_0 \approx 104\,\mathrm{mT}$ and microwave frequency $f_{\mathrm{MW}} = 12.3\,\mathrm{GHz}$. The points are the measured data points and the solid red and blue lines are the fits to the real and imaginary part, respectively, by using Eq. (5.39).

microwave frequencies f_{MW} the spatially dependent S_{21}-parameter as exemplarily shown for $\mu_0 H_0 = 104\,\mathrm{mT}$ and $f_{\mathrm{MW}} = 12.3\,\mathrm{GHz}$ in Fig. 5.18. The real and imaginary part of S_{21} are fitted simultaneously to Eq. (5.39) for each side of the antenna. From these fits the wavevector k and the propagation length ξ_{sw} are extracted.

The fitted wavevector k and the propagation length ξ_{sw} as a function of the microwave frequency f_{MW} are shown in Fig. 5.19. For $\mu_0 H_0 = 10\,\mathrm{mT}$ (panel (a)), we observe a negative dispersion ($\partial k/\partial f < 0$) as expected for a backward-volume-like spin wave mode as discussed in Section 5.1. In the second regime, where $\mu_0 H_0 = 50\,\mathrm{mT}$ (panel (b)), we find three different spin wave modes with increasing microwave frequency f_{MW}. We emphasize again that here we expect neither a clear backward-volume mode nor a Damon-Eshbach mode as the magnetization is in an intermediate state. Also here we find that we can excite and detect short wavelength spin waves close to the optical diffraction limit. In the last case, where we are in the Damon-Eshbach regime (panel (c)), we find a positive dispersion ($\partial k/\partial f > 0$) as expected from theory (cf. Chapter 5.1). The discrepancy in the propagation length ξ_{sw} between the different measurement schemes is attributed to the multimode character of the spin waves as a single linescan can lead to slightly different values (cf. Section 5.3.1.3).

5.3.2 Spin Wave Dynamics in the Non-Linear Regime

In this section, the focus of the magnetization dynamics of spin waves is shifted to the non-linear regime, which has been extensively studied in previous works focusing on the context of multi-magnon scattering [214]. These non-linear processes are often related to Suhl instabilities [215]. Previously, these non-linear processes have been investigated using BLS [161, 216–219] or TR-MOKE techniques. Especially

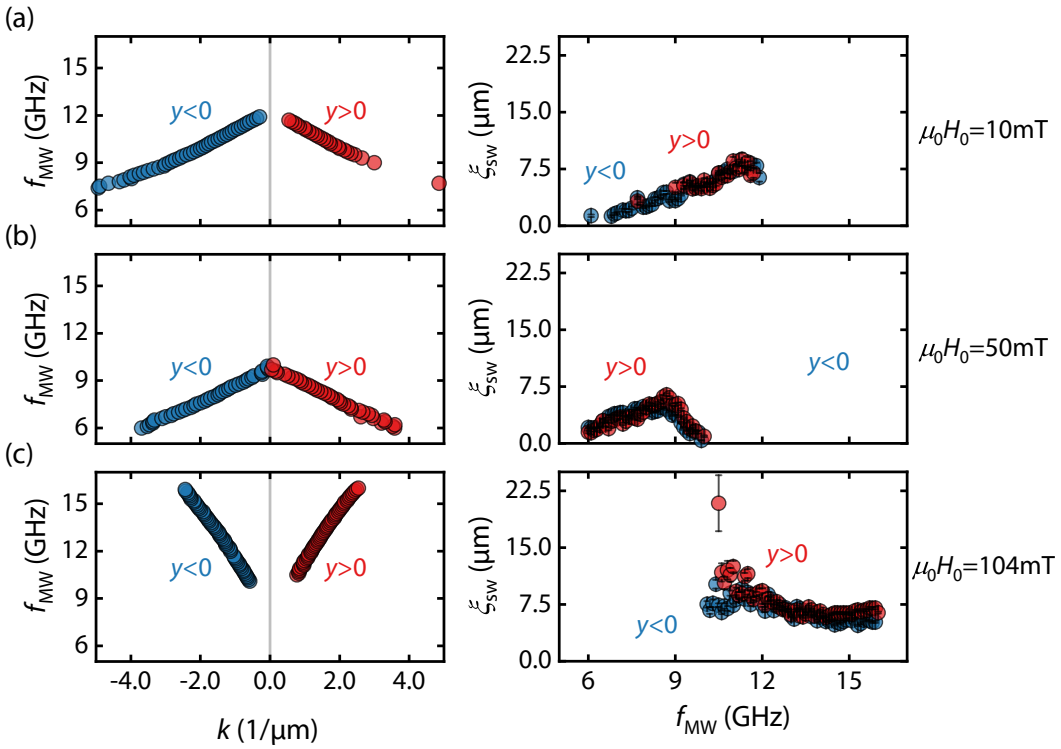

Fig. 5.19. Extracted wave vector of the spin wave k and spin wave propagation length ξ_{sw} as a function of the microwave frequency f_{MW} from the line scans with combined magnetic field sweep shown in Fig. 5.17 for magnetic fields (a) $\mu_0 H_0 = 10\,\mathrm{mT}$, (b) $\mu_0 H_0 = 50\,\mathrm{mT}$ and (c) $\mu_0 H_0 = 104\,\mathrm{mT}$ with µFR-MOKE spectroscopy. The error bars for the wavevector k are smaller than symbol size.

the BLS technique allows to investigate the frequency response of the magnetic system at a different frequency compared to the excitation frequency. The aim of this section is to test the capabilities of the µFR-MOKE technique and utilize the heterodyne detection scheme of the VNA. This section will be structured as follows: First, we will perform some preliminary µBLS measurements to get a first intuition of the physical processes of the system. Then, we will use the µFR-MOKE and µSNS-MOKE technique and capture the non-linear response of the system. Finally, we will perform 2-tone spectroscopy with the µFR-MOKE technique by applying two different excitation frequencies where one excites the system non-linearly and a second microwave to probe the system.

5.3.2.1. Power-dependence of the Spin Wave Response

For a first intuition, we perform µBLS spectroscopy measurements at fixed magnetic field $\mu_0 H_0 = 104\,\mathrm{mT}$ and microwave frequency $f_{\mathrm{MW}} = 12\,\mathrm{GHz}$ by locating the laser spot roughly $4.5\,\mu\mathrm{m}$ away from the microwave antenna as indicated by the green circle in Fig. 5.10(a). For this external magnetic field strength, the equilibrium magne-

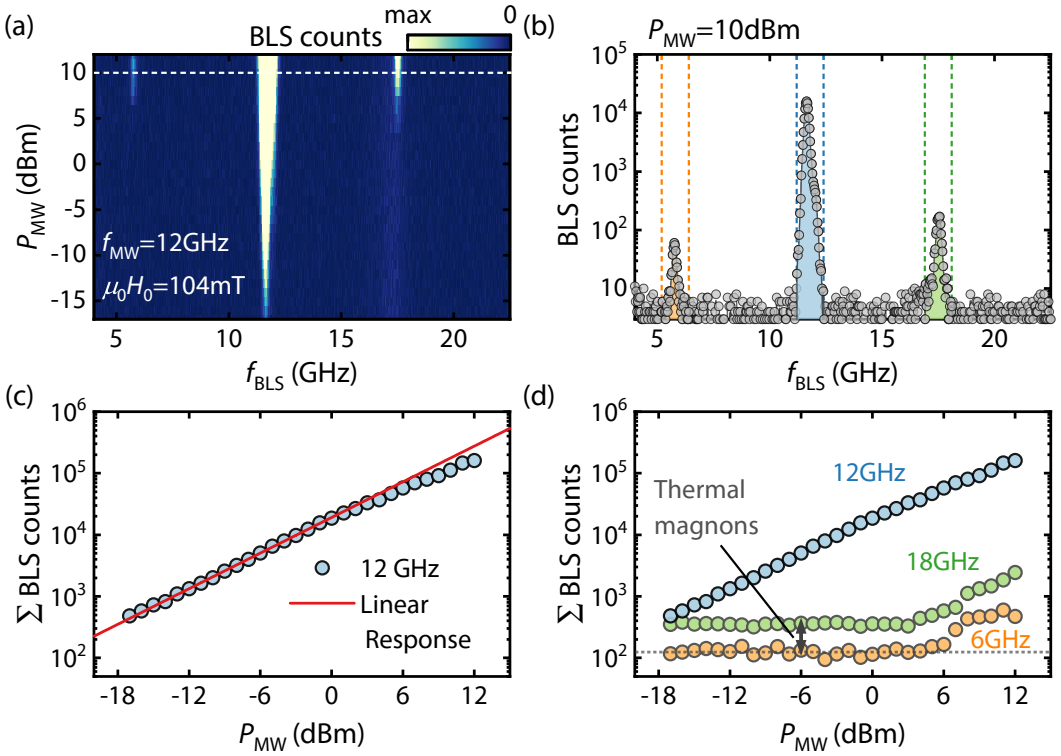

Fig. 5.20. Power sweep P_{MW} at fixed spot position (cf. Fig. 5.10(a), green spot), magnetic field $\mu_0 H_0 = 104\,\mathrm{mT}$ and microwave frequency $f_{\mathrm{MW}} = 12\,\mathrm{GHz}$ in a µBLS spectroscopy measurement. (a) Color-coded BLS counts as a function of the microwave power P_{MW} and interferometer frequency f_{BLS}. (b) Exemplary BLS spectrum as a function of the interferometer frequency f_{BLS} at fixed microwave power $P_{\mathrm{MW}} = 10\,\mathrm{dBm}$ as indicated by the dashed white line in (a). The dashed vertical lines indicate the region of interests with a width of 1.2 GHz, where the BLS counts are summed up. (c) Integrated BLS counts around the excitation frequency $f = 12\,\mathrm{GHz}$ as a function of the excitation power. The solid red line indicates the expected linear response which deviates from the data at large microwave power P_{MW}. (d) Integrated BLS counts at $f_{\mathrm{BLS}} = 6\,\mathrm{GHz}$ and $f_{\mathrm{BLS}} = 18\,\mathrm{GHz}$ corresponding to half and three half of the excitation frequency f_{MW}, respectively. The difference at low microwave powers P_{MW} is attributed to incoherent thermal magnons.

tization is oriented orthogonal to the magnonic waveguide (see Section 5.3.1.2). The microwave power is changed in the range $-17\,\mathrm{dBm} \leq P_{\mathrm{MW}} \leq 12\,\mathrm{dBm}$ with a step size of $1\,\mathrm{dBm}$ and the number of TFPI averages is set to 1500. The measured μBLS spectrum is shown in Fig. 5.20(a). At $f_{\mathrm{BLS}} = 12\,\mathrm{GHz}$, we find the linearly excited spin wave resonance with an increasing BLS intensity with increasing microwave power P_{MW}.[4] Around $f_{\mathrm{BLS}} = 17\,\mathrm{GHz}$, we find the thermally excited magnons, which are independent of the microwave power and can be seen as an enhanced background in the spectrum. At $P_{\mathrm{MW}} \approx 6\,\mathrm{dBm}$, additional stronger signals are observed at $f_{\mathrm{BLS}} = 6\,\mathrm{GHz}$ and $f_{\mathrm{BLS}} = 18\,\mathrm{GHz}$ corresponding to $f/2$ and $3f/2$ of the coherently excited spin wave at $f = f_{\mathrm{MW}}$. As we will see in the next section, these modes correspond to non-linearly excited spin waves due to three-magnon scattering processes [34, 210].

To get a quantitative understanding, we consider the BLS spectra at fixed microwave power P_{MW} as exemplarily shown for $P_{\mathrm{MW}} = 10\,\mathrm{dBm}$ in Fig. 5.20(b). For the power dependence of the BLS counts we define a region-of-interest (ROI) with a width of $1.2\,\mathrm{GHz}$ and sum up the BLS counts around $f_{\mathrm{BLS}} = 6\,\mathrm{GHz}$, $f_{\mathrm{BLS}} = 12\,\mathrm{GHz}$ and $f_{\mathrm{BLS}} = 18\,\mathrm{GHz}$, respectively, as indicated by dashed vertical lines. The summed up BLS counts are represented by the coloured area under the BLS counts.

The integrated BLS counts as a function of the microwave power P_{MW} are shown in Figs. 5.20(c) and (d). In panel (c) the power-dependence of the coherently excited magnons at $f = f_{\mathrm{MW}}$ is depicted. Fitting a linear function in the region $-18\,\mathrm{dBm} \leq P_{\mathrm{MW}} \leq 0\,\mathrm{dBm}$ to the data on the double-logarithmic scale, we extract a slope of 0.96 ± 0.01, which is close to the expected value of 1. Correspondingly, this results in an increase of counts by a factor of 9.6 when the microwave power P_{MW} is increased by one order of magnitude. Up to $P_{\mathrm{MW}} \simeq 3\,\mathrm{dBm}$ the integrated BLS counts follow the linear trend with increasing excitation power. Above this value, the data starts to deviate from the linear function, indicating non-linear processes to start to take place. From the power dependence of the frequencies $f_{\mathrm{BLS}} = 6\,\mathrm{GHz}$ and $f_{\mathrm{BLS}} = 18\,\mathrm{GHz}$ shown in panel (d), we can determine a threshold where the integrated BLS counts start to increase compared to the background counts. We determine a threshold power for the non-linear processes of approx. $5\,\mathrm{dBm}$. For the magnons around $f_{\mathrm{BLS}} = 6\,\mathrm{GHz}$ the integrated BLS counts do not increase further with excitation power. The difference in the background between $6\,\mathrm{GHz}$ and $18\,\mathrm{GHz}$ is due to the thermal magnons at around $f_{\mathrm{BLS}} = 17\,\mathrm{GHz}$.

[4] The power P_{MW} describes the applied microwave power by the microwave source or vector network analyzer. The microwave power at the on-chip antenna, which is proportional to the Oersted field generated by the microwave to excite the dynamics of the spin waves, is lower due to losses in the microwave cables, bond wires, impedance mismatch etc. The relevant quantity to describe the excitation power of the spin wave dynamics is the m_z-component of the magnetization, which is challenging to quantify.

5.3.2.2. Three-Magnon Scattering of Spin Waves

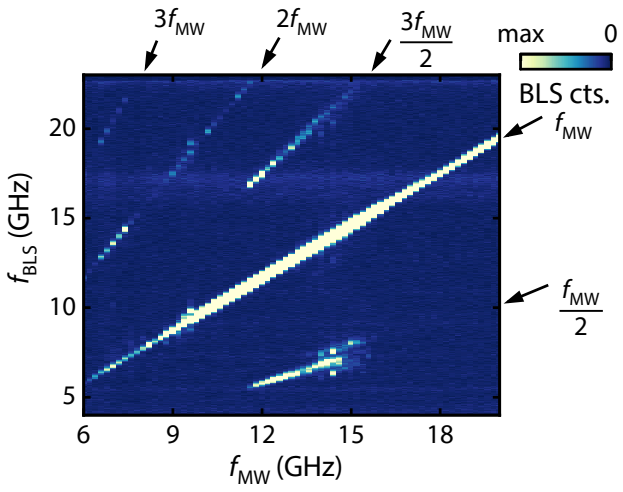

Fig. 5.21. BLS intensity plotted as a function of the microwave frequency f_{MW} and f_{BLS} measured at fixed spot position (cf. Fig. 5.10(a), green spot), magnetic field $\mu_0 H_0 = 104\,\mathrm{mT}$ and excitation power $P_{\mathrm{MW}} = 10\,\mathrm{dBm}$.

As a second preliminary experiment, we measure with the μBLS at the same laser spot position as before (cf. Fig. 5.10(a), green spot) and set the microwave power fixed to $P_{\mathrm{MW}} = 10\,\mathrm{dBm}$. The magnetic field is adjusted to $\mu_0 H_0 = 104\,\mathrm{mT}$ and the excitation frequency is changed in the range $6\,\mathrm{GHz} \leq f_{\mathrm{MW}} \leq 20\,\mathrm{GHz}$ with a step size of 200 MHz. The measured BLS spectrum is shown in Fig. 5.21 with the BLS counts colorcoded as a function of the TFPI frequency f_{BLS} and the excitation frequency f_{MW}. The strong diagonal signal are stemming from spin waves directly excited at the microwave frequency $f_{\mathrm{BLS}} = f_{\mathrm{MW}}$.

Besides this strong signal, additional signals originating from spin waves generated as the system is driven in the non-linear regime. These non-linear effects generate spin waves with integer multiple frequencies $(2f, 3f, \ldots)$ and non-integer frequencies $(f/2, 3f/2, \ldots)$. For the generation of modes with $f/2$ and $2f$ the dominant process is the so-called three-magnon scattering [210] where one magnon excited at f_{MW} generates two magnons f_1 and f_2 under the conservation of momentum and energy $(f_1 + f_2 = f_{\mathrm{MW}})$. The lower threshold frequency for the $f/2$-mode is determined by the bottom of the spin wave band. Spin wave irradiation (multi-magnon scattering effects) is observed at combination frequencies $3f/2$, $3f$ etc. [210]. The next higher-order process is the four-magnon scattering, where two magnons excited at f_{MW} scatter into two magnons [161, 217]. This process is not observed, which would be indicated by a significant broadening around f_{MW}, because the applied microwave power is presumably slightly too low to observe this process and due to the selected large scanning region of the interferometer.

From these preliminary μBLS experiments we find our low-damping $Co_{25}Fe_{75}$ system in the non-linear regime and correspondingly observe non-linear effects, mainly three-magnon scattering. The idea is now to measure the three magnon scattering using μFR-MOKE and μSNS-MOKE. Before discussing our data, we need to make ourselves familiar with the functional principle of a VNA.

5.3.2.3. Detecting the Non-linear Response of Spin Waves by VNA-based Optical Spectroscopy

The μBLS technique has itself established as a reliable spectroscopy technique to measure non-linearities. The crucial part is the tandem Fabry-Pérot interferometer, which works as a frequency analyzer and allows to freely adjust the frequency within the free-spectral-range of the TFPI. In the μFR-MOKE, this is different due to the usage of a vector network analyzer (VNA). A schematic electrical diagram of the VNA is shown in Fig. 5.22. A thorough discussion of the working principle of a VNA can be found in Ref. [95]. The VNA has a microwave source (Src) generating a microwave with a certain frequency f_{MW}, which is either sourced at port 1 (P1) or port 2 (P2). The generated microwave is partially coupled into the reference port (Ref1/2) through a directional coupler. The reflected and transmitted microwave through the device under test (connected to P1 and P2) are coupled to the detector port (Det1/2). Note that the detector and reference ports are internal ports and not directly accessible.

The VNA uses a heterodyne detection scheme, which means that the signal is (generally) downconverted to an intermediate frequency f_{IF} (IF), which is different from the excitation frequency f_{MW} using the tunable local oscillator (LO) with frequency f_{LO}. The downconversion fully retains the phase information of the original signal. The downconverted IF signal is then bandpass-filtered (adjustable by the IF bandwidth), amplified, and digitized. A subsequent I/Q-demodulation of the digitized signal is performed to calculate the S-parameters [Eq. (3.7)] [95]. To retain the phase information, it is necessary to synchronize the LO and the microwave source to prevent additional phase shifts due to the downmixing of the signals. For this purpose, a phase-locked loop (PLL) is used, where the microwave source and the LO are synchronized to a reference oscillator (typically quartz oscillator). With changing the microwave frequency also the reference receivers are shifted in frequency due to the PLL. Before each measurement the local oscillator (LO) is reset, which ensures that the phase of the generated wave starts from zero again.

When investigating frequency-translating devices (FTDs) the frequency response is shifted relative to the stimulating frequency f_{MW}. The large dynamical range of the VNA is achieved by tuning the receivers in a narrow frequency range of the stimulus signal. To evaluate a signal with a frequency different from f_{MW}, the receiver frequency needs to be independently tuned from the microwave source [220]. In the

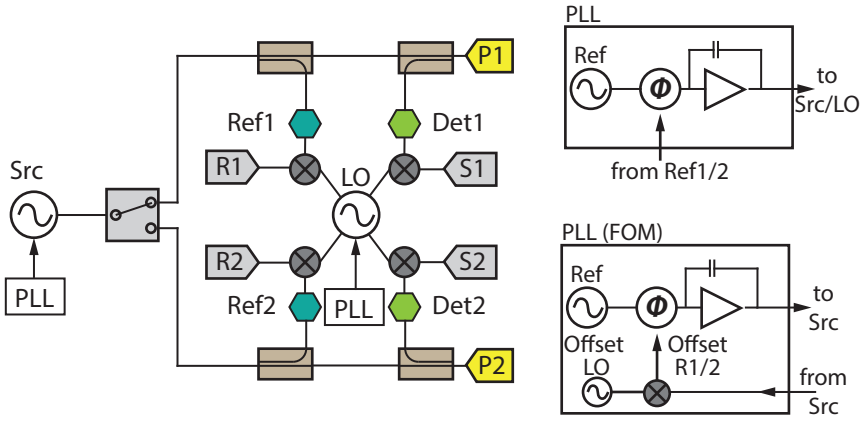

Fig. 5.22. Schematic electrical diagram of a vector network analyzer equipped with the frequency-offset mode (FOM). The difference between the standard measurement and a FOM measurement is the phase-locked loop (PLL) to synchronize the phase of the microwave source (Src) and the local oscillator (LO) to frequency downconvert the signal at the reference (Ref) and signal detector (Det). Note that multiplexer, filters, amplifiers and additional frequency conversion stages are not depicted in the electrical circuit for clarity. For details refer to main text. Figure adapted from [220].

so-called frequency offset mode (FOM) additional PLL hardware is used as depicted in Fig. 5.22. The PLL is modified by an offset LO detuning the PLL frequency for the microwave source by the desired frequency offset. For the LO, the PLL remains unchanged. Typically the FOM is only present in 4-port VNAs, where two microwave sources are present and the second microwave is utilized as the offset LO. We want to emphasize that by using the FOM, the phase information is typically lost. This is easily seen by considering two sinusoidal waves with two arbitrary frequencies. If the frequencies are not integer-valued multiples of each other, the relative phase is a function of time and not constant anymore.

To test the FOM feature of the VNA, we perform magnetic field sweep µFR-MOKE measurements with the laser spot positioned roughly $4.5\,\mu\mathrm{m}$ away from the antenna as indicated in Fig. 5.10(a) by the green circle and measure the non-linear response from the three magnon scattering at half the excitation frequency. The microwave frequency is set to $f_{\mathrm{MW}} = 12\,\mathrm{GHz}$ and the applied power is $P_{\mathrm{MW}} = 10\,\mathrm{dBm}$. The magnetic field is applied in the range $\mu_0 H_0 = 145\,\mathrm{mT} - 0\,\mathrm{mT}$ with a step size of $1.0\,\mathrm{mT}$ and the field sweep is repeated in total for 50 times. For this measurement the receiver frequency of the VNA is adjusted to $6\,\mathrm{GHz}$. With the VNA, we simultaneously measure the S_{21}-parameter as well as the S_{11} scattering parameter as shown in Fig. 5.23.

The S_{11}-parameter gives the reflection of the applied microwave at port 1 and electrically measures the non-linear conversion of the magnetization dynamics close to the antenna. The microstrip antenna not only inductively excites the magnetization

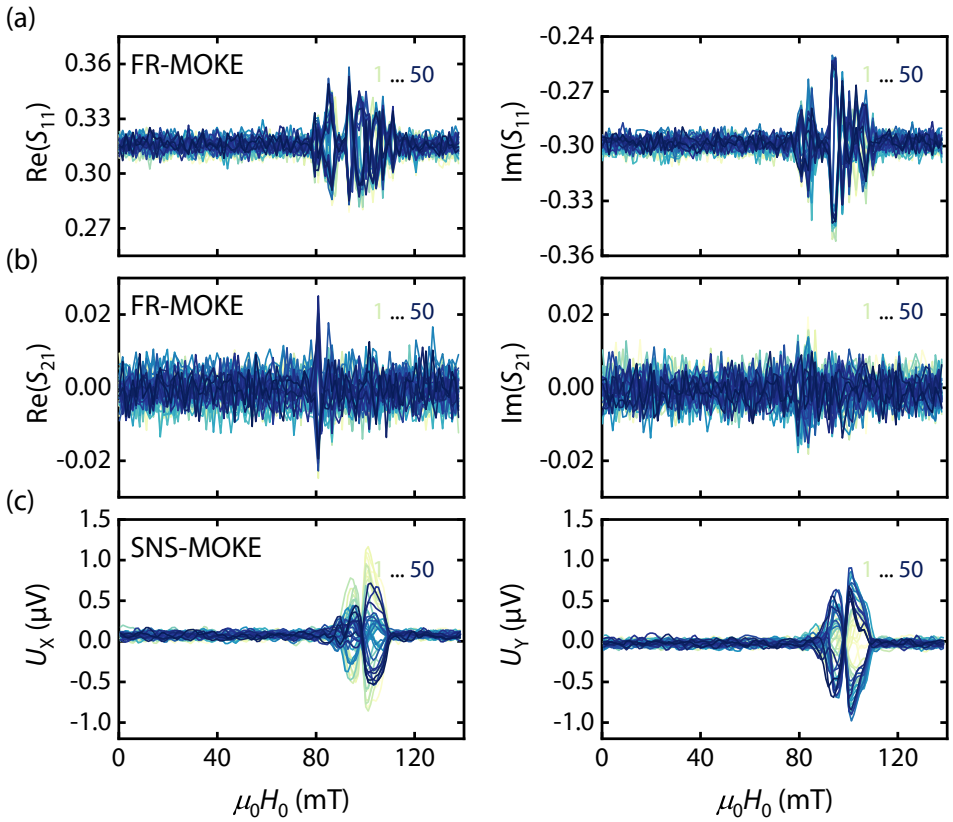

Fig. 5.23. Measured spectra at fixed excitation power $P_{\mathrm{MW}} = 10\,\mathrm{dBm}$ and microwave frequency $f_{\mathrm{MW}} = 12\,\mathrm{GHz}$ with the detector shifted to 6 GHz in a magnetic field sweep H_0 measurement repeated 50 times, indicated by the color gradient and the numbers in the top right corners of the panels. (a) Complex reflection parameter S_{11} showing the electrically detected non-linear response at the antenna measured with the VNA. (b) Real and imaginary part of the complex transmission parameter S_{21} measured with µFR-MOKE spectroscopy at a fixed spot position roughly 4.5 µm away from the antenna (cf. Fig. 5.10(a), green spot). (c) Measured real and imaginary part of the lock-in voltage U_i with µSNS-MOKE technique at nominally the same spot position as in the µFR-MOKE measurement.

dynamics at the antenna but also inductively detects resonantly excited dynamics by Faraday's law. The physical principle is equivalent to the already discussed broadband magnetic resonance spectroscopy utilizing a coplanar waveguide (cf. Section 3.3.1). In the measured S_{11}-spectrum shown in Fig. 5.23(a) with the receiver frequency at 6 GHz, we observe large signals in the magnetic field range $\mu_0 H_0 \simeq 80\,\mathrm{mT} - 110\,\mathrm{mT}$. We observe multiple signals due to the fact that a broad spectrum of spin waves excited at f_{MW} in the Damon-Eshbach regime decomposes into spin waves with frequency $f_{\mathrm{MW}}/2$.

The S_{21}-parameter shown in Fig. 5.23(b) is the optically detected, non-linear response of the spin waves. Relative to the background, the signal is much smaller compared to the electrically detected signal. The signal now does not feature a broad response but a rather sharp double peak around $\mu_0 H_0 = 80\,\mathrm{mT}$. To check this optical response, we use the µSNS-MOKE technique to detect this response. In order to be sensitive with the lock-in amplifier to the response at $f_{\mathrm{MW}}/2$, the excitation frequency of the microwave source is set to $f_{\mathrm{MW}} = 12\,\mathrm{GHz} + \delta$ with $\delta = 20\,\mathrm{kHz}$. For the linear response, the lock-in frequency is set to $80\,\mathrm{MHz} + \delta$. We confirmed that we measure the same signal as shown in Fig. 5.11(b). For the non-linear response, we need to consider $f_{\mathrm{MW}}/2 = 6\,\mathrm{GHz} + \delta/2$. The lock-in frequency is therefore set to $80\,\mathrm{MHz} + \delta/2$, basically to half the frequency offset δ. The result of the µSNS-MOKE measurement for the non-linear response is shown in Fig. 5.23(c). We observe the same double peak and measure a smaller background signal due to the use of a balanced photodetector. The double peak is at larger field ($\mu_0 H_0 \simeq 100\,\mathrm{mT}$) compared to the µFR-MOKE data due to the aforementioned small offset of the laser spot position and the divergence of the laser spot from the pulsed laser. The divergence might lead to the observation of the uniform magnon mode additional to the propagating spin wave modes.

A prominent feature observable in all measurements is the changing signal phase with each measurement iteration. As for example in $\mathrm{Re}\,(S_{21})$ in Fig. 5.23(b), the signal at $\mu_0 H_0 \simeq 80\,\mathrm{mT}$ changes from a peak to a dip and vice versa and changes with each iteration. Taking a closer look at the phase at the resonance field $\mu_0 H_{\mathrm{res}} = 80.7\,\mathrm{mT}$ for the µFR-MOKE and $\mu_0 H_{\mathrm{res}} = 101.8\,\mathrm{mT}$ in the µSNS-MOKE measurement as a function of the measurement iteration as depicted in Fig. 5.24. In the µFR-MOKE the phase is calculated using $\theta = \arctan\left(\mathrm{Im}\,(S_{21}) \,/\, \mathrm{Re}\,(S_{21})\right)$ and for the µSNS-MOKE by $\theta = \arctan\left(U_Y/U_X\right)$. For the situation that the receiver frequency equals the excitation frequency $f = f_{\mathrm{MW}} = 12\,\mathrm{GHz}$, the phase remains constant with each measurement repetition. In the case that the receiver frequency is half the excitation frequency $f = f_{\mathrm{MW}}/2 = 6\,\mathrm{GHz}$, the phase jumps between two values with a phase shift of roughly 180° within errors. In the µSNS-MOKE we observe a linear shift of the 180° jumps, which we attribute to the changing amplitude observed in the

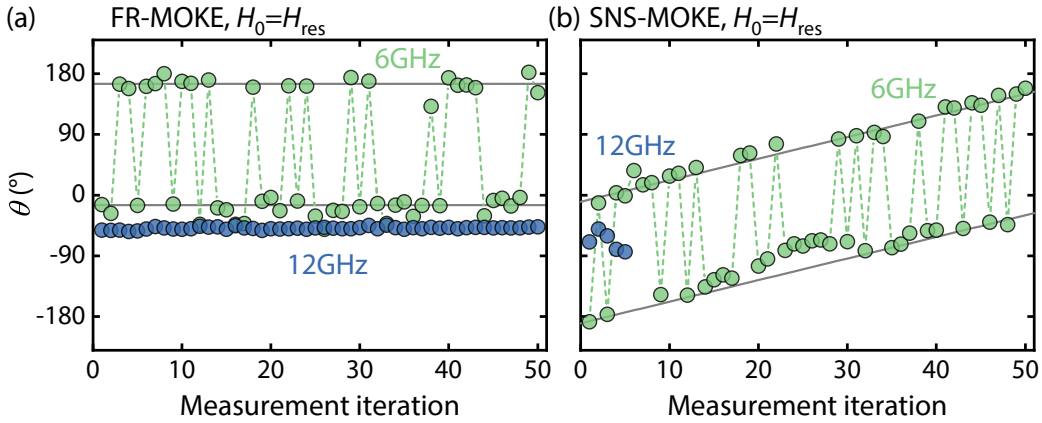

Fig. 5.24. Phase of (a) the complex S_{21}-parameter calculated by $\theta = \arctan\left(\mathrm{Im}\left(S_{21}\right)/\mathrm{Re}\left(S_{21}\right)\right)$ and of (b) the lock-in voltage U_i calculated by $\theta = \arctan\left(U_Y/U_X\right)$ at fixed magnetic field $H_0 = H_{\mathrm{res}}$ as a function of the number of measurement iteration. The detector frequency is either equal to the excitation frequency 12 GHz (blue) or at half the excitation frequency at 6 GHz (green). The grey vertical lines indicate a phase difference of 180°. Note in (b) that the linear change of the phase in the µSNS-MOKE measurement is originating from the changing measured amplitude due to stronger heating of the pulsed laser.

measurement presumably due to an instable focus routine used in the µSNS-MOKE measurement and due to stronger heating of the pulsed laser.

We will briefly discuss the origin of these 180° phase-jumps using Fig. 5.25. In a simple picture, consider two sinusoidal waves with the same frequency $f_1 = f_2$ (panel (a)), an arbitrary amplitude offset and an arbitrary phase shift. The phase shift between these two waves is determined by considering one full period of the wave τ. We calculate the difference in time Δt between e.g. the maximum values of the waves and convert it to a phase difference as the signal is periodic. Changing to the situation of two sinusoidal waves with a factor of 2 difference in frequency $f_1 = f_2/2$ (panel (b)) and an arbitrary phase difference. Again, considering one full period of the wave τ with the smaller frequency, we calculate the time difference of the maximum values of the waves. In this case we will find two solutions Δt_1 and Δt_2. As the ratio of the frequencies is $1/2$, the phase difference between the solutions is 180°. In our experiment, the VNA cannot distinguish between the solutions and returns arbitrarily one of the phases.

After the discussion about the phase of the measured signals, we want to turn our focus to the amplitude of the signals. Form the measurement data shown in Fig. 5.23 it is clear that the complex data cannot be averaged by the arithmetic mean as the measured phase changes with each measurement iteration. The apparent signal would be averaged to zero by this approach. Therefore, we use a different averaging procedure, where we do not average the complex values of S_{21} and U_i but rather

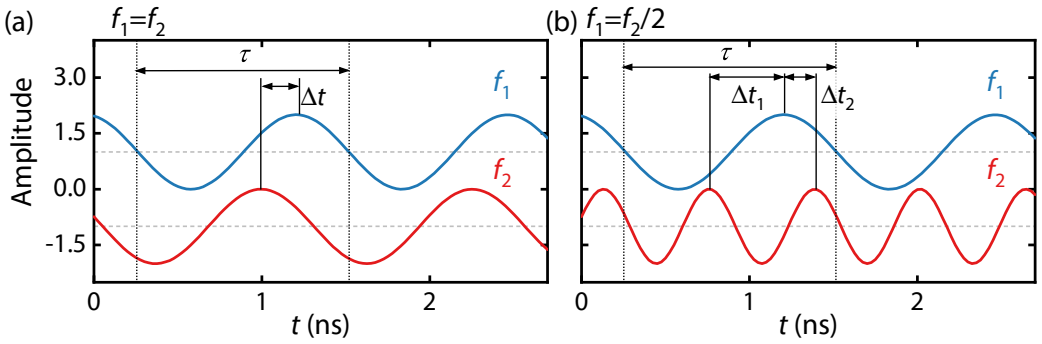

Fig. 5.25. Schematic depiction of the determination of the phase difference of two sinusoidal waves with (a) the same frequency $f_1 = f_2$ and (b) with a frequency difference of $f_1 = f_2/2$. For details refer to main text.

average their magnitudes. The phase consequently does not play a role anymore. We calculate

$$S_{21}^{\mathrm{avg}}(H_0) = \frac{1}{N}\sum_{n=1}^{N} |S_{21,n}(H_0)| \quad \text{and} \quad U_{\mathrm{avg}}(H_0) = \frac{1}{N}\sum_{n=1}^{N} |U_{Xn}(H_0) + i\, U_{Yn}(H_0)|\,, \tag{5.42}$$

where $N = 50$ is the total number of measurements. The results are collected in Fig. 5.26, where the averaged magnitudes are normalized to the maximum signal for a qualitative comparison. In panels (a) and (b) we first compare µFR-MOKE measurements at different microwave powers, which are at large power $P_{\mathrm{MW}} = 10\,\mathrm{dBm}$ and at low power $P_{\mathrm{MW}} = -5\,\mathrm{dBm}$, where we do not expect any non-linear dynamics. With the receiver frequency equal to the excitation frequency $f = f_{\mathrm{MW}}$ as depicted in Fig. 5.26(a), the signal strength decreases with increasing microwave power P_{MW}, indicating the presence of additional losses due to the occurrence of non-linear processes. Changing the receiver frequency to half the excitation frequency $f = f_{\mathrm{MW}}/2$ as shown in Fig. 5.26(b), no signal is observed at the lower microwave power $P_{\mathrm{MW}} = -5\,\mathrm{dBm}$ and only noise is observed. At the larger microwave powers $P_{\mathrm{MW}} = 10\,\mathrm{dBm}$ a response of the system is observed, confirming that the signal we observe is due to the non-linear response of the magnetization dynamics.

Finally, we compare the signals from the linear and non-linear signals measured by all three optical spectroscopy techniques. In Fig. 5.26(c) the normalized averaged magnitude of the linear response of the magnetization dynamics at microwave power $P_{\mathrm{MW}} = 10\,\mathrm{dBm}$ and the receiver frequency equal to the excitation frequency $f = f_{\mathrm{MW}}$ is shown. The data shown here is taken from Fig. 5.11. The signals observed with the different optical spectroscopy techniques are in good agreement.

For the comparison of the non-linear signature at half the excitation frequency $f = f_{\mathrm{MW}}/2$, we use for µBLS the data shown in Fig.5.11(c) and extract the magnetic

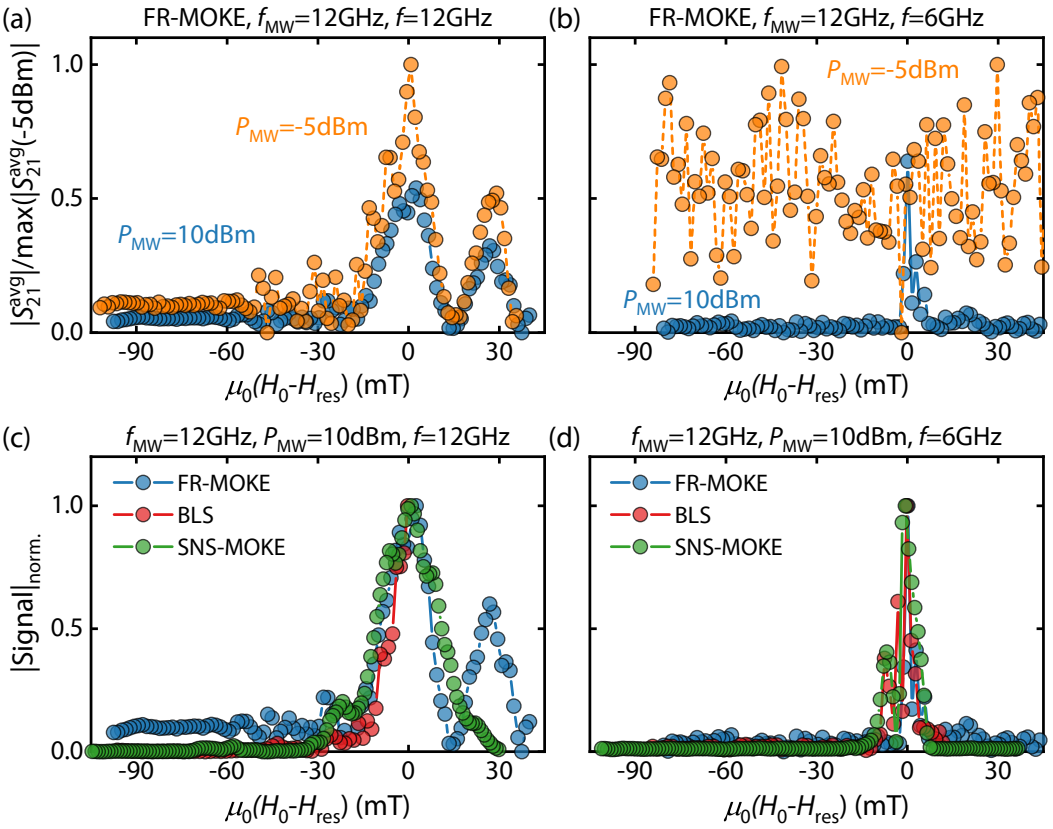

Fig. 5.26. (a),(b) Comparison of the normalized magnitude of the S_{21}^{avg}-parameter as a function of the external magnetic field H_0 at high $P_{\mathrm{MW}} = 10\,\mathrm{dBm}$ and low microwave power $P_{\mathrm{MW}} = -5\,\mathrm{dBm}$ for (a) the detector frequency equal to the excitation frequency $f = f_{\mathrm{MW}} = 12\,\mathrm{GHz}$ and (b) the detector frequency at half the excitation frequency $f = f_{\mathrm{MW}}/2 = 6\,\mathrm{GHz}$. (c),(d) Comparison of the normalized magnitude between the different measurement techniques at microwave power $P_{\mathrm{MW}} = 10\,\mathrm{dBm}$ with (c) the detector frequency equal to the excitation frequency $f = f_{\mathrm{MW}} = 12\,\mathrm{GHz}$ and (d) the detector frequency at half the excitation frequency $f = f_{\mathrm{MW}}/2 = 6\,\mathrm{GHz}$.

field-dependence at the TFP frequency $f_{\mathrm{BLS}} = 6\,\mathrm{GHz}$. For the µFR-MOKE and µSNS-MOKE, the data shown in Figs. 5.23(b) and (c) are used, respectively. The normalized intensity of the µBLS and the normalized averaged magnitude data of the µFR-MOKE and the µSNS-MOKE are shown in Fig. 5.26(d). All three optical measurement techniques show qualitatively the same signature.

These experiments demonstrate that the signals of spin waves, either originating from linear or non-linear processes, measured by the well-established µBLS technique can also be detected by the µFR-MOKE and µSNS-MOKE techniques. While for linear signatures, such as spin wave propagation, this is well known, for non-linear processes this has not been demonstrated. In these first experiments, we demonstrated that the magnetic field-dependence of the signals from the magnetization dynamics at a fixed spot location lead to the same results as in µBLS.

In future experiments, a more thorough and systematic investigation is required to also compare spin wave propagation and frequency-dependence of the non-linearly excited spin waves.

5.3.2.4. Electrical 2-Tone Spectroscopy of Spin Waves

After we demonstrated in the previous section, that it is possible to measure the response of the non-linear signature of spin waves using the frequency-offset mode of the VNA in a µFR-MOKE measurement, we want to measure the susceptibility of the non-linearly generated spin wave. As we have seen, the frequency-offset mode cannot be directly used to measure the phase of the non-linear signal, but can detect its amplitude. Inspired by previous experiments [48], we will perform an electrical 2-tone spectroscopy technique equivalently to an electrical pump-probe experiment. The idea is to "pump" the magnons with large microwave power to undergo three-magnon scattering and then "probe" at half the excitation frequency with low power to test the response of the non-linear magnons. In the low-damping $Co_{25}Fe_{75}$ alloy we have seen that very low microwave powers are required to excite spin waves (cf. Fig. 5.20). This means that we always need to confirm our results with conventional single-tone to distinguish between signals from linear and non-linear origin. For these experiments we will use the full capability of the used VNA performing µFR-MOKE measurements as explained in the following.

In Fig. 5.27 the two different microwave path configurations of the used VNA for 1-tone and 2-tone spectroscopy are shown. The used 4-port VNA (Keysight N5242A PNA-X) features two microwave sources, which can be used independently, where microwave source 1 (Src1) can apply a microwave to port 1 and 2 and source 2 (Src2) supplies port 3 and 4. For the single-tone experiment shown in Fig. 5.27(a) the internal microwave path does not change compared to the previous µFR-MOKE experiments (compare microwave path shown in Fig. 5.22). Note that the detection electronics shown in Fig. 5.22 is omitted in Fig. 5.27 for clarity. The VNA excites with Src1 a microwave and applies it to port 1 and measures the response of the device-under-test (DUT), which in our case is the optical setup including the sample, at port 2. Consequently, it calculates the complex transmission parameter S_{21}.

In the 2-tone scheme shown in Fig. 5.27(b), a microwave with a certain frequency is additionally generated with Src2. Due to the additional microwave switches and directional couplers, it is possible to couple this microwave to the port 1. As a consequence, two microwaves with (potentially) different microwave frequencies and powers are emitted at port 1. As both microwaves are coupled to the reference receiver (Ref1), it is possible to measure phase-sensitively at both frequencies of the microwave. This is a big advantage over the frequency-offset mode technique explained above. The microwave generated by Src2 has a significantly lower output

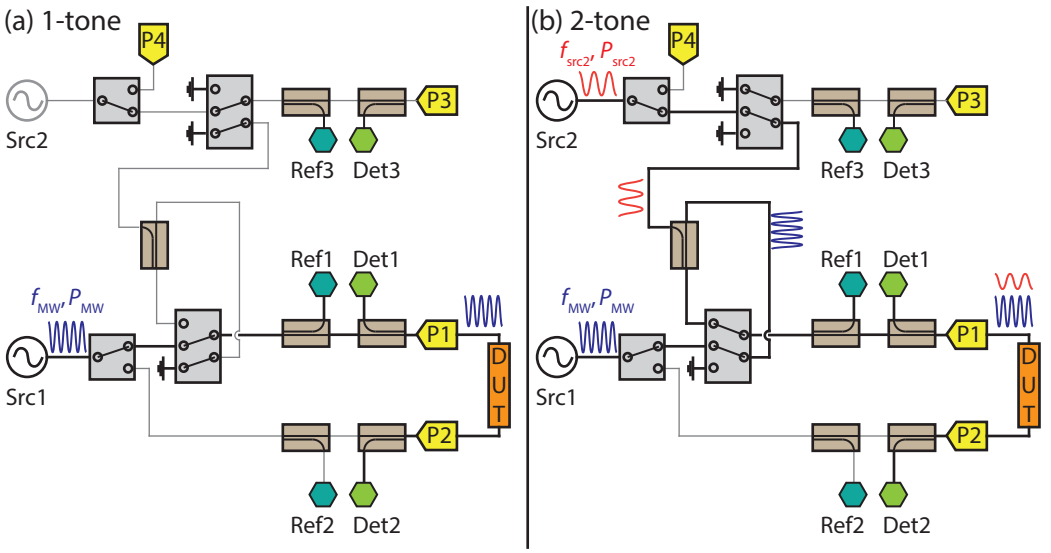

Fig. 5.27. Internal microwave path of a Keysight PNA-X N5242A with two microwave sources (Src1/2). (a) 1-tone measurement configuration, where the second source Src2 is not coupled into the path of Src1. (b) 2-tone measurement configuration, where the microwave of Src2 is superimposed via a directional coupler onto the microwave of Src1. Note that the reference receiver (Ref1) frequency can still be detuned from Src1. The detection electronics from Fig. 5.22 is omitted for simplicity. Figure adapted from [221].

power at port 1 due to the additional directional coupler. In our experiments the maximum possible power at port 1 of the Src2 microwave is $P_{\mathrm{src2}} < 1\,\mathrm{dBm}$. We thus refer to the microwave of Src1 as the pump signal and the microwave of Src2 with lower power as the probe tone. The receiver frequency of the VNA is always set to the same frequency as the probe frequency, which for the 2-tone measurement is f_{src2} and for the 1-tone measurement f_{MW}. For consistency, the parameters of the pump tone will be subscripted by MW and the probe tone from Src2 will be denoted by $\mathrm{src2}$. As for the 1-tone experiment, the pump and probe signal are the same, it will be subscripted as MW.

In the following, we perform two different experiments to test the 2-tone technique. The laser spot is set to a fixed location at roughly $4.5\,\mu\mathrm{m}$ away form the antenna (cf. Fig. 5.10(a), green circle) and the magnetic field is swept form $\mu_0 H_0 = 141\,\mathrm{mT} - 0\,\mathrm{mT}$ with a step size of approx. $1.5\,\mathrm{mT}$. Each magnetic field sweep is performed 10 times and the arithmetic mean of the complex transmission parameter S_{21} is calculated.

In the first measurement, we fix the microwave frequency of Src1 to $f_{\mathrm{MW}} = 12\,\mathrm{GHz}$ and its power to $P_{\mathrm{MW}} = 10\,\mathrm{dBm}$. For the probe tone, we use for Src2 a microwave frequency of $f_{\mathrm{src2}} = 6\,\mathrm{GHz}$ and change the power P_{src2} from $-27\,\mathrm{dBm}$ to $1\,\mathrm{dBm}$ with a step size of $1\,\mathrm{dBm}$. The measured S_{21}-parameter is shown colorcoded in Fig. 5.28(a). To distinguish between linear and non-linear dynamics, the same measurement procedure is performed for a single-tone measurement with the microwave frequency

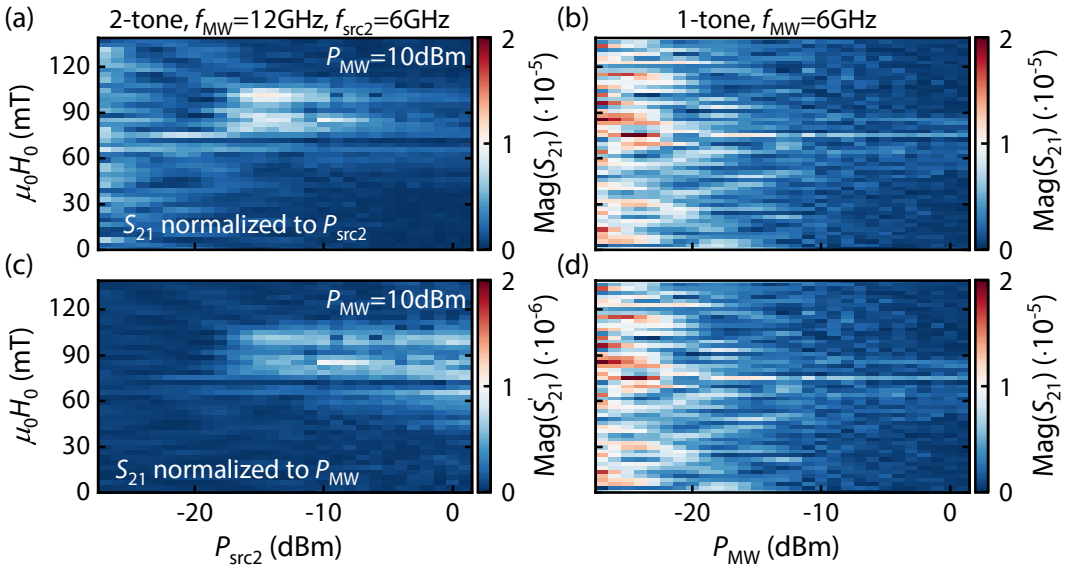

Fig. 5.28. Color-coded magnitude of the S_{21}-parameter in a (a),(c) 2-tone µFR-MOKE measurement and in a (b),(d) 1-tone µFR-MOKE measurement as a function of the external magnetic field H_0 and the applied microwave power of (a),(c) the probe power P_{src2} and (b),(d) the driving power P_{MW}. (a),(c) The excitation frequency is $f_{\mathrm{MW}} = 12\,\mathrm{GHz}$ with a microwave power of $P_{\mathrm{MW}} = 10\,\mathrm{dBm}$ and microwave frequency of the second microwave source and of the receiver $f_{\mathrm{src2}} = 6\,\mathrm{GHz}$. In (a) the S_{21}-parameter is normalized to the probe power P_{src2} and in (c) to the pump power P_{MW}. Note the different scales of the colorcode. (b),(d) The microwave frequency in the 1-tone measurement is set to $f_{\mathrm{MW}} = 6\,\mathrm{GHz}$ where at low microwave powers P_{MW} the power is too low to excite spin waves. The data in (b) and (d) are the same.

$f_{\mathrm{MW}} = 6\,\mathrm{GHz}$ and the same microwave power P_{MW} as for the probe tone P_{src2} in the 2-tone measurement. The 1-tone measurement procedure is equivalent to the measurements performed in Section 5.3.1. The result is shown in Fig. 5.28(b).

Comparing the two colorcoded S_{21}-parameters of the single- and 2-tone measurement, we observe different behaviours of the magnetization dynamics. The most prominent feature in the spectra is the signal at roughly $\mu_0 H_0 = 105\,\mathrm{mT}$ and at $\mu_0 H_0 = 85\,\mathrm{mT}$ which are present in the 2-tone measurement but not in the 1-tone. This indicates that the signal stems from the non-linear dynamics of the spin wave at half the excitation frequency. The dependence of the S_{21}-parameter on the probe power P_{src2} might be due to the wrong calculation of S_{21} as intuitively it is not expected. Therefore, we recalculate the S_{21}-parameter by normalizing S_{21} to the pump power P_{MW} by using $S_{21}' = S_{21} \cdot \sqrt{P_{\mathrm{src2}}/P_{\mathrm{MW}}}$. The resulting dependence of S_{21}' as a function of the probe power P_{src2} is shown in Fig. 5.28(c). As emphasized before, the power-dependence of S_{21}' is not observed anymore with this recalculation of S_{21}. We conclude from these measurements that it is possible with this 2-tone method to detect the non-linear response of the spin waves at half their excitation frequency phase-sensitively.

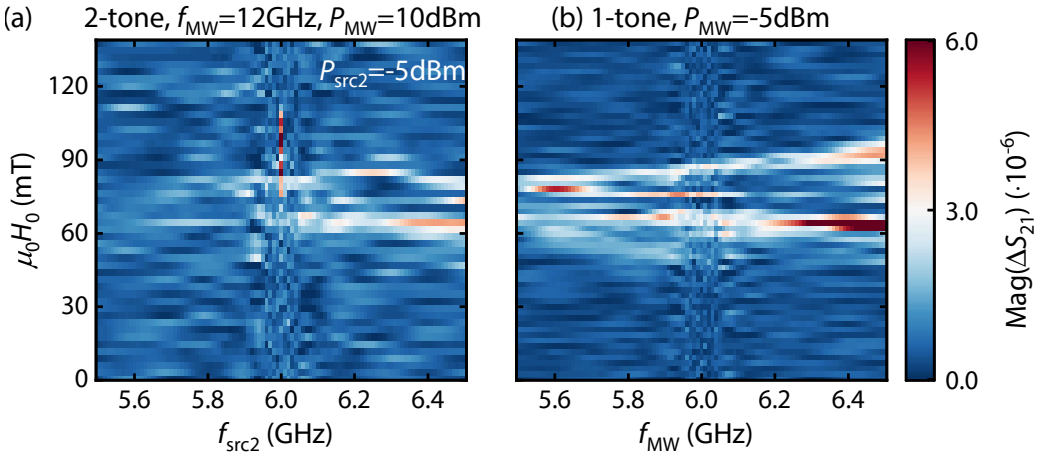

Fig. 5.29. Color-coded magnitude of the S_{21}-parameter in a (a) frequency-locking experiment of the non-linear spin wave at 6 GHz with an excitation at $f_{\mathrm{MW}} = 12$ GHz as a function of the magnetic field H_0 and the tuning frequency f_{src2}. The excitation power is $P_{\mathrm{MW}} = 10$ dBm and the tuning power is $P_{\mathrm{src2}} = -5$ dBm. (b) The 1-tone measurement at microwave frequency $f_{\mathrm{MW}} = 6$ GHz and power $P_{\mathrm{MW}} = -5$ dBm is performed to distinguish between direct excitation at 6 GHz and non-linear locking in the 2-tone measurement in panel (a).

An intriguing question is now wether it is possible to "lock" the non-linear spin wave with the second microwave and tune the frequency of the resonance. This is inspired by phase-locking experiments using spin Hall nano-oscillators [222, 223]. To this end, we will set the pump frequency fixed to $f_{\mathrm{MW}} = 12$ GHz and with microwave power $P_{\mathrm{MW}} = 10$ dBm. The probe tone f_{src2} is swept from 5.5 GHz to 5.9 GHz and from 6.1 GHz to 6.5 GHz with a step size of 0.1 GHz, and from 5.9 GHz to 6.1 GHz with a resolution of 0.01 GHz. The power of the second microwave source is chosen to $P_{\mathrm{src2}} = -5$ dBm. The magnetic field is swept again in the range $\mu_0 H_0 = 141$ mT-0 mT with a step size of 1.5 mT. Each magnetic field sweep is repeated 10 times and the arithmetic mean of the complex transmission parameter S_{21} is calculated.

The measured S_{21}-parameter as a function of the external field and frequency is shown in Fig. 5.29. Due to the changing microwave frequency, we subtract the arithmetic mean of each magnetic field trace for each frequency and subtract it, similar to the procedure presented in Section 5.3.1.4. The main resonances shown between $\mu_0 H_0 \simeq 60$ mT $- 100$ mT at frequencies $f > 6.05$ GHz and $f < 5.9$ GHz are attributed to the linearly excited dynamics at 6.00 GHz. Close to half the excitation frequency $f_{\mathrm{MW}}/2$ where the frequency step size is decreased, the behaviour between 2-tone and 1-tone does not differ besides exactly at 6.00 GHz. Here, we observe in the 2-tone spectroscopy a signal at $\mu_0 H_0 \approx 105$ mT, which is not present in the single-tone experiment.

From the magnetic field spectra of the complex transmission parameter S_{21} recorded at three different microwave frequencies as depicted in Fig. 5.30, the situation be-

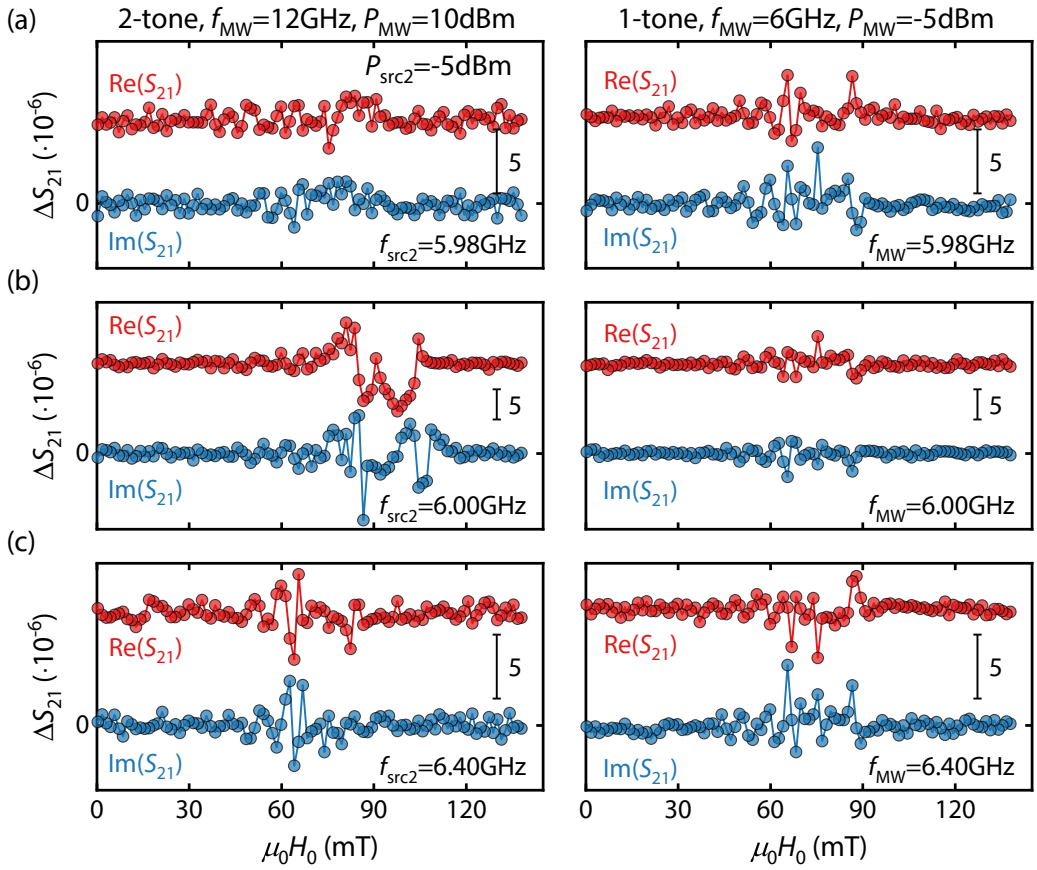

Fig. 5.30. Fieldtraces of the complex S_{21}-parameter for the measurement data shown in Fig. 5.29 for fixed frequencies (a) $f = 5.98\,\mathrm{GHz}$, (b) $f = 6.00\,\mathrm{GHz}$ and (c) $f = 6.40\,\mathrm{GHz}$. In the left column, the 2-tone measurements and in the right column the 1-tone measurements are shown. Note that there is an offset added to $\mathrm{Re}(S_{21})$ for clarity. The y-axis scale for each figure is indicated by the black bar and is for (b) different compared to (a) and (c) for clarity.

comes more evident. The largest response of the system is observed at exactly half the excitation frequency $f_{\mathrm{src2}} = f_{\mathrm{MW}}/2 = 6.00\,\mathrm{GHz}$ shown in panel (b), as we would expect. Comparing this signal to the corresponding 1-tone experiment (right column), it is clear that the signal is stemming from the non-linear response of the system. If we decrease the probe frequency to $f_{\mathrm{src2}} = 5.98\,\mathrm{GHz}$, the response vanishes. The same behaviour is observed if we increase the probe frequency to $f_{\mathrm{src2}} = 6.4\,\mathrm{MHz}$, where we recover the linear response of the system (cf. right column).

We also performed the same measurement with the smallest frequency steps, within the specified phase noise of the microwave source, possible $1\,\mathrm{kHz}$ in the frequency range $f_{\mathrm{src2}} = 6.0\,\mathrm{GHz} \pm 10\,\mathrm{kHz}$ and observe the same behaviour as explained above. Furthermore, the same experiment was conducted with the maximum available probe power of $P_{\mathrm{src2}} = 1\,\mathrm{dBm}$, where we also do not see any signature of locking or tuning behaviour as it becomes more difficult to distinguish between linearly and non-linearly excited spin waves. Consequently, a tunability of the res-

onance frequency of the non-linear spin waves by frequency-locking could not be observed within the available sensitivity and microwave power. From the data at hand, we emphasize that the frequency linewidth of the non-linearly generated spin waves at half the excitation frequency seems to be smaller than $1\,\mathrm{kHz}$ as we do not find any signal signature comparable to exactly half the excitation frequency. This is not the natural linewidth of the spin wave but originating from the coherent narrow-band excitation of spin waves at the driving frequency f_{MW}. Therefore, the spin waves involved in the three-magnon scattering process decompose to the same magnon state within a small frequency linewidth. Note that the detected linewidth of the non-linear spin waves in the µBLS (cf. Figs. 5.11(c) and 5.20) is not the "real" linewidth of the magnon system but limited by the resolution of the TFP. In a future experiment, it may be necessary to try to pump the spin waves with even larger microwave power P_{MW} to receive a larger non-linear response from the non-linearly excited spin waves.

5.4 Summary and Outlook

In conclusion, we investigated the magnetization dynamics of a micro-patterned magnonic waveguide consisting of the low-damping alloy $Co_{25}Fe_{75}$ in a spatially and phase-resolved manner. The dynamics were excited using a static magnetic field applied in the sample plane, perpendicular to the magnonic waveguide and by using an on-chip antenna, micropatterned on top of the ferromagnet. We used three different optical spectroscopy techniques namely the microfocused frequency-resolved magneto-optic Kerr effect (µFR-MOKE), microfocused Brillouin light scattering (µBLS) and microfocused super Nyquist-sampling magneto-optic Kerr effect (µSNS-MOKE). These spectroscopy techniques are integrated into a single optical setup allowing the comparison between these methods and to use the best suited technique to measure the dynamics of dipolar-exchange spin waves.

We tested the magnetization dynamics in the linear and non-linear regime. In the linear regime the $50\,\mathrm{nm}$ thick and $1.5\,\mu\mathrm{m}$ wide $Co_{25}Fe_{75}$ waveguide shows excellent spin wave propagation lengths of up to $30\,\mu\mathrm{m}$, which could be confirmed by µFR-MOKE and µSNS-MOKE. Due to the large saturation magnetization of $Co_{25}Fe_{75}$, the consequently large demagnetization fields lead to a pronounced magnetically easy axis along the magnonic waveguide. By increasing the magnetic field applied perpendicular to the waveguide, we measured the transition from backward-volume spin waves to Damon-Eshbach modes is a promising property for application oriented devices. Additionally, we could resolve the wavefronts of the propagating spin waves with our phase-resolved techniques confirming the multi-mode character of the Damon-Eshbach modes and the very short-wavelength excitations at intermediate

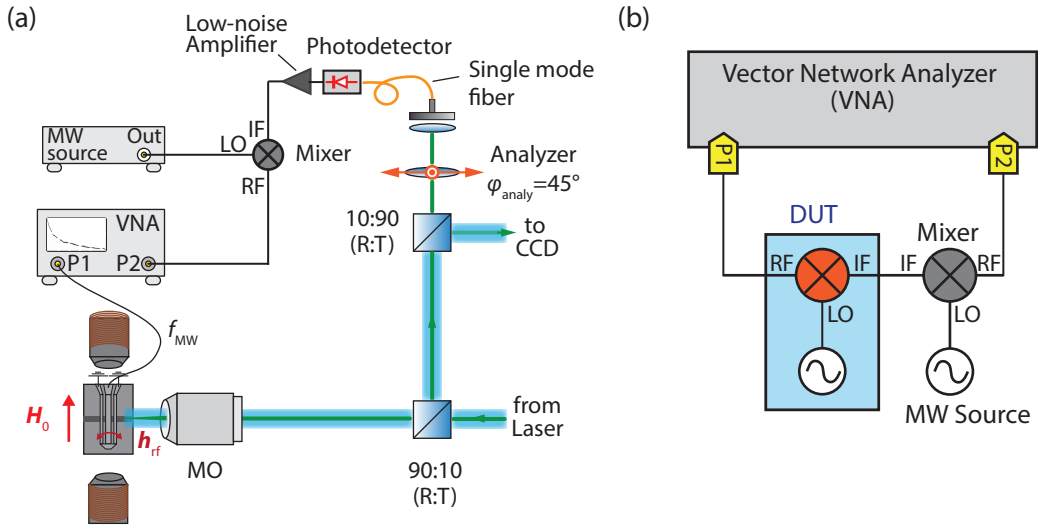

Fig. 5.31. Upconversion/downconversion technique to phase-sensitively measure the non-linear spin wave response based on Ref. [224]. (a) The optical setup remains unchanged compared to Fig. 5.6 but on the microwave path an additional mixer with a microwave source at the local oscillator input (LO) is inserted. (b) Reduced diagram of the upconversion/downconversion technique. The non-linear spin waves can be modelled as a frequency-translating device with an embedded local oscillator, where the additional mixer up- or downconverts the frequency translation of the non-linear spin waves back to the excitation frequency.

magnetic fields between the backward-volume (low-field) and Damon-Eshbach spin wave excitations (high field).

For the investigation of the non-linear dynamics, we used μBLS to confirm the three-magnon scattering process as the relevant physical mechanism in the non-linear regime. With the μFR-MOKE and μSNS-MOKE method, we could measure this non-linear response at half the excitation frequency with the use of the so-called frequency-offset mode with the disadvantage of losing the phase-sensitivity of the vector network analyzer (VNA) and lock-in amplifier, respectively. In an electrical 2-tone experiment, where we apply a “pump” microwave with large power and a “probe” microwave with smaller power and different frequency to the on-chip antenna, we were able to detect the susceptibility of the non-linearly generated spin wave using the μFR-MOKE technique. Further, we did not find any sign of tunability of the spin wave frequency at half the excitation frequency but rather conclude that within the specifications of the microwave source in the VNA, the frequency of the spin waves generated by three-magnon scattering are determined by the linewidth of the used microwave source.

These experiments demonstrate the expected consistency between the measurement results of the different optical spectroscopy techniques to characterize the magnetization dynamics of micropatterned devices. Up to now, the non-linear characteristics of spin waves were optically determined by the established μBLS

technique. The frequency-offset mode and 2-tone FR-MOKE techniques shown here offer potentially new approaches to measure non-linear properties of spin waves. One caveat of the frequency-offset mode is the reduced dynamical range of the VNA and the loss of the phase-sensitivity. In a future experiment, an adaption of the so-called upconversion/downconversion technique [224] could be realized. A potential experimental setup is shown in Fig. 5.31. The optical setup shown in panel (a) based on the µFR-MOKE technique remains unchanged. The idea of the up-/downconversion method is to convert the optical sidebands generated by the non-linear processes of the spin waves back to the excitation frequency of the VNA. Therefore, the VNA detects at the same microwave frequency as it excites and consequently the full dynamical range of the VNA can be accessed and the phase-sensitivity is retained. To perform the frequency conversion, a mixer is integrated between the detection port (P2) of the VNA and the low-noise amplifier. The local oscillator (LO) input of the mixer is connected to an additional microwave source and converts the input signal at the IF-port to $f_{\mathrm{RF}} = |f_{\mathrm{IF}} \pm f_{\mathrm{LO}}|$.

In a schematic electrical circuit as shown in Fig. 5.31(b) the idea of this technique becomes more obvious. The sample with non-linear spin wave generation can be modelled as a frequency-translating device (DUT) with an embedded local oscillator. By converting this frequency translation back with the additional mixer and microwave source, the VNA can at least measure a relative phase-shift. This technique is then limited in frequency by the used microwave equipment and allows to further investigate the underlying physical mechanism of non-linear spin wave generation.

Summary and Outlook

6

This thesis explores hybrid magnon dynamics in several qualitatively different systems. Hybrid magnon systems play an important role, since magnons frequently couple to other quantized excitations such as photons, phonons, plasmons etc. or other types of magnon modes forming so-called hybridized modes. In particular, we study spin dynamics in (quasi-)antiferromagnets, metallic ferromagnets and skyrmion host materials. These material systems and hybrids are interesting models systems to address current challenges in spintronics. In particular, the research area of spintronics is dedicated to utilize the spin degree of freedom of the electron to store and transport information. In this thesis, we revealed a new coupling mechanism for magnon-magnon coupling in compensated ferrimagnets close to their compensation temperature. The ensuing quasi-antiferromagnetic dynamics leads to an exchange-enhancement of the magnon-magnon coupling rate. We further demonstrated magnon-photon coupling between a chiral magnet and a three-dimensional microwave cavity. In this hybrid system, the magnon-photon cooperativity can be drastically tuned at the topological phase transition of the chiral magnet with an external control parameter. Besides the detailed study of these fundamentally novel hybrid spin dynamic phenomena, we also developed advanced optical spectroscopy tools such as microfocused frequency-resolved magneto-optic Kerr effect (μFR-MOKE). They allow for the development of novel magnonic devices that might exploit hybrid magnon dynamics. We performed a comprehensive characterization of linear and non-linear magnon dynamics in microstructured prototype magnonic devices using our optical spectroscopy methods. A quantitative comparison of three different optical spectroscopy methods has thereby been carried out and reveals several key advantages of the novel techniques developed during this thesis compared to established optical magnon spectroscopy tools.

The results presented in this thesis are obtained in different magnetically ordered systems using different, phase-sensitive measurement techniques. They are either based on fully electrical methods, such as broadband magnetic resonance using a coplanar waveguide or a microwave cavity, or entirely optical techniques, like microfocused Brillouin light scattering, or the combination of optical and electrical detection principles, such as frequency-resolved magneto-optical Kerr effect spectroscopy. In the following, we give an overview of the key results of this thesis by summarizing the main findings of each chapter:

Chapter 2 introduces the basic physical concepts of magnetization dynamics. A simple approach on how to derive and solve the characteristic equation of motion to describe the dynamics of the macroscopic magnetization, namely the Landau-Lifshitz-Gilbert equation, is presented. Furthermore, we discuss the ferromagnetic resonance, which is the resonant uniform precession of the magnetic moments in the magnetic system driven by a coherent microwave tone. Based on this theoretical introduction, we extended the presented physical concepts to the subsequent chapters.

In **Chapter 3**, we use the compensated ferrimagnet gadolinium iron garnet (GdIG) to demonstrate exchange-enhanced ultrastrong magnon-magnon coupling. Gadolinium iron garnet features a compensation temperature, where the sublattice magnetizations compensate each other and the magnetic system, including the magnetization dynamics, mimics a quasi-antiferromagnet. In order to investigate the magnetization dynamics of GdIG close to the compensation temperature, a (111)-oriented, disk-shaped single-crystal is placed onto a coplanar waveguide and investigated using broadband magnetic resonance spectroscopy with the magnetic field applied in the disk plane. Due to the axial symmetry breaking by the magneto-crystalline cubic anisotropy, the two magnon modes hybridize, forming two orthogonal, linearly polarized magnon modes. Due to the Heisenberg exchange interaction the generally small coupling rate mediated by the small cubic anisotropy is exchange-enhanced. The coupling rate reaches a maximum value of almost $37\,\%$ of the characteristic magnon frequency, denoting the system in the ultrastrong coupling regime. Additionally, we demonstrate the tunability of the coupling strength by changing the direction of the external magnetic field in the disk plane. The coupling rate is changed from the aforementioned maximum value to a minimum value, where the coupling rate is in the range of the loss rates of both magnon modes. The presented coupling mechanism is independent of sample size and not restricted to GdIG or ferrimagnets. This opens exciting perspectives for studying ultrastrong coupling effects in nanoscale devices.

In **Chapter 4** a large tunability of the magnon-photon cooperativity is realized by inducing a phase transition of the magnetic system with an external control parameter. As a prototypical system, we use the chiral magnet Cu_2OSeO_3 and put the single-crystal into a self-designed three-dimensional cavity. Cu_2OSeO_3 features a rich magnetic phase diagram including a topologically-stabilized skyrmion lattice phase. The uniform magnon modes in the skyrmion lattice phase, which are the two gyrating modes (clockwise and counter-clockwise mode) and the breathing mode, differ in their excitation geometries. Due to the homogenous and clearly defined oscillating magnetic field inside the cavity, it is possible to selectively excite either the breathing mode or the gyrating modes and all other uniform magnon modes in Cu_2OSeO_3 by changing the external magnetic field direction relative to the oscillating driving field. By changing the external magnetic field magnitude by a few mT in the parallel excitation geometry and inducing a magnetic phase transition from the conical to the

skyrmion lattice phase, the cooperativity can be tuned from unity to $C \lesssim 60$. Utilizing this property for hybrid devices, might enable interesting new approaches to read-out the state of e.g. a magnon-qubit system in a dispersive read-out scheme.

In **Chapter 5** we use microfocused, optical measurement techniques to characterize the magnetization dynamics of a microstructured ferromagnet in the linear and non-linear regime. To this end, three different optical techniques are employed, namely the micro-focused frequency-resolved magneto-optic Kerr effect (µFR-MOKE), micro-focused Brillouin light scattering (µBLS) and micro-focused super-Nyquist sampling MOKE (µSNS-MOKE), all integrated into a single optical setup. Besides demonstrating the capabilities and limitations of these techniques, we systematically characterize the dynamics of spin waves in the low-damping alloy $Co_{25}Fe_{75}$ structured into a $1.5\,\mu m$ wide and $50\,nm$ thick waveguide with a micro-patterned gold antenna on top to excite the magnetization dynamics. Due to the large saturation magnetization in the system, the magnetization is aligned parallel to the waveguide. With increasing external magnetic field applied perpendicular to the waveguide, the magnetization starts to orient along the external magnetic field. Therefore, with changing field magnitude, the dynamics of the dipolar-exchange spin waves propagating along the waveguide are investigated from the Backward-volume regime to the Damon-Eshbach regime. We find a maximum propagation length of approx. $30\,\mu m$ in the Damon-Eshbach regime. The combination of a large propagation length with high saturation magnetization found in $Co_{25}Fe_{75}$ is unique for metallic ferromagnets and interesting for potential applications in magnon based devices. Additionally, we investigated the non-linear dynamics of spin waves, where we focused on three-magnon scattering. The occurrence of three-magnon scattering is typically analyzed with µBLS. In our experiments, we measure this mechanism for the first time using µFR-MOKE with the frequency-offset mode and with µSNS-MOKE by detuning the demodulation frequency of the lock-in amplifier. We probe the non-linear spin waves with electrical pump-probe experiments with optical detection. The combination of the presented optical measurement techniques allows us to better understand the magnetization dynamics in a spatially-resolved manner. This provides a powerful tool for the study of future spintronic devices.

In conclusion, the presented optical and electrical measurement techniques and their very high sensitivity are powerful methods to characterize the magnetization dynamics in the GHz regime. Using these methods, we presented novel coupling mechanisms and approaches for hybrid magnon systems, which might contribute to a better understanding of the spin dynamics in coupled systems with microscale dimensions.

Appendix

A

A.1 Optical Setup

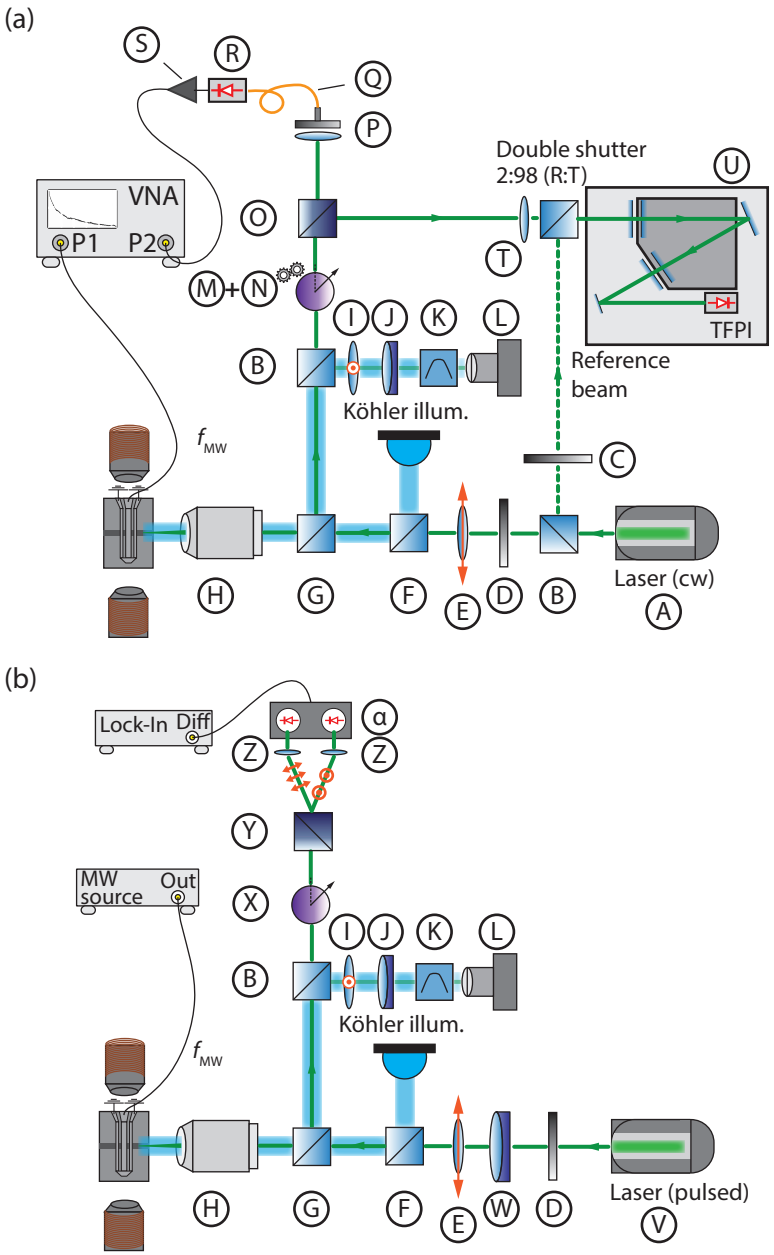

Fig. A.1. Full optical setup with all relevant optical elements labelled for the (a) combined µFR-MOKE/µBLS setup and the (b) µSNS-MOKE setup. The full parts list is given in Tab. A.1. Note that the optical path from (E)-(L) is identical in both setups. The Köhler illumination is separately shown in Fig. A.2.

Tab. A.1. Parts list of the optical elements used in the optical setup depicted in Fig. A.1.

Label	Optical element	Part number
A	Laser	Laser Quantum Torus 532
B	10:90 Beam Splitter Cube	Thorlabs BS025
C	Neutral Density Filter (NDF)	Thorlabs NDC-25C-2M
D	Neutral Density Filter (NDF)	Thorlabs NDL-25C-2
E	Glan-Thompson polarizer	Thorlabs GTH10-A
F	30:70 Beam Splitter Cube	Thorlabs BS019
G	90:10 Beam Splitter Cube	Thorlabs BS028
H	Microscope Objective	Zeiss LD EC Epiplan-Neofluar 100x/0,75 HD DIC M27
I	Film Polarizer	Thorlabs LPVISE2X2
J	Achromatic Lens	Thorlabs AC254-150-A-ML
K	Bandpass Filter	Thorlabs FB450-40
L	EMCCD Camera	Andor Luca DL-658M-OEM
M	Zero-Order Half-Wave Plate	Thorlabs WPH10ME-532
N	Motorized Rotation Stage	Thorlabs DDR25/M
O	Polarizing Beam Splitter Cube	Thorlabs PBS251
P	Fiber coupling + lens	Thorlabs KT100/M (modified) + Thorlabs C240TME-A
Q	FC/APC Optical Fiber	Thorlabs P5-460AR-2
R	Fast Broadband Photodetector	New Focus 1414
S	Low-Noise Amplifier	Narda-MITEQ AFS4-02001 800-24-10P-4
T	Aspheric lens	Thorlabs A280TM-A
U	Tandem Fabry-Pérot interferometer (TFPI)	The Table Stable Ltd. Tandem Interferometer TFP-1
V	Pulsed Laser + 2x Dichroic mirrors	NKT Photonics Origami 05 LP + 2x Thorlabs DMLP650
W	Achromatic Lens	Thorlabs AC254-400-A-ML
X	Zero-Order Half-Wave Plate	Thorlabs WPH05M-514
Y	Wollaston Prism	Thorlabs WP10-A
Z	15mm lens mounted on XYZ Dovetail stage	Thorlabs LA1222-A + Thorlabs DT12XYZ/M
α	Balanced Photodetector	Thorlabs PDB435A

A.1.1 Köhler Illumination

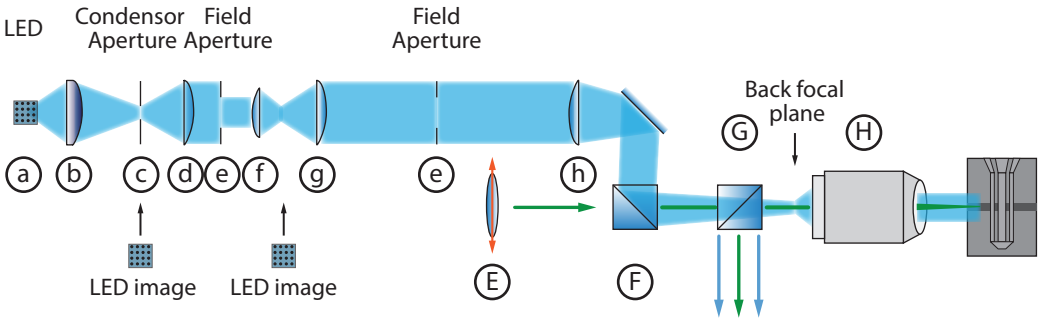

Fig. A.2. Optical path of the Köhler illumination used in the optical setup. The idea of a Köhler illumination is to focus the LED onto the back-focal plane of the microscope objective (MO) so that the light of the LED is parallel after the MO. The first iris adjusts the brightness and the second iris ("field aperture") controls the size of the illuminated area. The used optical elements are listed in Tab. A.2

Tab. A.2. Parts list of the optical elements used in the Köhler illumination depicted in Fig. A.2.

Label	Optical element	Focal length	Part number
a	Blue LED ($\lambda = 455$ nm)		Thorlabs M455L4
b	Aspheric condenser lens	40 mm	Thorlabs ACL5040U-A
c	Iris diaphragms		Thorlabs SM1D25
d	Plano-convex lens	75 mm	Thorlabs LA1145-A
e	Plano-convex lens	30 mm	Thorlabs LA1805-A
f	Iris diaphragms		Thorlabs ID36/M
g	Plano-convex lens	200 mm	Thorlabs LA1979-A
h	Plano-convex lens	300 mm	Thorlabs LA1256-A

A.2 Measurement and Auto-Stabilization Software for a Tandem Fabry-Pérot Interferometer

The Brillouin light scattering (BLS) technique requires the use of a tandem Fabry-Pérot interferometer (TFPI) to analyze the inelastically scattered photons in a frequency-resolved manner. To this end it is necessary to assure long-term stability of the optical alignment in the TFPI which crucially depends on the parallelism of the FP1 and FP2 mirrors and on the precise synchronization of the mirror distance difference between FP1 and FP2. The employed TFPI (JRS Systems, TFP1) has a control unit with analog circuits inside and only possesses an analog remote interface in the form of a D-Sub 15 connector. The use of this remote connector disables the auto-stabilization circuit in the control unit. Due to the required compatibility with the existing measurement software, which is not featured in commercially available software, a new software called “BLScontrol” was developed during this thesis. The user interface of the software is shown in Fig. A.3(a).

We use a compact digital data acquisition (cDAQ) system from National Instruments (NI cDAQ-9174) featuring four slots for input/output modules and is connected via USB to the PC. The used cDAQ possesses an integrated TTL pulse counter running with a maximum base clock of 80 MHz, which we use to count the TTL pulses generated by the detected photons of the single-photon counter (Hamamatsu H10682), and more importantly allows to synchronously run tasks across the modules. On the PC the tasks for each module are programmed via LabView and then triggered (internal trigger in cDAQ) simultaneously. This is crucial because while the mirror spacing is permanently changed, the TTL pulses of the single photon detector are counted and correlated to the current mirror spacing and additionally the double shutter needs to switch between the measurement and reference beam at the correct timing.

From the available four slots of the cDAQ, three are occupied. The analog output module NI 9264 is used to apply voltages (± 5 V) that are control inputs for the piezos at the mirrors of FP1 and FP2. These voltages are amplified by the control unit and applied to the piezos at the mirrors. The piezos X1/X2 and Y1/Y2 are for the tilting of the mirror in horizontal and vertical direction of FP1 and FP2, respectively. The piezo dZ is for changing the mirror spacing of FP2 so the higher orders of the free-spectral-range of the TFPI are suppressed (cf. Section 5.2.4). Following the auto-stabilization procedure proposed in Ref. [225], these piezos are kept constant while scanning the stage and only changed between two scans.

The digital input/output module NI 9403 is used for boolean 5V-TTL logic which is necessary to switch between the optical alignment and tandem path inside the TFPI [206] and to control the double shutter. Furthermore, it would allow to control an additional shutter before the single photon detector, which is not present in our

system. The last module is another digital input/output module (NI 9401) but with a faster refresh time of 100 ns used for measuring TTL signals. On the one hand this module is used to determine the current optical path inside the TFPI (alignment or tandem path), check wether the optics is currently changed or not (busy) and counting the TTL pulses generated by the single-photon counter. The wiring of the modules is shown in Fig. A.3(b). The D-Sub 15 connector is found at the back of the control unit. The BNC output of the photodetector with the TTL pulses is first looped into the control unit of the TFPI, where the pulses are stretched for easier detection [206]. The stretched pulses from TTL out are then connected via a BNC cable to the NI 9401 module.

The LabView program "BLScontrol" is divided into five independently executed while-loops. In total three loops are responsible for the remote connection so other programs or PCs can connect via the TCP/IP protocol and control the TFPI. One loop just establishes and manages TCP/IP connections ("Connection manager"), the second loop processes received commands and the third loop sends data or parameters of current TFPI settings back to the client. For this purpose the NI Simple Messaging (STM) reference library[1] is used. The "User interface" loop processes commands either from the user via the LabView interface or from the remote interface and are consequently sent to the last loop, the "TFPI control" loop. The main task of this while-loop is to keep the TFPI aligned over time using the auto-stabilization algorithm proposed in Ref. [225] and to program the cDAQ to perform BLS measurements. The measured and averaged data is first sent to the user interface, where the data can be viewed in real time, and then to the remote interface if the measurement was started via the remote connection. This software is consequently fully compatible with the measurement software "DollRotate" used at the WMI to allow fully automated measurements, like for example complete xy-spatial scans of the magnetization dynamics.

[1] https://sine.ni.com/nips/cds/view/p/lang/de/nid/212055

(a)

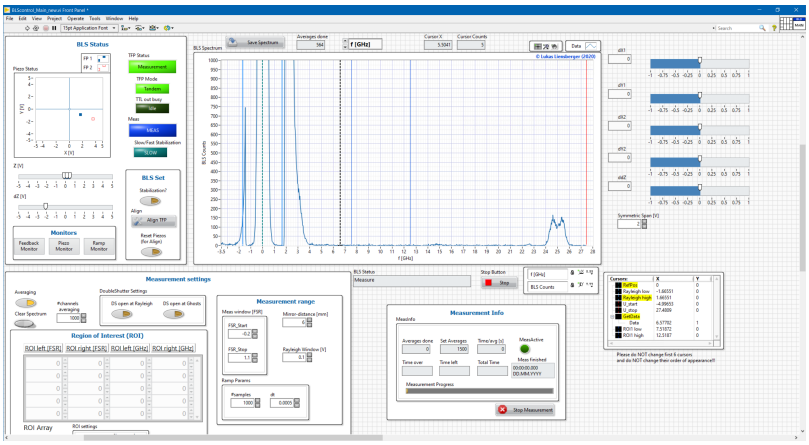

(b)

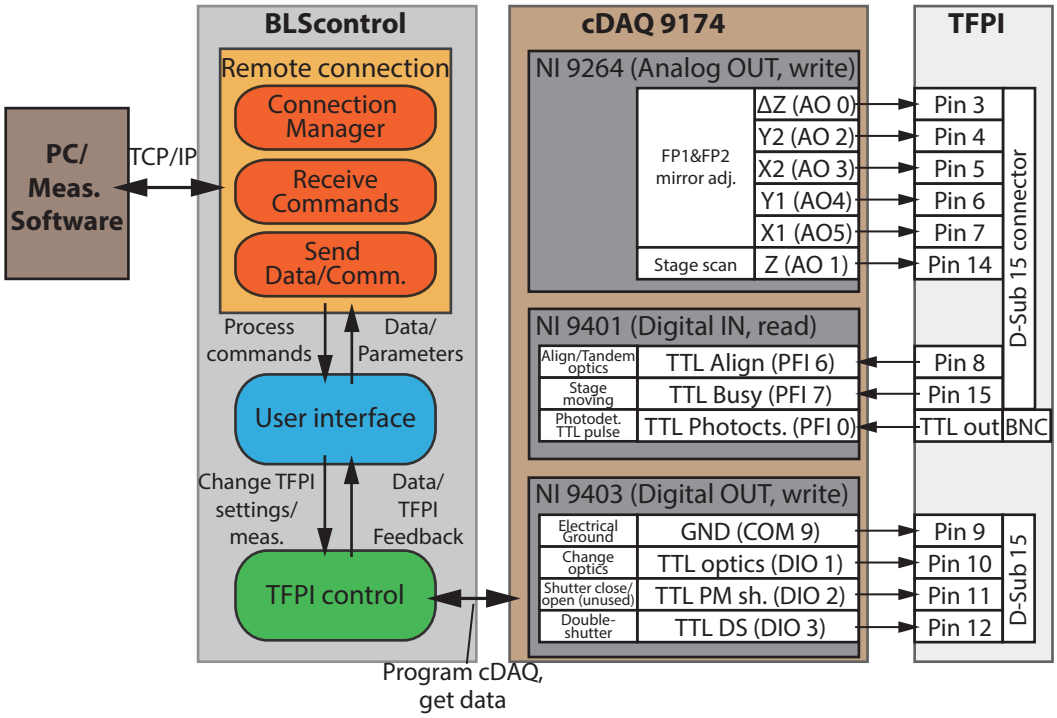

Fig. A.3. (a) Screenshot of the LabView user interface of the "BLScontrol" software developed during this thesis. (b) Block diagram of the working principle of the BLScontrol software. The rounded rectangles in BLScontrol denote independently running LabView while-loops. For details refer to text.

A.3 Sample Fabrication

In the following we list the process steps to fabricate the sample investigated in Chapter 5:

1. Cleaning of substrate in acetone and isopropyl.
2. Spincoating using PMMA 33% (AR-P 617.08) at 4000 rpm for 1 min and bake-out at 170 °C for 2 min.
3. Electron beam lithography with base dose $6.5\,\mathrm{C/m^2}$.
4. Development of sample in AR600-46 for 2 min and then in isopropyl for 30 s while puddling.
5. Sputtering (see below)
6. Lift-off in hot acetone using a pipette and cleaning with isopropyl.

For the sample we used a $6 \times 10 \times 0.525\,\mathrm{mm^3}$ Si substrate with 1000 nm of thermal oxide, where in total 10 structures with different widths of the magnonic waveguide and two different microwave antenna designs were patterned. In the first step, platinum markers with a size of $10 \times 10\,\mu\mathrm{m^2}$ and thickness 50 nm were structured, which are used for aligning the different layers during the electron beam lithography step. In the second step the magnonic waveguide is structured. For the dc-sputtering process in the SUPERBOWL facility of the WMI, the parameters shown in Tab. A.3 were used. In the last step, the on-chip antenna is patterned.

Tab. A.3. Sputtering parameters for the magnonic waveguide and the on-chip antenna of the sample used in Chapter 5. The rates were determined prior the sputtering process of the samples using the quartz crystal. The pressure inside the sputtering chamber is 5×10^{-3} mbar.

Material	Nominal thickness	Power	Rate	Tilt
Pt	3 nm	6 W	1.12 Å/s	tilt out
Cu	3 nm	20 W	1.08 Å/s	tilt in
$Co_{25}Fe_{75}$	50 nm	20 W	1.70 Å/s	tilt out
Cu	3 nm	20 W	1.08 Å/s	tilt in
Ta	3 nm	30 W	0.71 Å/s	tilt in
SiOx	30 nm	60 W	0.34 Å/s	tilt in
Au	100 nm	25 W	1.46 Å/s	tilt in

List of Publications

- L. Liensberger, L Flacke, D. Rogerson, M. Althammer, R. Gross, and M. Weiler, *Spin-wave propagation in metallic $Co_{25}Fe_{75}$ films determined by microfocused frequency-resolved magneto-optic Kerr effect*, IEEE Magnetics Letters **10**, 5503905 (2019)
- L. Liensberger, A. Kamra, H. Maier-Flaig, S. Geprägs, A. Erb, S. T. B. Goennenwein, R. Gross, W. Belzig, H. Huebl, and M. Weiler, *Exchange-Enhanced Ultrastrong Magnon-Magnon Coupling in a Compensated Ferrimagnet*, Physical Review Letters **123**, 117204 (2019)
- T. Wimmer, M. Althammer, L. Liensberger, N. Vlietstra, S. Geprägs, M. Weiler, R. Gross, and H. Huebl, *Spin transport in a magnetic insulator with zero effective damping*, Physical Review Letters **123**, 257201 (2019)
- L. Flacke, L. Liensberger, M. Althammer, H. Huebl, S. Geprägs, K. Schultheiss, A. Buzdakov, T. Hula, H. Schultheiss, E. R. J. Edwards, H. T. Nembach, J. M. Shaw, R. Gross, M. Weiler, *High Spin-Wave Propagation Length Consistent with Low Damping in a Metallic Ferromagnet*, Applied Physics Letters **115**, 122402 (2019)
- D. Schwienbacher, M. Pernpeintner, L. Liensberger, E. R. J. Edwards, H. T. Nembach, J. M. Shaw, M. Weiler, R. Gross, H. Huebl, *Magnetoelasticity of Co25Fe75 thin films*, Journal of Applied Physics **126**, 103902 (2019)
- T. Hula, K. Schultheiss, A. Buzdakov, L. Körber, M. Bejarano, L. Flacke, L. Liensberger, M. Weiler, J. M. Shaw, H. T. Nembach, J. Fassbender, H. Schultheiss, *Nonlinear losses in magnon transport due to four-magnon scattering*, Applied Physics Letters **117**, 042404 (2020)
- M. Meinert, B. Gliniors, O. Gueckstock, T. S. Seifert, L. Liensberger, M. Weiler, S. Wimmer, H. Ebert, T. Kampfrath, *High-throughput techniques for measuring the spin Hall effect*, Physical Review Applied **14**, 064011 (2020)
- M. Müller, L. Liensberger, L. Flacke, H. Huebl, A. Kamra, W. Belzig, R. Gross, M. Weiler, M. Althammer, *Temperature-dependent spin-transport and current-induced torques in superconductor/ferromagnet heterostructures*, Physical Review Letters **126**, 087201 (2021)

- E. Shigematsu, L. Liensberger, M. Weiler, R. Ohshima, Y. Ando, T. Shinjo, H. Huebl, M. Shiraishi, *Spin to charge conversion in Si/Cu/ferromagnet systems investigated by ac inductive measurements*, Physical Review B **103**, 094430 (2021)
- M. Müller, R. Hoepfl, L. Liensberger, S. Geprägs, H. Huebl, M. Weiler, R. Gross, M. Althammer, *Growth optimization of TaN for superconducting spintronics*, arXiv:2102.09018 (2021) (submitted for publication)
- L. Flacke, V. Ahrens, S. Mendisch, L. Körber, T. Böttcher, E. Meidinger, M. Yaqoob, M. Müller, L. Liensberger, A. Kákay, M. Becherer, P. Pirro, M. Althammer, S. Geprägs, H. Huebl, R. Gross, M. Weiler, *Robust formation of nanoscale magnetic skyrmions in easy-plane thin film multilayers with low damping*, arXiv:2102.11117 (2021) (submitted for publication)
- L. Liensberger, F. X. Haslbeck, A. Bauer, H. Berger, R. Gross, H. Huebl, C. Pfleiderer, M. Weiler, *Tunable Cooperativity in Coupled Spin-Cavity Systems*, arXiv:2102.11713 (2021) (submitted for publication)

Bibliography

[1] M. M. Waldrop, *The chips are down for Moore's law*, Nature **530**, 144–147 (2016).

[2] N. Fu, Y. Liu, X. Ma, and Z. Chen, *EUV Lithography: State-of-the-Art Review*, Journal of Microelectronic Manufacturing **2**, 1–6 (2019).

[3] G. M. Moore, *Cramming more components onto integrated circuits*, Electronics **38**, 114 (1965).

[4] M. N. Baibich, J. M. Broto, A. Fert, F. N. Van Dau, F. Petroff, P. Etienne, G. Creuzet, A. Friederich, and J. Chazelas, *Giant Magnetoresistance of (001)Fe/(001)Cr Magnetic Superlattices*, Physical Review Letters **61**, 2472–2475 (1988).

[5] G. Binasch, P. Grünberg, F. Saurenbach, and W. Zinn, *Enhanced magnetoresistance in layered magnetic structures with antiferromagnetic interlayer exchange*, Physical Review B **39**, 4828–4830 (1989).

[6] A. Fert, *Nobel Lecture: Origin, development, and future of spintronics*, Reviews of Modern Physics **80**, 1517–1530 (2008).

[7] M. Julliere, *Tunneling between ferromagnetic films*, Physics Letters A **54**, 225–226 (1975).

[8] A. Fert and F. N. Van Dau, *Spintronics, from giant magnetoresistance to magnetic skyrmions and topological insulators*, Comptes Rendus Physique **20**, 817–831 (2019).

[9] S. Bhatti, R. Sbiaa, A. Hirohata, H. Ohno, S. Fukami, and S. Piramanayagam, *Spintronics based random access memory: a review*, Materials Today **20**, 530–548 (2017).

[10] J. Åkerman, *Toward a universal memory*, Science **308**, 508–510 (2005).

[11] H.-S. P. Wong and S. Salahuddin, *Memory leads the way to better computing*, Nature Nanotechnology **10**, 191–194 (2015).

[12] S. Peng, Y. Zhang, M. Wang, Y. Zhang, and W. Zhao, *Magnetic Tunnel Junctions for Spintronics: Principles and Applications*, Wiley Encyclopedia of Electrical and Electronics Engineering **1936**, 1–16 (2014).

[13] X. Fong, Y. Kim, R. Venkatesan, S. H. Choday, A. Raghunathan, and K. Roy, *Spin-Transfer Torque Memories: Devices, Circuits, and Systems*, Proceedings of the IEEE **104**, 1449–1488 (2016).

[14] S. Umesh and S. Mittal, *A survey of spintronic architectures for processing-in-memory and neural networks*, Journal of Systems Architecture **97**, 349–372 (2019).

[15] S. S. P. Parkin, M. Hayashi, and L. Thomas, *Magnetic Domain-Wall Racetrack Memory*, Science **320**, 190–194 (2008).

[16] A. Hirohata and K. Takanashi, *Future perspectives for spintronic devices*, Journal of Physics D: Applied Physics **47**, 193001 (2014).

[17] S. Parkin and S.-H. Yang, *Memory on the racetrack*, Nature Nanotechnology **10**, 195–198 (2015).

[18] A. Hirohata, K. Yamada, Y. Nakatani, I.-l. Prejbeanu, B. Diény, P. Pirro, and B. Hillebrands, *Review on spintronics: Principles and device applications*, Journal of Magnetism and Magnetic Materials **509**, 166711 (2020).

[19] A. V. Chumak, V. I. Vasyuchka, A. A. Serga, and B. Hillebrands, *Magnon spintronics*, Nature Physics **11**, 453–461 (2015).

[20] A. Mahmoud, F. Ciubotaru, F. Vanderveken, A. V. Chumak, S. Hamdioui, C. Adelmann, and S. Cotofana, *Introduction to spin wave computing*, Journal of Applied Physics **128**, 161101 (2020).

[21] G. Kurizki, P. Bertet, Y. Kubo, K. Mølmer, D. Petrosyan, P. Rabl, and J. Schmiedmayer, *Quantum technologies with hybrid systems*, Proceedings of the National Academy of Sciences **112**, 3866–3873 (2015).

[22] D. Lachance-Quirion, Y. Tabuchi, A. Gloppe, K. Usami, and Y. Nakamura, *Hybrid quantum systems based on magnonics*, Applied Physics Express **12**, 070101 (2019).

[23] Y. Li, W. Zhang, V. Tyberkevych, W.-K. Kwok, A. Hoffmann, and V. Novosad, *Hybrid magnonics: Physics, circuits, and applications for coherent information processing*, Journal of Applied Physics **128**, 130902 (2020).

[24] Y. Tabuchi, S. Ishino, A. Noguchi, T. Ishikawa, R. Yamazaki, K. Usami, and Y. Nakamura, *Coherent coupling between a ferromagnetic magnon and a superconducting qubit*, Science **349**, 405–408 (2015).

[25] A. Barman and J. Sinha, *Spin Dynamics and Damping in Ferromagnetic Thin Films and Nanostructures*, 1st ed. (Springer International Publishing, Cham, 2018) p. 166.

[26] J. M. D. Coey, *Magnetism and Magnetic Materials*, 1st ed. (Cambridge University Press, 2001) p. 633.

[27] N. W. Ashrocft and D. N. Mermin, *Festkörperphysik*, 4th ed. (Oldenbourg Wissenschaftsverlag, München, 2012) p. 1050.

[28] S. Blundell, *Magnetism in Condensed Matter*, oxford mas ed. (Oxford University Press, 2000) p. 238.

[29] H. Zabel and M. Farle, *Magnetic Nanostructures*, 1st ed., edited by H. Zabel and M. Farle, Springer Tracts in Modern Physics, Vol. 246 (Springer Berlin Heidelberg, Berlin, Heidelberg, 2013) p. 268.

[30] E. Beaurepaire, J.-C. Merle, A. Daunois, and J.-Y. Bigot, *Ultrafast Spin Dynamics in Ferromagnetic Nickel*, Physical Review Letters **76**, 4250–4253 (1996).

[31] A. Barman and A. Haldar, *Solid State Physics - Advances in Research and Applications*, 1st ed., Vol. 65 (Elsevier Inc., 2014) p. 108.

[32] B. Lax and K. Button, *Microwave ferrites and ferrimangetics* (McGraw-Hill, 1962) p. 752.

[33] S. Vonsovskii, *Ferromagnetic Resonance* (Pergamon Press, 1964) p. 340.

[34] A. Gurevich and G. Melkov, *Magnetization Oscillations and Waves* (CRC Press, Taylor & Francis Group, 1996) p. 445.

[35] D. D. Stancil and A. Prabhakar, *Spin Waves*, 1st ed. (Springer US, Boston, MA, 2009) p. 348.

[36] W. Heisenberg, *Zur Theorie des Ferromagnetismus*, Zeitschrift für Physik **49**, 619–636 (1928).

[37] L. Dreher, M. Weiler, M. Pernpeintner, H. Huebl, R. Gross, M. S. Brandt, and S. T. B. Goennenwein, *Surface acoustic wave driven ferromagnetic resonance in nickel thin films: Theory and experiment*, Physical Review B **86**, 134415 (2012).

[38] R. Gross and A. Marx, *Festkörperphysik*, 2nd ed. (Walter de GruyterVerlag, 2014) p. 1024.

[39] R. C. O'Handley, *Modern Magnetic Materials: Principles and Applications*, 1st ed. (Wiley, 1999) p. 740.

[40] T. Miyazaki and H. Jin, *The Physics of Ferromagnetism*, 1st ed., Springer Series in Materials Science, Vol. 158 (Springer Berlin Heidelberg, Berlin, Heidelberg, 2012) p. 484.

[41] H. S. Körner, M. A. W. Schoen, T. Mayer, M. M. Decker, J. Stigloher, T. Weindler, T. N. G. Meier, M. Kronseder, and C. H. Back, *Magnetic damping in poly-crystalline Co25Fe75 : Ferromagnetic resonance vs. spin wave propagation experiments*, Applied Physics Letters **111**, 132406 (2017).

[42] J. A. Osborn, *Demagnetizing Factors of the General Ellipsoid*, Physical Review **67**, 351–357 (1945).

[43] B. Heinrich and J. A. C. Bland, *Ultrathin Magnetic Structures II*, 1st ed., edited by B. Heinrich and J. A. C. Bland (Springer Berlin Heidelberg, Berlin, Heidelberg, 2005) p. 350.

[44] L. D. Landau and E. Lifshitz, *On the theory of the dispersion of magnetic permeability in ferromagnetic bodies*, Physikalische Zeitschrift der Sowjetunion **8**, 153 (1935).

[45] J. A. C. Bland and B. Heinrich, *Ultrathin Magnetic Structures III*, 1st ed., edited by J. A. C. Bland and B. Heinrich (Springer-Verlag, Berlin/Heidelberg, 2005) p. 318.

[46] M. A. W. Schoen, J. M. Shaw, H. T. Nembach, M. Weiler, and T. J. Silva, *Radiative damping in waveguide-based ferromagnetic resonance measured via analysis of perpendicular standing spin waves in sputtered permalloy films*, Physical Review B **92**, 184417 (2015).

[47] T. Gilbert, *A Phenomenological Theory of Damping in Ferromagnetic Materials*, IEEE Transactions on Magnetics **40**, 3443–3449 (2004).

[48] L. Liensberger, *Spin-Orbit Torques and Magnetization Dynamics in Non-collinear Magnets*, Master's thesis, Technische Universität München (2017).

[49] D. Polder, *VIII. On the theory of ferromagnetic resonance*, The London, Edinburgh, and Dublin Philosophical Magazine and Journal of Science **40**, 99–115 (1949).

[50] C. Kittel, *On the Theory of Ferromagnetic Resonance Absorption*, Physical Review **73**, 155–161 (1948).

[51] L. Flacke, L. Liensberger, M. Althammer, H. Huebl, S. Geprägs, K. Schultheiss, A. Buzdakov, T. Hula, H. Schultheiss, E. R. J. Edwards,

H. T. Nembach, J. M. Shaw, R. Gross, and M. Weiler, *High spin-wave propagation length consistent with low damping in a metallic ferromagnet*, Applied Physics Letters **115**, 122402 (2019).

[52] D. I. Schuster, A. P. Sears, E. Ginossar, L. DiCarlo, L. Frunzio, J. J. L. Morton, H. Wu, G. A. D. Briggs, B. B. Buckley, D. D. Awschalom, and R. J. Schoelkopf, *High-Cooperativity Coupling of Electron-Spin Ensembles to Superconducting Cavities*, Physical Review Letters **105**, 140501 (2010).

[53] Y. Kubo, F. R. Ong, P. Bertet, D. Vion, V. Jacques, D. Zheng, A. Dréau, J.-F. Roch, A. Auffeves, F. Jelezko, J. Wrachtrup, M. F. Barthe, P. Bergonzo, and D. Esteve, *Strong Coupling of a Spin Ensemble to a Superconducting Resonator*, Physical Review Letters **105**, 140502 (2010).

[54] N. Samkharadze, G. Zheng, N. Kalhor, D. Brousse, A. Sammak, U. C. Mendes, A. Blais, G. Scappucci, and L. M. K. Vandersypen, *Strong spin-photon coupling in silicon*, Science **359**, 1123–1127 (2018).

[55] H. Huebl, C. W. Zollitsch, J. Lotze, F. Hocke, M. Greifenstein, A. Marx, R. Gross, and S. T. B. Goennenwein, *High Cooperativity in Coupled Microwave Resonator Ferrimagnetic Insulator Hybrids*, Physical Review Letters **111**, 127003 (2013).

[56] X. Zhang, C. L. Zou, L. Jiang, and H. X. Tang, *Strongly coupled magnons and cavity microwave photons*, Physical Review Letters **113**, 156401 (2014).

[57] L. Bai, M. Harder, Y. P. Chen, X. Fan, J. Q. Xiao, and C.-M. Hu, *Spin Pumping in Electrodynamically Coupled Magnon-Photon Systems*, Physical Review Letters **114**, 227201 (2015).

[58] T. Liu, X. Zhang, H. X. Tang, and M. E. Flatté, *Optomagnonics in magnetic solids*, Physical Review B **94**, 060405(R) (2016).

[59] S. Viola Kusminskiy, H. X. Tang, and F. Marquardt, *Coupled spin-light dynamics in cavity optomagnonics*, Physical Review A **94**, 033821 (2016).

[60] M. Harder and C.-M. Hu, *Cavity Spintronics: An Early Review of Recent Progress in the Study of Magnon–Photon Level Repulsion*, in *Solid State Physics 69*, edited by R. E. Camley and R. L. Stamps (Academic Press, Cambridge, 2018) pp. 47–121.

[61] R. Hisatomi, A. Osada, Y. Tabuchi, T. Ishikawa, A. Noguchi, R. Yamazaki, K. Usami, and Y. Nakamura, *Bidirectional conversion between microwave and light via ferromagnetic magnons*, Physical Review B **93**, 174427 (2016).

[62] S. Klingler, H. Maier-Flaig, R. Gross, C.-M. Hu, H. Huebl, S. T. B. Goennenwein, and M. Weiler, *Combined Brillouin light scattering and microwave absorption study of magnon-photon coupling in a split-ring resonator/YIG film system*, Applied Physics Letters **109**, 072402 (2016).

[63] C. Eichler, A. J. Sigillito, S. A. Lyon, and J. R. Petta, *Electron Spin Resonance at the Level of 10^4 Spins Using Low Impedance Superconducting Resonators*, Physical Review Letters **118**, 037701 (2017).

[64] M. Tavis and F. W. Cummings, *Exact Solution for an N-Molecule-Radiation-Field Hamiltonian*, Physical Review **170**, 379–384 (1968).

[65] H. Maier-Flaig, M. Harder, S. Klingler, Z. Qiu, E. Saitoh, M. Weiler, S. Geprägs, R. Gross, S. T. B. Goennenwein, and H. Huebl, *Tunable magnon-photon coupling in a compensating ferrimagnet - from weak to strong coupling*, Applied Physics Letters **110**, 132401 (2017).

[66] B. Zare Rameshti and G. E. W. Bauer, *Indirect coupling of magnons by cavity photons*, Physical Review B **97**, 014419 (2018).

[67] Ø. Johansen and A. Brataas, *Nonlocal Coupling between Antiferromagnets and Ferromagnets in Cavities*, Physical Review Letters **121**, 087204 (2018).

[68] S. Klingler, V. Amin, S. Geprägs, K. Ganzhorn, H. Maier-Flaig, M. Althammer, H. Huebl, R. Gross, R. D. McMichael, M. D. Stiles, S. T. Goennenwein, and M. Weiler, *Spin-Torque Excitation of Perpendicular Standing Spin Waves in Coupled YIG/Co Heterostructures*, Physical Review Letters **120**, 127201 (2018).

[69] J. Chen, C. Liu, T. Liu, Y. Xiao, K. Xia, G. E. W. Bauer, M. Wu, and H. Yu, *Strong Interlayer Magnon-Magnon Coupling in Magnetic Metal-Insulator Hybrid Nanostructures*, Physical Review Letters **120**, 217202 (2018).

[70] H. Qin, S. J. Hämäläinen, and S. van Dijken, *Exchange-torque-induced excitation of perpendicular standing spin waves in nanometer-thick YIG films*, Scientific Reports **8**, 5755 (2018).

[71] T. Kampfrath, A. Sell, G. Klatt, A. Pashkin, S. Mährlein, T. Dekorsy, M. Wolf, M. Fiebig, A. Leitenstorfer, and R. Huber, *Coherent terahertz control of antiferromagnetic spin waves*, Nature Photonics **5**, 31–34 (2011).

[72] L. Liensberger, A. Kamra, H. Maier-Flaig, S. Geprägs, A. Erb, S. T. B. Goennenwein, R. Gross, W. Belzig, H. Huebl, and M. Weiler, *Exchange-Enhanced Ultrastrong Magnon-Magnon Coupling in a Compensated Ferrimagnet*, Physical Review Letters **123**, 117204 (2019).

[73] G. F. Dionne, *Magnetic Oxides* (Springer US, Boston, MA, 2009).

[74] V. Cherepanov, I. Kolokolov, and V. L'vov, *The saga of YIG: Spectra, thermodynamics, interaction and relaxation of magnons in a complex magnet*, Physics Reports **229**, 81–144 (1993).

[75] J. D. Adam, L. E. Davis, G. F. Dionne, E. F. Schloemann, and S. N. Stitzer, *Ferrite devices and materials*, IEEE Transactions on Microwave Theory and Techniques **50**, 721–737 (2002).

[76] E. Mallmann, A. Sombra, J. Goes, and P. Fechine, *Yttrium Iron Garnet: Properties and Applications Review*, Solid State Phenomena **202**, 65–96 (2013).

[77] C. D. Stanciu, A. V. Kimel, F. Hansteen, A. Tsukamoto, A. Itoh, A. Kirilyuk, and T. Rasing, *Ultrafast spin dynamics across compensation points in ferrimagnetic GdFeCo : The role of angular momentum compensation*, Physical Review B **73**, 220402 (2006).

[78] G. P. Rodrigue, H. Meyer, and R. V. Jones, *Resonance Measurements in Magnetic Garnets*, Journal of Applied Physics **31**, S376–S382 (1960).

[79] S. Koohpayeh, *Single crystal growth by the traveling solvent technique: A review*, Progress in Crystal Growth and Characterization of Materials **62**, 22–34 (2016).

[80] G. F. Dionne, *Molecular Field Coefficients of Substituted Yttrium Iron Garnets*, Journal of Applied Physics **41**, 4874–4881 (1970).

[81] G. F. Dionne, *Molecular Field and Exchange Constants of Gd^{3+}-Substituted Ferrimagnetic Garnets*, Journal of Applied Physics **42**, 2142–2143 (1971).

[82] G. P. Espinosa, *Crystal Chemical Study of the Rare-Earth Iron Garnets*, The Journal of Chemical Physics **37**, 2344–2347 (1962).

[83] H. Maier-Flaig, *Magnetic Resonance of Ferrimagnetic Insulators*, Phd thesis, Technische Universität München (2017).

[84] A. Kamra, U. Agrawal, and W. Belzig, *Noninteger-spin magnonic excitations in untextured magnets*, Physical Review B **96**, 020411(R) (2017).

[85] A. Kamra and W. Belzig, *Super-Poissonian Shot Noise of Squeezed-Magnon Mediated Spin Transport*, Physical Review Letters **116**, 146601 (2016).

[86] D. MacNeill, J. T. Hou, D. R. Klein, P. Zhang, P. Jarillo-Herrero, and L. Liu, *Gigahertz Frequency Antiferromagnetic Resonance and Strong Magnon-Magnon Coupling in the Layered Crystal CrCl3*, Physical Review Letters **123**, 047204 (2019).

[87] A. Kamra, E. Thingstad, G. Rastelli, R. A. Duine, A. Brataas, W. Belzig, and A. Sudbø, *Antiferromagnetic magnons as highly squeezed Fock states underlying quantum correlations*, Physical Review B **100**, 174407 (2019).

[88] F. Keffer and C. Kittel, *Theory of Antiferromagnetic Resonance*, Physical Review **85**, 329–337 (1952).

[89] A. Kamra, R. E. Troncoso, W. Belzig, and A. Brataas, *Gilbert damping phenomenology for two-sublattice magnets*, Physical Review B **98**, 184402 (2018).

[90] S. S. Kalarickal, P. Krivosik, M. Wu, C. E. Patton, M. L. Schneider, P. Kabos, T. J. Silva, and J. P. Nibarger, *Ferromagnetic resonance linewidth in metallic thin films: Comparison of measurement methods*, Journal of Applied Physics **99**, 093909 (2006).

[91] C. Wen, *Coplanar Waveguide: A Surface Strip Transmission Line Suitable for Nonreciprocal Gyromagnetic Device Applications*, IEEE Transactions on Microwave Theory and Techniques **17**, 1087–1090 (1969).

[92] D. Pozar, *Microwave Engineering*, 4th ed. (Wiley, 2011) p. 752.

[93] O. Karlqvist, *Calculation of the magnetic field in the ferromagnetic layer of a magnetic drum.* (Elanders boktr., Göteborg; [Stockholm], 1954) pp. 3–27.

[94] T. J. Silva, H. T. Nembach, J. M. Shaw, B. Doyle, K. Oguz, K. O'brien, and M. Doczy, *Characterization of Magnetic Nanostructures for Spin-Torque Memory Applications with Macro- and Micro-Scale Ferromagnetic Resonance*, in *Metrology and Diagnostic Techniques for Nanoelectronics* (CRC Press, Taylor & Francis Group, 2016) Chap. 16, p. 1454.

[95] M. Hiebel, *Fundamentals of vector network analysis* (Rohde & Schwarz, 2007) p. 419.

[96] A. J. Berger, E. R. J. Edwards, H. T. Nembach, A. D. Karenowska, M. Weiler, and T. J. Silva, *Inductive detection of fieldlike and dampinglike ac inverse spin-orbit torques in ferromagnet/normal-metal bilayers*, Physical Review B **97**, 094407 (2018).

[97] P. D. Louis, *Broadband-Spectroscopy of Magnetic Materials at Low Temperatures*, Master thesis, Technische Universität München (2016).

[98] T. J. Silva, C. S. Lee, T. M. Crawford, and C. T. Rogers, *Inductive measurement of ultrafast magnetization dynamics in thin-film Permalloy*, Journal of Applied Physics **85**, 7849–7862 (1999).

[99] M. Meinert, B. Gliniors, O. Gueckstock, T. S. Seifert, L. Liensberger, M. Weiler, S. Wimmer, H. Ebert, and T. Kampfrath, *High-Throughput Techniques for Measuring the Spin Hall Effect*, Physical Review Applied **14**, 064011 (2020).

[100] H. Maier-Flaig, S. T. B. Goennenwein, R. Ohshima, M. Shiraishi, R. Gross, H. Huebl, and M. Weiler, *Note: Derivative divide, a method for the analysis of broadband ferromagnetic resonance in the frequency domain*, Review of Scientific Instruments **89**, 076101 (2018).

[101] T. Niemczyk, F. Deppe, H. Huebl, E. P. Menzel, F. Hocke, M. J. Schwarz, J. J. Garcia-Ripoll, D. Zueco, T. Hümmer, E. Solano, A. Marx, and R. Gross, *Circuit quantum electrodynamics in the ultrastrong-coupling regime*, Nature Physics **6**, 772–776 (2010).

[102] A. Frisk Kockum, A. Miranowicz, S. De Liberato, S. Savasta, and F. Nori, *Ultrastrong coupling between light and matter*, Nature Reviews Physics **1**, 19–40 (2019).

[103] B. A. Calhoun and M. J. Freiser, *Anisotropy of Gadolinium Iron Garnet*, Journal of Applied Physics **34**, 1140–1145 (1963).

[104] E. C. Stoner and E. P. Wohlfarth, *A Mechanism of Magnetic Hysteresis in Heterogeneous Alloys*, Philosophical Transactions of the Royal Society A: Mathematical, Physical and Engineering Sciences **240**, 599–642 (1948).

[105] S. Geschwind and L. R. Walker, *Exchange Resonances in Gadolinium Iron Garnet near the Magnetic Compensation Temperature*, Journal of Applied Physics **30**, S163–S170 (1959).

[106] A. Kamra, W. Belzig, and A. Brataas, *Magnon-squeezing as a niche of quantum magnonics*, Applied Physics Letters **117**, 090501 (2020).

[107] Y. Shiota, T. Taniguchi, M. Ishibashi, T. Moriyama, and T. Ono, *Tunable Magnon-Magnon Coupling Mediated by Dynamic Dipolar Interaction in Synthetic Antiferromagnets*, Physical Review Letters **125**, 017203 (2020).

[108] S. Mühlbauer, B. Binz, F. Jonietz, C. Pfleiderer, A. Rosch, A. Neubauer, R. Georgii, and P. Boni, *Skyrmion Lattice in a Chiral Magnet*, Science **323**, 915–919 (2009).

[109] F. Jonietz, S. Mühlbauer, C. Pfleiderer, A. Neubauer, W. Munzer, A. Bauer, T. Adams, R. Georgii, P. Boni, R. A. Duine, K. Everschor, M. Garst, and A. Rosch, *Spin Transfer Torques in MnSi at Ultralow Current Densities*, Science **330**, 1648–1651 (2010).

[110] T. Adams, A. Chacon, M. Wagner, A. Bauer, G. Brandl, B. Pedersen, H. Berger, P. Lemmens, and C. Pfleiderer, *Long-Wavelength Helimagnetic Order and Skyrmion Lattice Phase in Cu_2OSeO_3*, Physical Review Letters **108**, 237204 (2012).

[111] T. Schulz, R. Ritz, A. Bauer, M. Halder, M. Wagner, C. Franz, C. Pfleiderer, K. Everschor, M. Garst, and A. Rosch, *Emergent electrodynamics of skyrmions in a chiral magnet*, Nature Physics **8**, 301–304 (2012).

[112] S. Seki, X. Z. Yu, S. Ishiwata, and Y. Tokura, *Observation of Skyrmions in a Multiferroic Material*, Science **336**, 198–201 (2012).

[113] X. Yu, N. Kanazawa, W. Zhang, T. Nagai, T. Hara, K. Kimoto, Y. Matsui, Y. Onose, and Y. Tokura, *Skyrmion flow near room temperature in an ultralow current density*, Nature Communications **3**, 988 (2012).

[114] A. Fert, V. Cros, and J. Sampaio, *Skyrmions on the track*, Nature Nanotechnology **8**, 152–156 (2013).

[115] N. Nagaosa and Y. Tokura, *Topological properties and dynamics of magnetic skyrmions.*, Nature Nanotechnology **8**, 899–911 (2013).

[116] M. Garst, J. Waizner, and D. Grundler, *Collective spin excitations of helices and magnetic skyrmions: review and perspectives of magnonics in non-centrosymmetric magnets*, Journal of Physics D: Applied Physics **50**, 293002 (2017).

[117] N. Kanazawa, S. Seki, and Y. Tokura, *Noncentrosymmetric Magnets Hosting Magnetic Skyrmions*, Advanced Materials **29**, 1603227 (2017).

[118] A. Bauer, A. Chacon, M. Halder, and C. Pfleiderer, *Skyrmion Lattices Far from Equilibrium*, in *Topology in Magnetism*, edited by J. Zang, V. Cros, and A. Hoffmann (Springer, Cham, 2018) Chap. 5, pp. 151–176.

[119] Y. Onose, Y. Okamura, S. Seki, S. Ishiwata, and Y. Tokura, *Observation of Magnetic Excitations of Skyrmion Crystal in a Helimagnetic Insulator Cu_2OSeO_3*, Physical Review Letters **109**, 037603 (2012).

[120] T. Schwarze, J. Waizner, M. Garst, A. Bauer, I. Stasinopoulos, H. Berger, C. Pfleiderer, and D. Grundler, *Universal helimagnon and skyrmion excitations in metallic, semiconducting and insulating chiral magnets*, Nature Materials **14**, 478–483 (2015).

[121] M. Weiler, A. Aqeel, M. Mostovoy, A. Leonov, S. Geprägs, R. Gross, H. Huebl, T. T. M. Palstra, and S. T. B. Goennenwein, *Helimagnon Reso-*

nances in an Intrinsic Chiral Magnonic Crystal, Physical Review Letters **119**, 237204 (2017).

[122] I. Stasinopoulos, S. Weichselbaumer, A. Bauer, J. Waizner, H. Berger, S. Maendl, M. Garst, C. Pfleiderer, and D. Grundler, *Low spin wave damping in the insulating chiral magnet Cu2OSeO3*, Applied Physics Letters **111**, 032408 (2017).

[123] L. V. Abdurakhimov, S. Khan, N. A. Panjwani, J. D. Breeze, M. Mochizuki, S. Seki, Y. Tokura, J. J. L. Morton, and H. Kurebayashi, *Magnon-photon coupling in the noncollinear magnetic insulator Cu2OSeO3*, Physical Review B **99**, 140401(R) (2019).

[124] I. Dzyaloshinskii, *A thermodynamic theory of "weak" ferromagnetism of antiferromagnetics*, Journal of Physics and Chemistry of Solids **4**, 241–255 (1958).

[125] T. Moriya, *Anisotropic Superexchange Interaction and Weak Ferromagnetism*, Physical Review **120**, 91–98 (1960).

[126] H. T. Nembach, J. M. Shaw, M. Weiler, E. Jué, and T. J. Silva, *Linear relation between Heisenberg exchange and interfacial Dzyaloshinskii–Moriya interaction in metal films*, Nature Physics **11**, 825–829 (2015).

[127] M. Weiler, *Magnetization Dynamics and Spin Torques in Exchange-Coupled Spin Systems*, Habilitation dissertation, Technische Universität München (2019).

[128] M. Halder, A. Chacon, A. Bauer, W. Simeth, S. Mühlbauer, H. Berger, L. Heinen, M. Garst, A. Rosch, and C. Pfleiderer, *Thermodynamic evidence of a second skyrmion lattice phase and tilted conical phase in Cu2OSeO3*, Physical Review B **98**, 144429 (2018).

[129] J. Kindervater, I. Stasinopoulos, A. Bauer, F. X. Haslbeck, F. Rucker, A. Chacon, S. Mühlbauer, C. Franz, M. Garst, D. Grundler, and C. Pfleiderer, *Weak Crystallization of Fluctuating Skyrmion Textures in MnSi*, Physical Review X **9**, 041059 (2019).

[130] P. Milde, L. Köhler, E. Neuber, P. Ritzinger, M. Garst, A. Bauer, C. Pfleiderer, H. Berger, and L. M. Eng, *Field-induced reorientation of helimagnetic order in Cu2OSeO3 probed by magnetic force microscopy*, Physical Review B **102**, 024426 (2020).

[131] P. Bak and M. H. Jensen, *Theory of helical magnetic structures and phase transitions in MnSi and FeGe*, Journal of Physics C: Solid State Physics **13**, L881–L885 (1980).

[132] S. Seki and M. Mochizuki, *Skyrmions in Magnetic Materials*, SpringerBriefs in Physics (Springer International Publishing, Cham, Switzerland, 2016) p. 69.

[133] S. Woo, K. Litzius, B. Krüger, M.-Y. Im, L. Caretta, K. Richter, M. Mann, A. Krone, R. M. Reeve, M. Weigand, P. Agrawal, I. Lemesh, M.-A. Mawass, P. Fischer, M. Kläui, and G. S. D. Beach, *Observation of room-temperature magnetic skyrmions and their current-driven dynamics in ultrathin metallic ferromagnets*, Nature Materials **15**, 501–506 (2016).

[134] I. Kézsmárki, S. Bordács, P. Milde, E. Neuber, L. M. Eng, J. S. White, H. M. Rønnow, C. D. Dewhurst, M. Mochizuki, K. Yanai, H. Nakamura, D. Ehlers, V. Tsurkan, and A. Loidl, *Néel-type skyrmion lattice with confined orientation in the polar magnetic semiconductor GaV4S8*, Nature Materials **14**, 1116–1122 (2015).

[135] M. C. Langner, S. Roy, S. K. Mishra, J. C. T. Lee, X. W. Shi, M. A. Hossain, Y.-D. Chuang, S. Seki, Y. Tokura, S. D. Kevan, and R. W. Schoenlein, *Coupled Skyrmion Sublattices in Cu2OSeO3*, Physical Review Letters **112**, 167202 (2014).

[136] S. L. Zhang, A. Bauer, D. M. Burn, P. Milde, E. Neuber, L. M. Eng, H. Berger, C. Pfleiderer, G. van der Laan, and T. Hesjedal, *Multidomain Skyrmion Lattice State in Cu2OSeO3*, Nano Letters **16**, 3285–3291 (2016).

[137] X. Z. Yu, Y. Onose, N. Kanazawa, J. H. Park, J. H. Han, Y. Matsui, N. Nagaosa, and Y. Tokura, *Real-space observation of a two-dimensional skyrmion crystal*, Nature **465**, 901–904 (2010).

[138] P. Milde, D. Kohler, J. Seidel, L. M. Eng, A. Bauer, A. Chacon, J. Kindervater, S. Mühlbauer, C. Pfleiderer, S. Buhrandt, C. Schutte, and A. Rosch, *Unwinding of a Skyrmion Lattice by Magnetic Monopoles*, Science **340**, 1076–1080 (2013).

[139] P. Milde, E. Neuber, A. Bauer, C. Pfleiderer, H. Berger, and L. M. Eng, *Heuristic Description of Magnetoelectricity of Cu2OSeO3*, Nano Letters **16**, 5612–5618 (2016).

[140] M. Mochizuki, *Spin-Wave Modes and Their Intense Excitation Effects in Skyrmion Crystals*, Physical Review Letters **108**, 017601 (2012).

[141] M. J. Collett and C. W. Gardiner, *Squeezing of intracavity and travelling-wave light fields produced in parametric amplification*, Physical Review A **30**, 1386–1391 (1984).

[142] D. F. Walls and G. J. Milburn, *Quantum Optics* (Springer Berlin Heidelberg, Berlin, Heidelberg, 1994) p. 351.

[143] Ö. O. Soykal and M. E. Flatté, *Size dependence of strong coupling between nanomagnets and photonic cavities*, Physical Review B **82**, 104413 (2010).

[144] Ö. O. Soykal and M. E. Flatté, *Strong Field Interactions between a Nanomagnet and a Photonic Cavity*, Physical Review Letters **104**, 077202 (2010).

[145] E. Abe, H. Wu, A. Ardavan, and J. J. L. Morton, *Electron spin ensemble strongly coupled to a three-dimensional microwave cavity*, Applied Physics Letters **98**, 251108 (2011).

[146] A. A. Clerk, M. H. Devoret, S. M. Girvin, F. Marquardt, and R. J. Schoelkopf, *Introduction to quantum noise, measurement, and amplification*, Reviews of Modern Physics **82**, 1155–1208 (2010).

[147] G. A. Rinard and G. R. Eaton, *Loop-Gap Resonators*, in *Biomedical EPR, Part B: Methodology, Instrumentation, and Dynamics* (Kluwer Academic Publishers-Plenum Publishers, Boston, MA, 2005) Chap. 2, pp. 19–52.

[148] A. Bauer, A. Chacon, M. Wagner, M. Halder, R. Georgii, A. Rosch, C. Pfleiderer, and M. Garst, *Symmetry breaking, slow relaxation dynamics, and topological defects at the field-induced helix reorientation in MnSi*, Physical Review B **95**, 024429 (2017).

[149] N. J. Lambert, A. Rueda, F. Sedlmeir, and H. G. L. Schwefel, *Coherent Conversion Between Microwave and Optical Photons—An Overview of Physical Implementations*, Advanced Quantum Technologies **3**, 1900077 (2020).

[150] P. F. Herskind, A. Dantan, J. P. Marler, M. Albert, and M. Drewsen, *Realization of collective strong coupling with ion Coulomb crystals in an optical cavity*, Nature Physics **5**, 494–498 (2009).

[151] S. Seki, S. Ishiwata, and Y. Tokura, *Magnetoelectric nature of skyrmions in a chiral magnetic insulator Cu2OSeO3*, Physical Review B **86**, 060403 (2012).

[152] J. S. White, K. Prša, P. Huang, A. A. Omrani, I. Živković, M. Bartkowiak, H. Berger, A. Magrez, J. L. Gavilano, G. Nagy, J. Zang, and H. M. Rønnow, *Electric-Field-Induced Skyrmion Distortion and Giant Lattice Rotation in the Magnetoelectric Insulator Cu2OSeO3*, Physical Review Letters **113**, 107203 (2014).

[153] Y. Okamura, F. Kagawa, S. Seki, and Y. Tokura, *Transition to and from the skyrmion lattice phase by electric fields in a magnetoelectric compound*, Nature Communications **7**, 12669 (2016).

[154] S. P. Wolski, D. Lachance-Quirion, Y. Tabuchi, S. Kono, A. Noguchi, K. Usami, and Y. Nakamura, *Dissipation-Based Quantum Sensing of Magnons with a Superconducting Qubit*, Physical Review Letters **125**, 117701 (2020).

[155] B. Dieny, I. L. Prejbeanu, K. Garello, P. Gambardella, P. Freitas, R. Lehndorff, W. Raberg, U. Ebels, S. O. Demokritov, J. Akerman, A. Deac, P. Pirro, C. Adelmann, A. Anane, A. V. Chumak, A. Hirohata, S. Mangin, S. O. Valenzuela, M. C. Onbaşli, M. D'Aquino, G. Prenat, G. Finocchio, L. Lopez-Diaz, R. Chantrell, O. Chubykalo-Fesenko, and P. Bortolotti, *Opportunities and challenges for spintronics in the microelectronics industry*, Nature Electronics **3**, 446–459 (2020).

[156] A. Talalaevskij, M. Decker, J. Stigloher, A. Mitra, H. S. Körner, O. Cespedes, C. H. Back, and B. J. Hickey, *Magnetic properties of spin waves in thin yttrium iron garnet films*, Physical Review B **95**, 064409 (2017).

[157] A. V. Chumak, *Fundamentals of magnon-based computing*, arXiv:1901.08934 (2019).

[158] A. V. Chumak, A. A. Serga, and B. Hillebrands, *Magnon transistor for all-magnon data processing*, Nature Communications **5**, 4700 (2014).

[159] M. A. W. Schoen, D. Thonig, M. L. Schneider, T. J. Silva, H. T. Nembach, O. Eriksson, O. Karis, and J. M. Shaw, *Ultra-low magnetic damping of a metallic ferromagnet*, Nature Physics **12**, 839–842 (2016).

[160] L. Liensberger, L. Flacke, D. Rogerson, M. Althammer, R. Gross, and M. Weiler, *Spin-Wave Propagation in Metallic $Co_{25}Fe_{75}$ Films Determined by Microfocused Frequency-Resolved Magneto-Optic Kerr Effect*, IEEE Magnetics Letters **10**, 5503905 (2019).

[161] T. Hula, K. Schultheiss, A. Buzdakov, L. Körber, M. Bejarano, L. Flacke, L. Liensberger, M. Weiler, J. M. Shaw, H. T. Nembach, J. Fassbender, and H. Schultheiss, *Nonlinear losses in magnon transport due to four-magnon scattering*, Applied Physics Letters **117**, 042404 (2020).

[162] J. P. Park and P. A. Crowell, *Interactions of Spin Waves with a Magnetic Vortex*, Physical Review Letters **95**, 167201 (2005).

[163] Z. Liu, F. Giesen, X. Zhu, R. D. Sydora, and M. R. Freeman, *Spin Wave Dynamics and the Determination of Intrinsic Damping in Locally Excited Permalloy Thin Films*, Physical Review Letters **98**, 087201 (2007).

[164] J.-Y. Chauleau, H. G. Bauer, H. S. Körner, J. Stigloher, M. Härtinger, G. Woltersdorf, and C. H. Back, *Self-consistent determination of the key*

spin-transfer torque parameters from spin-wave Doppler experiments, Physical Review B **89**, 020403 (2014).

[165] V. E. Demidov, S. O. Demokritov, B. Hillebrands, M. Laufenberg, and P. P. Freitas, *Radiation of spin waves by a single micrometer-sized magnetic element*, Applied Physics Letters **85**, 2866–2868 (2004).

[166] V. E. Demidov and S. O. Demokritov, *Magnonic Waveguides Studied by Microfocus Brillouin Light Scattering*, IEEE Transactions on Magnetics **51**, 0800215 (2015).

[167] T. Sebastian, K. Schultheiss, B. Obry, B. Hillebrands, and H. Schultheiss, *Micro-focused Brillouin light scattering: imaging spin waves at the nanoscale*, Frontiers in Physics **3**, 00035 (2015).

[168] S. O. Demokritov, V. E. Demidov, O. Dzyapko, G. A. Melkov, A. A. Serga, B. Hillebrands, and A. N. Slavin, *Bose–Einstein condensation of quasi-equilibrium magnons at room temperature under pumping*, Nature **443**, 430–433 (2006).

[169] A. A. Serga, T. Schneider, B. Hillebrands, S. O. Demokritov, and M. P. Kostylev, *Phase-sensitive Brillouin light scattering spectroscopy from spin-wave packets*, Applied Physics Letters **89**, 063506 (2006).

[170] F. Fohr, A. A. Serga, T. Schneider, J. Hamrle, and B. Hillebrands, *Phase sensitive Brillouin scattering measurements with a novel magneto-optic modulator*, Review of Scientific Instruments **80**, 043903 (2009).

[171] K. Vogt, H. Schultheiss, S. J. Hermsdoerfer, P. Pirro, A. A. Serga, and B. Hillebrands, *All-optical detection of phase fronts of propagating spin waves in a Ni81Fe19 microstripe*, Applied Physics Letters **95**, 182508 (2009).

[172] R. Dreyer, N. Liebing, E. R. J. Edwards, and G. Woltersdorf, *Local spin-wave dispersion and damping in thin yttrium-iron-garnet films*, arXiv: 1803.04943 (2018).

[173] B. A. Kalinikos and A. N. Slavin, *Theory of dipole-exchange spin wave spectrum for ferromagnetic films with mixed exchange boundary conditions*, Journal of Physics C: Solid State Physics **19**, 7013–7033 (1986).

[174] J.-H. Moon, S.-M. Seo, K.-J. Lee, K.-W. Kim, J. Ryu, H.-W. Lee, R. D. McMichael, and M. D. Stiles, *Spin-wave propagation in the presence of interfacial Dzyaloshinskii-Moriya interaction*, Physical Review B **88**, 184404 (2013).

[175] K. Di, V. L. Zhang, H. S. Lim, S. C. Ng, M. H. Kuok, J. Yu, J. Yoon, X. Qiu, and H. Yang, *Direct Observation of the Dzyaloshinskii-Moriya Interaction in a Pt/Co/Ni Film*, Physical Review Letters **114**, 047201 (2015).

[176] R. Damon and J. Eshbach, *Magnetostatic modes of a ferromagnet slab*, Journal of Physics and Chemistry of Solids **19**, 308–320 (1961).

[177] A. A. Serga, A. V. Chumak, and B. Hillebrands, *YIG magnonics*, Journal of Physics D: Applied Physics **43**, 264002 (2010).

[178] J. Kerr, *XLIII. On rotation of the plane of polarization by reflection from the pole of a magnet*, The London, Edinburgh, and Dublin Philosophical Magazine and Journal of Science **3**, 321–343 (1877).

[179] Z. Q. Qiu and S. D. Bader, *Surface magneto-optic Kerr effect*, Review of Scientific Instruments **71**, 1243–1255 (2000).

[180] M. Freiser, *A survey of magnetooptic effects*, IEEE Transactions on Magnetics **4**, 152–161 (1968).

[181] J. Zak, E. Moog, C. Liu, and S. Bader, *Universal approach to magneto-optics*, Journal of Magnetism and Magnetic Materials **89**, 107–123 (1990).

[182] S. Bader, *SMOKE*, Journal of Magnetism and Magnetic Materials **100**, 440–454 (1991).

[183] Z. J. Yang and M. R. Scheinfein, *Combined three-axis surface magneto-optical Kerr effects in the study of surface and ultrathin-film magnetism*, Journal of Applied Physics **74**, 6810–6823 (1993).

[184] S. Sugano and N. Kojima, eds., *Magneto-Optics*, 1st ed., Springer Series in Solid-State Sciences, Vol. 128 (Springer Berlin Heidelberg, Berlin, Heidelberg, 2000) p. 338.

[185] W. Kuch, R. Schäfer, P. Fischer, and F. U. Hillebrecht, *Magnetic Microscopy of Layered Structures*, 1st ed., Springer Series in Surface Sciences, Vol. 57 (Springer Berlin Heidelberg, Berlin, Heidelberg, 2015) p. 246.

[186] J. D. Jackson, *Klassische Elektrodynamik*, 5th ed. (De Gruyter, Berlin/Boston, 2014) p. 938.

[187] L. Onsager, *Reciprocal Relations in Irreversible Processes. I.*, Physical Review **37**, 405–426 (1931).

[188] L. Bergmann and C. Schaefer, *Lehrbuch der Experimentalphysik Band 3: Optik*, 10th ed. (Walter de Gruyter, Berlin, New York, 2004) p. 1430.

[189] F. Träger, ed., *Springer Handbook of Lasers and Optics*, 2nd ed. (Springer Berlin Heidelberg, Berlin, Heidelberg, 2012) p. 1694.

[190] S. Yamamoto and I. Matsuda, *Measurement of the Resonant Magneto-Optical Kerr Effect Using a Free Electron Laser*, Applied Sciences **7**, 662 (2017).

[191] J. Hamrle, J. Pištora, B. Hillebrands, B. Lenk, and M. Münzenberg, *Analytical expression of the magneto-optical Kerr effect and Brillouin light scattering intensity arising from dynamic magnetization*, Journal of Physics D: Applied Physics **43**, 325004 (2010).

[192] J. Zak, E. Moog, C. Liu, and S. Bader, *Additivity of the Kerr effect in thin-film magnetic systems*, Journal of Magnetism and Magnetic Materials **88**, L261–L266 (1990).

[193] A. Hubert and G. Traeger, *Magneto-optical sensitivity functions of thin-film systems*, Journal of Magnetism and Magnetic Materials **124**, 185–202 (1993).

[194] V. Kamberský, L. Wenzel, and A. Hubert, *Magneto-optical interference and diffraction in isotropic and uniaxial multilayers*, Journal of Magnetism and Magnetic Materials **189**, 149–164 (1998).

[195] J. Hamrle, J. Ferré, M. Nývlt, and Š. Višňovský, *In-depth resolution of the magneto-optical Kerr effect in ferromagnetic multilayers*, Physical Review B **66**, 224423 (2002).

[196] V. Vlaminck and M. Bailleul, *Spin-wave transduction at the submicrometer scale: Experiment and modeling*, Physical Review B **81**, 014425 (2010).

[197] Y. Zhang, T. Yu, J. lei Chen, Y. guang Zhang, J. Feng, S. Tu, and H. Yu, *Antenna design for propagating spin wave spectroscopy in ferromagnetic thin films*, Journal of Magnetism and Magnetic Materials **450**, 24–28 (2018).

[198] W. Demtröder, *Experimentalphysik 2*, 6th ed., Springer-Lehrbuch (Springer Berlin Heidelberg, Berlin, Heidelberg, 2013) p. 482.

[199] M. L. Schneider, J. M. Shaw, A. B. Kos, T. Gerrits, T. J. Silva, and R. D. McMichael, *Spin dynamics and damping in nanomagnets measured directly by frequency-resolved magneto-optic Kerr effect*, Journal of Applied Physics **102**, 103909 (2007).

[200] J. M. Shaw, T. J. Silva, M. L. Schneider, and R. D. McMichael, *Spin dynamics and mode structure in nanomagnet arrays: Effects of size and thickness on linewidth and damping*, Physical Review B **79**, 184404 (2009).

[201] H. T. Nembach, J. M. Shaw, C. T. Boone, and T. J. Silva, *Mode- and Size-Dependent Landau-Lifshitz Damping in Magnetic Nanostructures: Evidence for Nonlocal Damping*, Physical Review Letters **110**, 117201 (2013).

[202] C. W. Sandweg, M. B. Jungfleisch, V. I. Vasyuchka, A. A. Serga, P. Clausen, H. Schultheiss, B. Hillebrands, A. Kreisel, and P. Kopietz, *Wide-range wavevector selectivity of magnon gases in Brillouin light scattering spectroscopy*, Review of Scientific Instruments **81**, 073902 (2010).

[203] O. Büttner, M. Bauer, S. O. Demokritov, B. Hillebrands, Y. S. Kivshar, V. Grimalsky, Y. Rapoport, and A. N. Slavin, *Linear and nonlinear diffraction of dipolar spin waves in yttrium iron garnet films observed by space- and time-resolved Brillouin light scattering*, Physical Review B - Condensed Matter and Materials Physics **61**, 11576–11587 (2000).

[204] A. A. Serga, S. O. Demokritov, B. Hillebrands, and A. N. Slavin, *Self-Generation of Two-Dimensional Spin-Wave Bullets*, Physical Review Letters **92**, 117203 (2004).

[205] T. Brächer, F. Heussner, P. Pirro, T. Fischer, M. Geilen, B. Heinz, B. Lägel, A. A. Serga, and B. Hillebrands, *Time- and power-dependent operation of a parametric spin-wave amplifier*, Applied Physics Letters **105**, 232409 (2014).

[206] J. R. Sandercock, *Tandem Fabry-Perot Spectrometers TFP-1 and TFP-2 HC - Operator Manual*, Tech. Rep. (Mettmenstetten, Switzerland, 2020).

[207] I. Neudecker, G. Woltersdorf, B. Heinrich, T. Okuno, G. Gubbiotti, and C. Back, *Comparison of frequency, field, and time domain ferromagnetic resonance methods*, Journal of Magnetism and Magnetic Materials **307**, 148–156 (2006).

[208] G. Woltersdorf, O. Mosendz, B. Heinrich, and C. H. Back, *Magnetization Dynamics due to Pure Spin Currents in Magnetic Double Layers*, Physical Review Letters **99**, 246603 (2007).

[209] Zurich Instruments, *UHF User Manual*, Tech. Rep. (Zurich, Switzerland, 2020).

[210] H. Schultheiss, X. Janssens, M. van Kampen, F. Ciubotaru, S. J. Hermsdoerfer, B. Obry, A. Laraoui, A. A. Serga, L. Lagae, A. N. Slavin, B. Leven, and B. Hillebrands, *Direct Current Control of Three Magnon Scattering Processes in Spin-Valve Nanocontacts*, Physical Review Letters **103**, 157202 (2009).

[211] M. Bailleul, D. Olligs, and C. Fermon, *Propagating spin wave spectroscopy in a permalloy film: A quantitative analysis*, Applied Physics Letters **83**, 972–974 (2003).

[212] M. Nakayama, K. Yamanoi, S. Kasai, S. Mitani, and T. Manago, *Thickness dependence of spin wave nonreciprocity in permalloy film*, Japanese Journal of Applied Physics **54**, 083002 (2015).

[213] V. E. Demidov, S. O. Demokritov, K. Rott, P. Krzysteczko, and G. Reiss, *Self-focusing of spin waves in Permalloy microstripes*, Applied Physics Letters **91**, 252504 (2007).

[214] P. Krivosik and C. E. Patton, *Hamiltonian formulation of nonlinear spin-wave dynamics: Theory and applications*, Physical Review B **82**, 184428 (2010).

[215] H. Suhl, *The theory of ferromagnetic resonance at high signal powers*, Journal of Physics and Chemistry of Solids **1**, 209–227 (1957).

[216] V. E. Demidov, H. Ulrichs, S. O. Demokritov, and S. Urazhdin, *Nonlinear scattering in nanoscale magnetic elements: Overpopulation of the lowest-frequency magnon state*, Physical Review B **83**, 020404 (2011).

[217] H. Schultheiss, K. Vogt, and B. Hillebrands, *Direct observation of nonlinear four-magnon scattering in spin-wave microconduits*, Physical Review B **86**, 054414 (2012).

[218] H. G. Bauer, P. Majchrak, T. Kachel, C. H. Back, and G. Woltersdorf, *Nonlinear spin-wave excitations at low magnetic bias fields*, Nature Communications **6**, 8274 (2015).

[219] K. Schultheiss, R. Verba, F. Wehrmann, K. Wagner, L. Körber, T. Hula, T. Hache, A. Kákay, A. A. Awad, V. Tiberkevich, A. N. Slavin, J. Fassbender, and H. Schultheiss, *Excitation of Whispering Gallery Magnons in a Magnetic Vortex*, Physical Review Letters **122**, 097202 (2019).

[220] Keysight Technologies, *Mixer Transmission Measurements Usingthe Frequency Converter Application in the PNA Microwave Network Analyzers - Application Note*, Tech. Rep. (USA, 2014).

[221] Keysight Technologies, *U3042AM04 - User's and Service Guide*, Tech. Rep. (USA, 2018).

[222] V. E. Demidov, H. Ulrichs, S. V. Gurevich, S. O. Demokritov, V. S. Tiberkevich, A. N. Slavin, A. Zholud, and S. Urazhdin, *Synchronization of spin Hall nano-oscillators to external microwave signals*, Nature Communications **5**, 3179 (2014).

[223] T. Hache, T. Weinhold, K. Schultheiss, J. Stigloher, F. Vilsmeier, C. Back, S. S. P. K. Arekapudi, O. Hellwig, J. Fassbender, and H. Schultheiss, *Combined frequency and time domain measurements on injection-locked, constriction-based spin Hall nano-oscillators*, Applied Physics Letters **114**, 102403 (2019).

[224] Keysight Technologies, *Improving Network Analyzer Measurements of Frequency-Translating Devices - Application Note*, Tech. Rep. (USA, 2014).

[225] B. Hillebrands, *Progress in multipass tandem Fabry–Perot interferometry: I. A fully automated, easy to use, self-aligning spectrometer with increased stability and flexibility*, Review of Scientific Instruments **70**, 1589–1598 (1999).

Acknowledgements – Danksagung

Die vergangenen drei Jahre meiner Doktorarbeit waren geprägt von Höhen und Tiefen. Die vorliegenden Ergebnisse wären ohne die Unterstützung von zahlreichen Personen nicht möglich gewesen. Bei den folgenden Personen möchte ich mich insbesondere bedanken:

Meinem Doktorvater *Prof. Dr. Rudolf Gross* für die Möglichkeit meine Doktorarbeit am Walther-Meißner-Institut durchführen zu können, für die sehr hilfreichen Kommentare zu diversen Manuskripte und zur vorliegenden Doktorarbeit und dafür bei schwierigen physikalischen Fragen immer ein einfaches Bild oder Erklärung parat zu haben. Weiters möchte ich mich für Ihren Einsatz bedanken, dass es noch zeitlich mit der Abgabe dieser Arbeit vor meinem Berufseinstieg geklappt hat.

Meinem Betreuer *Prof. Dr. Mathias Weiler* für seine intensive Unterstützung während der gesamten Promotionszeit. Vielen Dank für deine Hilfe und Zeit bei der Interpretation von Messdaten, beim Korrekturlesen der vorliegenden Arbeit und von Manuskripten und für dein stetes Interesse an meinem Fortschritt bei neuen Messungen/Projekten und beim Laboraufbau. Danke auch für die Freiheit, die du mir gelassen hast, dass ich meine Ideen selbstständig ausprobieren und umsetzen konnte, dass du mir bei Problemen unkompliziert geholfen und mit mir dein technisches (Labor-)Wissen und deine wissenschaftliche Leidenschaft geteilt hast. Ich wünsche dir alles Gute und viel Erfolg beim Aufbau deiner neuen Gruppe in Kaiserslautern.

PD Dr. habil. Hans Huebl für seine Hilfe bei messtechnischen und physikalischen Problemen und das stete Interesse an meinem Fortschritt. Danke für die vielen guten Ideen bei neuen Messungen und zur Verbesserung der Messaufbauten. Auch möchte ich mich für deine sehr kritischen Fragen zu jeglichen Messergebnissen und zu Manuskripten bedanken, die zu einem besseren Verständnis beigetragen haben. Ich habe erheblich von deinem profunden Wissen profitiert.

Dr. Matthias Althammer für seine Hilfe bei Fragen rund um Fabrikation, Sputtern am SUPERBOWL und bei Problemen mit dem Heliumkyrostaten. Danke für deine Ratschläge und Unterstützung bei der Umsetzung und Fehlerbehebung von dc-Experimenten, wenn sie zunächst nicht funktioniert haben.

Dr. Stephan Geprägs für seine humorvolle Art und für das ein oder andere offene Gespräch bei einem Kaffee. Vielen Dank für deine zahlreichen Ratschläge auch abseits unseres gemeinsamen Projekts und für deine Bemühungen bei der Übungsorganisation und den dazugehörigen Vorbesprechungen.

Prof. Dr. Wolfgang Belzig und *Dr. Akashdeep Kamra* für ihre Hilfe und theoretische Unterstützung zur Beschreibung der Magnon-Magnon Hybridisierung in Gadolinium Eisengranat. Mein besonderer Dank gebührt *Akash* für seine pragmatische Art schwierige physikalische Themen auch Experimentalphysikern verständlich zu erklären und für ein stets offenes Ohr für jegliche Art von (physikalischen) Fragen.

Dr. Andreas Bauer, *Franz Haslbeck* und *Prof. Dr. Christian Pfleiderer* für die langjährige Zusammenarbeit bei diversen Projekten rund um Skyrmionen in Cu_2OSeO_3, die zwar oft durch langwierge Diskussionen geprägt, aber gleichzeitig sehr lehrreich waren und für die Möglichkeit bei einigen Messzeiten am Forschungsreaktor FRM2 mithelfen zu können.

Ei Shigematsu und *Prof. Masashi Shiraishi* für die interessante Kollaboration zum Thema Spin-Orbit Torques in Ferromagnet-Halbleiter Bilagen und den kulturellen Austausch während der Forschungsaufenthalte hier in München.

Amine Wahada, *Lukas Geiling* und *Prof. Dr. Georg Woltersdorf* für die Unterstützung bei der Entwicklung der BLS-Software, insbesondere beim Testen und Debuggen der Software.

Meinen Bürokollegen, *Janine Gückelhorn*, *Yuki Nojiri*, *Leander Peis*, *Gabriele Rager*, *Stefan Weichselbaumer* und *Edwar Xie*, für die unterhaltsame und produktive Arbeitsatmosphäre im Büro.

Meinen Doktorandenkollegen der Magnetismus-Gruppe, *Luis Flacke*, *Janine Gückelhorn*, *Thomas Luschmann*, *Manuel Mueller*, *Daniel Schwienbacher* und *Tobias Wimmer*, für die produktive Zusammenarbeit, dass man sich gegenseitig bei Problemen unkompliziert geholfen hat und auch für die Einbringung von guten Ideen. Insbesondere möchte ich mich bei Daniel und Thomas für die “Coffee talks” bedanken, bei welchen nicht nur über Physik, sondern auch über Themen des täglichen Lebens gesprochen wurde, und auch für die Verlegung dieser ins Digitale während des Corona-Lockdowns.

Meinen “Vorgängern”, *Stefan Klingler* und *Hannes Maier-Flaig*, die mich während meiner Masterarbeit in die Breitband-FMR und in die Magnetisierungsdynamik eingeführt und mir die experimentiellen Feinheiten dieser Messtechnik beigebracht haben und somit ein solides Fundament für diese Doktorarbeit geliefert haben.

Meinen Bachelorstudenten *David Rogerson* und *Leonhard Hölscher* für ihren Einsatz und ihre Unterstützung bei der Fabrikation von Proben unter Verwendung des beliebten Laserschreibers für optische Spinwellen-Experimente.

Dem IT-Team, *Dieter Guratzsch*, *Matthias Opel* und *Michael Renger*, für ihre unkomplizierte Hilfe bei Computer-, Netzwerk- und Domänenrichtlinienproblemen.

Der Werkstatt, *Georg Nitschke*, *Mario Nodes*, *Christian Reichlmeier* und *Alexander Rößl*, für die Realisierung diverser Konstruktionen und für die unkomplizierte Hilfe bei kleineren oder größeren Problemen. Danke auch für die zahlreichen Ratschläge zum Zeichnen und zur Umsetzung von Bauteilen.

Andreas Russo und *Christoph Kastl* für ihre Hilfe bei elektronischen Problemen am Messequipment und elektrischen Problemen im Labor.

Tom Brenninger, *Astrid Habel* und *Sebastian Kammerer* für ihre Hilfe bei Problemen rund um die Dünnschichttechnik und Chemie.

Der Helium-Halle, *Peter Binkert*, *Jan Naundorf* und *Harald Schwaiger*, für die (kurzfristige) Bereitstellung von flüssigem Helium und Stickstoff für die Tieftemperaturexperimente.

Der Verwaltung, *Martina Meven*, *Andrea Person*, *Carola Siegmayer*, *Ludwid Ossiander*, und insbesondere *Emel Dönertas* für die unkomplizierte und unbürokratische Erledigung von administrativen Angelegenheiten, wodurch mehr Zeit für Physik blieb.

Meinen Eltern, *Ute* und *Bernhard*, für eure Unterstützung und für euren Rückhalt. Vielen Dank, dass ihr mir mein Studium ermöglicht habt und immer an mich geglaubt habt! Ohne euch wäre das alles nicht möglich gewesen.